



N70-34006
CR-109851

GESP-7041
JULY 1970

**A DESIGN STUDY FOR A
MAGNETOHYDRODYNAMIC POWER SYSTEM
FOR A NUCLEAR ELECTRIC PROPELLED
UNMANNED SPACECRAFT**

FINAL REPORT

COVERING THE PERIOD 26 MAY 1969 TO 25 MAY 1970

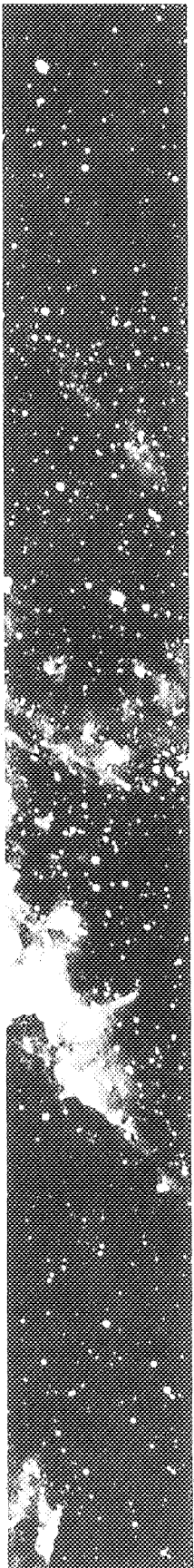
PREPARED UNDER CONTRACT JPL 952415

FOR

PROPULSION RESEARCH AND ADVANCED CONCEPTS SECTION
JET PROPULSION LABORATORY
4800 OAK GROVE DRIVE
PASADENA, CALIFORNIA, 91103

**CASE FILE
COPY**

GENERAL  ELECTRIC



**A DESIGN STUDY FOR A
MAGNETOHYDRODYNAMIC POWER SYSTEM
FOR A NUCLEAR ELECTRIC PROPELLED
UNMANNED SPACECRAFT**

FINAL REPORT

COVERING THE PERIOD 26 MAY 1969 TO 25 MAY 1970

PREPARED UNDER CONTRACT JPL 952415

FOR

PROPULSION RESEARCH AND ADVANCED CONCEPTS SECTION
JET PROPULSION LABORATORY
4800 OAK GROVE DRIVE
PASADENA, CALIFORNIA, 91103

THIS WORK WAS PERFORMED FOR THE JET PROPULSION LABORATORY,
CALIFORNIA INSTITUTE OF TECHNOLOGY AS SPONSORED BY THE
NATIONAL AERONAUTICS AND SPACE ADMINISTRATION UNDER
CONTRACT NAS7-100

ISOTOPE POWER SYSTEMS OPERATION

GENERAL  ELECTRIC

SPACE DIVISION

KING OF PRUSSIA PARK

P. O. Box 8661 • Philadelphia, Penna. 19101

This report contains information prepared by the General Electric Company under JPL subcontract. Its content is not necessarily endorsed by the Jet Propulsion Laboratory, California Institute of Technology, or the National Aeronautics and Space Administration.

The study reported in this document was led by R. M. Bernero under the direction of Dr. D. G. Elliott of JPL; the principal contributors were R. W. Drummond, Jr., Dr. N. A. Evans, A. S. Jacobsen, and Dr. D. D. Knight.

ABSTRACT

This report discusses the progress made in a one-year design study of nuclear-electric propelled unmanned spacecraft using a liquid metal magnetohydrodynamic (MHD) power system. The study guidelines and approach are defined here, and the characteristics of the launch vehicle, the thruster subsystem, and the payload and communications system are presented.

The MHD power conversion system is described and methods used to calculate MHD system parameters are discussed. This report includes a discussion of the arrangement and structural arguments used to select system configuration. The system startup technique is identified, and the detailed design and weight summaries are presented for systems of 100 kWe to 3 MWe power rating.

TABLE OF CONTENTS

<u>Section</u>		<u>Page</u>
1	INTRODUCTION	1-1
2	TECHNICAL DISCUSSION	2-1
2.1	MHD Power System Operation and Analysis	2-1
	2.1.1 Two-Component Liquid Metal MHD Power System	2-1
	2.1.2 MHD System Analysis	2-6
2.2	MHD Spacecraft Guidelines and Requirements	2-19
	2.2.1 Payload	2-19
	2.2.2 Thrust Subsystem	2-20
	2.2.3 Launch Vehicles	2-22
	2.2.4 MHD Baseline and Alternate Design Guidelines	2-27
2.3	Power System Synthesis	2-30
	2.3.1 MHD Power System Startup	2-30
	2.3.2 Shutdown and Restart	2-34
	2.3.3 Part Power Operation	2-36
	2.3.4 One or Two-Loop System	2-38
2.4	Configuration Tradeoffs	2-58
	2.4.1 General Arrangement Guidelines	2-58
	2.4.2 MHD Equipment Bay	2-58
	2.4.3 Spacecraft Structure	2-62
	2.4.4 Configuration Choice	2-74
2.5	Major Design Areas	2-76
	2.5.1 Reactor and Shield Design	2-76
	2.5.2 MHD Generator	2-83
	2.5.3 MHD Nozzle Assembly	2-99
	2.5.4 Valves, Piping and Pumps	2-106
	2.5.5 Radiator Design	2-115
	2.5.6 Structure and Insulation	2-136
	2.5.7 Electrical System Design	2-143
	2.5.8 Reliability and Redundancy	2-164
2.6	Parametric Analysis	2-166
	2.6.1 Special Detailed Analyses	2-167
	2.6.2 Selection of Baseline Design Parameters	2-182
	2.6.3 Cycle Efficiency Variation	2-189
	2.6.4 Cycle Temperature Variation	2-191
	2.6.5 Output Variation	2-200
2.7	Spacecraft Designs	2-203
	2.7.1 Baseline Design	2-203
	2.7.2 Alternate Baseline Design	2-216
	2.7.3 200 kWe Spacecraft	2-229
	2.7.4 400 kWe Spacecraft	2-239

TABLE OF CONTENTS (Cont'd.)

<u>Section</u>	<u>Page</u>
2.8	Mission Engineering 2-239
2.8.1	Spacecraft Guidance and Control 2-239
2.8.2	Mission Analysis 2-251
2.8.3	Operations 2-260
3	CONCLUSIONS 3-1
4	RECOMMENDATIONS 4-1
5	NEW TECHNOLOGY 5-1
6	REFERENCES 6-1
	APPENDIX A A-1

LIST OF ILLUSTRATIONS

<u>Figure</u>		<u>Page</u>
2-1	Lithium-Cesium MHD Cycle	2-1
2-2	NaK/N ₂ MHD Test System	2-3
2-3	NaK/N ₂ MHD Test System - Cutaway	2-3
2-4	Variable Velocity MHD Induction Generator	2-4
2-5	Sensitivity Factors for Net Power	2-11
2-6	Sensitivity Factors for Net Efficiency	2-11
2-7	Effects of Varying T _{wall} from One to Ten Millimeters	2-12
2-8	Cesium-Lithium MHD Power System with Impinging Jet Separator	2-13
2-9	Flight Fairing Weight and Payload Penalty (Titan IIIC/7)	2-24
2-10	Effect of Shroud Retention on Payload Capability (Titan IIIC/7)	2-25
2-11	MHD Fluid System Startup Schematic	2-32
2-12	MHD Loop without Separate Reactor Loop	2-39
2-13	MHD Loop with Separate Reactor Loop	2-39
2-14	MHD Cesium Mass/Flow/Time Model	2-45
2-15	Arrangement of Cesium Pipes Near Payload	2-55
2-16	Cesium Pipe Shielding	2-57
2-17	MHD Equipment Arrangement with One Recuperator	2-60
2-18	MHD Equipment Arrangement with Two Recuperators	2-61
2-19	MHD Spacecraft Configuration No. 1, Conical Radiator	2-63
2-20	MHD Spacecraft Configuration No. 2, Conical Radiator	2-64
2-21	MHD Spacecraft Configuration No. 3, Conical and Cylindrical Radiator	2-65
2-22	MHD Spacecraft Configuration No. 4, Triform Radiator	2-66
2-23	MHD Spacecraft Configuration No. 5, Triform Radiator	2-68
2-24	Cylindrical/Conical Radiator, Typical Cross-Section	2-71
2-25	Triform Configuration, Typical Section with Stabilizing Bracing	2-73
2-26	Triform Support Structure	2-73
2-27	MHD Reactor Diameter	2-77
2-28	MHD Reactor Weight	2-77
2-29	MHD Reactor and Shield	2-78
2-30	MHD Reactor Control Actuator	2-79
2-31	NASA LeRC Fast Reactor	2-80
2-32	Shield Heating Rates	2-82
2-33	Variation of Radiation Shield Thickness with Reactor Power Level and Payload Separation Distance	2-83
2-34	Baseline Design MHD Generator	2-84
2-35	Cooling Pipes in MHD Stator Block	2-90
2-36	MHD Stator Cooling Passages at Lithium Duct Face	2-90
2-37	Proposed MHD Generator Duct	2-96
2-38	Comparison of Theoretical and Experimental Pressure Profiles in a Two-Phase Nozzle	2-100

LIST OF ILLUSTRATIONS (Cont'd.)

<u>Figure</u>		<u>Page</u>
2-39	MHD Nozzle and Diffuser Size - Baseline Design	2-100
2-40	Creep Rupture Data for Nb-1Zr Alloy Sheet Tested in Vacuum at in Vacuum at 982 ^o C	2-103
2-41	Effect of One-Hour Pre-Test Annealing Treatment on Creep Rupture Strength of Nb-1Zr Alloy Sheet Tested in Vacuum at 982 ^o C	2-103
2-42	Four-Nozzle Assembly	2-105
2-43	Schematic View of High Temperature Alkali Metal Valve	2-108
2-44	Potassium Boiler Feed Pump - Cutaway	2-112
2-45	Potassium Boiler Feed Pump - Final Assembly.	2-112
2-46	DC Conduction Pump	2-113
2-47	Specific Weight Relationship - Three-Phase Helical Induction Pump	2-116
2-48	Concept 1, Cylindrical or Elliptical Tube Fin	2-117
2-49	Concept 2, Rectangular Channel	2-117
2-50	Concept 3, Hexagonal Honeycomb	2-118
2-51	Concept 4, Rectangular Channel Fin	2-118
2-52	Comparison of Condensing Configurations	2-119
2-53	Fluid Comparison-Finned Cylinder Geometry	2-119
2-54	Duct - Chamber Concepts - Unpenetrated Duct	2-120
2-55	Duct - Chamber Concepts - Penetrated Duct	2-120
2-56	Evaluation Summary and Recommendations	2-124
2-57	Vapor Chamber Wick Geometry	2-126
2-58	Main Radiator Panel Details	2-127
2-59	Cruciform and Conical Total Radiator Weight Comparison	2-129
2-60	Offset Conduction Fin Radiator Geometry	2-130
2-61	Effect of Redundancy on Radiator Weight for the Indirect Condensing System	2-134
2-62	Coefficient of Thermal Expansion vs. Temperature for Various Radiator Materials	2-135
2-63	Main Radiator Assembly (Section)	2-138
2-64	MHD - Size of Disposable Structure	2-140
2-65	MHD - Spacecraft, Unit Force and Moment Distribution	2-140
2-66	MHD Spacecraft Main Radiator Weight of Non-Disposable Support Structure vs. Length of Radiator and Reactor Weight	2-141
2-67	MHD Spacecraft Main Radiator Weight of Disposable Support Structure vs. Length of Radiator and Reactor Weight	2-141
2-68	MHD Spacecraft Electrical Power System	2-149
2-69	Power Inverter	2-151
2-70	Capacitor Specific Weight, T = 200 ^o C	2-157
2-71	Interconnection, First and Last Winding	2-158
2-72	Typical Circuit, Screen Circuit Interrupter	
2-73	Relation Between Coil Loss Factor, α and External Conductor Resistance Factor, γ	2-171

LIST OF ILLUSTRATIONS (Cont'd.)

<u>Figure</u>		<u>Page</u>
2-74	MHD Stator Winding Geometry	2-173
2-75	Coil Geometry and Temperatures	2-177
2-76	Coil Cooling Fins	2-177
2-77	Auxiliary Radiator Geometry	2-180
2-78	Capacitor Heat Rejection	2-182
2-79	Total Weight Variation	2-186
2-80	Secondary Radiator Area Variation	2-186
2-81	Primary Radiator Area Variation	2-187
2-82	Effect of Velocity Factor Variation	2-190
2-83	Variation of Powerplant Weight with System Efficiency	2-193
2-84	Effect of Temperature and Li/Cs Mass Ratio on Efficiency	2-196
2-85	Effect of Temperature on Weight	2-197
2-86	Optimization of Case 11 (Run 35)	2-199
2-87	Effect of Inlet Field on Weight	2-199
2-88	Power Output Definition	2-201
2-89	Cycle Conditions, MHD Power System Baseline Design	2-204
2-90	Fluid Schematic Diagram, MHD Power System	2-205
2-91	MHD Baseline Design Spacecraft, In-Board Profile	2-207
2-92	MHD Bay Arrangement	2-211
2-93	Fluid Schematic Diagram, Alternate MHD Power System	2-217
2-94	Inboard Profile, Alternate Baseline Design with Cylindrical Radiator	2-219
2-95	Inboard Profile, Alternate Baseline Design with Tripanel Radiator	2-225
2-96	NaK-Cooled Cesium Condenser	2-227
2-97	Equivalent Weight of Radiator Feed Pipe vs. Pipe Diameter	2-228
2-98	Cycle Conditions, 200 kWe MHD Power System	2-230
2-99	Inboard Profile, 200 kWe MHD Spacecraft	2-231
2-100	Cycle Conditions, 400 kWe MHD Power System	2-240
2-101	Inboard Profile, 400 kWe MHD Spacecraft	2-241
2-102	Jupiter Orbiter, All Low Thrust	2-253
2-103	Capture Time to Achieve Jovian Orbit of 1.17×10^6 Miles	2-253
2-104	Net Payload vs. Trip Time - Saturn V Hybrid Thrust	2-256
2-105	Net Payload vs. Trip Time - Titan III L4 Hybrid Thrust	2-258
2-106	Launch Vehicle Payload Capability - Intermediate Class	2-259
2-107	Launch Vehicle Payload Capability High Energy Class	2-259
2-108	MHD Powered Spacecraft Modules	2-261
2-109	Overall Ground Flow Plan	2-264

LIST OF TABLES

<u>Table</u>		<u>Page</u>
2-1	Communications Subsystems Characteristics	2-19
2-2	Guidelines for Thrust Subsystem Design	2-20
2-3	Thruster Power Supply Requirements	2-21
2-4	Thrust Subsystem Weights	2-22
2-5	Candidate Launch Vehicles for MHD Spacecraft (Titan III C/7)	2-23
2-6	Maximum Payload Capability with Shroud Ejection at 280 Seconds	2-26
2-7	Maximum Earth Orbital Altitude for a 30,000 Pound Payload with Shroud Jettison at 280 Seconds (Titan III C/7)	2-26
2-8	Maximum Payload Capability at 630 nm with Shroud Ejection After Achieving Earth Orbit (Titan III C/7)	2-26
2-9	Part Power Operation	2-37
2-10	Cesium-133 (N, γ) Cross Sections	2-44
2-11	MHD Spacecraft - Weight Estimates for Configuration Tradeoff	2-69
2-12	Spacecraft Weight and Tip Deflection Summary	2-70
2-13	MHD Reactor Design Characteristics	2-76
2-14	Baseline Design MHD Generator Dimensions	2-86
2-15	Baseline Design MHD Generator Dynamic Characteristics	2-87
2-16	Baseline Design MHD Generator Power Summary	2-88
2-17	Constant Slip 200 kWe MHD Generator Dimensions	2-93
2-18	Constant Slip 200 kWe MHD Generator Dynamic Characteristics	2-94
2-19	Constant Slip 200 kWe MHD Generator Power Summary	2-95
2-20	MHD Nozzle Wall Thickness	2-104
2-21	MHD System Valves - Baseline Design	2-107
2-22	Lithium Accumulator Design Parameters - Baseline Design	2-110
2-23	Cesium Accumulator Design Parameters - Baseline Design	2-111
2-24	Summary of Radiator Weights (No Structural Considerations)	2-121
2-25	Summary of Radiator Weights	2-123
2-26	Radiator Comparisons	2-133
2-27	Auxiliary Radiators - Baseline Design	2-137
2-28	Generator Electrical Characteristics	2-146
2-29	Spacecraft Electrical Load Requirements	2-147
2-30	MHD Baseline System Power Balance	2-150
2-31	Electrical System Weight Summary	2-151
2-32	Capacitor Designs	2-156
2-33	Compensating Capacitance Weight	2-158
2-34	Total Capacitance Weight	2-159
2-35	Auxiliary Power Conditioning Characteristics	2-162
2-36	Parameters Varied in Design Selection (Runs 1 to 11)	2-183
2-37	Parametric Weights and Areas (Runs 1 to 11)	2-185
2-38	Parameters Varied in Design Selection (Runs 12 to 20)	2-187
2-39	Parametric Weights and Area (Runs 12 to 20)	2-188

LIST OF TABLES (Cont'd.)

<u>Table</u>		<u>Page</u>
2-40	Runs with Velocity Factor Varied	2-190
2-41	Effect of Efficiency Variation	2-192
2-42	Effect of Temperature and Li/Cs Ratio	2-195
2-43	Runs for Optimization at 1900 ^o F and 2000 ^o F	2-198
2-44	Weights for Optimization at 1900 ^o F and 2000 ^o F	2-198
2-45	Output Power Variation	2-202
2-46	Specific Power Comparison	2-202
2-47	MHD Baseline Spacecraft Weight Summary	2-209
2-48	MHD Baseline Spacecraft Weight Summary Corrected for Conversion to Alternate Design	2-221
2-49	NaK-Cooled Cesium Condenser Design Characteristics	2-228
2-50	Weights - 200 kWe MHD Spacecraft	2-233
2-51	Weights - Baseline Design Spacecraft	2-234
2-52	200 kWe MHD Generator Dimensions	2-235
2-53	200 kWe MHD Generator Dynamic Characteristics	2-236
2-54	200 kWe MHD Generator Power Summary	2-237
2-55	200 kWe Generator Electrical Characteristics	2-238
2-56	Weights - 400 kWe MHD Spacecraft	2-243
2-57	400 kWe MHD Generator Dimensions	2-244
2-58	400 kWe MHD Generator Dynamic Characteristics	2-245
2-59	400 kWe MHD Generator Power Summary	2-246
2-60	400 kWe Generator Electrical Characteristics	2-247
2-61	Power Plant Weights Used for Mission Analysis	2-254
2-62	Jupiter Orbiter Payloads, All Low Thrust	2-255

1. INTRODUCTION

1. INTRODUCTION

From May 26, 1969, to May 25, 1970, the General Electric Company performed a design study for the magnetohydrodynamic (MHD) power system for a nuclear-electric propelled unmanned spacecraft. This work was performed for the Jet Propulsion Laboratory under contract number JPL-952415 and was based on MHD system technology being developed by the Jet Propulsion Laboratory. The purpose of this study was to provide size, weight and mission performance estimates for nuclear-electric propelled unmanned spacecraft using liquid metal MHD power systems rated at 100 kWe to 3 MWe. This study is also intended to guide future MHD development by discovering specific requirements associated with spacecraft power system design. The spacecraft design of principal interest was one whose unconditioned power output is a nominal 300 kWe. The weight goal for this spacecraft was 10,000 pounds including reactor, shielding, MHD conversion equipment, power distribution and conditioning equipment, thruster subsystems, and structure.

The work of this study program was divided into four principal tasks:

- a. Task 1 - System Evaluation - The purpose of this task is to establish guidelines and design requirements for the program and to measure the designs generated in the program against these guidelines and requirements.
- b. Task 2 - Power Plant Design - The purpose of this task is to provide the engineering analysis and design information necessary for spacecraft design layout. This will include parametric analyses to identify the influence of major plant variables on power plant and spacecraft characteristics. This task also includes evaluation of the effects of changes in technology levels associated with the power plant components.
- c. Task 3 - Spacecraft Design - The purpose of this task is to define the arrangement, mechanical design, and weight estimation for the MHD spacecraft designs.
- d. Task 4 - Mission Analysis and Engineering - The purpose of this task is to perform the analysis necessary to evaluate the mission capabilities of the various spacecraft, and to perform a preliminary assessment of prelaunch, launch and flight operations, specifically with respect to aerospace nuclear safety.

In the first half of this one-year study, a baseline design spacecraft and power plant were developed. This baseline design is a 275 kWe system and assumes reasonable extension

of component technology based on current test work. In the second half of the study, the spacecraft and the power plant design were varied parametrically to evaluate the effects of changes in output power level and operating parameters, and to evaluate the effects of improvements in the technology of key components.

The MHD spacecraft study was performed concurrently with a design study of a thermionic reactor power system for nuclear-electric propelled unmanned spacecraft (JPL Contract No. 952381). Wherever possible, design bases for the MHD spacecraft were made the same as those for the thermionic spacecraft in order to provide a clear comparison of these two power systems. In particular, the MHD spacecraft baseline design uses the same payload thruster subsystem and mission profile as the Phase I thermionic reactor spacecraft.

The one-year study has been completed and a series of spacecraft designs have been synthesized. These include a baseline design with a nominal 275 kWe power plant, an alternate baseline which uses a conduction fin radiator instead of a vapor chamber fin radiator, a 200 kWe system and a 400 kWe system; systems of 100 kWe to 3MWe were also analyzed.

2. TECHNICAL DISCUSSION

2. TECHNICAL DISCUSSION

2.1 MHD POWER SYSTEM OPERATION AND ANALYSIS

2.1.1 TWO-COMPONENT LIQUID METAL MHD POWER SYSTEM

2.1.1.1 Power System Fluid Flow

Figure 2-1 illustrates the flow arrangement by which a two component (i. e., Li/Cs) liquid metal MHD power system can generate useful amounts of electrical energy with no moving parts except the fluids themselves. As the illustration shows, lithium is heated in a heat source and injected into expansion nozzles with liquid cesium. Upon mixing in the nozzles, heat transfer from the lithium causes the cesium to boil. The lithium liquid does not boil but is dispersed in the stream by the boiling of the cesium. As the lithium breaks up into smaller and smaller drops its surface-to-volume ratio increases, enhancing heat transfer to the cesium vapor. The high specific heat of lithium along with a relatively high lithium mass flow to cesium mass flow ratio enables the cesium boiling and expansion in the nozzles to take place at almost isothermal conditions.

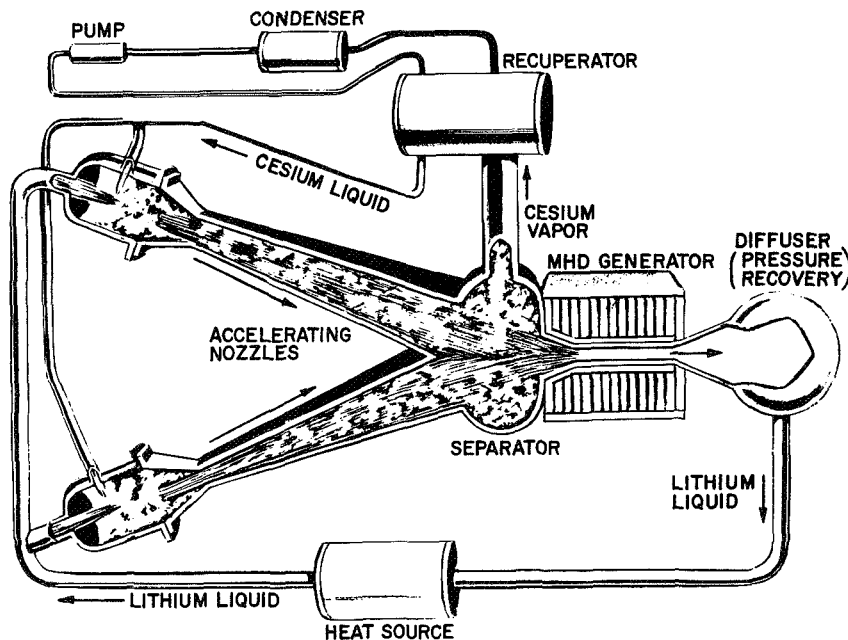


Figure 2-1. Lithium - Cesium MHD Cycle

The expansion of the cesium vapor as it travels down the nozzles accelerates the entrained lithium liquid droplets to high velocities. At the convergence of the two nozzles the impingement of the two streams requires each to undergo a change in direction. The resulting lateral acceleration imposed on the flow stream causes its phases to separate into strata with the lithium collecting in the center of the combined stream and the cesium vapor moving out to the sides of the stream. The combined lithium streams enter a diffuser where the stream pressure is raised threefold to dissolve any remaining cesium bubbles and the lithium stream then passes through the MHD generator duct where much of the stream's kinetic energy is converted to electrical energy. (See Paragraph 2.1.1.2, following). At the MHD generator exit, the lithium stream passes into a diffuser where most of its remaining kinetic energy is converted to pressure head in order to pump the lithium through the heat source and back around to the nozzle entrance with more heat.

The cesium vapor, separated from the lithium streams at the nozzle exists, is passed out through a recuperator to a condenser. The condensed cesium is pumped electromagnetically back through the recuperator to the nozzle entrances where it can be vaporized again.

A simpler method of stream separation is used in the single nozzle MHD test system shown in Figures 2-2 and 2-3. This system, which is currently being used for development testing by Dr. D. G. Elliott at Jet Propulsion Laboratory, operates at about room temperature with NaK alloy in place of lithium and compressed nitrogen gas expanding to accelerate the liquid phase. In this arrangement, the vapor and liquid streams are separated by impingement on an inclined plate, see Figure 2-3. The single nozzle system, although simpler to construct, is less desirable because of the skin friction losses the liquid stream suffers in passing across the separator plate. In the dual nozzle system the opposing streams, moving at equal speeds, provide the flow diversion thus eliminating this friction loss and improving system overall efficiency from about six and one-half percent to almost eight percent. Although the dual nozzle system will require flow balancing, its improved efficiency makes it the more attractive design.

2.1.1.2 The Variable-Velocity MHD Induction Generator

The induction MHD generator is attractive because it allows:

- a. A. C. power generation with a better capability of transformation and conditioning.

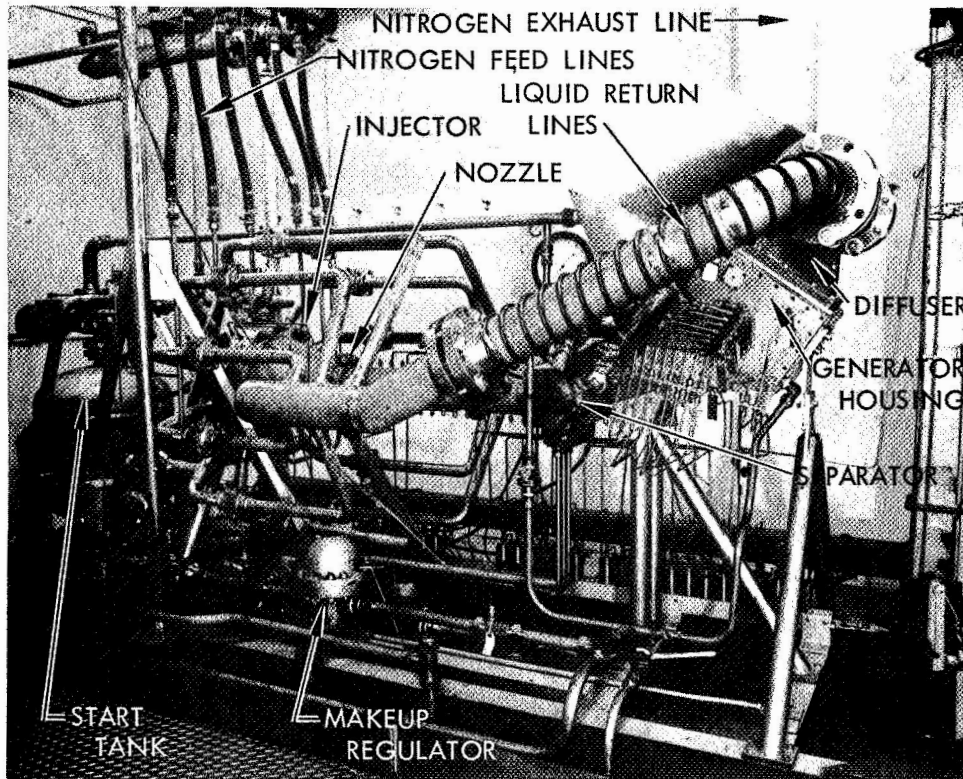


Figure 2-2. NaK/N₂ MHD Test System

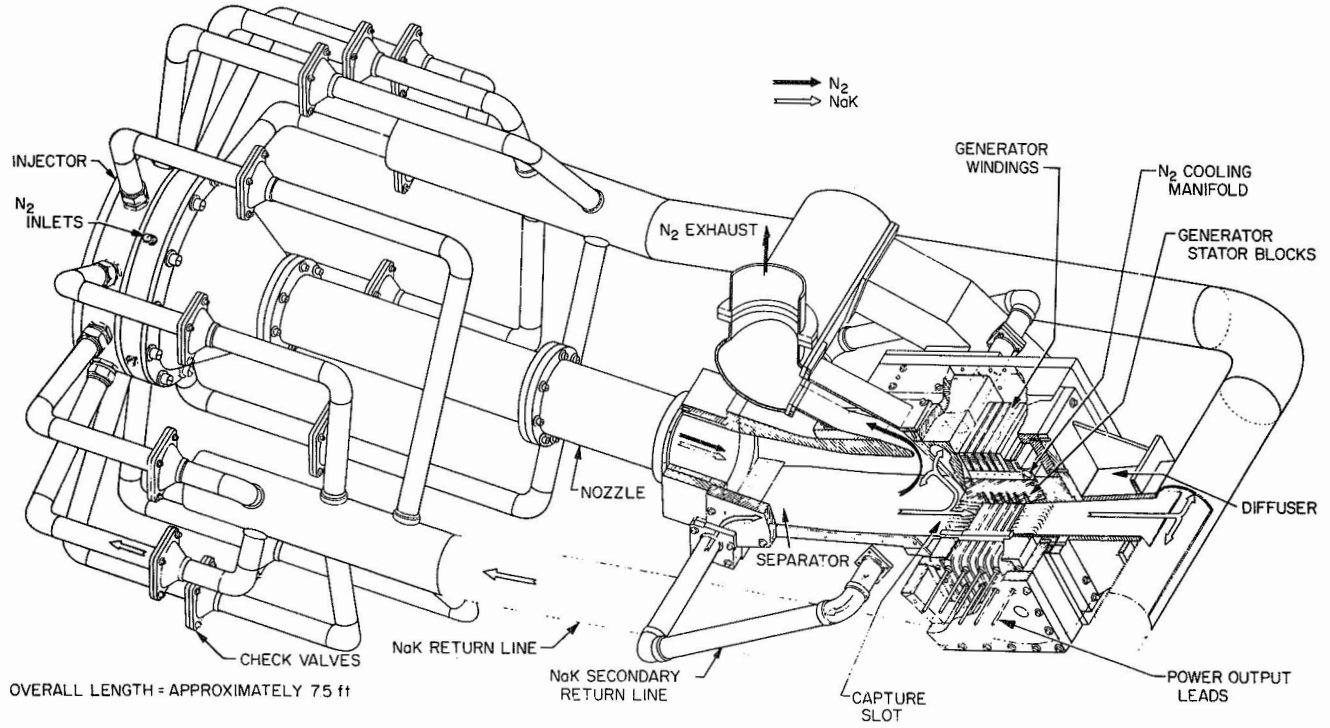


Figure 2-3. NaK/N₂ MHD Test System - Cutaway

- b. Electrodeless operation in the presence of high temperature corrosive working fluids
- c. Control over the output voltage by appropriate choice of winding turns.

One form of such a generator is essentially a flat development of the more familiar rotating, solid conductor generator, and consists of a pair of iron stators separated by conducting side plates to form a duct through which a liquid metal conductor is forced to flow (Figure 2-4). The stator blocks are slotted to carry windings which produce a travelling wave magnetic field in the direction of fluid flow. The liquid metal travels faster than the field, causing currents to be induced in the direction shown. The fluid retardation caused by the currents must be accommodated by progressive expansion of the channel. Completion of the current loop, and the resulting magnetic field induces an AC voltage in the windings with, typically, a resultant power output.

The simple, flat development briefly described above has the very serious drawback that the original, continuously rotating magnetic field has been interrupted between the cut, and separated, ends. There is an ohmic power loss in the windings when producing the travelling

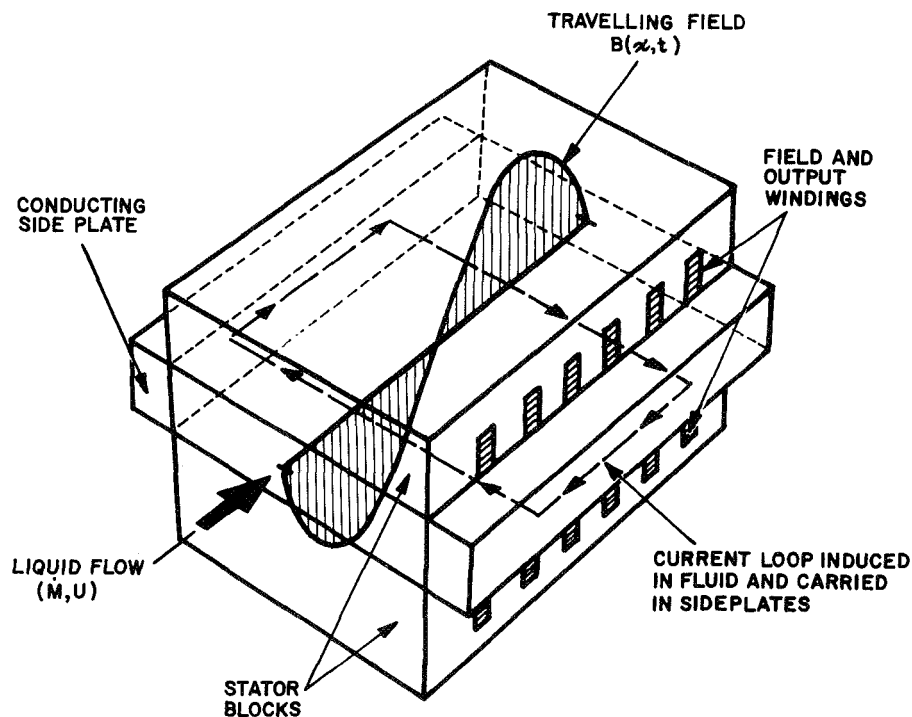


Figure 2-4. Variable Velocity MHD Induction Generator

wave, and for a fixed wave amplitude, the winding dissipation increases proportionately with the number of wavelengths imposed on the generator. The use of a single wavelength generator minimizes the winding loss, but maximizes the end losses due to the abrupt initiation and termination of the magnetic field. However, analysis (Reference 3) has shown that, the proper inclusion of a compensating pole in slots at each end of the generator together with the design constraint along the generator that $cBU_s = \text{constant}$ (where c is the duct width, B the magnetic field rms value at x , and U_s is the velocity of the zero crossing of the magnetic field at x), will re-produce exactly the familiar rotating induction machine voltage, $V_i(x, \theta) = cBU_s \sin(\theta_x - \omega t)$ where:

$$s = \frac{U - U_s}{U_s}$$

is the slip between the fluid and wave velocities, and U is the fluid velocity at x , with θ the value of ωt when the zero field crossing is at x .

The fact that $cBU_s = \text{constant}$ allows considerable design flexibility. However, it has been found (Reference 3), for simpler conditions, more beneficial to hold c constant rather than B constant, so that the design constraint becomes $BU_s = \text{constant}$. In the face of frictional effects, it turns out that the maximum local internal generator efficiency is

$$\eta_x = \frac{1 - s}{1 + s}$$

with the optimal slip being $s = \left(1 + H_a^2\right)^{-1/2}$ where

$$H_a^2 = \frac{\sigma b B^2}{\rho c C_f}$$

is the Hartmann number, with

- σ = The fluid conductivity,
- b = the channel height
- ρ = the liquid density and
- C_f = the skin friction coefficient.

This optimal s then sets the relation $U_s = U_s(U)$ to produce the maximum electric output, P_o , through the resulting maximum η_x . A first choice of inlet magnetic field B_1 then establishes $B = B(U)$ since $BU_s = \text{constant}$, with the final value of B_1 resulting from optimization of the generator efficiency, η_g . This latter optimization results from the fact that, although P_o increases indefinitely with field, the winding losses start increasing rapidly at a certain field value.

With the generator width c fixed as indicated above, the duct height distribution is determined directly from the mass continuity requirement, while the duct length results from electrically (and frictionally) retarding the fluid at constant pressure and optimal slip to the desired exit velocity. This exit velocity is such that, with satisfactory diffusion, sufficient pressure is available to return the liquid to the energy source without pumping.

2.1.2 MHD SYSTEM ANALYSIS

As described in Reference 2, the analysis of the MHD Power System is based on the analytical approach developed by Dr. D. G. Elliott and others at Jet Propulsion Laboratory. During the first half of this study, the computer programs developed at JPL were converted from CAL to basic FORTRAN IV, combined into a single MHD System program and modified to calculate other parameters of interest to the spacecraft designer.

2.1.2.1 MHD Generator Analysis

2.1.2.1.1 Generator Analysis Assumption - The assumptions employed in analyzing the generator are as follows:

1. The slip and the field are varied to maintain rotating-machine internal electrical efficiency $\eta_o = (1 + s)^{-1}$ at each point, where s is the slip $(U - U_s)/U_s$ between the fluid velocity U and the magnetic field wave velocity U_s .
2. The pressure is constant from inlet to exit of the traveling-wave region.
3. The losses in the generator consist only of (1) fluid ohmic losses from the fluid current necessary for the required retarding force, (2) shunt end currents and eddy currents in the compensating poles, (3) wall friction, (4) winding loss, and (5) the increase in those losses due to the limitations on field amplitude and slot area from iron saturation. There are no losses from: (1) variation of magnetic

field and current density across the height of the channel, (2) boundary layer currents, (3) increased friction due to MHD effects, (4) ohmic losses in the copper side-electrodes, (5) departure of the magnetic field from sinusoidal wave-form, and (6) eddy currents in the walls.

Assumption 1 requires the generator to operate with the product of field and wave velocity, BU_s , held constant from the inlet to the exit of the traveling-wave region. With this constraint, the current in the fluid is the same at every point as it would be in a constant-velocity generator and the efficiency of power generation in the fluid is $(1 + s)^{-1}$ at every point. The possible disadvantage of a constant- BU_s design is that the field in the upstream part of the generator must be lower than would be optimum at the same fluid velocity in a constant velocity generator, because of the reduced upstream field required to maintain $BU_s =$ constant while not saturating the iron at the downstream end. The possibility of higher overall efficiency with a departure from the constant- BU_s case assumed here has not been explored.

Assumption 2, constant pressure in the traveling-wave region, is adopted for simplicity. There is a possibility of higher cycle efficiency with a pressure rise in the generator, because of lower velocity and friction loss and because of reduced pressure recovery requirement in the downstream diffuser, but pressure-rise operation has not been explored.

Assumption 3 is the key one. Five loss mechanisms are adopted as being the only significant ones. All other losses, six of which are enumerated, are assumed to be negligible. The arguments for neglecting the six losses enumerated will be reviewed briefly:

1. Field and Current Density Variation Across the Channel Height - The efficiency of a constant-velocity generator using the exact field equations (both x and y variations accounted for) was calculated by Pierson (Reference 3) and the results compared with the "slit-channel case" ($B_x = 0$ and $B_y = \text{const}$) assumed here. Pierson found negligible efficiency decrease using the exact equations when $\pi b/L \ll 1$, where b is the channel height and L is the wavelength. In a typical lithium generator, the value of $\pi b/L$ is 0.2, and there was no more than 0.1 percent efficiency loss at this value in Pierson's analysis.
2. Boundary-Layer Currents - Boundary-layer currents of high density flow in the near-stationary part of the fluid near the wall. If the velocity profile is a fully-developed 1/7-power profile extending to the center of the channel, then the internal electrical efficiency cannot exceed 0.78 (Reference 4). But there is evidence (Reference 5) that the velocity profile is highly flattened in the generator, in which case the

boundary-layer shunt currents may cause only negligible losses. There is also the possibility of designing the generator with a wall that is retracted from the boundary of the flow, giving a "free-jet" effect which could further flatten the velocity profile.

3. Friction Increase - Friction increase due to MHD effects has been studied and found to exist, but only by about 10 percent at ratios of Reynolds number to Hartmann number of interest in this application. To account for this and other possible effects, a factor of increase in friction of 1.3 is employed in the program.
4. Side-electrode Losses - The ohmic losses in the canned copper side-electrodes can be reduced as much as desired by giving them a large cross section, but at some point they begin to interfere with the coils. Thus, this loss reduces to an optimization problem between coil loss and axial-conductor loss. Preliminary design studies have indicated that the side-electrodes can have sufficient area for negligible loss if skin effect is not too great, but further studies are required.
5. Non-sinusoidal Waveform - The loss due to the finite number and width of the winding slots was analyzed in Reference 6. An efficiency loss of 3 percentage points was calculated for a generator employing 24 slots. The calculations were pessimistic in that they did not consider the smoothing out of the waveform that occurs in practice due to fringing. Hence, a 15 degree spacing between slots can be expected to give negligible loss compared with a continuous current sheet. In the power system energy balance, account is taken of this inefficiency by deducting 3 percent from the generator output.
6. Wall Currents - Operation without wall currents requires achievement of a wall which is both thermally and electrically insulating. A slotted, cesium-purged refractory-metal wall with ceramic between it and the stator, and a vacuum interface with the stator, is one concept proposed; alternatives include bare ceramic walls and coated ceramic walls.

The net effect of excluding the six losses enumerated is to make the calculations optimistic by an amount which might only be a few percentage points but could be much larger. Pending further experiments, the present analysis will be considered to predict the generator performance ultimately achievable after careful development.

2.1.2.1.2 Generator Program Analysis - Input data for the lithium mass flow, lithium density, the inlet and outlet velocities and the chosen constant duct width immediately allow calculation of the duct entry and exit heights, using the mass continuity equation. This is followed by calculation of the inlet Reynolds member (based on the inlet hydraulic diameter) and allows determination of an average, corrected turbulent skin friction coefficient to account for the

changing duct height, side wall contributions and MHD effects on the velocity profile. A calculation of the fluid input kinetic power to the travelling wave region is followed by a determination of the assumed constant travelling wave iron gap (based on duct inert height and wall thickness input data), compensating pole iron gaps and copper coil conductivity based on a chosen operating temperature.

With a chosen value of inlet magnetic field B_1 the inlet Hartmann number can be calculated. This leads to a value of optimum inlet slip s_1 for maximum local efficiency and determination of the inlet wave velocity V_{s_1} , thus fixing the required constant value of $BU_s = B_1 U_{s_1}$. The exit slip s_2 can be calculated iteratively and will then allow determination of the generator frequency duct length and the gross power output. Calculation of the gap flux voltage induced per coil turn completes the set of quantities dependent on the chosen value of inlet magnetic field.

The next section of the program deals with the coordinates and the value of slip s for each copper winding slot. The desired number of slots is an input parameter, but the actual number may be slightly less due to geometric constraints at the end of the duct. With s known at a slot, then calculations can be made for lithium velocity, duct height, wave velocity, magnetic field, and currents through the fluid and the windings.

The next calculations are related to the slot dimensions, the sector length over which each slot is assumed to be effective, and the electrical aspects of the windings. The slots in the travelling wave region are treated separately from the end slots which carry the current for the compensating poles. Advantage is also taken of the less restrictive iron and copper losses by appropriate shaping and positioning of the end slots in the last section of calculations.

The electrical performance of each winding slot is calculated by using the previously computed appropriate slip value. Results are obtained for the various contributions to the power balance (including friction and ohmic effects), together with the induced voltage per turn and the reactive power which dictates the corrective capacitance requirement.

2.1.2.1.3 Generator Variable Sensitivity - Before the generator and cycle programs were combined, the generator program was run with parameter variation to determine variable sensitivity. The rounded input data for the base case used for this determination are:

M1	U1	U2	c	I8(1) UPSTREAM COMP POLE EDDY CURRENT AMP. TURNS	I8(2) DWNSTRM COMP POLE EDDY CURRENT AMP TURNS	L(1) UPSTR COMP POLE LENGTH	L(2) DWNSTRM COMP POLE LENGTH	H1 INLET CHANNEL HEIGHT	H2 EXIT CHANNEL HEIGHT	I(1) WALL THICKNESS	I(6) INLET FIELD (RMS)
FLOW RATE Kg/sec	INLET VEL. m/sec	EXIT VEL. m/sec	CHANNEL WIDTH m	Amp	Amp	cm	cm	cm	cm	mm	Tesla
90	118	61	0.23	175	140	5	5	1.7	1.7	2.5	0.46

The principal results for this case were:

$$P_{\text{induc}} = 337.9 \text{ kW},$$

$$P_{\text{coil}} = 8.04 \text{ kW},$$

$$P_{\text{net}} = 329.8 \text{ kW},$$

$$P_{\text{reac}} = 1248.5 \text{ kW}, \text{ and}$$

$$\text{net efficiency } \eta_{\text{net}} = 0.730.$$

The program was then run to determine the effect on the base case values of varying one input quantity at a time. This quantity X (=U1, M1, etc. in turn) was varied over a small range about the base case value, X_{ref} , to determine a sensitivity factor

$$\frac{dQ}{dX} \times \frac{X_{\text{ref}}}{Q_{\text{ref}}}$$

where Q was an output quantity such as P_{net} , η_{net} , P_{reac} and P_{coil}

The sensitivity actors for P_{net} in Figure 2-5 show that U1, M1 and U2 are by far the most influential on net power, while, from Figure 2-6, M1, U2 and C have the most effect on net efficiency. These sensitivity factors can be useful for interpolation when a particular operating point is required.

It should be noted that the variation of X about X_{ref} probably produces values of η_{net} less than the optimum value presumed associated with the reference base case by adjustment of B_1 .

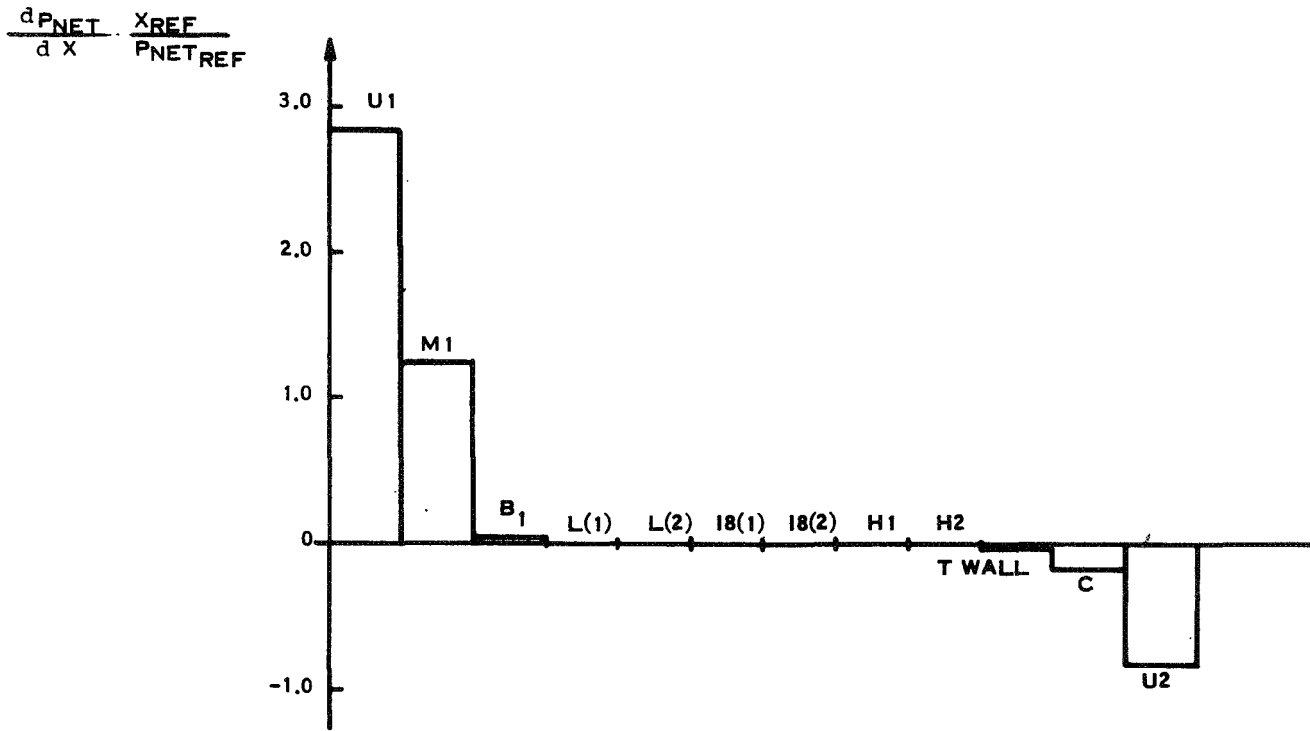


Figure 2-5. Sensitivity Factors for Net Power

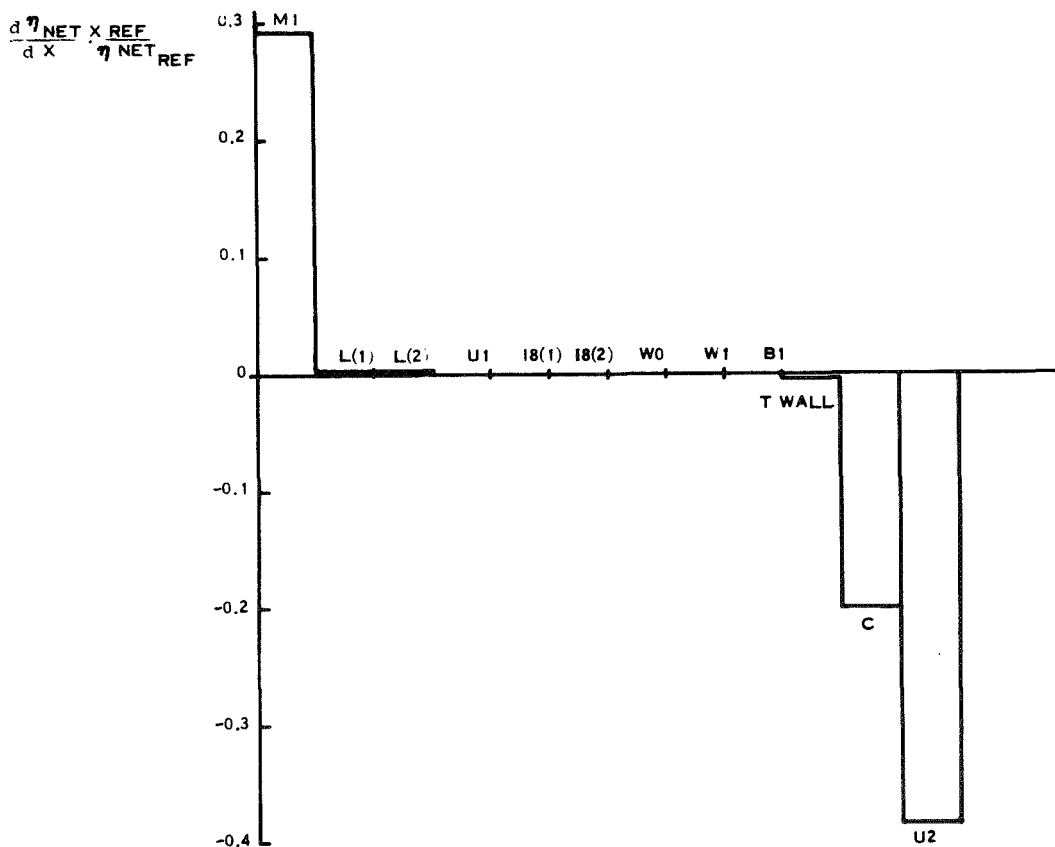


Figure 2-6. Sensitivity Factors for Net Efficiency

It was initially rather surprising that the wall thickness, t_{wall} , had almost no effect on P_{net} and η_{net} . Since wall thickness has a direct bearing on lithium duct heat transfer to the stator block, and incorporation of methods to suppress wall currents, its effects were investigated further. As seen in Figure 2-7 the principal effects of increasing t_{wall} from one to ten millimeters are to double the reactive power and produce a roughly proportionate increase in copper coil dissipation. These cause significant penalties in capacitor weight and low temperature radiator area.

The decrease in P_{net} and η_{net} are relatively modest, being, of course, directly coupled to P_{coil} .

2.1.2.2 MHD Cycle Analysis

A cesium-lithium MHD power system with an impinging-jet separator is shown schematically in Figure 2-8.

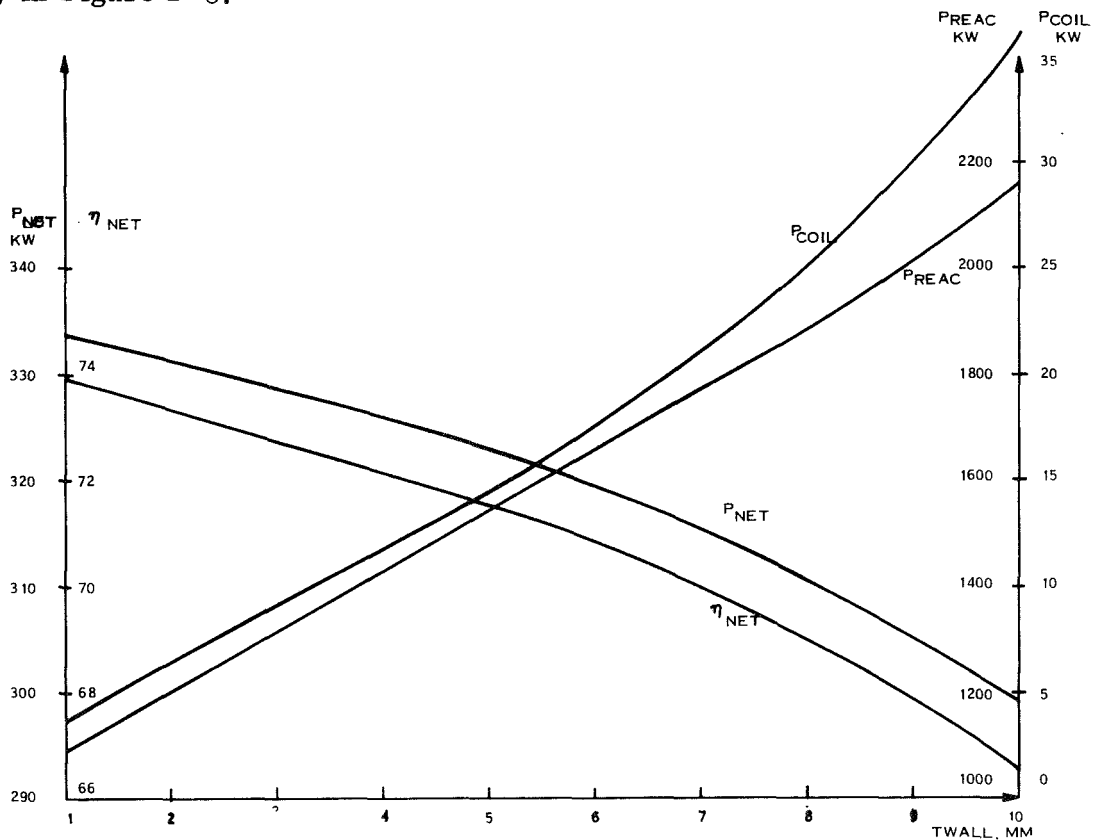


Figure 2-7. Effects of Varying T_{wall} From One to Ten Millimeters

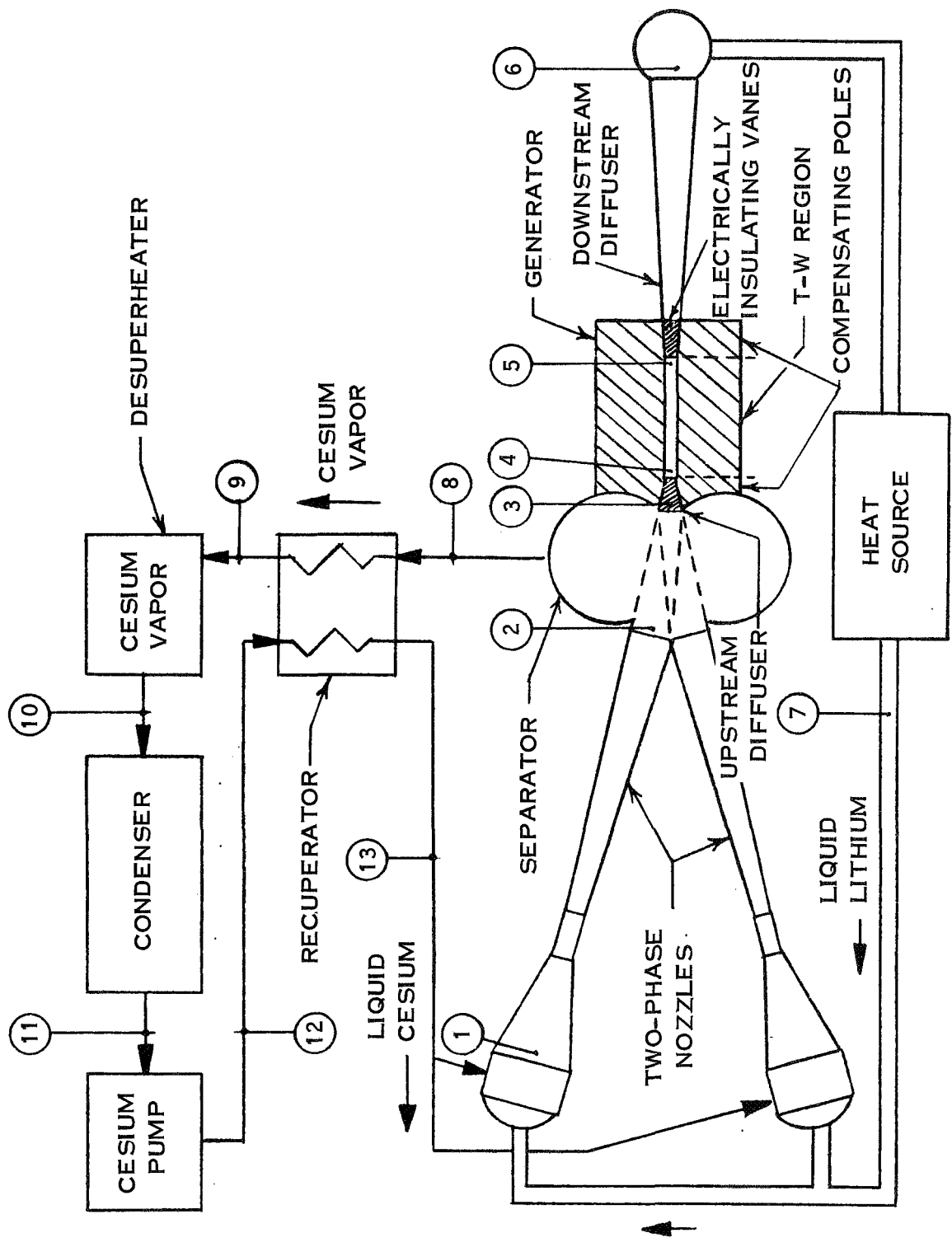


Figure 2-8. Cesium-Lithium MHD Power System with an Impinging-Jet Separator

Liquid lithium and liquid cesium enter a pair of two-phase nozzles and mix at low velocity and high pressure. Heat transfer from the lithium to the cesium vaporizes the cesium. The two-phase mixture expands to low pressure at the nozzle exits, accelerating the liquid lithium to high velocity.

The two-phase jets from the nozzles impinge on each other at an angle, and the inward momentum drives the lithium drops together to form a coalesced two-phase jet of substantially reduced vapor void fraction.

The jet enters the upstream diffuser where the pressure of the cesium-lithium mixture is increased until the cesium is dissolved in the lithium. The liquid stream then enters the generator.

In the generator the stream of lithium (containing a few percent of cesium) is decelerated by electromagnetic retarding force. The force is adjusted to leave sufficient velocity for the lithium to flow through the downstream diffuser to the pressure required at the inlet of the heat source. The lithium is reheated in the heat source and returned to the nozzles.

The cesium vapor leaving the impinging-jet separator flows to a recuperator where the cesium is desuperheated, and where the lithium vapor is condensed, to the extent permitted by the heat sink capacity of the liquid cesium leaving the cesium pump.

The remaining cesium superheat is removed in a desuperheater. The saturated cesium vapor is condensed in the condenser, and the condensate is pumped to the liquid side of the recuperator by the cesium pump. After being heated in the recuperator the cesium is returned to the nozzles.

2.1.2.2.1 Cycle-Analysis Assumptions - The assumptions employed in analyzing the cycle are as follows:

1. The concentration of cesium dissolved in the lithium is the equilibrium value for the prevailing temperature and pressure at each point in the system.
2. The nozzle exit conditions are those given by the two-phase, two-component nozzle program of Reference 7.

3. Any liquid lithium entrained with the cesium vapor leaving the separator is separated out and returned to the impinging jets or elsewhere in the lithium loop before the cesium vapor enters the recuperator.
4. A compensated AC generator is used, and the compensating poles coincide with the upstream diffuser and with the vaned portion of the downstream diffuser.
5. The losses in the upstream diffuser consist of: (1) friction on the walls and insulating vanes (used for electrical loss reduction) corresponding to 1.3 times flat-plate skin friction and (2) electrical losses due to the AC compensating field of the generator.
6. The efficiency of the downstream diffuser without vane-friction or electrical losses is 0.85.
7. The additional losses in the downstream diffuser are: (1) friction on the insulating vanes corresponding to 1.3 times flat-plate skin friction and (2) electrical losses due to the AC compensating field of the generator.
8. There are no electrical losses in the walls of the upstream or downstream diffusers, or in the generator channel, due to the AC generator.
9. The pressure in the generator is constant from inlet to exit.
10. The temperature difference between the cesium vapor entering the recuperator and the liquid cesium leaving the recuperator is 50°K.
11. The cesium pump is driven by electric power from the MHD generator, and all power dissipated is transferred to the cesium being pumped.
12. The heat rejected by the cycle is the heat required to cool and condense the cesium vapor from the recuperator exit condition to the saturated liquid state at the condenser exit pressure, including the heat required to cool the small amount of lithium mixed with the cesium.
13. The pressure drop across the nozzle injection orifices is 5 psi, and the injection velocity is 30 ft/sec.

Assumption 1, equilibrium cesium dissolving, implies transfers of several percent of cesium into and out of liquid solution in fractions of a millisecond. No information is available on cesium-lithium solution rate, and the validity of this assumption is not known.

If equilibrium concentration did not occur, the nozzle performance would be improved but the efficiency of the diffusers would be decreased. Calculations assuming non-dissolving cesium in a system with a surface-impingement separator showed that the two effects would be about equal and the cycle efficiency with non-dissolving cesium would be about the same as with equilibrium dissolving. With an impinging-jet separator however, the upstream diffuser losses with non-dissolving cesium would probably be unacceptable without some added mechanical removal of cesium vapor from the jet before entering the capture slot. Thus, the rate of cesium dissolving affects the design of the system, but it probably does not greatly affect overall cycle efficiency.

Assumption 2, the validity of nozzle exit conditions from Reference 7, is well verified by experiments with water-nitrogen mixtures. Uncertainties in cesium-lithium properties, including the dissolving rate, could change the nozzle exit velocity a few percent from the values given by the nozzle program.

An additional requirement for Assumption 2 to be valid is that the separator duct must have about 40 percent more area than the nozzle exit to allow radial expansion of the cesium jet as its velocity equalizes with that of the slower liquid jet.

Assumption 3 requires removal from the cesium exhaust of a liquid flow equal to 0.5 to 1.0 percent of the nozzle liquid flow rate, in the case of the best present surface-impingement separators. Several times as much lithium might have to be removed with an impinging-jet separator where a curved target is not available for collecting the smaller drops. A satisfactory method of returning the collected liquid to the lithium stream with an impinging-jet separator has not yet been demonstrated; reinjection into the impinging jets causes increased dispersion. The penalty of liquid remaining with the cesium might be preferable, since the recuperator liquid-side sink capacity would increase almost as much as the added heat load, falling short only by the 50°K minimum ΔT (Assumption 10). A velocity reduction factor is one of the inputs to the cycle analysis program, and with this factor the user can supply any penalty believed attributable to returning the lithium from the cesium exhaust. Supplying a factor of 1.0

implies that either there is no liquid loss or that all lithium is returned and remixed at full velocity with the impinging jets.

Assumption 4, the utilization of an AC induction generator, represents the best choice both for generator efficiency and ease of power conditioning. A DC generator might be thought to offer better efficiency, but the voltage across the channel in a DC generator causes shunt end currents extending farther upstream and downstream than can be suppressed by insulating vanes of reasonable length. An AC generator, on the other hand, operates at ground potential throughout the fluid, except locally in the compensating poles where relatively short insulating vanes can suppress the losses.

The second part of Assumption 4, overlapping of the compensating poles and diffusers, represents a logical combining of processes within a single region to reduce friction losses.

Assumption 5 restricts the upstream diffuser losses to 1.3 x flat-plate friction, plus electrical losses from the compensating flux. The friction losses observed in the limited tests conducted to date with vaned upstream diffusers could be correlated by applying a factor of between 2 and 3 to flat-plate friction, or they could be correlated by an impact loss in which all of the flow intercepted by the ~ 0.02 -inch thick vanes (5 percent of the total flow) was stagnated. Another source of loss, and perhaps the most likely, is two-phase slip or shock effects at the diffuser entrance. Whatever the loss source, Assumption 5 postulates a reduction in upstream diffuser loss from an observed 2.5 x, to an assumed 1.3 x, flat-plate friction.

The electrical losses included in Assumption 5 are calculated by a procedure which agreed roughly with some limited data on a small-scale generator, but accurate experiments on the fluid electrical losses in the compensating poles are lacking.

Assumption 6, an efficiency of 0.85 for the downstream diffuser before adding vanes and electrical losses, is well verified by liquid diffuser experiments (Reference 8).

Assumption 7 for the losses added to the downstream diffuser by the vanes and electrical effects has the same uncertainties as Assumption 5, but to a lesser extent because only liquid flow is involved.

Assumption 8, no electrical losses in the walls, is contingent on development of a thermally insulating, electrically insulating wall which exposes only metal to the lithium stream.

Assumption 9, constant pressure in the generator, is adopted for simplicity.

Assumption 10, 50°K minimum recuperator ΔT , should allow adequate heat flux at the hot end. The ΔT at the cold end is typically 200 to 300°K because of the lithium condensation on the vapor side.

Assumption 11 specifies a cesium pump design utilizing power from the AC generator either directly or after conditioning, with the electrical components at the cesium temperature. If lower electrical temperatures were employed there would be a requirement for radiation of some power at the lower temperature, but the cesium sink capacity would increase by an equal amount and there would be no change in cycle heat rejection.

Assumption 12 limits the heat rejection considered to that from the cesium vapor (and the lithium vapor mixed with it) only. Additional heat losses from cooling of the generator and other components and from stray losses are not considered in the heat balance or cycle efficiency.

Assumption 13, 5 psi injection pressure drop, is a value at which stable nozzle operation has been demonstrated. The assumed inlet velocity of 30 ft/sec, required only in calculating the nozzle inlet area (the effect on exit velocity is negligible), corresponds to 2.0 psi dynamic pressure of the lithium, and should be attainable with 5 psi injector pressure drop.

2.1.2.2.2 Cycle Program Analysis - The MHD cycle program employs twenty independent variables, including η_g (efficiency of the travelling wave region of the generator), f (generator frequency) and ϕ_c (compensating pole flux) which are supplied by the generator program. These generator supplied terms are used in the cycle program's energy balance to calculate the raw generator output (η_g) and the compensating pole losses (f and ϕ_c). Reference 2 contains a detailed description of the cycle program analysis.

2.2 MHD SPACECRAFT GUIDELINES AND REQUIREMENTS

2.2.1 PAYLOAD

For the purpose of this study, an allowance of one metric ton, 2205 pounds, was specified for the scientific payload and its communication system; an allowance of 1 kWe was made for payload power. The communications subsystem characteristics were tentatively identified (see Table 2-1) and seem reasonable. No detailed breakdown of the composition of the one ton payload is available. A payload equipment bay approximately nine feet in diameter and 15 inches high was allowed to contain the payload equipment, excluding the deployable antenna; its surface area is adequate for the payload thermal control radiator. It was not deemed necessary to pursue detailed payload definition and description in this study because the study results and conclusions drawn are relatively insensitive to even large changes in payload weight, volume, and power. In a net spacecraft weight of 10,000 to 20,000 pounds, another thousand pounds more or less is not a drastic change; in the 60 to 100-foot long spacecraft, the 15-inch payload bay is a short section; 1 kWe is a mere fraction of the 200 to 400 kWe available.

TABLE 2-1. COMMUNICATIONS SUBSYSTEM CHARACTERISTICS

Low Gain Antenna (Receiving)	
Diameter	6 inches
Weight (including cable)	2.5 pounds
Deployment Structure Weight	Negligible
High Gain Antenna (Transmitting)	
Diameter	9 feet
Weight (including cable)	31 pounds
Deployment Structure Weight	8 pounds
Power Input	800 watts
Power Transmitted	200 watts
Bit Rate (120 feet diameter receiving antenna)	10^4 bits/sec
Transmitter	
Weight	20 pounds
Size	6 x 6 x 20 inches

2.2.2 THRUST SUBSYSTEM

The thrust subsystem for the MHD spacecraft has been defined by Reference 9 and has the following general characteristics:

- a. Spacecraft propulsion is provided by 31 equal size electron bombardment ion thruster engines using mercury as the propellant.
- b. Six spare thrusters will be provided for a total of 37 units. Considering switching and power conditioning requirements, six spares provide one spare for each group of five operating thrusters.
- c. Thrust vector control will be provided by a three-axis attitude control system (two-axis translation, one-axis gimbal).

Guidelines for thrust subsystem design are given in Table 2-2. Individual thruster power supply requirements are listed in Table 2-3, and subsystem weights are given in Table 2-4.

TABLE 2-2. GUIDELINES FOR THRUST SUBSYSTEM DESIGN

1. Total Conditioned Power to Thrusters	240 kW
2. True Specific Impulse	5000 seconds
3. Number of Thrusters	37
4. Thruster Redundancy	20 percent
5. Attitude Control	Electric Propulsion System
6. Maximum Envelope Diameter	10 feet
7. Thrust Duration	10,000 hours
8. Technology	Estimated for 1980

TABLE 2-3. THRUSTER POWER SUPPLY REQUIREMENTS

Supply Number	Supply Name	Type	Output (1)	Nominal Rating						Max Rating			Control Range, A
				Volts	Amps	Watts	Reg (%)	Peak Ripple	Volts	Amps	Amps Limit (2)		
1	Screen	DC	V	3100	2.32	7200	1.0 (V)	5	3200	2.32	2.60	2.0 - 2.4	
2	Accelerator	DC	F	2000	0.02	40	1.0 (V)	5@ 0.2A	2100	0.20(3)	0.21	----	
3	Discharge	DC	V	35	8.3	290	1.0 (V)	2	150@ 50 mA	9@ 37V	10	7.5 - 9.0	
4	Mag - Man.	DC	F	15	0.7	11	1.0 (I)	5	20	1.0	1.0	----	
5	Cath Htr(4)	AC	F	10	4.0	40	5.0	5	11	4.4	4.1	----	
6	Cath Keeper	DC	F	10	0.5	5	1.0 (I)	5	150@ 50 mA	1.0@ 20 V	1.0	----	
7	Main Vapor.	AC	V	0.6	1.0	1	Loop	5	8(5)	2.0	2.2	0.5 - 1.5	
8	Cath Vapor	AC	V	0.3	0.5	1	Loop	5	8(5)	1.0	1.1	0.2 - 0.8	
9	Neut Cath Htr	AC	F	10	2.0	20	5.0	5	11	2.2	2.2	----	
10	Neut Vapor.	AC	V	0.3	0.5	1	Loop	5	8 8(5)	1.0	1.1	0.2 - 0.8	
11	Neut Keeper	DC	F	10	0.5	5	1.0 (I)	5	150@ 50 mA	1.0@ 20 V	1.0	----	

(1) V = Variable, F = Fixed

(2) Current limit or overload trip level

(3) Current at this level for less than 5 min at low repetition rate

(4) Needed only during startup or until discharge reaches 3A

(5) Startup only

TABLE 2-4. THRUST SUBSYSTEM WEIGHTS

Component	Weight (pounds)
Thrusters (37)	585
Thrust Vector Control System	548
Miscellaneous (wiring, adapters, etc.)	<u>100</u>
	1,233

2.2.3 LAUNCH VEHICLE

This study began by considering the Titan IIC-7 and the Saturn V as the reference launch vehicles with the expectation that these two vehicles would offer the choice of either high thrust (chemical propulsion) or low thrust (ion propulsion) escape from earth with the different size MHD power plants. As spacecraft weights became available and the mission analysis was performed (see Section 2.8.2), it has become apparent that other launch vehicles may also be of interest. Table 2-5 lists the candidate launch vehicles and their principal characteristics. These are considered representative of the present and future launch vehicle capabilities which should be considered for an MHD-powered spacecraft. Development timing does, after all, limit flight by MHD-powered spacecraft to the 1980's and beyond; it is sufficient to identify launch vehicles which are now available or most probably will be available at the time of flight.

For spacecraft design and weight estimating purposes, the Titan IIC-7 launch vehicle with a 10-foot diameter flight fairing has been used.

Figure 2-9 shows the flight fairing weight and the payload penalty as a function of shroud length, assuming shroud jettison at 280 seconds into the mission. If the shroud is retained past earth orbital insertion, then the payload weight penalty will be equal to the shroud weight. It should be noted that as the terminal orbital altitude increases, the payload penalty decreases for normal shroud ejection since a larger portion of the ΔV is added after shroud ejection. The curves are based on the data supplied by the Martin Marietta Corporation.

TABLE 2-5. CANDIDATE LAUNCH VEHICLES FOR MHD SPACECRAFT

LAUNCH VEHICLE	FOR HIGH ENERGY ESCAPE FROM EARTH				FOR LOW ENERGY ESCAPE FROM EARTH			
	SA TURN V SIC/SII/SIVB	TIII L4/ CENTAUR (1)	TIII D7/ CENTAUR (1)	(1) (2) TIII D7/ CENTAUR BURNER II	TIII C7	TIII L2	TIII L4	SA TURN 2-STAGE SIC/SII
Core Diameters (ft)	33/33/22	15/10	10/10 Stretched	10/10/5.4	10 Stretched	15	15	33/33
Number of Strap-on Solids (3)	--	4	2	2	2	2	4	--
Payload into Circular Earth Orbit (lbs)	N/A	N/A	N/A	N/A	38,000 33,000 31,000	70,000 62,000 58,000	90,000 83,000 72,000	260,000 135,000 50,000
Payload to Jupiter (600 Days - L/V only)	20,000	8,000	3,500	3,600	N/A	N/A	N/A	N/A
Approximate Cost (Millions of Dollars)	> 100 (4)	35(5)	23(5)	24(5)	18.5(5)	21(5)	26(5)	~ 100(4)

(1) Centaur is a 10-ft. dia. core LH₂/LOX restartable upper stage.
(2) Burner II is a 5.4 ft. dia. core solid propellant final kick stage.
(3) All Titan III series vehicles listed here use 7-Segment 10-ft. dia. strap-on solid propellant zero stages.
(4) Estimated.
(5) Martin Marietta Corporation estimates.

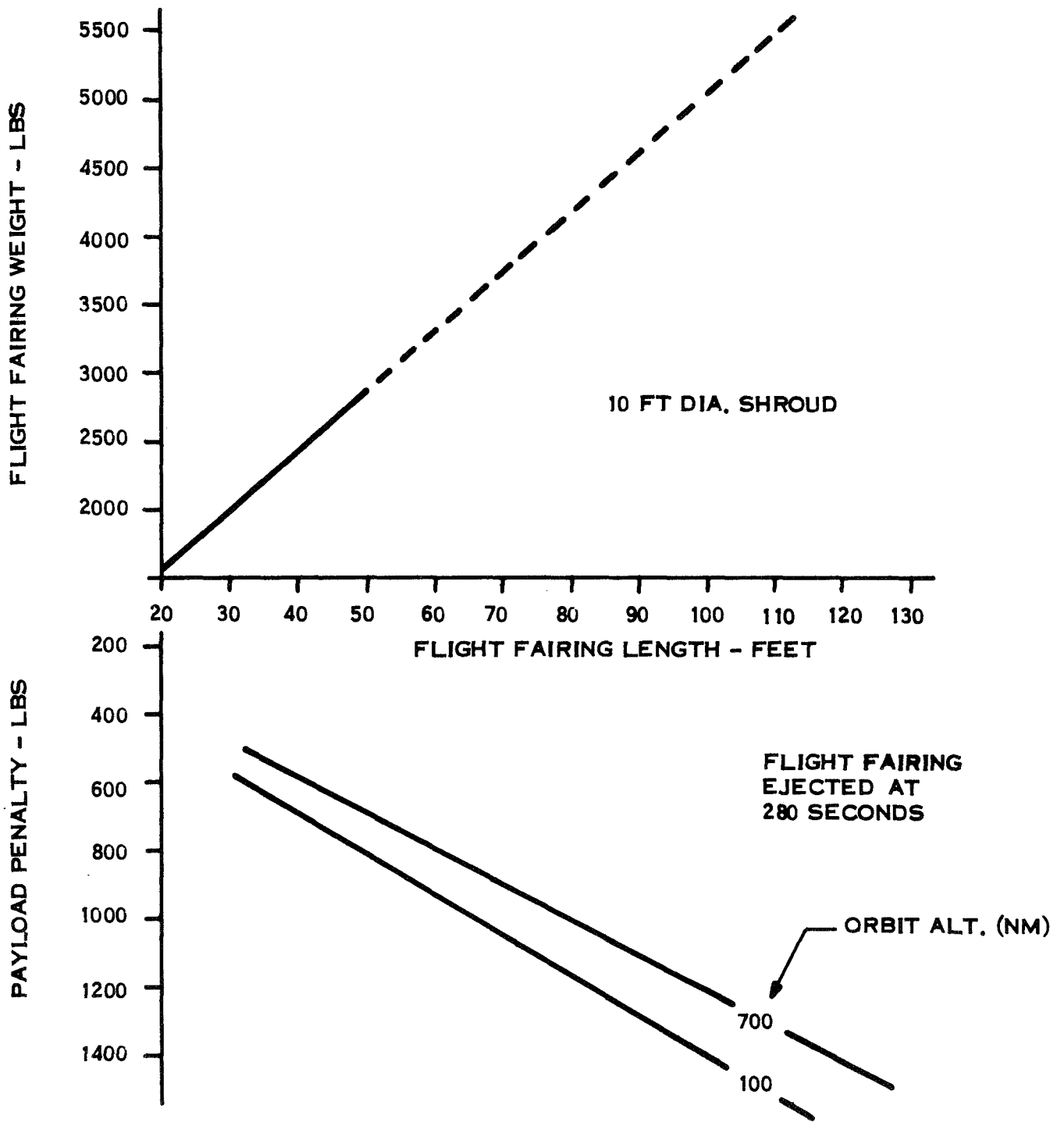


Figure 2-9. Flight Fairing Weight and Payload Penalty (Titan IIC/7)

The effect of shroud retention on payload capability is shown in Figure 2-10. The upper lines define the Titan IIC/7 payload capability for a 28.5 degree orbital inclination mission with shroud jettison occurring at 280 seconds into the mission. The lower curves show the effect of retaining the shroud through achievement of final Earth orbit.

Under nominal conditions, and with a 35-foot shroud, the vehicle can deliver 30,000 pounds into a 630 nm circular orbit. Employing longer shrouds, with jettison at 280 seconds, reduces the payload capability (initial mass in Earth orbit) as shown in Table 2-6.

Alternatively, injecting 30,000 pounds of payload into circular orbit will decrease the maximum possible orbit altitude as shown in Table 2-7.

If the shroud is jettisoned after achieving earth orbit (630 nm), the payload capability will be reduced as shown in Table 2-8.

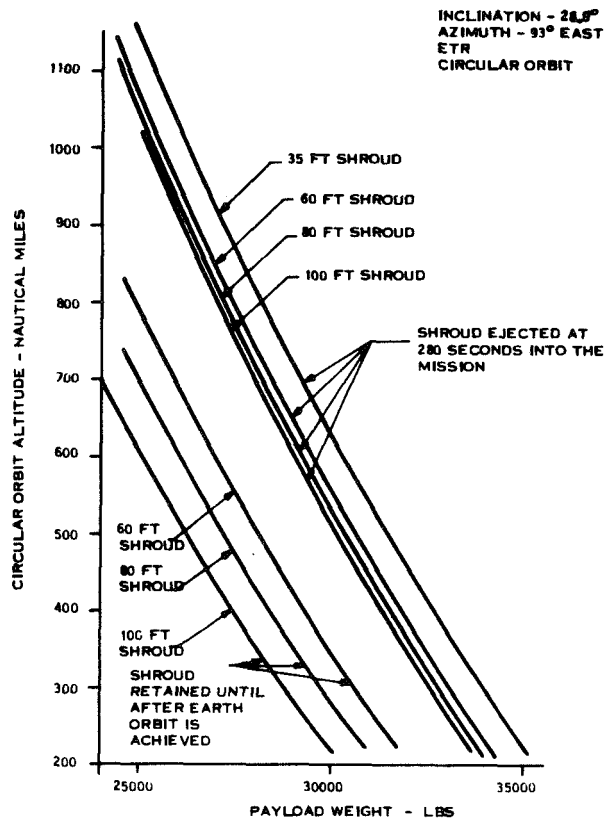


Figure 2-10. Effect of Shroud Retention on Payload Capability (Titan IIC/7)

TABLE 2-6. MAXIMUM PAYLOAD CAPABILITY WITH SHROUD EJECTION AT 280 SECONDS (Titan IIC/7)

Shroud Length (feet)	Shroud Penalty (pounds)	Maximum Payload Weight (pounds)
60	808	29,191
80	1021	28,978
100	1234	28,765

TABLE 2-7. MAXIMUM EARTH ORBITAL ALTITUDE FOR A 30,000 POUND PAYLOAD, WITH SHROUD JETTISON AT 280 SECONDS (TITAN IIC/7)

Shroud Length (feet)	Maximum Orbit Altitude (nm)
60	555
80	530
100	512

TABLE 2-8. MAXIMUM PAYLOAD CAPABILITY AT 630 NM WITH SHROUD EJECTION AFTER ACHIEVING EARTH ORBIT (TITAN IIC/7)

Shroud Length (feet)	Shroud Penalty (pounds)	Maximum Payload Weight (pounds)
60	3300	26,700
80	4200	25,800
100	5000	25,000

2.2.4 MHD BASELINE AND ALTERNATE DESIGN GUIDELINES

2.2.4.1 Baseline Design Guidelines

The system requirements and design guidelines for the baseline design have been identified; they are:

- a. Power Output - A nominal 300 kWe adjusted as necessary to match thrust system and other load requirements
- b. Launch Vehicle - The Titan IIC-7
- c. Mission - Jupiter planetary orbiter. Starting from a 750 nm earth orbit, the spacecraft will use low, ion thrust to spiral away from earth, reach Jupiter and decelerate into Jovian orbit. The estimated time periods and power levels are as follows:

Mission Mode	Power Level (kWe)	Time (Days)
Spiral Escape from Earth	300	50
Accelerating Thrust	300	160
Coast	30	120
Decelerating Thrust	300	270
Jovian Orbit Operation	30	(one orbit, 17 days minimum)

- d. MHD Cycle - One stage with two nozzles using impinging stream separation
- e. Cycle Inlet Temperature - 1800°F (corresponds to reactor outlet temperature minus ~100°F in a one-loop system)
- f. MHD Loop Containment Material - Cb-1Zr
- g. Radiator Type - Triform, stainless steel heat pipe
- h. Permanent Shield Materials - Lithium hydride and tungsten
- i. Radiation Dose Limits for Payload, Power Conditioning and Communications Equipment -

Neutron	10^{12} nvt > 1 Mev
Gamma	10^7 rad

j. Meteoroid Survival Criteria - The meteoroid model is based on the following:

1. Penetration Model

$$t = 0.5 m^{0.352} \rho_m^{1/6} v^{0.875}$$

2. Meteoroid Flux

$$\phi = \alpha m^{-\beta}$$

3. Non-Puncture Probability

$$P(0) = e^{-\phi AT}$$

4. Effective Thickness

$$t_{\text{eff}} = 0.432 t(\text{Jupiter})$$

where

t = radiator armor thickness, cm

ρ_m = meteoroid density, gm/cm³

m = meteoroid mass, gm

v = meteoroid velocity, km/sec

α = empirical coefficient

β = empirical exponent

P(O) = non-puncture probability

ϕ = cumulative meteoroid flux, number particles/m² sec

A = projected vulnerable area of the spacecraft (radiator), m²

T = exposure time, sec

Assumed Values

$$\rho_m = 0.5 \text{ gm/cm}^3$$

$$\alpha = 6.62 \times 10^{-15}$$

$$V = 20 \text{ km/sec}$$

$$\beta = 1.34$$

$$T = 7.2 \times 10^7 \text{ sec} \\ (20,000 \text{ hr})$$

$$P(O) = 0.95$$

2.2.4.2 Alternate Design Guidelines

The requirements and design guidelines for the alternate designs differ from those of the baseline design as follows:

- a. Power Output - 100 kWe, 300 to 500 kWe, and 3 MWe
- b. Launch Vehicle - Titan IIC-7 and Saturn V
- c. Missions
 1. 100 kWe to escape on Titan IIC-7
 2. 300 to 500 kWe to low orbit on Titan IIC-7
 3. 300 to 500 kWe to escape on Saturn V
 4. 3 MWe to low orbit on Saturn V
- d. MHD Cycle - 1-6 stage
- e. MHD Cycle Inlet Temperature - 1600 to 2200^oF
- f. MHD Containment Material - One advanced material
- g. Radiator Type - Flatplate or triform, stainless steel or columbium heat pipe.

In the course of the study, it became apparent that a system design using a condenser and conduction fin (pumped fluid) radiator should be investigated; as a result the "alternate baseline design" (Section 2.7.2) was so configured.

2.3 POWER SYSTEM SYNTHESIS

Before attempting the design and analysis of the baseline MHD powerplant, two basic questions had to be considered in order to synthesize a rational MHD power system. These two questions are the method of system startup and whether a one-loop or two-loop system is used.

2.3.1 MHD POWER SYSTEM STARTUP

Preliminary evaluation of startup techniques was made early in the study in order that the arrangements and design layouts could include all the components such as valves, lines, and reservoirs needed for plant operation.

2.3.1.1 Startup Requirements

Operation of this MHD power system requires steady two-phase flow in the MHD nozzles with phase separation at the generator entrance. The cesium needs heat from the lithium to boil and expand down the nozzle; the lithium needs the mechanical force of the expanding cesium to be accelerated down the nozzle. Thus, neither fluid stream can pass through the nozzles alone. In addition, some of the kinetic energy imparted to the lithium by the cesium in the nozzles is needed to pump the lithium. The first conclusion is, therefore, that the two streams must start into the nozzles together.

The NaK/N₂ test system (see Subsection 2.1) has been started by simultaneous injection of the two fluids into the empty nozzle with stable flow being achieved in seconds. The NaK/N₂ system is a cold test system with the compressed energy of the nitrogen providing the kinetic energy rather than heat taken from the NaK stream. In the hot Li/Cs system the simultaneous injection startup can be expected to work only if there is enough thermal energy in the lithium stream to cause boiling and expansion of the cesium at once, sufficiently to establish self-sustaining flow conditions. Some reduced temperature level may suffice to start system flow; however, lacking any detailed analysis or test data to support that conjecture, the second

conclusion is drawn with regard to startup technique - namely, that the two fluids will be injected at or near normal operating temperatures.

If the two fluids are to be injected into the nozzles for startup and steady state is to be achieved in seconds, the nuclear reactor heat source must already have been taken critical and warmed up since the nuclear reactor can probably be designed to take a large power swing in a matter of tens of seconds but requires hours to be taken critical and warmed up. It is reasonable to assume that aerospace nuclear safety considerations will require that the reactor does not go critical until the spacecraft is in a high, long-life orbit. Thus, a third conclusion about startup techniques can be drawn: startup injection will not take place until the spacecraft has been in orbit for hours. A reasonable time limit of five hours can be estimated by allowing one hour for orbit ephemeris verification and four hours for achieving criticality and warmup.

The two fluids of the MHD system, lithium and cesium, have melting points of 357°F and 84°F , respectively. Since the spacecraft will be in orbit at least one hour before the lithium begins to receive heat from the reactor, the lithium must be preheated before launch to prevent fluid freezing. The cesium, with a much lower freezing point, poses far less a problem. In order to fill the lithium system on the launch stand it will have to be preheated and then filled with hot molten lithium to assure complete fill. Thus, a fourth conclusion about startup is drawn, the lithium systems will be preheated and launched hot. The results of previous studies such as SNAP-50/SPUR indicate that preheat to 500°F should be adequate. The cesium system should receive enough heat from the lithium system to preclude freezing in it, although some way to warm up the radiator is needed.

The general requirements for the startup techniques can then be summarized:

- a. Startup will be by simultaneous injection of lithium and cesium into empty nozzles
- b. The two fluids will be injected at their normal operating temperatures
- c. Startup will take place only after about five hours in orbit
- d. The lithium system will be preheated to 500°F at launch.

2.3.1.2 System Arrangement for Startup

Figure 2-11 is a schematic diagram of the MHD fluid system with the necessary valves and other equipment added so that the system can be started. The entire system can be evacuated through the four evacuation and fill connections with the following valve lineup:

LV-1	open
LV-2	open
LV-4	open to reactor bypass line
CV-1	open
CV-2	open

After the system is evacuated, LV-1, LV-2, CV-1 and CV-2 are closed and the cesium and lithium sections are filled through their respective fill connections. Preheating of the lithium piping and the reactor can be accomplished by circulating hot inert gas through their insulating jackets.

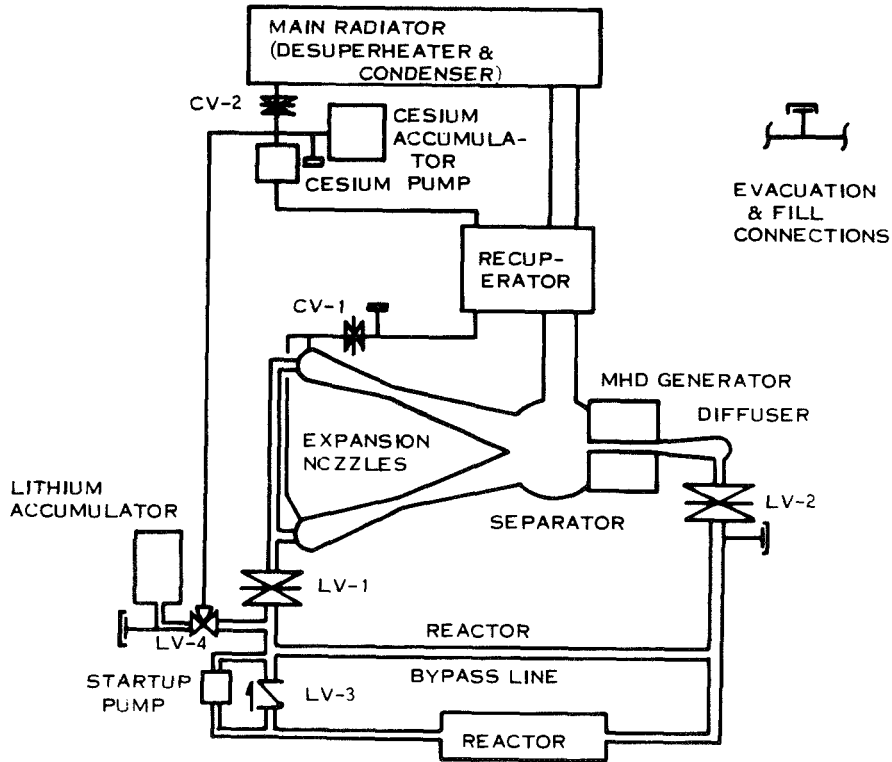


Figure 2-11. MHD Fluid System Startup Schematic

After reaching a safe orbit, the reactor is taken critical and warmed up, circulating the lithium at a low flow rate with the battery-powered startup pump located in parallel with check valve LV-3. The lithium flow path is normal through the reactor section but is reverse through the reactor by-pass line. The cesium system is stagnant but shares the same insulated enclosure with all of the lithium system except the reactor and is, therefore, warmed up by radiated and conducted heat. System pressures are maintained by controlling the gas pressure acting on the two bellows type accumulators; the two accumulators absorb the fluid expansion volume during warmup. Battery power is also provided to operate the auxiliary cooling pumps during warmup.

When operating temperatures are reached, accumulator gas pressures are increased and valves LV-1 and CV-1 open, injecting the two fluids into the nozzles. After appropriate intervals, valves LV-2 and CV-2 are opened to complete the normal flow paths. The startup pump is secured and valve LV-4 switches the lithium reservoir connection over to the cesium pump suction to minimize the containment pressure requirements during long term operation. Cesium and lithium makeup to the system for leakage or volume expansion due to creep enter the system at the cesium pump suction controlled by accumulator gas pressure.

2.3.1.3 Electrical System Startup

Electrical startup of the MHD induction generator requires special attention. In the rotating induction generator, residual magnetization of the rotor iron can be expected to build up the voltage to its operating point without special provisions, just as in a self-excited dc generator. In the MHD induction generator, however, there is no magnetic rotor (the equivalent of the rotor is the working fluid, a nonmagnetic material) but laboratory tests have shown that MHD generators will build up voltage while self-excited (see Reference 38).

Electrical loads on the MHD generator at startup are the excitation capacitors, and the vehicle electrical loads excluding the ion thruster accelerator and screens. This results in a configuration requiring approximately 20 percent of full electrical load. Thruster electrical loads energized at the initiation of the start sequence are the vaporizer, cathode and neutralizer heaters, arc and magnet supplies.

The first step of the startup sequence is to attain the desired lithium temperature using the battery-operated startup pump and the reactor by-pass line. Once the operating temperatures are reached, the two fluids are injected into the nozzles and through the generator. When sufficient flow velocity is reached, the voltage builds up, driving the cesium EM pump, thus maintaining the fluid flow.

When stable fluid flow and 20 percent power generation has been achieved, and the thruster heaters are up to temperature for sufficient time, the fluid temperature is raised to approximately 1800⁰F. With stabilization, the thruster screen supplies and accelerator supplies are sequenced on, bringing up the thrusters one at a time, until full load is achieved.

2.3.2 SHUTDOWN AND RESTART

The reference mission has a coast period halfway to Jupiter and the Jupiter orbit operation, both of which have a nominal 10 percent power demand (see Section 2.2.4.1). If operation at 10 percent rated output is achievable only at extremely low system efficiency, it might be worthwhile to shut down the MHD loop and operate the reactor at low power using an alternate conversion system, e.g., thermoelectrics, to generator power. (See Section 2.3.3 for discussion of part power operation.)

For the reference mission the low power demand time is $120 + 17 = 137$ days out of $50 + 160 + 120 + 270 + 17 = 637$ days or approximately 22 percent of the mission (more with longer time in Jovian orbit). If an alternate conversion system with equivalent efficiency (~ 7 to 8 percent) is available and the MHD loop can be shut down, the reactor core life required can be reduced to

$$\frac{500 + 0.08(137)}{637} \times 100 = 80\%$$

of the life required for continuous operation at rated power. Even without examining the possible difficulties of MHD loop shutdown and incorporation of a second power conversion system, the ~ 20 percent saving in core design life does not seem a strong incentive for incorporating an auxiliary power system or main power system variability.

To restart the MHD system after an in-space shutdown, it is assumed that the original startup conditions must be restored in shutting down the system. Two shutdown approaches were considered. In the first, an exhaust connection would be added to the diffuser downstream of the MHD generator. The system would be shutdown by closing valves, LV-1, LV-2, CV-1, and CV-2 and opening the exhaust port simultaneously. The hot fluids in the nozzles and vapor spaces would boil off into space and, with the exhaust port reclosed, the system would again be ready for startup if the accumulators contained sufficient fluid inventory. This method was rejected for many reasons, namely:

- a. The spacecraft would receive a large impulse from fluid exhaust just after its attitude control system (the thrusters) was shut down.
- b. The exhausted liquid metal may contaminate spacecraft surfaces
- c. The lithium and cesium reservoirs would require additional inventory for restart capability.

The second shutdown technique considered was to first close valves LV-1 and CV-1 and simultaneously lower the gas control pressures on the accumulators (the lithium accumulator is assumed to be valved back to the reactor by-pass line). The generator electrical circuits are then opened to minimize flow resistance and fluid momentum is relied upon to drive as much fluid as possible back into the accumulators. When sufficient fluid has been drawn out of the nozzle, generator and vapor spaces, valves LV-2 and CV-2 are closed to complete the shutdown. Successful execution of this type shutdown would require careful control and judgement of its feasibility would require extensive analysis. In the scope and context of this study and in view of the modest core life reduction to be attained, this analysis was not considered worthwhile.

2.3.3 PART POWER OPERATION

The reference mission described in Section 2.2.4 has a coast period during the helio-centric orbit of 120 days. During this period, a requirement of only 10 percent of full power is postulated. After Jovian orbit is attained, there is again a period of part power demand. In both these cases, the postulation of 10 percent power may be quite high; it was selected somewhat arbitrarily to be representative of standby power requirements.

There are two approaches to the provision of part power by the MHD power system. One is to maintain the power system at steady state and dump the excess power through a shunt regulator; the other is to reduce the MHD power system operating temperature and output power. A power flattening radiator would require only approximately 100 square feet (assuming radiator operation at 1000^o to 1200^o F) and would add less than four feet to the length of the spacecraft. The power flattening resistor might even be located within the lithium coolant system for liquid cooling.

Although part power operation by shunting excess power does not seem to pose serious problems, the possibilities of reduced temperature/reduced power operation were explored. Two sets of system calculations were made by JPL using fixed system geometry. The key assumptions made in these calculations are:

- a. No change in physical geometry and arrangement
- b. Excitation capacitance may be varied by electrical switching
- c. Pressure drops in the cesium loop are negligible at reduced flow.

The results of the full power and part power comparison are listed in Table 2-9. The independent variable used to start the calculation for reduced power was the 1300^oF cycle temperature; the resulting output power of 21 kWe (7.3 percent) is considered adequate for maintaining payload power, hotel load and perhaps some attitude control power.

There would be some design problems associated with reduction in power operation. The thrusters could be removed one at a time using the screen circuit interrupters; reactor power, fluid temperature and flow rate could be reduced proportionately. When the high voltage bus voltage drops below limits, or when the duty cycle of the low voltage Pulse Width Modulator (PWM) on the 250 volt converter outputs become greater than a selected value, then the additional capacitors for part power operation could be switched in.

Table 2-9. PART POWER OPERATION

PARAMETER	FULL POWER VALUE	PART POWER VALUE
Net Electric Power, kW	287	21
Percent Rated Power, %	100	7.3
Cycle Temperature, °F	1800	1300
Reactor Thermal Power, kW	3660	629
Cycle Efficiency, %	7.8	3.3
Nozzle Inlet Press, psia	137	20.3
Nozzle Exhaust Press, psia	10	0.84
Lithium Flow Rate, kg/sec	92	23
Cesium Flow Rate, kg/sec	5.8	1.1
Cesium Pump Power, kW	18.4	0.5
Coil I ² R Loss, kW	4.9	4.65
Total Reactive Power, KVAR	1300	480
Frequency, Hz	294	134
Total Excitation Capacitance, μf	937	4725
Average Coil Voltage, VAC	900	400

The machine would become stable again, with the additional excitation capacitors, at a lower voltage and frequency: The 250 volt PWM of the SCR's will ensure voltage regulation for the operating loads. The high voltage bus voltage is allowed to drop (to approximately 1400 volts dc) since the thrusters are shut down. To return to full power the reactor temperature and flow rate are increased. When voltage starts to rise again, or when the low voltage PWM cycle drops, the part power capacitors are switched out of the system.

It is probable that the number of power maneuvers such as just described would be limited by switchgear design. Any devices used to switch excitation capacitance into or out of the system would have to carry very large currents. Because of that and the many switches required, one per generator coil circuit, irreversible pyrotechnic switches would probably be used.

2.3.4 ONE OR TWO-LOOP SYSTEM

2.3.4.1 Reactor Loop Arrangement

In order to provide the MHD loop with 1600 to 2200^oF lithium, a fast spectrum, lithium-cooled reactor such as SNAP-50 is a logical choice. With such a reactor, the reactor coolant may be used directly in the MHD loop or an intermediate heat exchanger may be used to separate the reactor and MHD loops. Figure 2-12 shows the basic MHD cycle diagram with the reactor piped directly into the MHD loop. The movement of fluids in the MHD loop depends on the cesium stream receiving thermal energy from the lithium when the two streams are mixed in the nozzles. The boiling and expanding cesium then imparts kinetic energy to the lithium stream, part of which is converted to electrical energy in the MHD generator and part of which is converted to pumping pressure in the diffuser to circulate lithium back through the reactor and to the nozzles. The optional bypass shown in Figure 2-12 can be used to divert some of the lithium flow around the reactor in order to obtain a lower reactor pressure drop or a more compact reactor.

If the reactor loop is separated from the MHD loop by a heat source heat exchanger as shown in Figure 2-13, an additional pump is needed to circulate the lithium through the reactor loop.

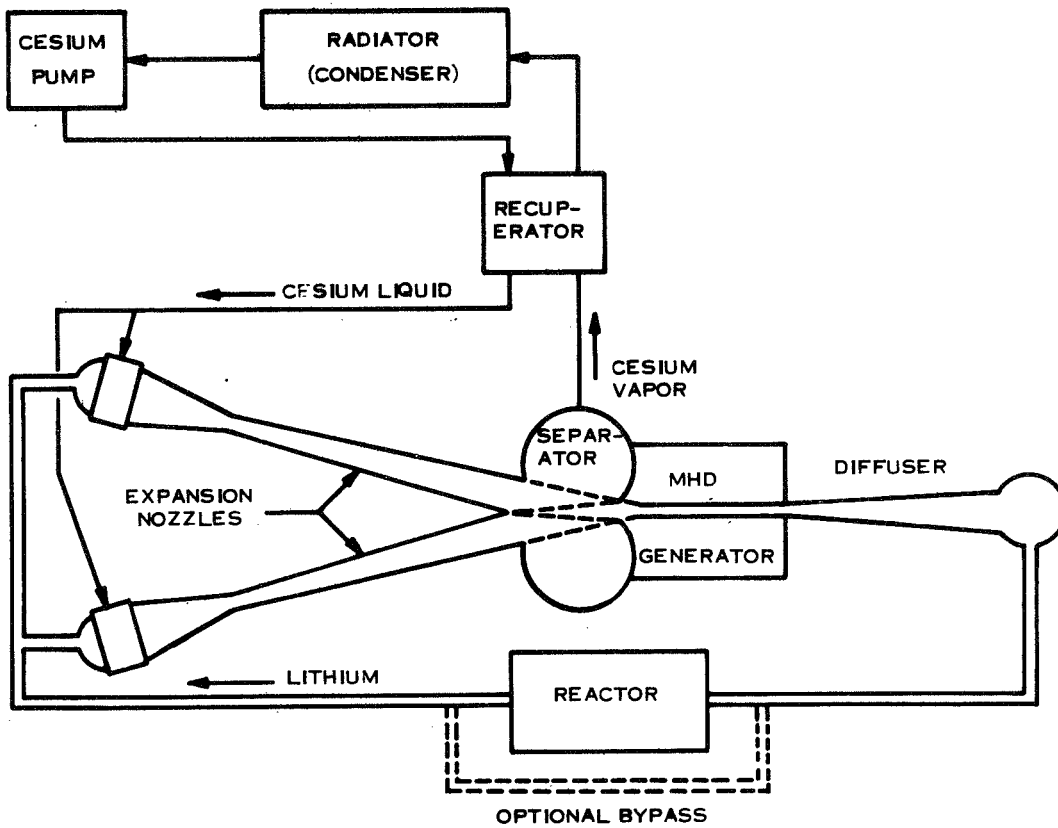


Figure 2-12. MHD Loop Without Separate Reactor Loop

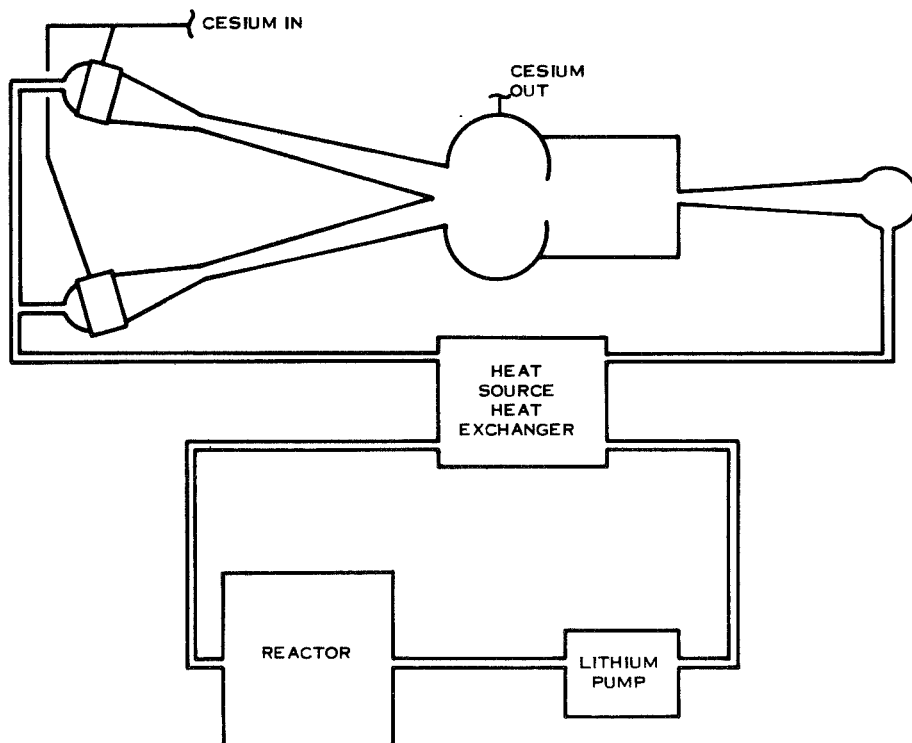


Figure 2-13. MHD Loop With Separate Reactor Loop

The incentives for use of a separate reactor loop are:

- a. The reactor pressure vessel may be designed for a containment pressure lower than the 150 psia typical of the MHD loop
- b. The possibility of ingestion of cesium vapor by the reactor is precluded
- c. Activated coolant is kept away from the payload

The incentives for a one-loop system are:

- a. The system is simpler and lighter
- b. Lithium can be circulated for prestart warmup (see startup discussion in Paragraph 2.3.1) using just one pump. A two-loop system could also use just one pump if all lithium in the MHD circuit is left stagnant and warmed by conducted heat.
- c. Only one lithium accumulator is needed
- d. No reactor coolant pumping is needed once the system is started.

2.3.4.1.1 Containment Pressure - The weight penalty associated with designing the reactor for MHD pressure may be approximated as follows:

- a. Assume a domed cylindrical pressure vessel of 12-inch diameter and 40-inch length made of Cb-1Zr. This size and material are typical of the MHD type reactor
- b. Assume that the reactor pressure vessel would have a minimum design pressure of 50 psia
- c. Assume that the reactor pressure vessel design stress for 20,000 hour operation is 1000 psi. This low design stress is quite conservative for temperatures below $\sim 2000^{\circ}\text{F}$. More advanced alloys of Cb can provide much greater creep strength.

Calculating a minimum vessel wall thickness:

$$t = \frac{Pr}{\sigma} = \frac{50 \text{ psi} \times 6 \text{ in.}}{1000 \text{ psi}} = 0.3 \text{ in.}$$

Design for 150 psia would revise this to:

$$t = \frac{150 \text{ psi} \times 6 \text{ in.}}{1000 \text{ psi}} = 0.9 \text{ in.},$$

an increase of 0.6 inch in wall thickness.

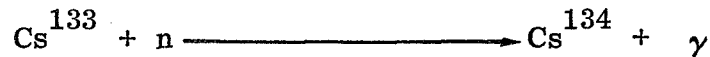
The surface area of the vessel is about 1500 square inches and the wall material density is 0.32 pounds per cubic inch, so the weight increase would be:

$$1500 \text{ in}^2 \times 0.6 \times 0.32 \text{ lb/in}^3 \approx 300 \text{ lb.}$$

Since the weight penalty is only about 300 pounds even with the conservative material and design stress selection, the additional complexity and weight of a separate reactor loop, pump and heat source heat exchanger would constitute a greater penalty. In weight comparison, the heat source heat exchanger alone, with one side designed for 150 psi, would weigh almost as much.

2.3.4.1.2 Cesium Bubbles - The second-listed incentive for a two-loop system is to keep cesium bubbles out of the reactor. The fluid conditions at the MHD generator inlet behind the upstream diffuser are such that all remaining cesium should be dissolved. If any bubbles do still exist at the generator exit they may still dissolve when static pressure is increased from ~ 40 psia to ~ 150 psia in the downstream diffuser. If still not dissolved, any cesium bubbles would more likely follow the bypass line (~ 80 to 85 percent of the flow) rather than enter the reactor line (~ 15 to 20 percent of the flow). Moreover, in the reactor flow, with lithium temperature increasing at nearly constant pressure more and more cesium could be taken into solution. Thus, ingestion of cesium vapor by the reactor does not appear to be a serious problem.

2.3.4.1.3 Coolant Activation - Radioactivity in the reactor coolant may reach areas near the payload in a one-loop system which may cause radiation damage. In the lithium-cooled MHD reactor two basic sources of coolant radioactivity can be identified - leakage of fission products from reactor core fuel elements into the coolant and irradiation of the coolant itself during its passage through the reactor. Considering coolant irradiation first, three nuclear reactions are of interest:



The first of these reactions poses no high radiation threat to equipment since tritium is a weak β emitter. However, the Li^6 reaction does produce non-reactive, non-condensable helium, which can buildup in the system. The tritium will react with lithium to form LiH . The Li^6 reaction can be suppressed by using lithium coolant which is at least 99.9 percent the Li^7 isotope. Such Li^7 enriched lithium is available; natural lithium is already ~ 93 percent Li^7 . The Li^7 reaction is of interest because the Li^8 isotope formed emits a very high energy β (~ 13 Mev). However, its half-life of 0.85 seconds is so short that most should decay before coming past the shield; this delay time can be extended by including an enlarged section in the reactor outlet line. In addition, the MHD loop itself keeps the lithium from approaching the payload.

2.3.4.1.4. Cs^{134} Activity - The $\text{Cs}^{133} (n, \gamma) \text{Cs}^{134}$ reaction produces two isomers, the 2.9 hour half-life Cs^{134m} and the 2.3 year Cs^{134} . These nuclides can be formed by irradiation in the reactor of the cesium dissolved in the lithium stream (natural cesium is 100 percent Cs^{133}). In order to evaluate this activity, one must have good knowledge of:

- a. Cesium flow distribution (residence time in reactor, residence time near the payload, mass flow rates, and total inventory)
- b. Definition of the reactor neutron flux by neutron energy level for each reactor region of interest (annulus, inlet plenum, core, and outlet plenum)
- c. Cs^{133} cross section data for each energy level of interest
- d. Location of sensitive components with respect to the activated cesium.

Since the system, and especially the reactor, designs are both conceptual at this time the cesium activation was analyzed by using the best available information, making estimates, where necessary, and trying to keep the analysis conservative.

Figure 2-14 depicts the mass/flow/time model which was set up to represent the cesium distribution in the system. The flow distributions and cesium inventory are based on initial baseline values. The radiation source is identified as the lowest of five radiator sections and it was assumed that 10 pounds of the calculated 31 pound cesium inventory of that radiator section would be two feet away from the payload on the average (see the arrangement in Figure 2-15 in the discussion of fission product leakage which follows). The cesium flow through the reactor will vary with system operating temperature and pressure (varying cesium solubility in lithium); the calculated baseline design value was used.

The Cs¹³³ (n, γ) cross sections which were used are listed in Table 2-10. The 29-hour Cs^{134m} was assumed to undergo 100 percent decay to 2.3 year Cs¹³⁴ with the emission of a 0.13 Mev γ. The decay of Cs¹³⁴ was assumed to be:

- a. 30 percent 0.3 Mev β- decay to Ba¹³⁴ followed by Ba decay with the emission of a single 1.75 Mev γ.
- b. 70 percent 0.68 Mev β- decay to Ba¹³⁴ followed by Ba decay with the emission of a pair of γ of energies 0.8 and 0.6 Mev.

The activation rate in the reactor

$$A = \int_E \int_V \Sigma(E) \phi(E, r) dV dE$$

requires a knowledge of the reactor neutron fluxes in various regions of the reactor. Since the MHD reactor design is still conceptual the following values were used:

TABLE 2-10. CESIUM - 133 (n, γ) CROSS SECTIONS

Thermal Neutrons

Production of 2.9 hour Cs^{134m} $\sigma = 2.6$ barns

Production of 2.3 year Cs^{134m} $\sigma = 29$ barns

0.215 ev $\leq E_n \leq 10$ kev

$\bar{\sigma}(n \gamma) \approx 5$ barns

Cs^{134m} $\sigma = 0.5$ barns

Cs¹³⁴ $\sigma = 5$ barns

$E_n = 20$ kev

Cs^{134m} $\sigma = 0.09$ barns

Cs¹³⁴ $\sigma = 1$ barn

Estimates for High E_n Range

<u>E_n</u>	<u>σ 134m (barns)</u>	<u>σ 134 (barns)</u>
10 to 100 kev	0.04	0.4
0.1 to 0.4 Mev	0.007	0.07
0.4 to 1.4 Mev	0.001	0.01
1.4 to 10 Mev	0.0004	0.004

DESIGN LIFE = 14,000 HRS

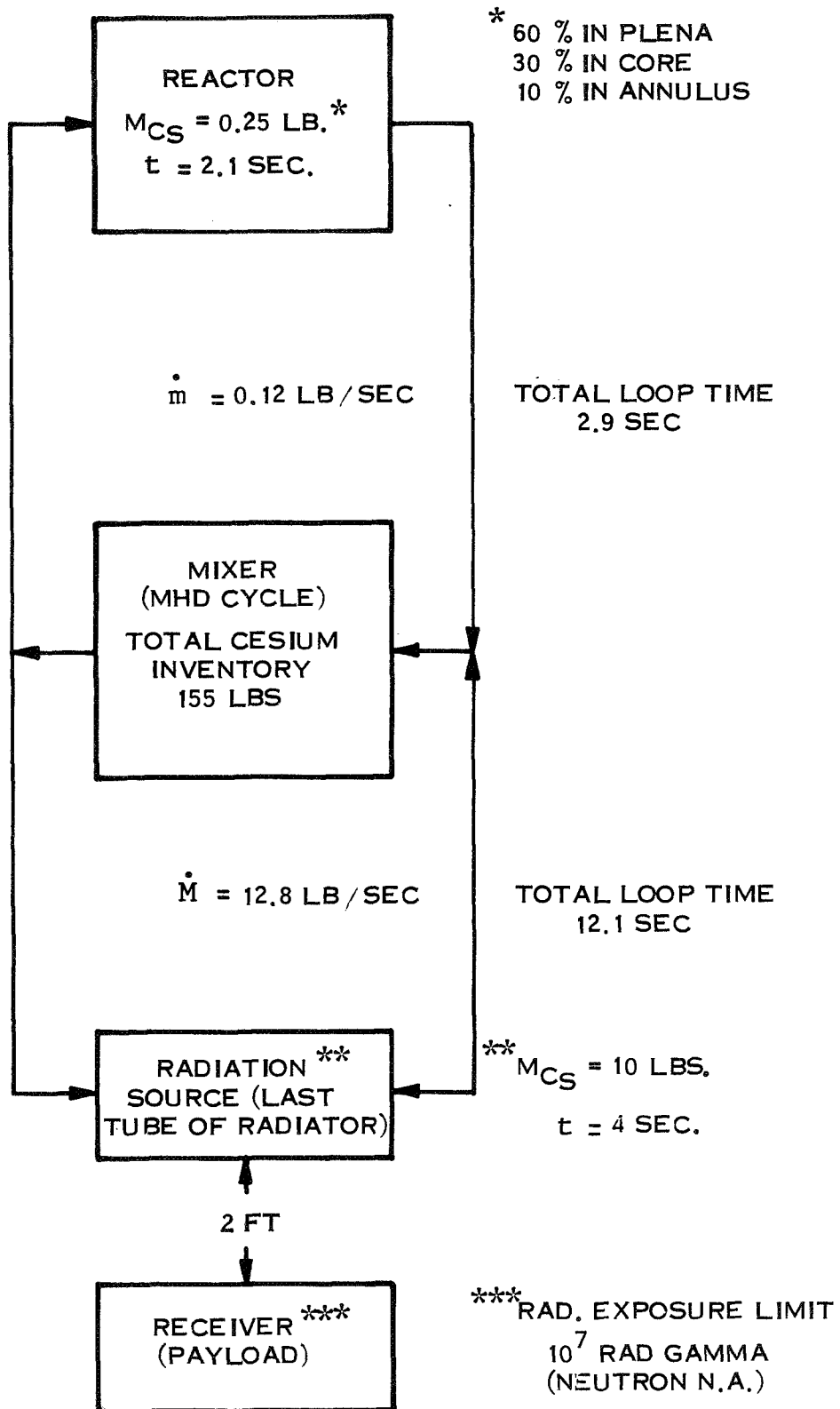


Figure 2-14. MHD Cesium Mass/Flow/Time Model

FLUX (nv)

<u>Group</u>	<u>Core</u>	<u>Annulus</u>	<u>Plena</u>
1	7×10^{13}	10^{13}	4×10^{12}
2	1.4×10^{14}	2×10^{13}	10^{13}
3	1.4×10^{14}	3×10^{13}	10^{13}
4	10^{14}	5×10^{13}	3×10^{13}
5	1.5×10^{13}	4×10^{13}	8×10^{13}
Thermal	10^{10}	5×10^{11}	2×10^{13}

These flux values are expected to be somewhat conservative for the MHD reactor since they are more closely related to reactor designs with a softer neutron energy spectrum.

The reactor average group fluxes were weighted for the time spent in the various reactor regions (see model in Figure 2-14), and the average group fluxes ϕ_g were used to calculate activated nuclei per second

$$A = V_{Cs} \sum_{g=1}^6 \Sigma_g \phi_g$$

where

$$\Sigma_g = \sigma_g \frac{\rho_{Cs} N}{A_{Cs}}$$

A_{Cs} = molecular weight of cesium

N = Avogadro's Number

$$\rho_{Cs} = \frac{M_{Cs}}{V_{Cs}}$$

M_{Cs} = mass of cesium

For Cs^{134m} this results in

$$A^m = 3.5 \times 10^{13} \text{ nuclei per sec.}$$

For Cs¹³⁴ this, and Cs^{134m} decay, gives

$$A^{134} = 3.8 \times 10^{14} \text{ nuclei per sec.}$$

Since Cs¹³⁴ has a half-life of 2.3 years its decay is not negligible, so correcting for decay and the 10/155 fraction which is close to the payload, the number of activated nuclei contributing dose to the payload is calculated.

$$N = 2.6 \times 10^{20} (1 - e^{-\lambda t})$$

where

N = nuclei contributing dose

λ = Cs¹³⁴ effective decay constant

t = time

The following dose-to-flux conversion factors were used for the emissions of interest:

$$0.6 \text{ Mev} \quad C = 8.4 \times 10^5 \text{ photons/cm}^2\text{sec per R/hr}$$

$$0.8 \text{ Mev} \quad C = 6.5 \times 10^5 \text{ photons/cm}^2\text{sec per R/hr}$$

$$1.75 \text{ Mev} \quad C = 3.5 \times 10^5 \text{ photons/cm}^2\text{sec per R/hr}$$

Assuming a point source geometry with no attenuation by the pipe walls or structure the dose as a function of time was calculated:

$$D(t) = \frac{1}{C} \int_0^t \frac{(3.6 \times 10^3) N \lambda}{4 \pi r^2} dt$$

to get the following results:

Time (Hrs)	Total Integrated Dose (R)
5,000	6×10^4
10,000	2.6×10^4
15,000	4.8×10^5
20,000	8.2×10^5

The highest dose rate resulting from these calculations, 8.2×10^5 , is less than 10 percent of the allowable payload dose. The dose rate at nominal design life, 14,000 hours, is about 5 percent of allowable. In view of the conservatism of the calculation, Cs¹³⁴ activation and consequent irradiation of the payload is not considered a severe enough problem to warrant changing to a two-loop system. It should be noted that Cs¹³⁴ activation should be reappraised in the future, when more specific information is available, to verify this conclusion.

2.3.4.1.5 Fission Product Leakage - An analytical model was developed to represent the case of fission products leaking from the fuel elements of the reactor core into the reactor coolant stream. The model was designed to give a rough estimate of the gamma dose due to the presence of fission products in the cooling system.

a. Analytical Model - In general, the dose rate at any given point in space due to fission product leakage will depend upon:

1. Fission product leakage rate
2. Reactor operating history
3. Distribution of the fission products throughout the cooling system

When incorporating these factors into an analytical model, use will be made of a few simplifying assumptions, i. e.,

1. The reactor power level is constant in time
2. The fission product distribution is constant in time except for an arbitrary delay time between the instant of leaking and the instant of appearing distributed throughout the cooling system (this will be explained further below).
3. Once a particle of fuel leaks from the reactor core, the fission process within that particle ceases altogether. No account is taken for possible fission due to

neutrons outside of the core nor is any account taken of the possibility of the fuel particle circulating through the core with the coolant stream.

Consider the following terms,

$l(t) \equiv$ the fraction of the fission products in the core at time t leaking into the coolant stream per unit time

$f(r) \equiv$ the fraction of the fission products that have leaked found per unit volume at the position r .

$P(t, T, E) dE =$ total photon energy emission rate from a mass of fissionable fuel at a time T after the fission process had ceased. The photon energies lie in the range E to $E + dE$. The fuel is taken to have been undergoing the fission process at a power level of one watt for a time period t .

$W \equiv$ actual reactor operating power level

Now consider an element of volume in the cooling system at the time t' , located at position r . The photon energy source can now be written as

$$S(\vec{r}, t', E) dE = WP(t, T, E) dE l(t) dt f(\vec{r})$$

where

$$t' = t + T$$

and t , which is the time at which a particle of fuel leaked, is also taken as the time for which the reactor has been operating. $S(\vec{r}, t', E) dE$ is the photon energy emission per unit time at time t' , per unit volume at position \vec{r} , for photons with energies between E and $E + dE$, due to fuel which leaked in the time interval from t to $t + dt$.

The total source strength at time t' , due to fuel which leaked from time t_0 to time t , is

$$S(\vec{r}, t') = Wf(\vec{r}) \int_E \int_{t_0}^{t'} P(t, t'-t, E) l(t) dt dE$$

where now $T = t' - t$, since t' is being held constant. The time t_0 at which leaking begins can have any value in the range

$$0 \leq t_0 \leq t'$$

If one wishes to introduce a delay time between the time of leakage and the time the fission products arrive at the point \vec{r} , then the above expression becomes,

$$S(\vec{r}, t') = Wf(\vec{r}) \int_E \int_{t_0}^{t'-\delta} P(t, t'-t, E) \ell(t) dt dE$$

where δ is the delay time.

This source strength can now be used to calculate the dose rate and integrated dose at any desired receiver point. Assume that there is no appreciable attenuation of the photons as they pass from the source to the receiver point. Furthermore, let the fission products that significantly contribute to the dose be contained in space region R. If \vec{x} is the distance between an element of volume of the source region and the receiver point, then the dose rate at the receiver point is

$$D(t') = WC \int_R \frac{S(\vec{r}, t') dV}{4 \pi x^2}$$

where it has been assumed that the source emits isotropically. The term dV is a volume element in the source region and C is a suitable averaged energy flux-to-dose conversion factor. The averaging of the conversion factor is complicated by the fact that the photon spectrum is time dependent. It should be kept in mind that the distance x in the above equation is a function of \vec{r} , the position vector of dV .

The time integrated dose at the receiver point up to time t_m is

$$D(t_m) = \int_{t_0 + \delta}^{t_m} D(t') dt'$$

Numerical values for the quantity $P(t, T, E) dE$ can be found in the literature (see "Reactor Handbook", second edition, vol. II, part B, or "Reactor Physics Constants", ANL-5800, second edition). The data is given in the form of curves for the photon energy emission rate as a function of reactor operating time and time since reactor shutdown. A family of curves is given, each one representing the energy emission rate for photons with energies in a given energy range.

The total photon energy emission rate can be expressed analytically through the use of the so-called Way and Wigner formula for the emission of photon energy as a function of time after a fission event. The formula is:

$$\Gamma(\tau) = 1.26 \tau^{-1.2} \text{mev/sec per fission}$$

where τ is the time since fission. This is a good approximation for τ greater than about 100 seconds. Using this equation to derive an expression for $P(t, T)$ results in

$$P(t, T) = 1.95 \times 10^{11} [T^{-0.2} - (T+t)^{-0.2}] \text{mev/sec-watt}$$

where

$$P(t, T) = \int P(t, T, E) dE$$

b. Application of the Model - Consider the case of a reactor whose fuel elements leak fission products at a constant rate into the reactor coolant system. The leakage rate will be assumed to be small enough such that control adjustments to compensate for the loss do not perturb the neutron flux appreciably. Under this condition, the fission rate will be essen-

tially constant with time as long as the reactor power level remains constant. Also assume that the power density is constant throughout the reactor core.

Let there be a total loss of fuel due to leaking of $p\%$ of the total fuel mass, and let this mass loss occur over the time period $(t_m - t_o)$. Then, the leakage rate from time t_o to time t_m will be

$$\frac{(p \times 10^{-2}) M}{(t_m - t_o)} \text{ mass per unit time}$$

where M is the total fuel mass. At the time t , the fuel within the reactor core would have a fission history such that if the fission process ceased at time t , then at item $t+T$, the total photon energy emission rate would be $W \cdot P(t, T)$, where W is the reactor operating power level. Now, the element of mass, dm , of fuel that leaks in the time interval t to $t + dt$ will have the fraction dm/M of this photon power, and, since the model assumes that no more fissions occur within dm after leaking, one can write for the photon power to be contained within dm

$$\frac{dm}{M} W P(t, T) \text{ mev/sec}$$

The element of mass dm can be written

$$dm = \frac{(p \times 10^{-2}) M}{(t_m - t_o)} dt$$

Hence, the photon power in dm is

$$\frac{(p \times 10^{-2})}{(t_m - t_o)} W P(t, T) dt \text{ mev/sec}$$

This is the photon energy emission rate, at a time T after leaking, from the mass of fuel that leaked during the time t to $t + dt$. It should also be kept in mind that the reactor started operating at $t = 0$.

The distribution of the fission products after leaking is here assumed to be a uniform distribution over the volume of the cooling system. If this volume is V , then the fraction of

the fission products found per unit volume in the cooling system is simply

$$f(\mathbf{r}) = 1/V$$

The source strength can now be written as

$$S(\mathbf{r}, t') = \frac{W}{V} \frac{(p \times 10^{-2})}{(t_m - t_o)} \int_{t_o}^{t'-\delta} P(t, T) dt$$

If the analytical expression is used for $P(t, T)$, then

$$S(\vec{\mathbf{r}}, t') = (1.95 \times 10^{11}) \frac{W}{V} \frac{(p \times 10^{-2})}{(t_m - t_o)} \left[\frac{(t'-t_o)^{0.8}}{0.8} + \frac{t_o}{(t')^{0.2}} - (t')^{0.8} \right]$$

The integrated dose at some receiver point is, if it is assumed that there is no attenuation of the photons,

$$D(t_m) = C \int_{t_o}^{t_m} \int_R \frac{S(\vec{\mathbf{r}}, t')}{4 \pi x^2} dV dt'$$

When the above expression for $S(\mathbf{r}, t')$ is inserted in the expression for $D(t_m)$, then

$$D(t_m) = \frac{(1.95 \times 10^{11}) W (p \times 10^{-2})}{4 \pi V (t_m - t_o)} C \left[\frac{(t_m - t_o)^{1.8}}{1.44} + \frac{t_o t_m^{0.8}}{0.8} - \frac{t_m^{1.8}}{1.8} - 0.694 t_o^{1.8} \right] \int_R \frac{dV}{x^2}$$

This last equation will now be used to calculate the integrated dose to the payload for the MHD-powered unmanned space vehicle. The coolant system includes both the Li and Cs

loops and, given their geometry and the receiver point of interest, the region R which significantly contributes to the dose includes only about 1 percent of the entire coolant system. As a further simplifying assumption, take the region R to be small enough so that x can be considered constant. Then,

$$\frac{1}{V} \int_R \frac{dV}{x^2} \approx \frac{1}{Vx^2} \int_R dV = \frac{V_R}{V} \frac{1}{x^2}$$

where V_R = volume of region R. Since V_R is assumed to be 1% of V, then

$$\frac{1}{V} \int_R \frac{dV}{x^2} = \frac{0.01}{x^2}$$

Now let

$$x = 2 \text{ feet}$$

$$W = 3.64 \times 10^6 \text{ watts}$$

$$p = 0.05 \text{ percent}$$

$$c = 1.4 \times 10^{-6} \text{ n/hr per mev/cm}^2\text{-sec}$$

$$t_m = 580 \text{ days}$$

$$t_o = 0$$

$$\delta = 0$$

The resulting integrated dose becomes

$$D(t_m) = 2 \times 10^7 \text{ r}$$

which is twice the allowable dose.

Figure 2-15 shows the arrangement of the payload bay region; the "region R" of interest is the cesium return pipe system at the bottom of the last radiator bay. Inspection of the arrangement indicates that $x = 2$ feet is a conservative assumption for the effective distance between a payload component and all the cesium-borne fission products in these pipes.

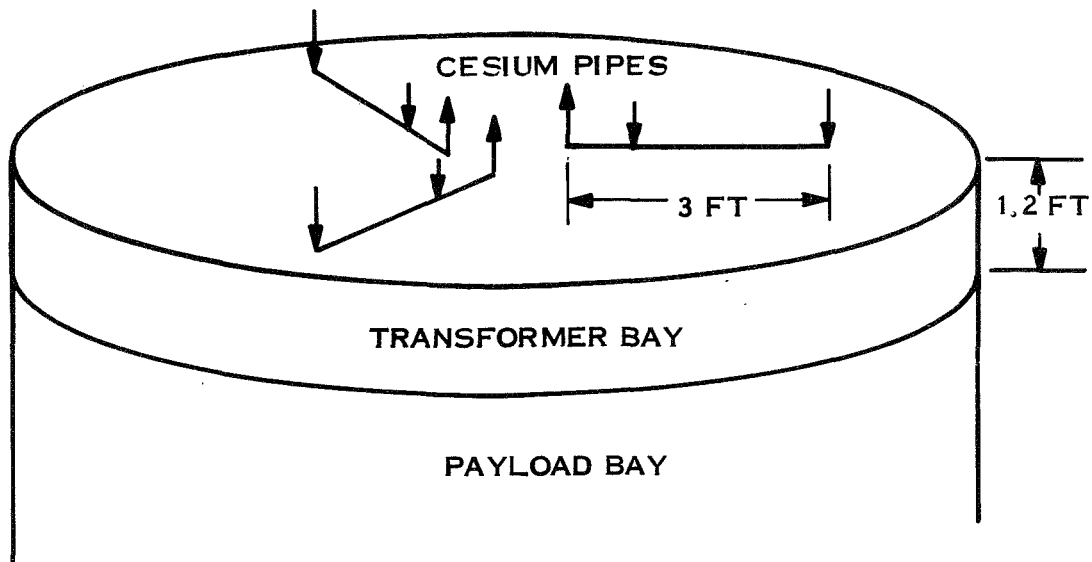


Figure 2-15. Arrangement of Cesium Pipes Near Payload

The fission product leakage of 0.05 percent is based on the assumption of 5 percent reactor fuel element failures with 100 percent fission gas release and 1 percent other fission product release from the failed elements. A gas trap was included in the cesium system to collect noncondensables which might hinder proper heat transfer in the recuperator and condensing radiator. Thus, the fluid-borne fission products are $5 \text{ percent} \times 0.01 = 0.05$ percent. This assumption, of course, is quite arbitrary since no reactor of this type has been developed. A fast reactor of the type required may have from 100 to 1000 individual fuel pins in its core. For a flight qualified reactor, the assumption of 5 percent failures immediately after starting the flight seems conservative.

As far as the release fraction from the failed elements is concerned, 100 percent release of gaseous products is, of course, the maximum, and the assumption of 1 percent release of non-gaseous fission products is based on the element failure being local rather than total and the use of a fuel form such as UN or UC which is relatively resistant to attack by the coolant.

There is one other assumption that deserves discussion; it has been assumed that any fission products which escape the core will immediately distribute themselves around the system in the liquid phase. Clearly, the gaseous fission products will not behave in this manner, being gases they will be stripped from the lithium stream in the nozzles and passed out to the radiator. In small quantities, the fission gases may be entrained in the cesium stream leaving the radiator. With this in mind, a centrifugal gas trap was placed in the cesium line at the pump discharge; here the fission gases can be collected and held in the MHD equipment bay, far from the payload. The nongaseous fission products, on the other hand, are not so predictable. Many of these fission products such as the iodines will react with the lithium reactor coolant immediately. The reactants or the fission products may remain in stable solution in the lithium. Or they may be volatile at system conditions and move out into the radiator.

The proceeding model and assumptions calculated a dose to the payload of twice the allowable. If such an overdose were considered highly probable, other design alternatives would have to be considered. The possibilities are:

1. Include a separate reactor coolant loop
2. Rearrange the spacecraft to obtain greater separation between the radioactive fluids and the payload
3. Shield the cesium pipe

The inclusion of a separate reactor coolant loop is estimated to incur a weight penalty of 500 pounds consisting of 300 pounds for a lithium pump and power conditioner and 200 pounds for a lithium-lithium heat exchanger, additional lithium, structure, etc. The pump weight is based on a polyphase ac helical induction pump moving 30 lb/sec of 1800^oF lithium with a developed pressure head of 10 psi. The gross power required for the pump including power conditioning losses is estimated to be 11 kWe, assuming 20 percent pump efficiency and 97 percent power conditioning efficiency (a cycloconverter). This additional power demand would require about a 4 percent increase in system rating.

Rearranging the spacecraft by adding fixed length between the radiator and the payload is not attractive because, at 82 feet, the spacecraft is already very long. If the central structure

of the radiator had the ability to telescope the payload section away by ~ 50 feet once in earth orbit, the dose rate could be reduced by a factor of three. A more attractive rearrangement would be to reverse the inlet and outlet of the last radiator bay so that the more dense liquid stream would be ~ 15 feet from the payload instead of ~ 2 feet. If the fission products would be dissolved in the cesium and not plating out on system surfaces, this would reduce the dose rate by a factor of about 50.

The weight penalty associated with shielding the cesium pipes was estimated assuming half-round tungsten shielding for 9 feet of cesium pipe. As Figure 2-16 shows, about 300 pounds of shielding would reduce the dose rate from the pipes by a factor of ten.

Thus, it appears that the dose rate to the payload could be reduced significantly by rearrangement or shielding without resorting to a separate reactor loop. In view of this, and the uncertainties of the fission product leakage and transport models, the separate reactor loop was not considered a necessity at this time. Again, as was said for Cs-134 activity, the problem of fission product leakage should be reappraised in the future when better knowledge of the reactor and other factors is available.

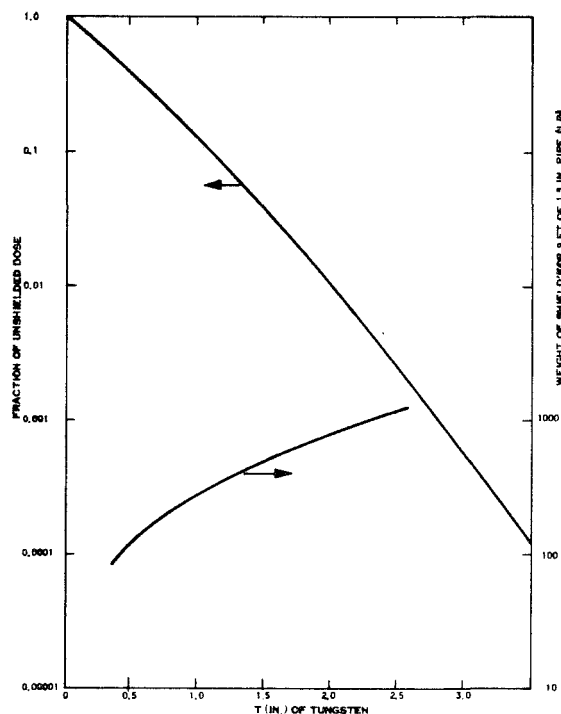


Figure 2-16. Cesium Pipe Shielding

2.4 CONFIGURATION TRADEOFFS

Since the MHD spacecraft was expected to be rather long with many heavy pieces of equipment, configuration tradeoffs were conducted to determine the most attractive design arrangement. As reported in Reference 2, a set of initial design parameters were drawn up and key component weights and areas were estimated for use in these tradeoffs.

2.4.1 GENERAL ARRANGEMENT GUIDELINES

To begin, some general conclusions were drawn about spacecraft arrangement:

- a. The ion thruster subsystem includes a significant amount of electronic control and power conditioning equipment. Since this equipment will have radiation exposure limits equivalent to the payload, the payload and thruster subsystem should be located together at one end of the spacecraft with the nuclear reactor at the opposite end.
- b. The ion thruster subsystem has a characteristic diameter of about ten feet in order to provide adequate mounting area for the thrusters. A nuclear reactor of the type needed here is of small diameter, no more than about three feet. Since a radiation shadow shield will be needed between the reactor and the payload/thruster area, the minimum shield diameter and weight will be obtained by locating the shield next to the reactor.
- c. Working in a ten foot diameter envelope, the MHD power system requires a total radiator section some 60 to 70 feet long. Since separation of the reactor and payload/thruster area minimizes shielding thickness requirements, the radiators should be located in a continuous section between the reactor and the payload/thruster area.
- d. The MHD power generating equipment is linked to the nuclear reactor by at least two lithium coolant pipes and is connected to the payload/thruster area by the main power output cables. In addition, the MHD power generating equipment apparently does not include any items which are especially sensitive to radiation. Since the power output cables can be kept small (MHD raw output is ~ 300 Hz, ~ 600 Vac), the preferred location for the MHD equipment is just behind the radiation shield, near the reactor.

With these guidelines as the starting point, the preliminary arrangement studies and configuration tradeoffs were conducted.

2.4.2 MHD EQUIPMENT BAY

The MHD nozzle assembly, the MHD generator, the excitation capacitors, the recuperator, and other closely related equipment are to be located in one section or bay. Some

of these items, such as the MHD generator and nozzle assembly, must be located next to one another in order to function. Others should be close together for efficient design; for example, the excitation capacitors should be close to the MHD generator to minimize the length and, consequently, the I^2R losses of the connecting cables which carry the large exciting currents which run from the capacitors to the generator and back. (The MHD generator exciting current is about four times greater than its output power current).

Arrangement of the MHD bay was studied to determine the minimum diameter envelope which could contain this equipment so that if it is located just behind the radiation shield, the shield subtended angle (and weight and volume) would be minimized. The MHD nozzle assembly was first laid out using dimensions taken from the computer analysis of the base-line system. A 40-inch nozzle length was assumed since the JPL investigators indicated that extension beyond this length was not worthwhile. The downstream diffuser half-angle can vary from three degrees to five degrees; a three degree half-angle was assumed in order to calculate the longest difuser.

Using the nozzle assembly as the basis, the key piping and component items were arranged to establish the MHD equipment envelope size. Figure 2-17 shows an arrangement which uses a single recuperator; Figure 2-18 shows an arrangement which uses two recuperators, one for each side of the nozzle. In both cases, the cylindrical segments flanking the diffuser are available for capacitor location providing more than the estimated three cubic feet required, an exposed surface which can reject $\sim 1500W$ of heat, and a simple interface to insulate the capacitors from the hot MHD equipment. Aside from the capacitors, the MHD stators and pump windings are the only items in the MHD bay which do not operate at $\sim 1800^\circ F$. It was therefore assumed that the MHD bay would be insulated on the outside surface of the envelope with the insulation envelope also providing micro-meteoroid protection. The internal components (MHD stators, etc.) which do not run at high temperature would be internally insulated and provided with a piped cooling system. The insulated exterior surface of the MHD bay can then be used as the mounting surface for this auxiliary cooling system.

The arrangements shown in Figures 2-17 and 2-18 show that the MHD equipment can be encased in a cone frustum about ten feet long with upper and lower diameters of 44

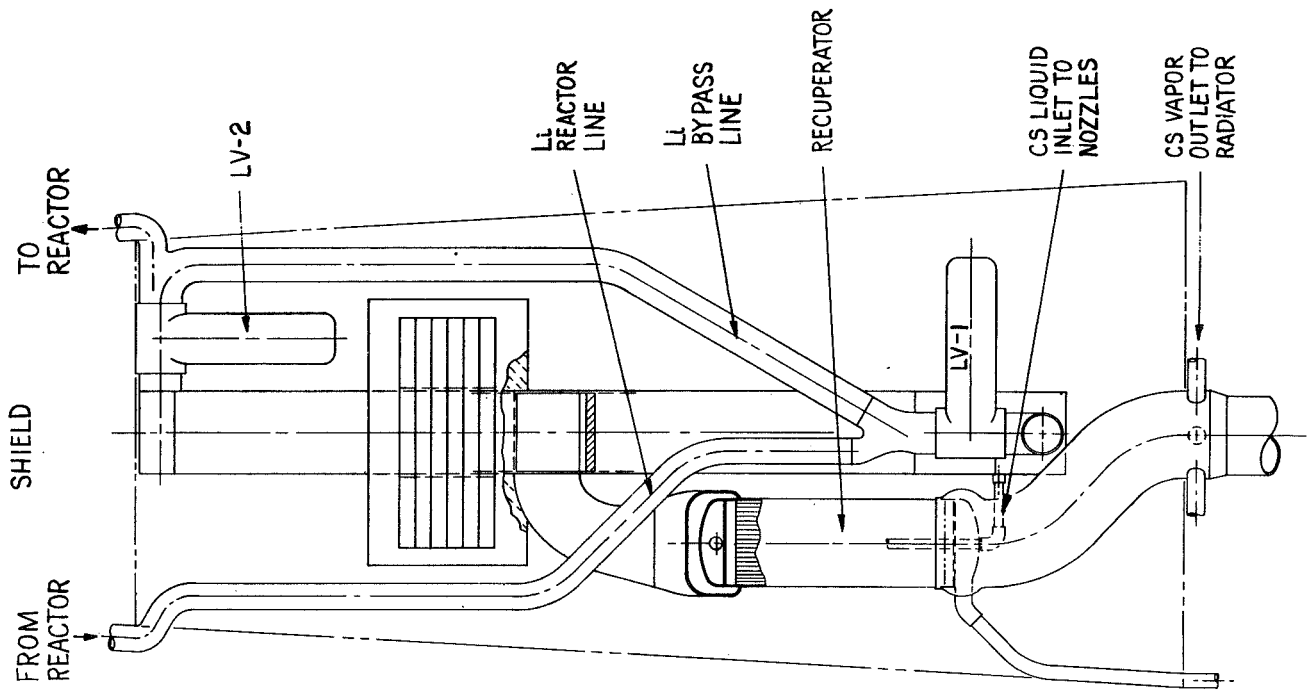
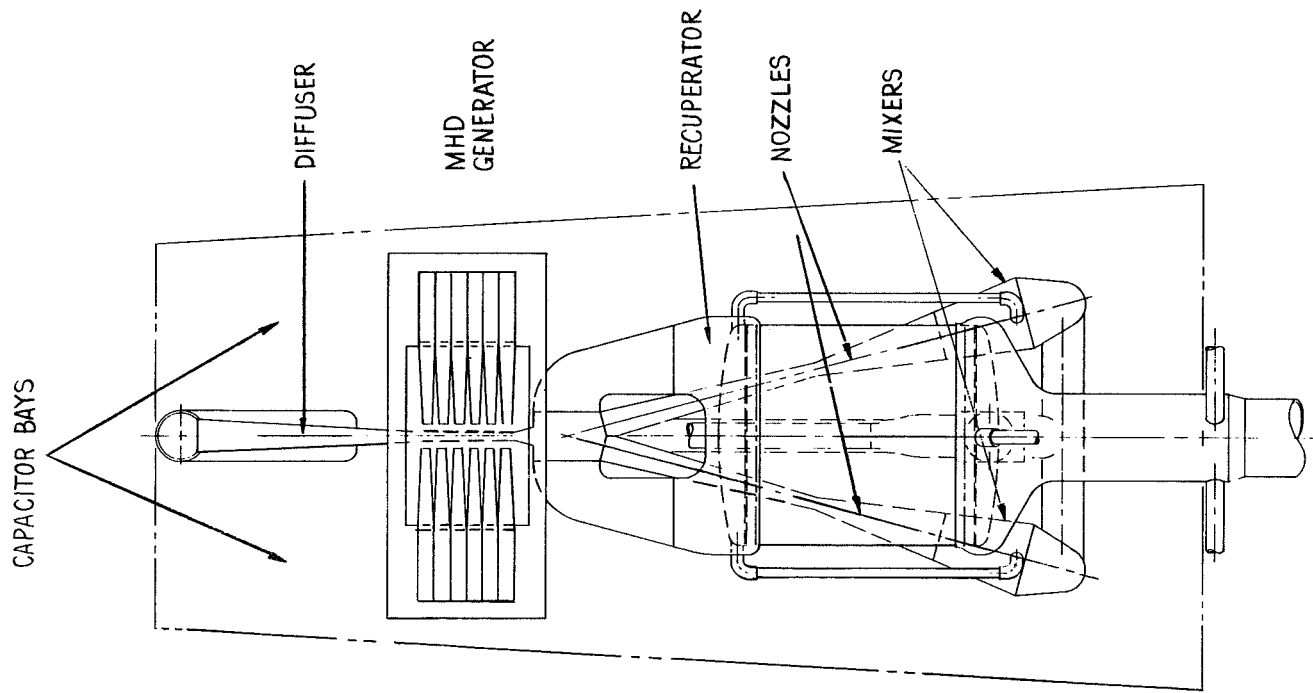


Figure 2-17. MHD Equipment Arrangement with One Recuperator

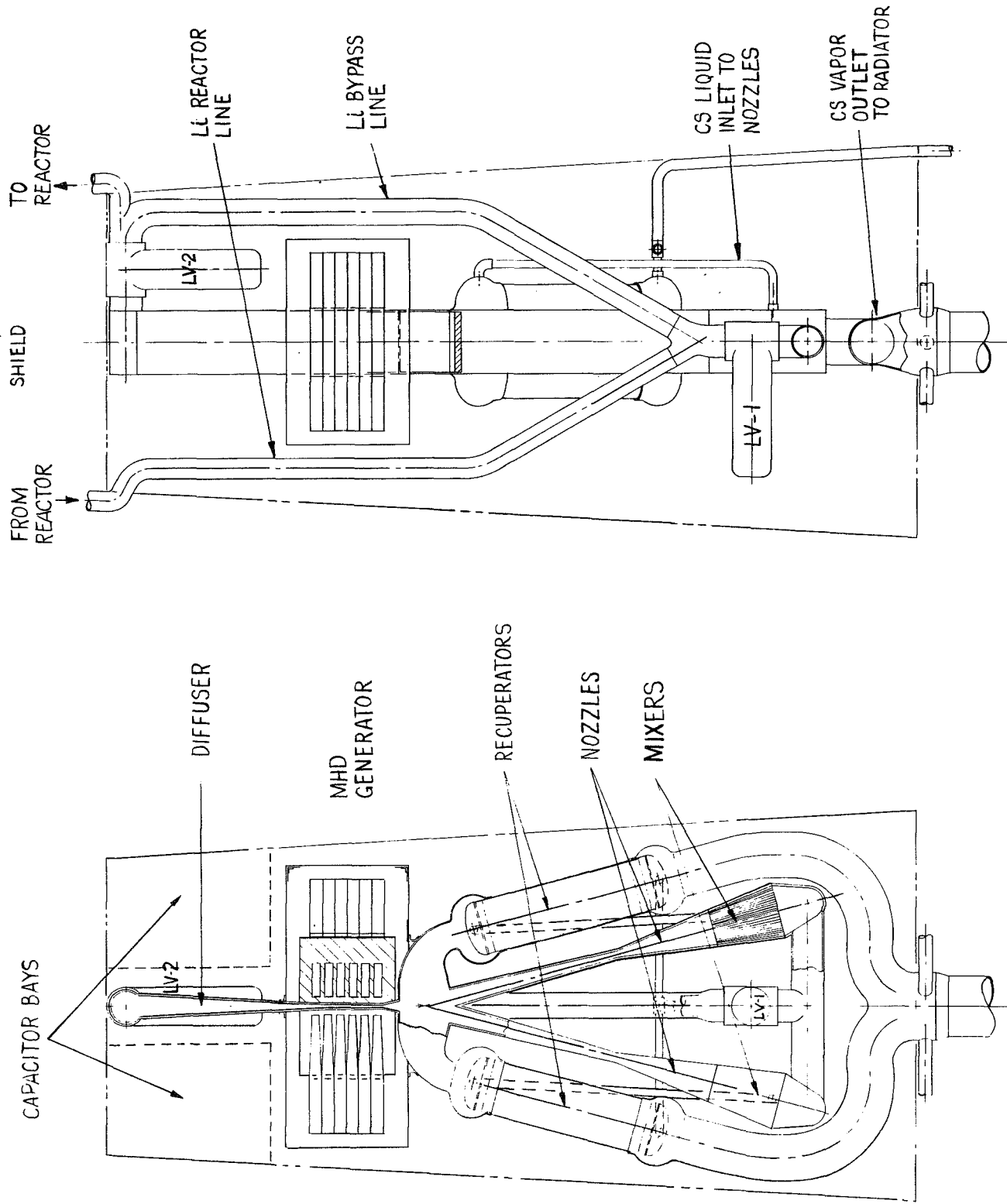


Figure 2-18. MHD Equipment Arrangement with Two Recuperators

inches and 58 inches. These diameters can be reduced somewhat by canting the MHD nozzle assembly and using a single recuperator or relocating the dual recuperators.

2.4.3 SPACECRAFT STRUCTURE

2.4.3.1 Candidate Configurations

Based on the MHD equipment arrangement possibilities which were available, five general configurations for the MHD spacecraft were drawn up. Since the Thermionic Spacecraft Study found that a cylindrical or conical radiator was lighter than a triform radiator (Reference 10), configurations with conical radiators were considered here even though the study guidelines specify a triform radiator.

Configuration No. 1 (Figure 2-19) uses a conical radiator with the radiation shield shadow projected to full diameter (ten foot nominal, nine and one-half foot actual) at the top of the payload bay. In this configuration, as in the other four, a 190 square foot secondary radiator is assigned and the MHD equipment is assumed to be located inside this radiator. In Configuration No. 1, the MHD bay is a bit slender with upper and lower diameters of 36 inches and 53 inches, but has extra length at 16.4 feet so it is reasonable to assume that all MHD equipment could be arranged in this bay.

Configuration No. 2 (Figure 2-20) differs from No. 1 only in that the MHD equipment bay is relocated down near the payload instead of just behind the radiation shield. This relocation might be made to reduce launch loads imposed on the main radiator or to move MHD equipment to a lower radiation region if the use of radiation sensitive components is found necessary.

Configuration No. 3 (Figure 2-21), using a conical/cylindrical radiator, projects the radiation shield shadow to full diameter about halfway down the spacecraft. This shield angle covers an envelope behind it which accommodates the MHD bay configurations discussed in the preceding sections.

Configuration No. 4 (Figure 2-22) projects the same shield angle but with a triform radiator and a triangular shield and MHD equipment bay. This size and shape MHD bay should accommodate all the equipment.

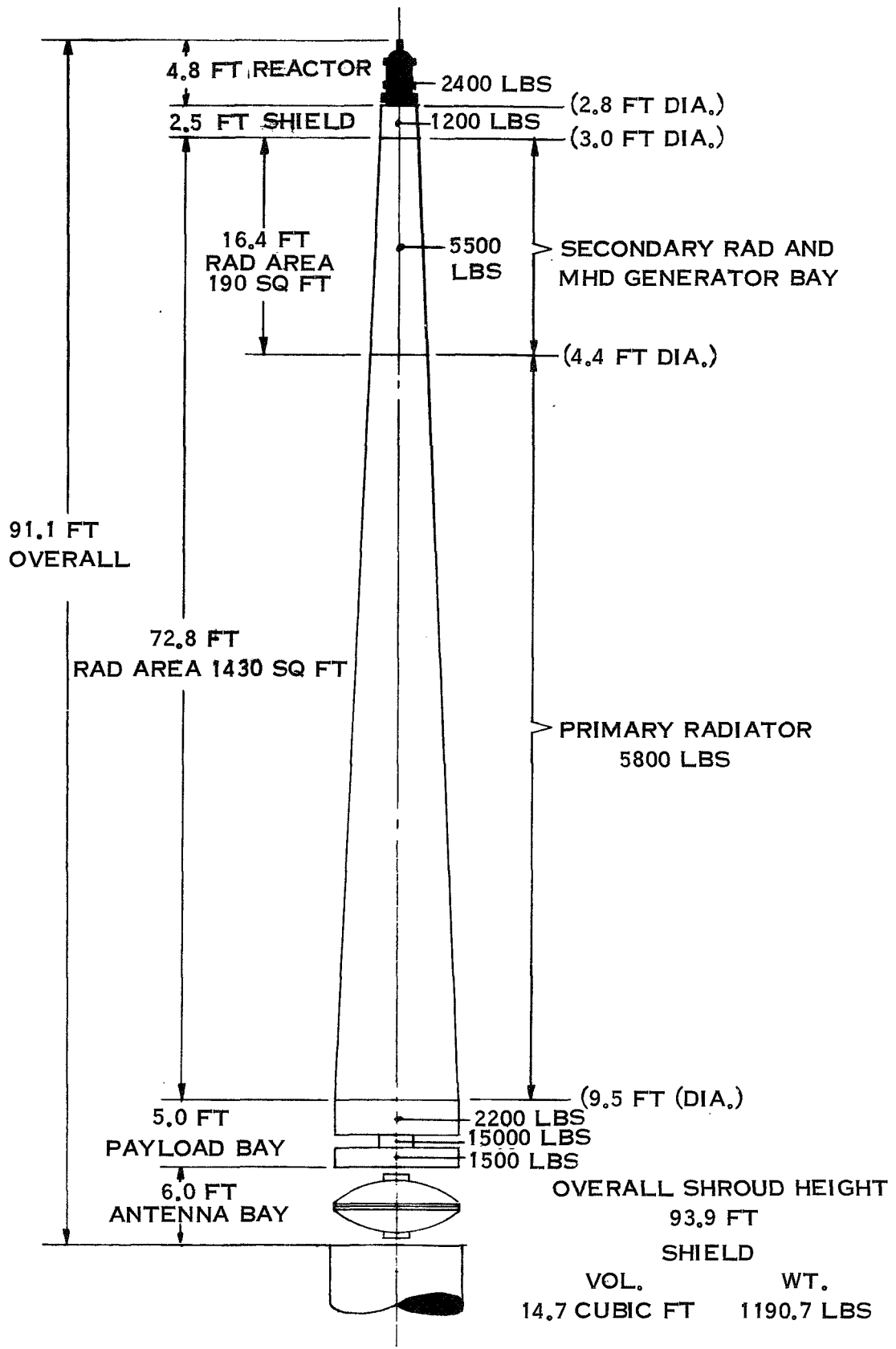


Figure 2-19. MHD Spacecraft Configuration No. 1, Conical Radiator

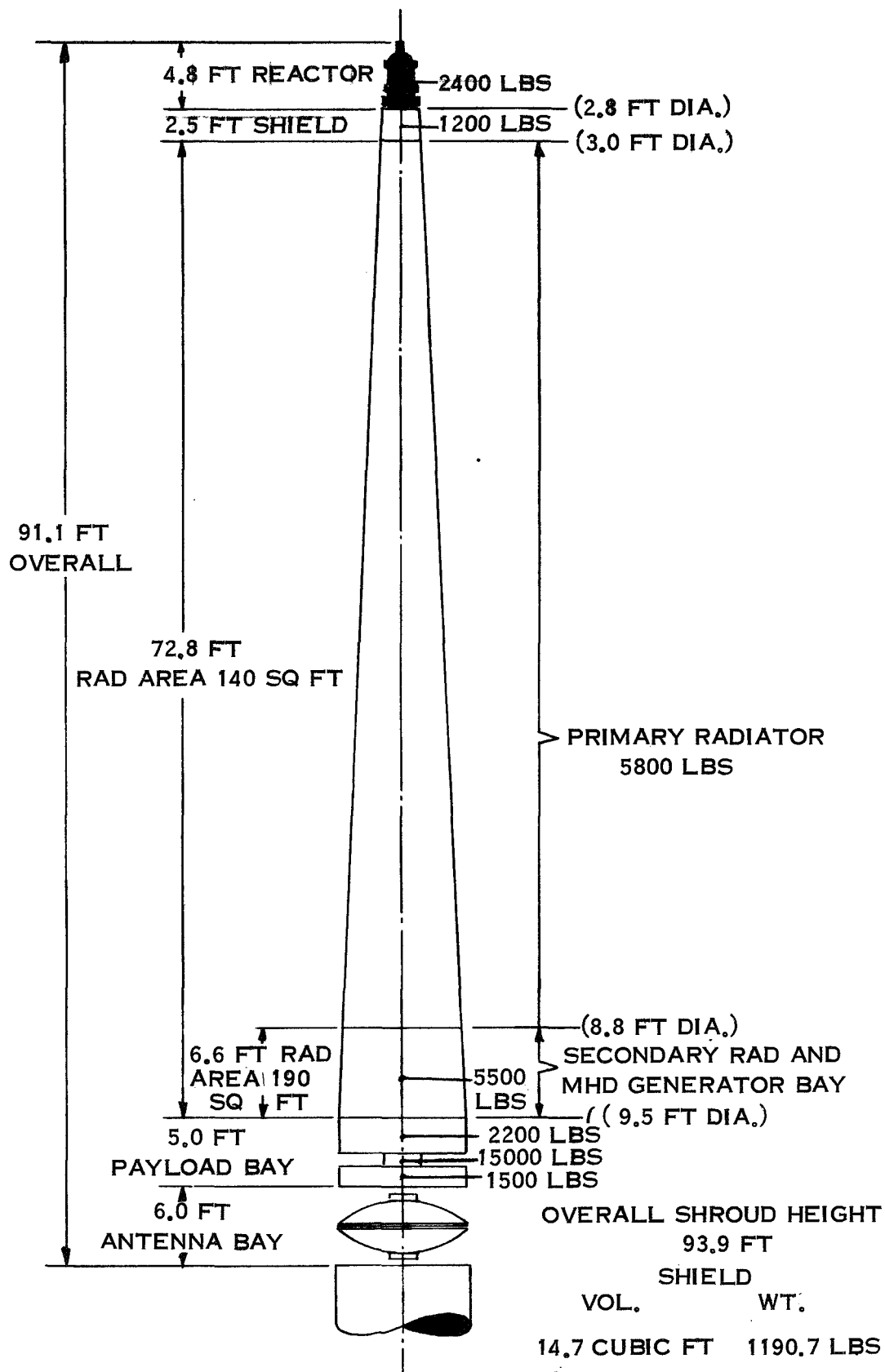


Figure 2-20. MHD Spacecraft Configuration No. 2, Conical Radiator

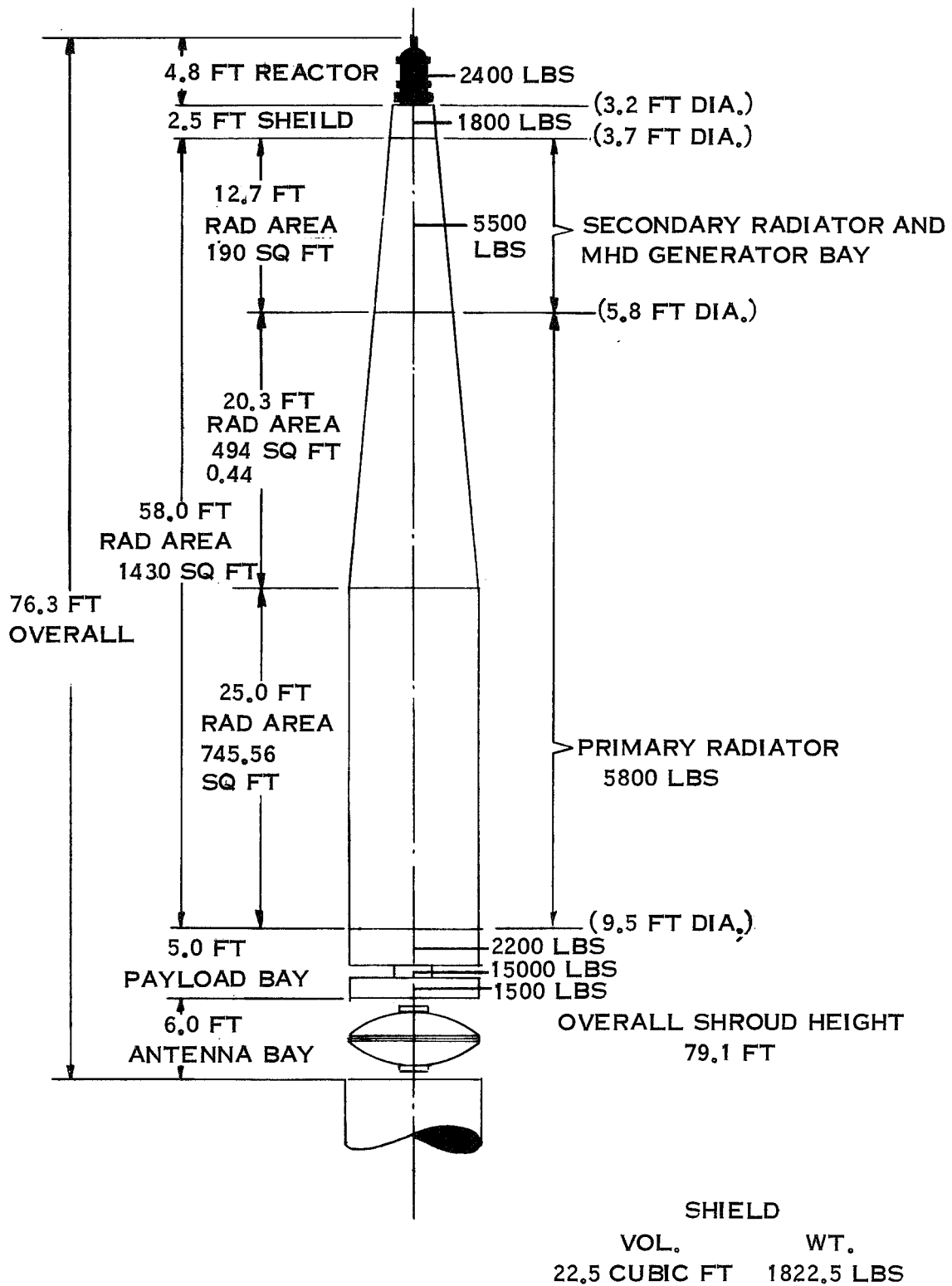


Figure 2-21. MHD Spacecraft Configuration No. 3, Conical and Cylindrical Radiator

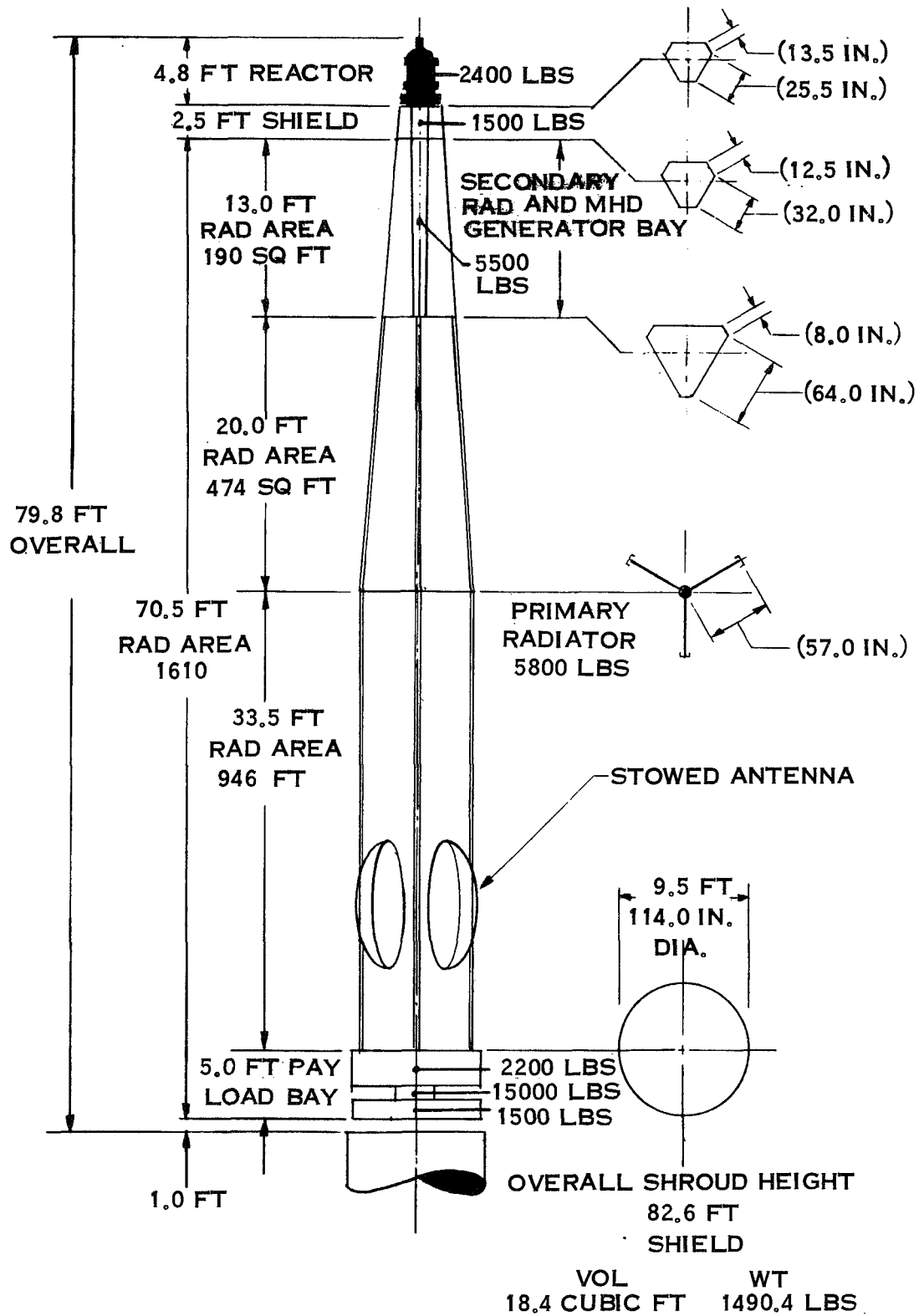


Figure 2-22.MHD Spacecraft Configuration No. 4, Triform Radiator

Configuration No. 5 (Figure 2-23) uses the triform radiator and projects the shield shadow to full diameter at the aft end of the MHD bay. This arrangement provides the shortest spacecraft and a roomy MHD equipment bay, but at the expense of increased shield weight.

In order to provide weights to be used in structural evaluation, the weights listed in Table 2-10 were assumed; these weights are based on the initial design parameters with the shield weights calculated on the basis of 80 pounds per cubic foot, assuming lithium hydride with three and one-half percent stainless steel density for structure and containment and approximately 10 pounds per cubic foot allowance for shield cooling equipment.

2.4.3.2 Structural Analysis

The purpose of this analysis is to define the structural requirements for the five candidate spacecraft configurations to enable them to survive the static and dynamic load environments. The results of this study will be factored into the selection of a basic configuration.

The candidate configurations consist of two conical configurations, one cylindrical-conical configuration and two triform configurations. In each case, the spacecraft is cantilevered from the booster interface and no structure ties exist between the shroud and the spacecraft.

Two load conditions were considered in the analysis, representing the combined static and dynamic loadings at Stage I burnout and at Stage II burnout. These are shown below:

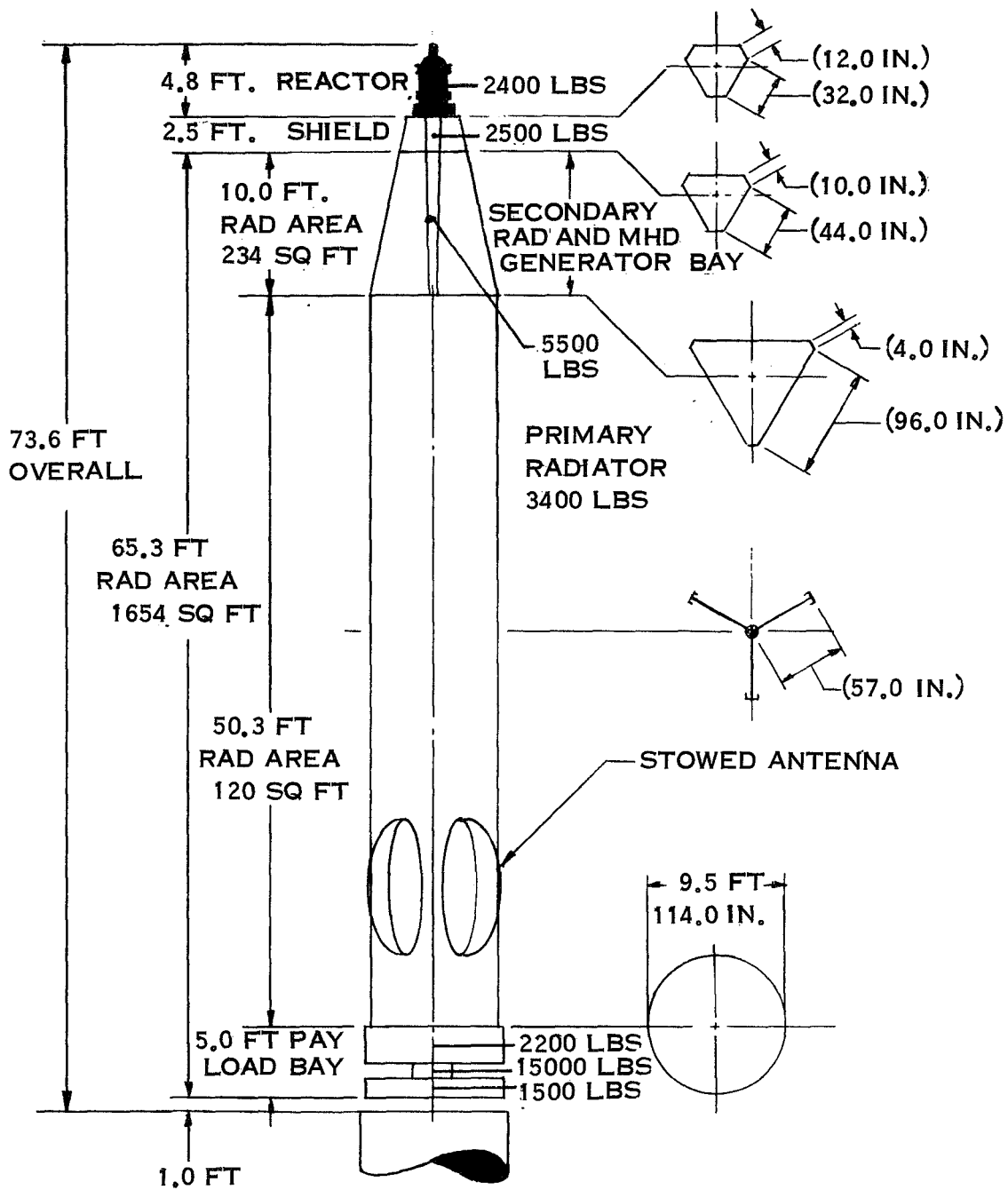
Stage I Burnout - 3 g's lateral and 6 g's axial.

Stage II Burnout - 0.67 g's lateral and 4 g's axial.

These load conditions constitute the limiting design cases according to the booster manufacturer (Reference 11).

This analysis was limited to the primary radiator section of the spacecraft. Maximum use was made of the structural material configured for thermal requirements. The additional structure required to meet the combined static and dynamic load conditions was then identified and sized.

A summary of the additional structural weight requirements along with the maximum lateral tip deflections for each configuration is presented in Table 2-11. It should be noted that



OVERALL SHROUD HEIGHT
 76.4 FT
 SHIELD
 VOL. WT.
 30.1 CUBIC FT 2438.1 LBS
 CYL. 2762.1 LBS

Figure 2-23. MHD Spacecraft Configuration No. 5, Triform Radiator

TABLE 2-11. MHD SPACECRAFT - WEIGHT ESTIMATES FOR CONFIGURATION TRADEOFF

ITEM	WEIGHT, POUNDS
Reactor	2400
Radiation Shield	1200 to 2500 *
Primary Radiator	3400 to 5800 **
MHD Bay	5500
Lithium Loop	400
Cs loop	1570
Auxiliary Cooling Loop	780
MHD Nozzle Assembly	250
MHD Generator	1500
Capacitors	500
Cables, Insulation, Etc.	500
Payload	2200
Thruster System	1500
Propellant	15,000

* Varies with included angle; assumes 30 inch LiH with no gamma shield needed.

** 3400 pounds if triform geometry; 5800 pounds if cylindrical.

TABLE 2-12. SPACECRAFT WEIGHT AND TIP DEFLECTION SUMMARY

Configuration No.	ΔW_T	ΔW_L	ΔW_D	W_L	W_O	S_{TIP}
1	3920	3920	0	37,500	37,500	22.8
2	980	980	0	34,580	34,580	22.0
3	1030	1030	0	35,140	35,140	12.5
4	2450	250	2200	33,950	31,750	12.0
5	2370	224	2146	34,870	32,724	12.3

NOTES

All weights in pounds

ΔW_T - Total additional structural weight required

ΔW_L - Non-disposable additional structural weight required

ΔW_D - Disposable additional structural weight required

W_L - Total spacecraft weight at lift-off

W_O - Total spacecraft weight in orbit

S_{TIP} - Maximum lateral tip deflection - inches

Configurations 1, 3, 4 and 5 each have the 5500 pound MHD generator and secondary radiator bay located near the tip of the spacecraft in contrast to Configuration No. 2 which has the MHD generator and secondary radiator bay located near the booster interface. Therefore, the loading in the secondary radiator is considerably lower for Configuration No. 2 resulting in lower structural weight. Configuration No. 3 has a comparably low structural weight because of its shorter overall length, larger bending moment of inertia, and the same number of load paths in each bay (18 vapor ducts in each bay).

The primary radiators of Configurations 1 and 2 consist of six longitudinal elements and having the shape of truncated cones with each conical element made up of a number of flat radiator panels as shown in Figure 2-24. Configurations 1 and 2 have two elements of 24 panels, two of 12 panels and two of 6 panels. Configuration No. 3 has two cylindrical elements and two conical elements containing 18 panels each.

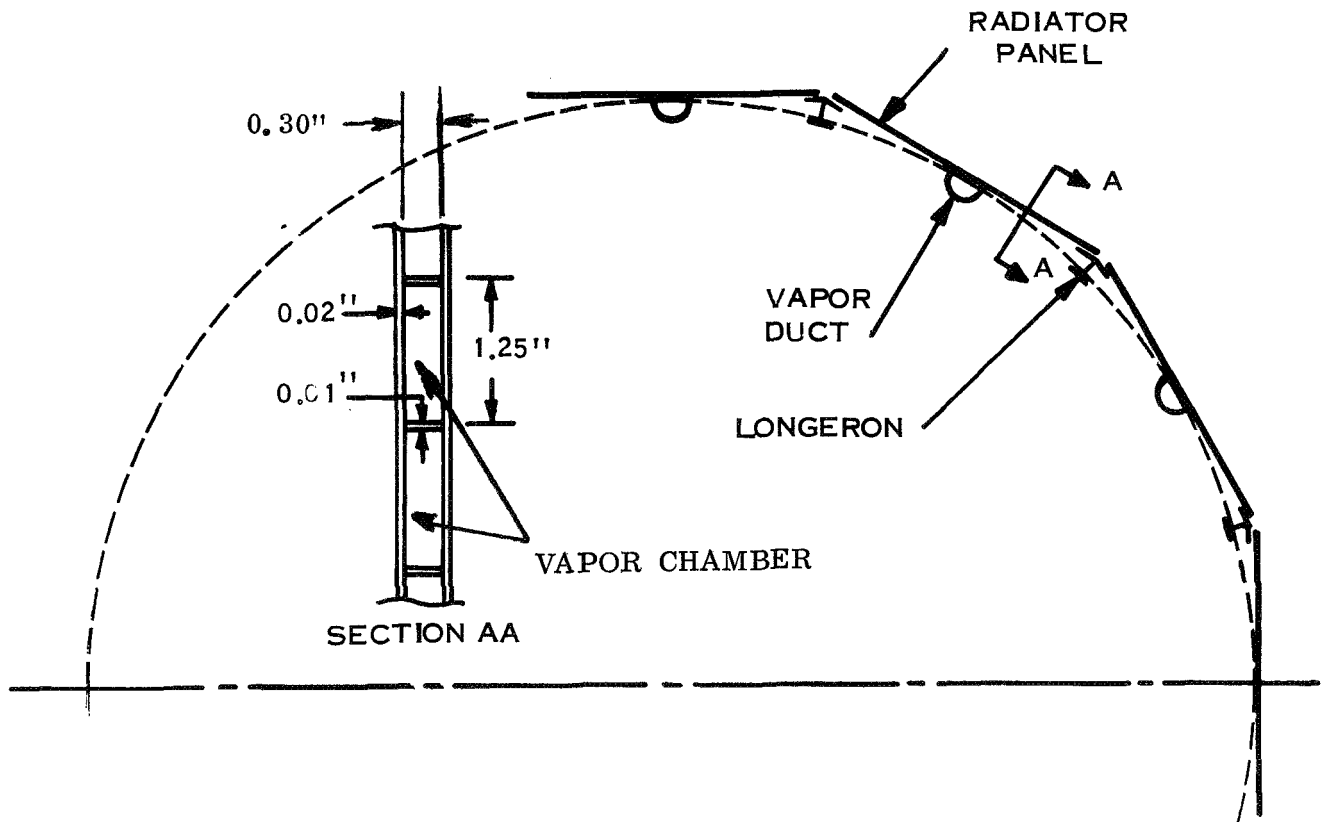


Figure 2-24. Cylindrical/Conical Radiator, Typical Cross-Section

A stability analysis of the 0.02-inch thick radiator panel skins employed in Configurations 1, 2 and 3 has shown that buckling will occur at about 8,000 psi, far below the 46,500 psi working stress of the 301-1/2 hard stainless steel structural material. Therefore, the panel skins were neglected as load carrying elements except in shear. The longitudinal loads are carried by the vapor ducts and the longerons located at the junctions of adjacent radiator panels. Four horizontal frames per conical or cylindrical element prevent buckling of the vapor duct and longerons. Because of the varying number of radiator panels in the conical elements of Configurations 1 and 2, load path discontinuities for the ducts and longerons exist at the junction of the conical elements. Therefore, shear panels have been provided at these junctions to redistribute the loads.

The conical-cylindrical configurations were assumed to have no disposable structure since the between-panel longerons and between-bay shear panels are expected to be impractical to jettison. Therefore, the structure sized for the maximum launch load must be carried throughout the complete mission.

The primary radiators of the triform configurations consist of flat panel elements maintained in a Y configuration by semibulkheads located at the junction of each longitudinal element. The length of a typical element is ten feet to twelve feet. Configuration No. 4 contains three 33.5-foot rectangular sections at the lower end and three 20-foot tapered sections at the upper end. Configuration No. 5 contains three 50.3-foot rectangular sections. The triform configurations have been designed using disposable structure to support the maximum Stage I burnout loads, leaving only that structure required to support the Stage II burnout loads to remain with the spacecraft throughout the mission.

To support the maximum Stage I burnout loads, 6.0 g's axial and 3.0 g's lateral, three disposable heavy channel sections are placed at the edge of the radiator and are joined to the launch vehicle at the base by a Marman clamp arrangement. Shear pins on 12-inch centers transmit the loads from the radiator structure to the support channels. Stabilizing bracing of 1-1/4 inch diameter tubes provide lateral torsional stability. A typical section of this disposable structure is shown in Figures 2-25 and 2-26.

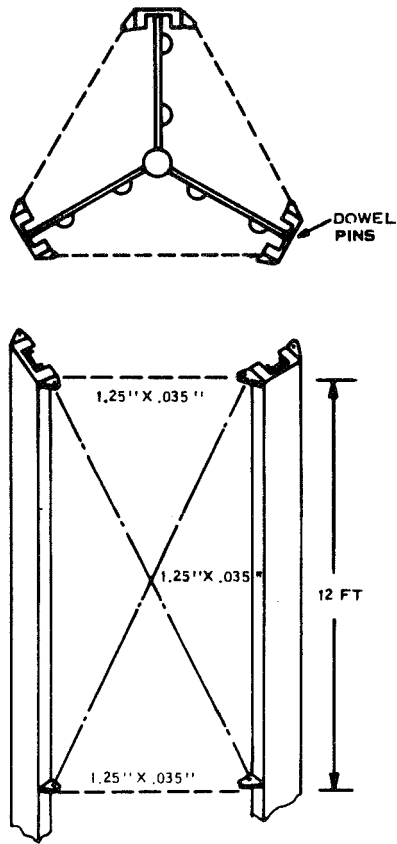


Figure 2-25. Triform Configuration, Typical Section with Stabilizing Bracing

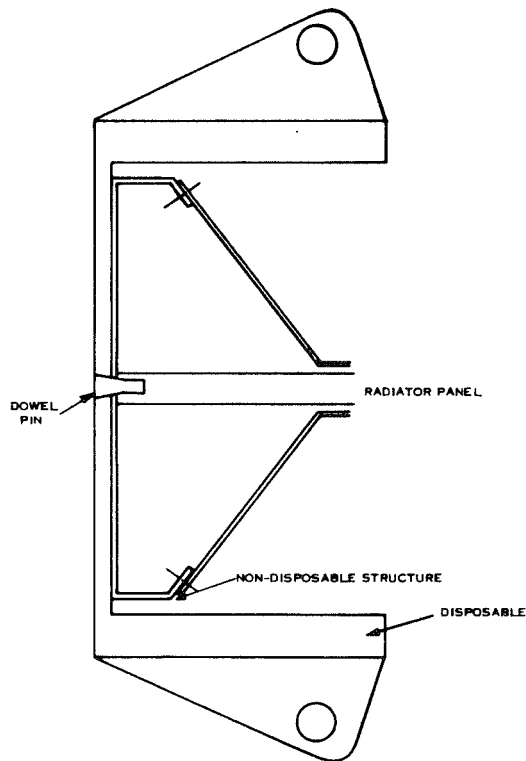


Figure 2-26. Triform Support Structure

The remaining structure, required to support the Stage II burnout loads, 4.0 g's axial and 0.67 g's lateral, consists of light channels permanently attached to the edges of the radiator.

In this appraisal, no methods of taking structural loads through a suitable reinforced flight fairing were considered. The flight fairing, at full diameter, offers the optimum bending moment of inertia per pound of material. However, reaching the load path would require that the payload and fairing diameters coincide or that load spreader members are included at suitably frequent intervals. It is not expected that a significantly lighter structural weight can be obtained by doubling up on the fairing; by using the separate structure, the analysis is simplified. An additional benefit of separate structure is that the payload is then acoustically isolated from the fairing; this is expected to be of significant advantage in the final design of small, poorly supported loads such as hoses and electrical leads.

Conclusions from this Structural Analysis include:

- a. The fundamental frequency of the selected configuration should be calculated and compared with the booster requirements. It is anticipated that the resulting frequency will be on the order of one Hz which is below the current booster requirement of \sim six Hz. The lower frequency can probably be accommodated by design changes in the booster autopilot
- b. The effects of using aluminum in place of stainless steel for the disposable support structure of the triform designs should be analyzed. Stainless steel was chosen to eliminate differential thermal expansion. Since the MHD radiator is launched at low temperature, it may be possible to achieve attractive weight savings by using aluminum
- c. The effects of locating the MHD generator and secondary radiator bay near the booster interface should be investigated.

2.4.4 CONFIGURATION CHOICE

The structural analysis preceding indicates that the triform radiator offers lower net weight than the conical radiator, so it will be used in the baseline design. The apparent success of the triform configuration here and its failure for the thermionic reactor spacecraft can be ascribed to the fact that the MHD radiator derives significant strength from the cesium vapor ducts. The conduction fin radiator in the thermionic reactor spacecraft uses many small tubes.

The configuration with the MHD bay located at the bottom of the radiator (No. 2) seems to offer significant structural weight savings, suggesting synthesis of a new configuration using a triform radiator with the MHD bay at the aft end. The attraction of this idea dims when one considers some of the problems and weights that were omitted from Configuration No. 2 in order to simplify its analysis. An estimate was made of the increase in lithium inventory, piping, and pumping that would accompany relocation of the MHD bay. If the reactor line size calculated for the baseline design were retained the pipe and coolant alone would increase in weight by approximately 1,000 pounds and the reactor line pressure drop would increase by approximately 30 psi. In addition, the lithium accumulator, the startup pump, etc. would have to increase in size. One can conclude, then, that relocation of the MHD bay to the aft end is possible but not attractive.

Configuration No. 4, therefore, was used as the basis for the baseline design arrangement.

2.5 MAJOR DESIGN AREAS

2.5.1 REACTOR AND SHIELD DESIGN

2.5.1.1 Reactor

The MHD power system requires a nuclear reactor heat source which can operate with coolant outlet temperatures ranging from 1600 to 2200^oF. If possible, the reactor should be lithium-cooled in order that there is at least an option to use the reactor coolant directly in the MHD cycle. Since no reactors of this type are under active development at present, it is important to base MHD reactor parameter estimates on reactor development work which has been done. The following reactor design characteristics were generated on the basis of the PWAR-20 SNAP-50 design of 2.2 MW output (Reference 12). These characteristics are considered representative for an MHD reactor with minimum development time and risk. Extrapolations to other power levels and temperatures are based on data in Reference 13. Size extrapolation assumes that core size grows only in diameter and not in length, with core sectional area proportional to power. This assumption will give a conservative shield size estimate. The reactor design characteristics are listed in Table 2-13. Figures 2-27 and 2-28 show the size and weight variation with output power and Figure 2-29 shows an elevation view of the baseline design (3.64 MW) reactor and shield.

TABLE 2-13. MHD REACTOR DESIGN CHARACTERISTICS

Reactor Type (spectrum)	Fast
Design Life (full power hours)	20,000
Fuel	95% dense UC/UN
Coolant	Lithium
Coolant Outlet Temperature	Nominal 2000 ^o F Range 1700 to 2300 ^o F
Inlet to Outlet Coolant Temperature Difference	Nominal 100 ^o F Range 75 to 125 ^o F
Reactor Coolant Pressure Drop	Nominal 10 psi
Reactor Coolant Inlet Pressure	Nominal 53 psi*

* Higher as necessary to suit MHD cycle conditions.

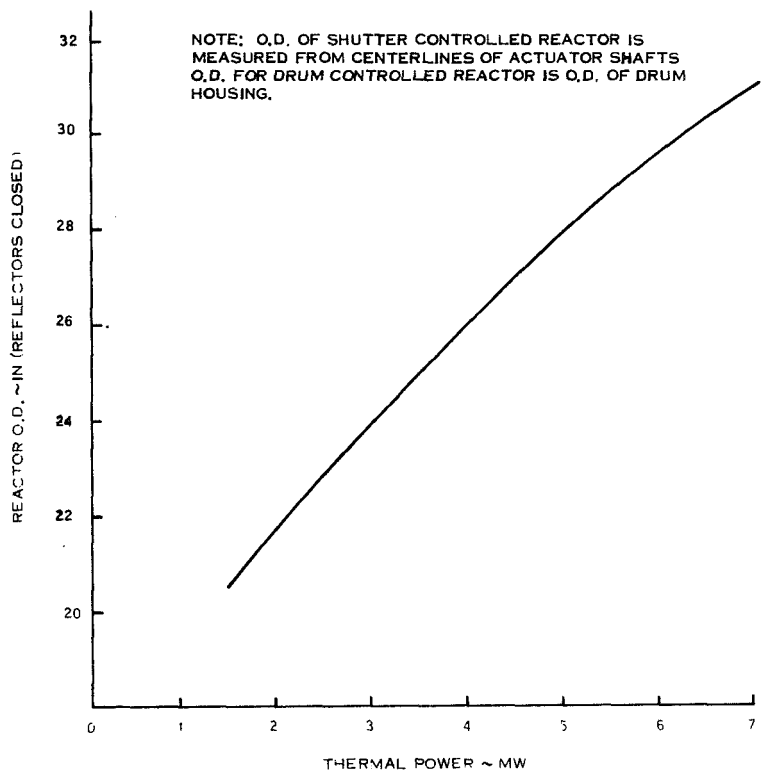


Figure 2-27. MHD Reactor Diameter

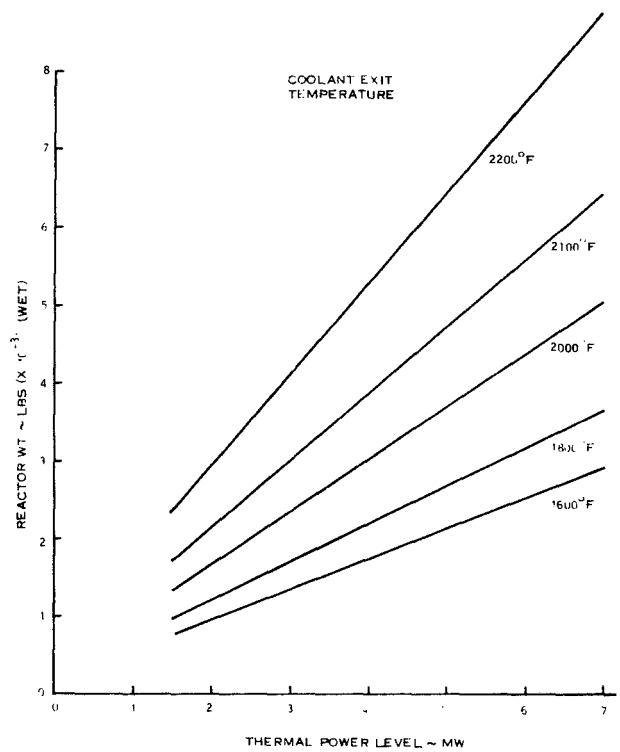


Figure 2-28. MHD Reactor Weight

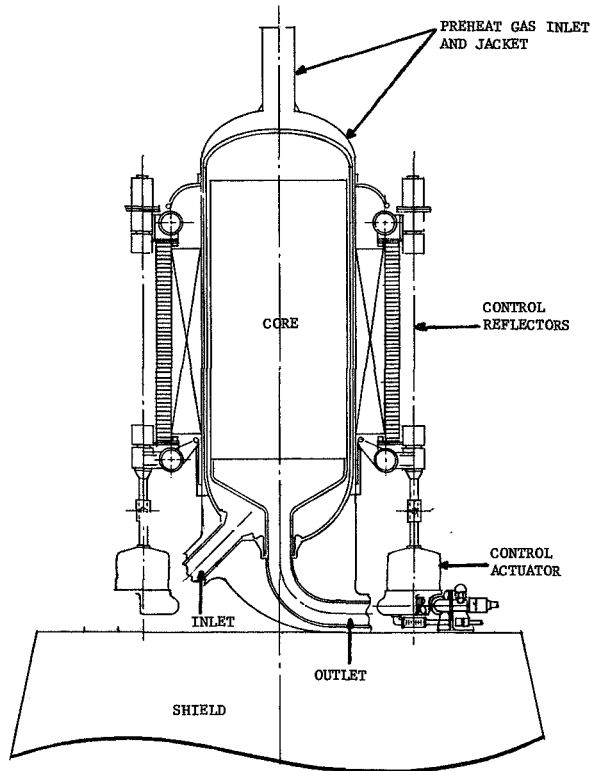


Figure 2-29. MHD Reactor and Shield

The reactor shown in Figure 2-29 uses six reflector shutters for control. The control drive shown in Figure 2-29 and in detail in Figure 2-30 is based on a nutating gear drive which may be used with a liquid-cooled drum control system and derives from a hydrogen flow control valve actuator which was designed by Bendix Corporation Aerospace Division for NASA in the NERVA program (Reference 14). This control drive actuator can be liquid cooled through the connections provided. This actuator can be used for a compact configuration. If desired, a more conventional drive could be installed below the shield with extension shafts running through the shield to the control reflectors. The actuator design could then be simpler but weight would probably be greater and the drives might occupy space below the shield which is desired for MHD equipment.

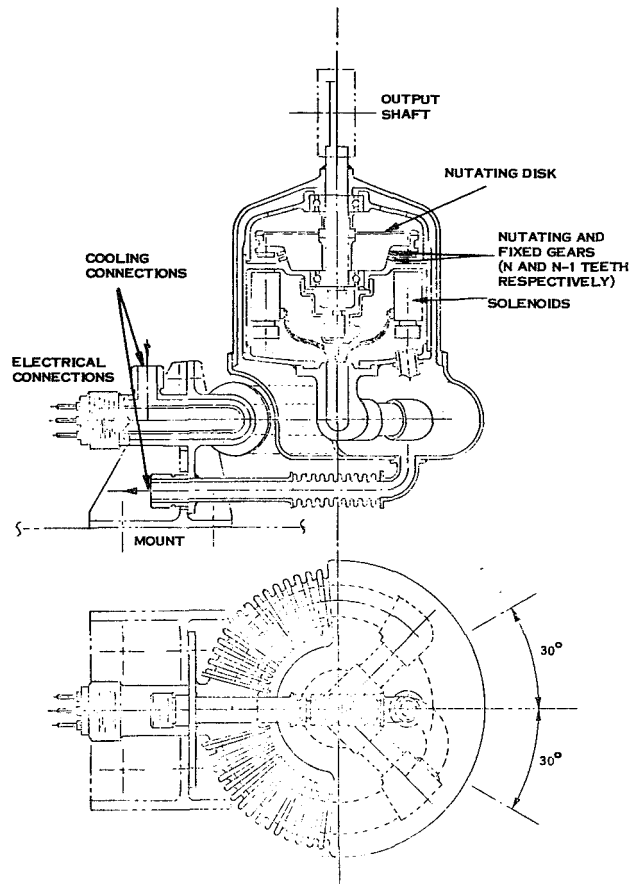


Figure 2-30. MHD Reactor Control Actuator

In addition to the PWAR-20 design, the NASA-Lewis Research Center is currently conducting a study of a fast 2 MW reactor (Reference 15). Both of these designs utilize fully enriched UN fuel pins as the basic core component and lithium as the reactor coolant. In the PWAR-20 case, control is effected by variation in the neutron leakage rate, while the NASA design employs rotating drums in the side reflector (see Figure 2-31). The drums each contain a neutron poison sector and a fuel element sector. The shutter type side reflector of the PWAR-20 is located outside of the pressure vessel and is cooled by radiation to space. The NASA LeRC reactor control drums are located within the pressure vessel and are cooled by the primary lithium coolant. Radiative cooling is feasible as long as the nuclear radiation shield is of the shadow type located on the reactor axis as is the case for the unmanned missions of interest here. However, if mission requirements were to specify the need for a 4π shield, control of the neutron leakage rate would become ineffective and drum control would be required. If this were the case, and if the control drums remained outside of the pressure vessel, a second coolant loop and associated pump and radiator would become necessary.

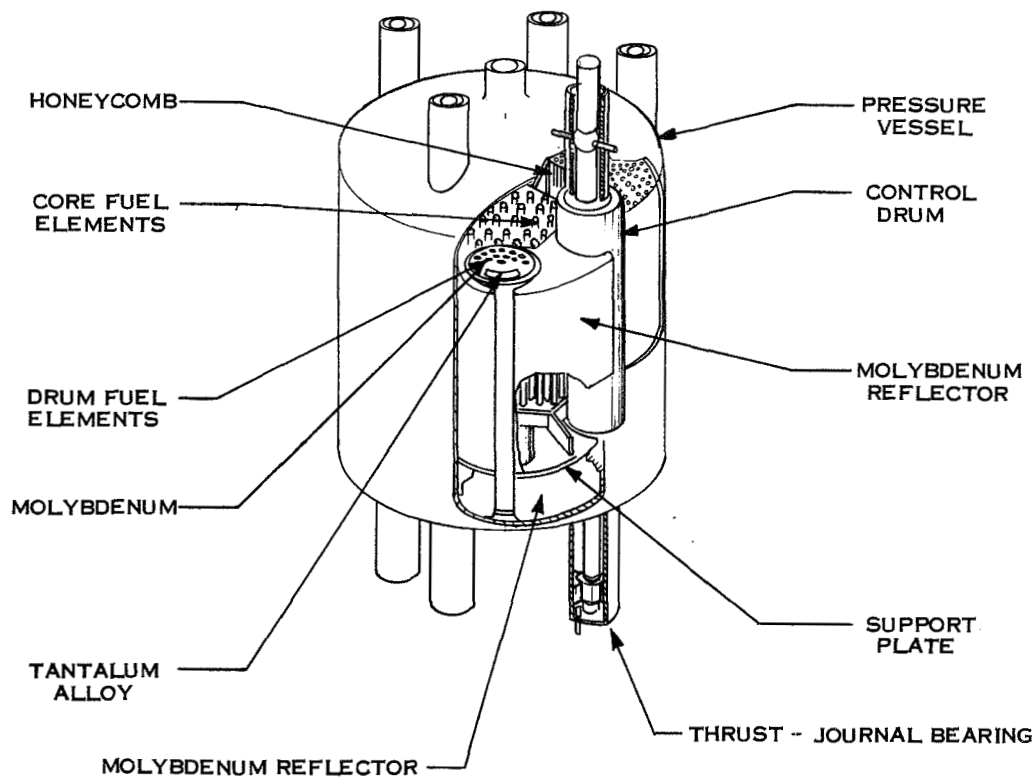


Figure 2-31. NASA LeRC Fast Reactor

In certain circumstances shield weight will be sensitive to control method. Ordinarily, the lateral extension of a shadow shield will be large enough to ensure that no radiation leaving the reactor can proceed directly to the radiation sensitive areas. Consequently, the greater the reactor outside dimensions, the larger the shield lateral dimensions and weight will become. A shutter type side reflector, designed to effect reactor control through the control of the neutron leakage rate, will tend to have the larger reactor diameter. There may be compensating effects, however; a larger core length to diameter ratio may be attainable which will tend to reduce the shadow shield axial thickness. This follows from the greater self-absorption within the core along the axial direction.

In terms of hardware development, one of the most significant programs has been fuel pin development. In-pile tests of fuel pins, clad with Cb-1Zr, have reached burnups of 5 percent with less than 2 percent diametral swelling in 10,000 hours of operation at clad temperatures of about 1800⁰F. These results are very promising and enhance the credibility of the parametric data assigned to the MHD reactor based on the PWAR-20 design.

2.5.1.2 Shield

The radiation shield used in the baseline design is a lithium hydride neutron shield. A 3.5 percent volume fraction of the shield is assumed to be stainless steel containment and support structure, giving the shield an average density of 0.0365 lb/in.³ (assuming a specific gravity of 0.78 for cast LiH). An additional 1/16 inch canning plate is allowed for the outside surface of the shield to assist in heat dissipation and to enhance resistance to micrometeorite puncture.

The 33-inch shield thickness is based on a conservative extrapolation of shield analysis reported in Reference 12; this same analysis and extrapolation indicates that no gamma shield is necessary. The radiation shield is assumed to be passively cooled, operating at a temperature of less than 1000^oF. Shield heating rate estimates made in Reference 16 (See Figure 2-32) were made for the in-core thermionic reactor. The MHD reactor would have a harder flux spectrum but these heating rates are considered usable for estimating purposes. These heating rates indicate that a small shadow shield such as is used here would generate only about one kW of combined neutron and gamma heat. With ~ 30 square feet of surface area viewing space, the shield can easily reject many times this much heat.

Estimates were made of the shielding requirements for the MHD reactor as a function of reactor power level and shield/payload separation distance. The separation distances considered here, 40 feet or greater, permit the simplifying assumption that the dose rate varies as the inverse square of the distance from the shield. This approximation will hold quite well for separation distances greater than about twice the diameter of the shield face, which in the present case would be about eight feet. It is also assumed that the dose rate will be directly proportional to the power level. This would be strictly true if the reactor geometry were to be fixed and increase in power were effected by an increase in the power density. It would be an overestimate of the dose rate if the power increase was brought about by maintaining the power density and increasing the core volume through an increase in its length. The added source volume in this case would be shielded in part by the original core volume and hence its contribution to the dose rate would be reduced. If the core volume were increased by increasing the core diameter, the contribution of the added source to the dose rate would be somewhere between the two cases discussed above.

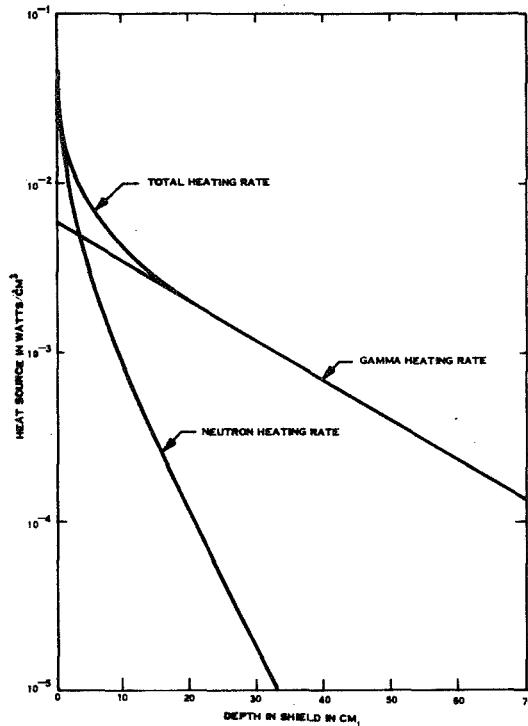


Figure 2-32. Shield Heating Rates

In order to minimize the dose rate at the payload due to radiation scattered from the radiator or other structures, the radiation and the equipment located directly behind the shield are to be within the shielded cone. This requirement results in a shield whose lateral extension is essentially unaffected by the variation in the shield/payload separation distance considered here. Hence, the rear shield face, viewed as a surface source of radiation, will have a constant area. The variation of the neutron flux with the thickness of the LiH shield is based upon the results of a calculation of fission spectrum neutrons in an infinite medium of LiH. The variation of the gamma dose with the thickness of the LiH shield is based upon the results of a shield calculation performed at Oak Ridge National Laboratory for the Unmanned Thermionic Spacecraft Study (Reference 16).

The neutron and gamma ray dose limits at the payload, for 1.4×10^4 equivalent full power operating hours, were set at 10^{12} nvt for neutrons with energies above 1 Mev, and 10^7 rads for gamma rays. It was found that the LiH shield required for the neutrons was more than adequate for the gamma rays. The LiH shield axial thickness as a function of reactor power level and shield/payload separation distance is given in Figure 2-33.

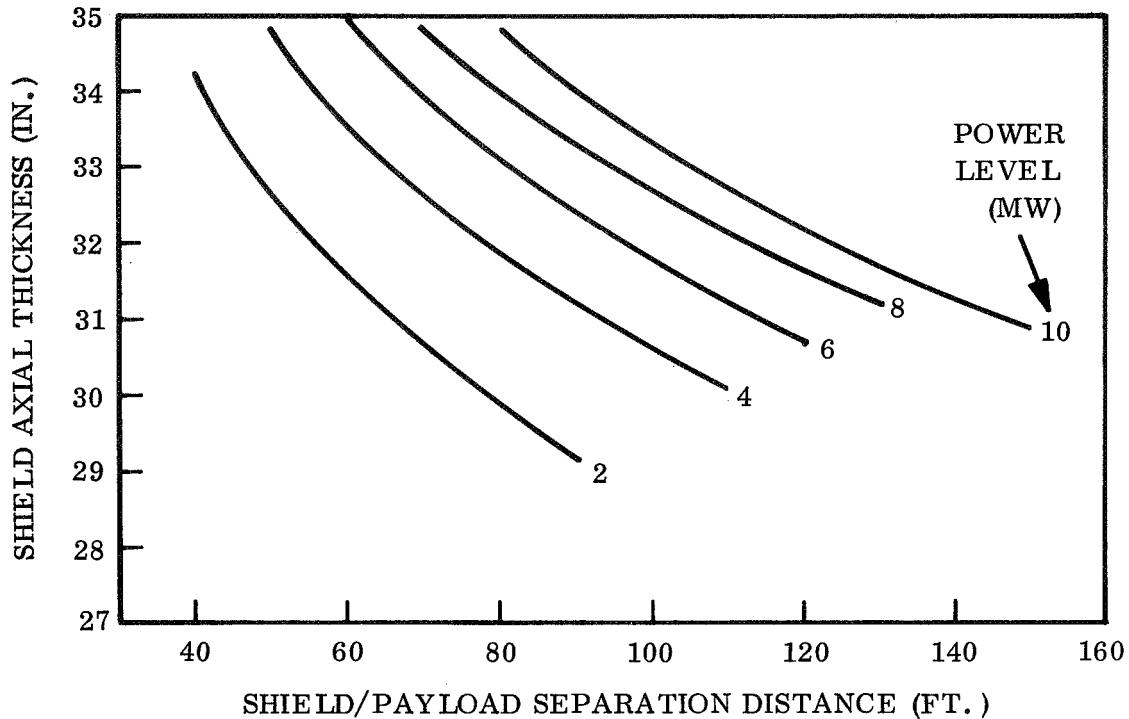


Figure 2-33. Variation of Radiation Shield Thickness With Reactor Power Level and Payload Separation Distance

2.5.2 MHD GENERATOR

2.5.2.1 Generator Design

The MHD generator in the baseline system consists of two laminated iron stator blocks with a wide, shallow lithium flow passage between them. The stator laminations run in the direction of flow, perpendicular to the broad side of the flow passage. The stator blocks are fitted with 25 copper winding (50 turns each) coils which run through slots in the stators normal to the laminations with each coil loop completed by coming over the outside face of the stator block, opposite the flow passage (see Figure 2-34). As the numbering in Figure 2-34 indicates, the coils are numbered and designated as slots serving various sections of the generator duct. Slots 0 and 22 have two coils each and serve the upstream and downstream compensating poles, as well as the first and last segments of the travelling wave region. Table 2-13 lists each slot, the location of its pole piece with respect to the travelling wave region of the generator, and the slot widths for the baseline design generator. Table 2-14 lists the slip, fluid velocity, field velocity and field intensity at each slot point; Table 2-15 lists the major energy quantities received or generated in each sector/

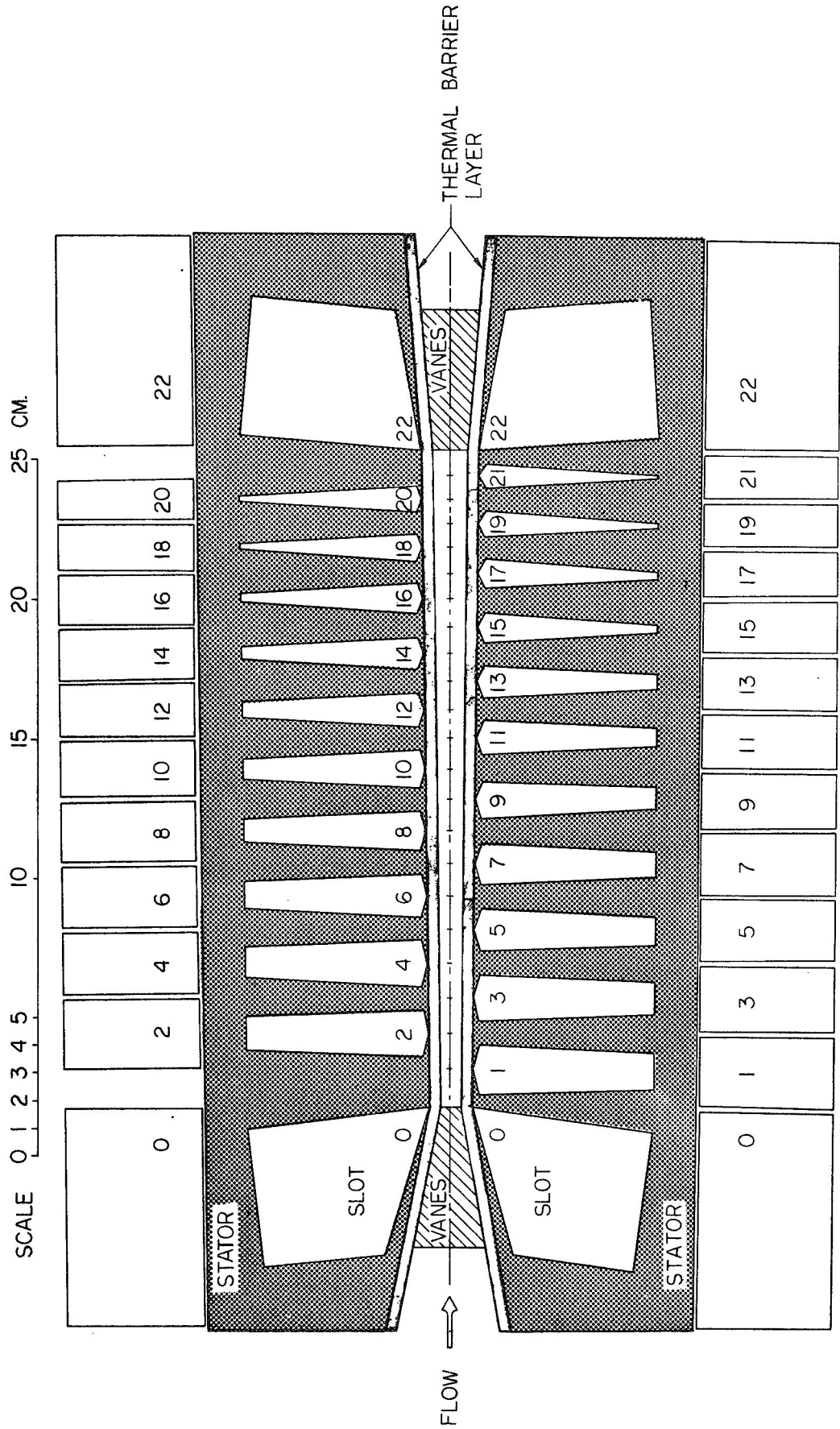


Figure 2-34. Baseline Design MHD Generator

slot, the kinetic energy input, $\frac{\dot{m}}{2} (V_i^2 - V_o^2)$, the winding loss ($I^2 R$), the net usable power generated in the winding and the reactive power of the winding. Note that the first coil of the generator (slot 0) has negative net power, requiring the input of 81.31 kWe of power, and that the last coil (slot 22) generates 138.15 kWe, almost half of the net power produced by the entire generator. This is characteristic of a linear generator of this type, the large powers demanded at the inlet and generated at the exit are due to the abrupt establishment and termination of the machine's magnetic field. This power generation asymmetry almost demands that slots 0 and 22 be wired together. Fortunately, these two slots are almost in phase with one another and are wired together with some additional phase correcting capacitance (see Paragraph 2.5.7). An additional advantage can be taken of the way the MHD generator produces power. Slots 0 and 22 are obviously vital, but the other slots produce only small amounts of power (between 1 and 7 percent). If vital auxiliaries are powered by slot 22, then an open-circuit failure of one of the other slots would not have a significant effect on power output, if the power conditioning system is not seriously perturbed by the input change. This is, in fact, one of the reasons for choosing the baseline design power conditioning system (again, see Paragraph 2.5.7).

The generator stator material is assumed to be Hyperco 27, saturating at about 2 Tesla ($\sim 130,000$ lines/in.²); there might be some advantage in using Hyperco 50 which saturates at about 2.4 Tesla. The winding material in the MHD generator is assumed to be copper with no cladding of any kind. In high temperature winding systems of this sort, it is usually advantageous to use silver conductors and, whether silver or copper, the conductors should be clad with a protective layer of nickel or Inconel to prevent diffusion of conductor material through the insulation at temperature. The baseline design calculations are based on the assumption that 80 percent of the slot cross-sectional area is occupied by conductor material. The inclusion of cladding material and heavier insulation may reduce this conductor area fraction to as little as 50 percent.

TABLE 2-14. BASELINE DESIGN MHD GENERATOR DIMENSIONS

Slot No.	Distance From Beginning Of Travelling Wave Region (cm)	Flow Channel Height At Slot Pole Piece (cm)	Width of Slot At Widest Point Near Point Piece (cm)	Width of Slot At Narrowest Point, Opposite Pole Piece (cm)
0	0.00	0.754	5.021	5.021
1	1.33	0.774	1.742	1.276
2	2.63	0.795	1.692	1.215
3	3.91	0.016	1.642	1.153
4	5.17	0.837	1.592	1.090
5	6.39	0.859	1.542	1.026
6	7.60	0.882	1.492	0.961
7	8.77	0.905	1.442	0.895
8	9.92	0.928	1.394	0.830
9	11.05	0.952	1.345	0.763
10	12.15	0.977	1.297	0.697
11	13.22	1.002	1.250	0.630
12	14.28	1.028	1.204	0.564
13	15.30	1.054	1.158	0.498
14	16.30	1.081	1.114	0.433
15	17.28	1.108	1.070	0.369
16	18.24	1.136	1.027	0.307
17	19.17	1.165	0.985	0.248
18	20.08	1.194	0.944	0.191
19	20.97	1.224	0.904	0.138
20	21.84	1.254	0.865	0.091
21	22.69	1.286	0.827	0.052
22	23.57	1.320	5.021	5.021

Slot Depth		= 6.58 cm
Wall Thickness (Stator-To-Fluid)		= 0.4 cm
Li Channel Width		= 25.1 cm
Duct		
Average		
<u>Compensating Pole</u>	<u>Length (cm)</u>	<u>Height (cm)</u>
Upstream	5.02	1.73
Downstream	5.02	1.66
		<u>No. of Vanes</u>
		18
		28

TABLE 2-15 BASELINE DESIGN MHD GENERATOR DYNAMIC CHARACTERISTICS

Slot No.	Slip	Fluid Velocity (M/sec)	Wave Velocity (M/sec)	Field Strength (TESLA)
0	0.212	114.4	94.4	0.470
1	0.203	111.4	92.6	0.479
2	0.194	108.6	90.9	0.488
3	0.186	105.8	89.2	0.497
4	0.178	103.0	87.5	0.507
5	0.170	100.4	85.8	0.517
6	0.163	97.8	84.1	0.527
7	0.156	95.4	82.5	0.538
8	0.149	92.9	80.9	0.549
9	0.143	90.6	79.3	0.560
10	0.136	88.3	77.7	0.571
11	0.130	86.1	76.2	0.583
12	0.125	83.9	74.6	0.594
13	0.119	81.8	73.1	0.607
14	0.114	79.8	71.7	0.619
15	0.109	77.8	70.2	0.632
16	0.104	75.9	68.8	0.645
17	0.100	74.1	67.4	0.659
18	0.095	72.2	66.0	0.673
19	0.091	70.5	64.6	0.687
20	0.087	68.8	63.3	0.701
21	0.083	67.1	62.0	0.716
22	0.079	65.4	60.6	0.732

TABLE 2-16. BASELINE DESIGN MHD GENERATOR,
POWER SUMMARY

Sector	Input Power (Kinetic Energy) (kW)	Winding Loss (kW)	Net Power (kW)	Reactive Power (KVA)
0	16.08	0.59	-81.31	151.8
1	30.72	0.22	18.51	51.4
2	29.10	0.23	17.72	51.1
3	27.56	0.24	16.94	50.9
4	26.10	0.25	16.17	50.7
5	24.71	0.26	15.41	50.6
6	23.39	0.28	14.66	50.5
7	22.14	0.29	13.92	50.4
8	20.97	0.31	13.21	50.3
9	19.86	0.33	12.50	50.3
10	18.80	0.36	11.80	50.3
11	17.80	0.39	11.12	50.4
12	16.86	0.42	10.46	50.4
13	15.97	0.46	9.80	50.5
14	15.13	0.51	9.16	50.6
15	14.34	0.56	8.53	50.7
16	13.59	0.63	7.91	50.9
17	12.89	0.71	7.29	51.1
18	12.22	0.80	6.67	51.3
19	11.59	0.92	6.05	51.5
20	11.00	1.07	5.41	51.7
21	10.44	1.26	4.75	52.0
22	5.72	1.05	138.15	190.7
Total	416.96	12.14	294.84	1410.2

2.5.2.2 Generator Cooling

The MHD generator stator iron and the coils must be protected from the high temperature of the lithium stream. The stator iron must be kept well below its Curie temperature ($\sim 1400^{\circ}\text{F}$) to maintain magnetic permeability; the copper coils should be held at a temperature low enough to keep the copper's resistance, and therefore the coil losses, at an acceptable level. Consideration was given at first to the use of cooling pipes running through the back iron of the stator blocks as shown in Figure 2-35. This technique is not attractive because analysis showed a stator temperature gradient of about 800°F between the channel wall and the cooling pipes, including transfer of coil losses into the stator. Cooling the coils independently reduces this gradient to 700°F , still an unacceptable value. Figure 2-36 shows a second alternative considered. The section shown in this figure is taken at one side of the lithium channel looking in the direction of flow. Heat transfer from the lithium to the stator is retarded by the ceramic plate and a vacuum gap provided by a layer of ceramic microspheres; then a thin layer of ducts carrying NaK coolant, lying between the ceramics and the stator, remove the heat that does come through. The coolant ducts are small and separated from one another by strips of electrical insulation to prevent the generation of transverse eddy currents. Analysis showed these small ducts to be an attractive way to cool the stator iron but not effective for cooling the windings. With NaK coolant and heat loads in the realm of 25 to 50 kW, the size of these cooling ducts is limited by fabrication capabilities; pressure drop and pumping power are very small. The slotted wall and ceramic layer, proposed in Reference 17, is assumed to be sufficient in limiting heat load to 35 kW (2 sides) if the back side is $\sim 800^{\circ}\text{F}$. The 0.10 inch ducts shown in Figure 2-36 are more than adequate for removing this heat; for the baseline design the combined layer was assumed to be not 0.200 inches, but 0.158 inches (4 mm) for purpose of calculation. The effect of the thickness of this layer on generator performance is discussed in Paragraph 2.1.2.1.2.

To remove the winding loss heat, a finned aluminum winding loom with stainless steel NaK coolant passages is used to cool the external run of each coil. This loom and the cooling analysis are discussed in Paragraph 2.6.1.3.

2.5.2.3 MHD Generator Design Problems

An appraisal of the MHD generator design reveals a number of areas where serious development problems exist or where modification of analytical assumptions or methods should be considered.

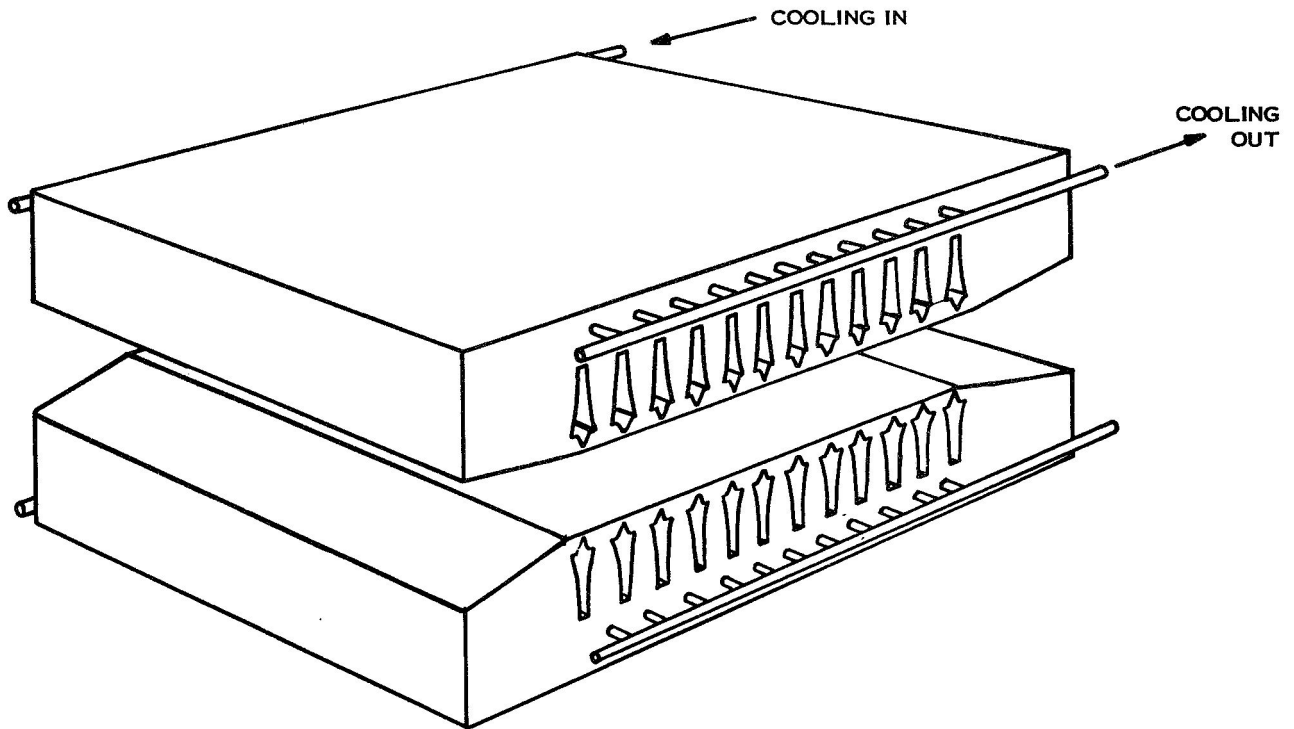


Figure 2-35. Cooling Pipes in MHD Stator Block

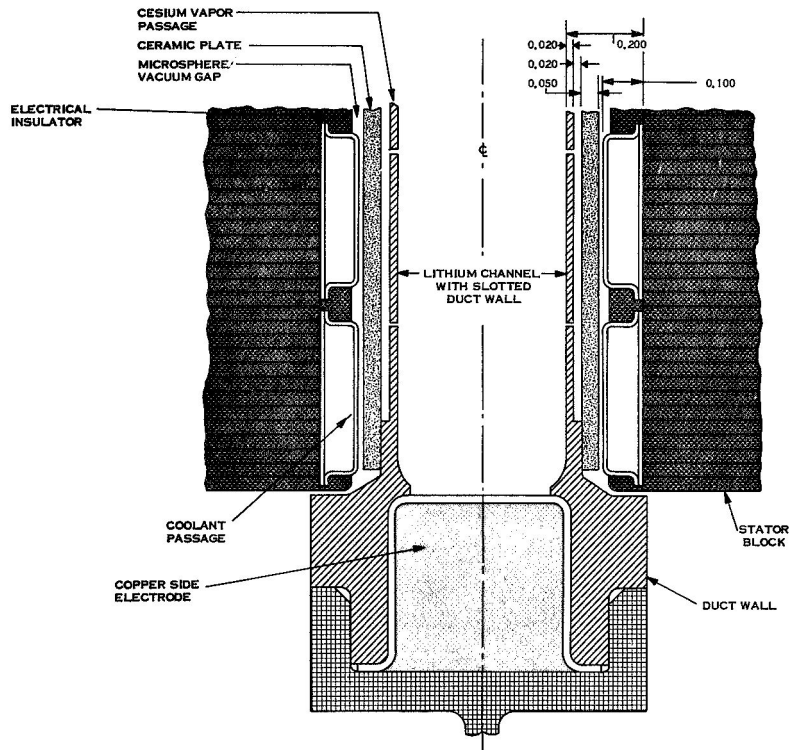


Figure 2-36. MHD Stator Cooling Passages at Lithium Duct Face

2.5.2.3.1 Vanes - The upstream and downstream compensating pole regions of the MHD generator are fitted with many small vanes to suppress transverse fluid currents in this region. These vanes constitute a mechanical design problem since they should be as thin as possible, electrically resistive and must withstand the erosive force of hot lithium for long periods. Should a vane be carried away, its absence would have little effect on generator performance but a loose piece of metal in the flow stream could have disastrous effects. This problem has been recognized by the workers at JPL and design development is underway to re-optimize the generator duct geometry to greater height and narrower width in order that the vanes may be eliminated altogether, or fewer, and thicker, vanes used. The attendant change in system efficiency is slight; reliability is increased greatly, and the can loss problem is alleviated by the narrower duct, as indicated in the following section.

2.5.2.3.2 Can Loss - In order to assess the degree of need for a nonconducting or at least segmented duct, an approximate calculation was made for the duct loss assuming a 0.060 inch refractory metal duct. Duct loss is given by (Reference 18 and 19) the following formula for a moving field of amplitude B lines/in.² with a wave velocity of V_R in./sec. The duct electrical resistivity (ohm-in.) is ρ.

$$\frac{\text{Loss (kW)}}{\text{in.}^3 \text{ duct wall}} = V_R^2 B^2 \times \frac{12.5}{\rho} \times 10^{-20}$$

Taking B = 38,400 lines/in.² (0.607T) and V_R = 2880 in./sec (73.1 m/sec) corresponding to values given at slot No. 13 near the center of the duct. The loss per unit duct volume is (ρ = 20 x 10⁻⁶ ohm-in.) 75 kW/in.³ for the baseline generator.

For a duct wall volume of approximately 12 in.³ (2 x 10 in. x 10 in. x 0.06 in.) the total loss is of the order of 900 kW. This result is of course meaningless in the sense that the electromagnetic effect of such large duct wall currents would greatly increase the winding load current and would completely invalidate the present design. The result is only shown to emphasize the absolute need for a nonconducting, (or at least segmented) duct. The use of a refractory metal duct in the manner of current state of the art induction type EM pumps, which operate at duct flux density levels approximately 1/4 that of this design and at field wave velocities approximately 1/6 of that used here, is completely out of the question.

No ceramics have been identified which can resist 1800°F lithium for long periods. The cesium vapor buffer scheme depicted in Figure 2-36 is complex. Although the preceding calculations of can loss rules out ordinary duct walls, one possibility remains. As noted in the preceding section, generator redesign to eliminate the vanes in the compensating pole region leads to a narrower duct. This geometry change alone reduces can losses significantly by reducing the area affected. In addition, the can losses can be further reduced by reducing the field intensity. For example, a 200 kWe system design recently calculated has the parameters listed in Tables 2-17, 2-18 and 2-19. Using the values for Slot 12,

$$V_{12} = 72.0 \text{ M/sec} = 2840 \text{ in/sec}$$

$$B_{12} = 0.348 \text{ T} = 22,000 \text{ lines/in.}$$

the can loss if calculated and found to be 24.4 kW/in³, about one-third of the value calculated for the baseline design. Thus, if some wall design with an equivalent metal thickness of the order of 0.010 inch can be developed, a duct wall with acceptably low loss can be made; the loss for 0.010 inch thickness is 28 kWe out of the 200 kWe, about 14 percent.

Current work at General Electric in ceramic/refractory metal technology has suggested a design solution for the MHD duct wall. If a matrix of Al₂O₃ and Cb-1Zr is formed in a special manner, a layer of appropriate thickness, about 0.2 inch, can be made which has a relatively low thermal conductivity (see Figure 2-37). This layer would be made with graded seal addition to present a solid Cb-1Zr face to the lithium for corrosion resistance, and increase rapidly in Al₂O₃ content so that electrical conductivity in the plane decreases rapidly. With a layer of ceramic microspheres between it and the stator cooling passages (Figure 2-36) to provide one thermal radiation gap, this would provide adequate thermal resistance. Since Al₂O₃ and Cb-1Zr have similar coefficients of thermal expansion, the structural performance of this layer should also be acceptable. Development work in this area is recommended as discussed in Appendix A.

TABLE 2-17. Constant Slip 200 kWe MHD Generator Dimensions

Slot No.	Distance From Beginning of Travelling Wave Region (cm)	Flow Channel Height at Slot Pole Piece (cm)	Width of Slot at Widest Point Near Pole Piece (cm)	Width of Slot At Narrowest Point, Opposite Pole Piece (cm)
0	0.000	1.417	7.421	7.421
1	1.69	1.440	2.506	1.846
2	3.35	1.464	2.452	1.777
3	4.98	1.489	2.398	1.706
4	6.59	1.514	2.343	1.635
5	8.17	1.541	2.288	1.564
6	9.72	1.568	2.233	1.491
7	11.24	1.597	2.178	1.417
8	12.74	1.627	2.122	1.341
9	14.21	1.659	2.066	1.265
10	15.65	1.692	2.009	1.187
11	17.06	1.726	1.952	1.107
12	18.44	1.763	1.894	1.026
13	19.79	1.801	1.836	0.943
14	21.12	1.842	1.777	0.859
15	22.41	1.885	1.717	0.773
16	23.68	1.930	1.656	0.684
17	24.91	1.979	1.595	0.595
18	26.11	2.032	1.532	0.504
19	27.28	2.088	1.468	0.412
20	28.42	2.149	1.402	0.321
21	29.53	2.215	1.335	0.232
22	30.60	2.287	1.267	0.148
23	31.64	2.366	1.196	0.075
24	32.64	2.454	7.421	7.421
Slot Depth			=	7.42 cm
Wall Thickness (Stator-to-Fluid)			=	0.4 cm
Li Channel Width			=	11.6 cm

TABLE 2-18. Constant Slip 200 kWe MHD Generator Dynamic Characteristics

Slot No.	Slip	Fluid Velocity (M/sec)	Wave Velocity (M/sec)	Field Strength (TESLA)
0	0.300	116.5	89.6	0.280
1	0.300	114.6	88.2	0.285
2	0.300	112.7	86.7	0.289
3	0.300	110.9	85.3	0.294
4	0.300	109.0	83.9	0.299
5	0.300	107.1	82.4	0.304
6	0.300	105.2	81.0	0.310
7	0.300	103.3	79.5	0.316
8	0.300	101.4	78.0	0.321
9	0.300	99.5	76.6	0.328
10	0.300	97.6	75.1	0.334
11	0.300	95.6	73.6	0.341
12	0.300	93.7	72.0	0.348
13	0.300	91.7	70.5	0.356
14	0.300	89.6	69.0	0.364
15	0.300	87.6	67.4	0.372
16	0.300	85.5	65.8	0.381
17	0.300	83.4	64.2	0.391
18	0.300	81.2	62.5	0.401
19	0.300	79.1	60.8	0.412
20	0.300	76.8	59.1	0.425
21	0.300	74.5	57.3	0.438
22	0.300	72.2	55.5	0.452
23	0.300	69.8	53.7	0.467
24	0.300	67.3	51.7	0.485

TABLE 2-19. Constant Slip 200 kWe MHD Generator Power Summary

Sector	Input Power (Kinetic Energy) (kW)	Winding Loss (kW)	Net Power (kW)	Reactive Power (KVA)
0	9.04	0.20	-28.90	29.3
1	17.87	0.16	10.19	20.9
2	17.61	0.17	10.18	20.8
3	17.36	0.18	10.17	20.6
4	17.13	0.18	10.15	20.5
5	16.90	0.19	10.14	20.4
6	16.69	0.20	10.13	20.2
7	16.48	0.21	10.11	20.1
8	16.29	0.22	10.10	20.0
9	16.10	0.23	10.08	19.9
10	15.92	0.25	10.06	19.7
11	15.76	0.26	10.04	19.6
12	15.60	0.28	10.02	19.5
13	15.45	0.30	9.99	19.4
14	15.30	0.32	9.96	19.3
15	15.17	0.35	9.93	19.2
16	15.04	0.38	9.89	19.2
17	14.92	0.42	9.84	19.1
18	14.80	0.46	9.79	19.0
19	14.69	0.52	9.72	19.0
20	14.59	0.59	9.64	18.9
21	14.50	0.68	9.54	18.9
22	14.41	0.81	9.40	18.9
23	14.33	0.99	9.21	18.9
24	7.16	0.21	34.19	20.9
TOTAL	379.10	8.77	233.58	502.1

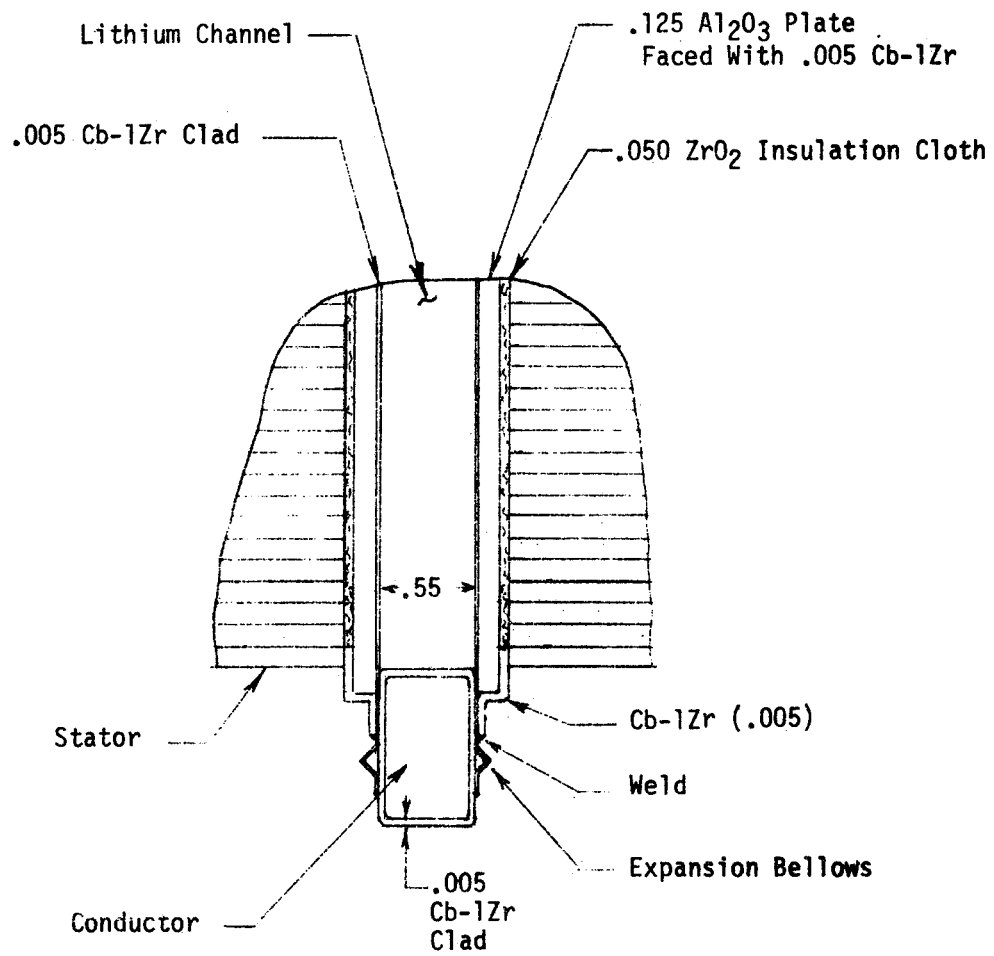
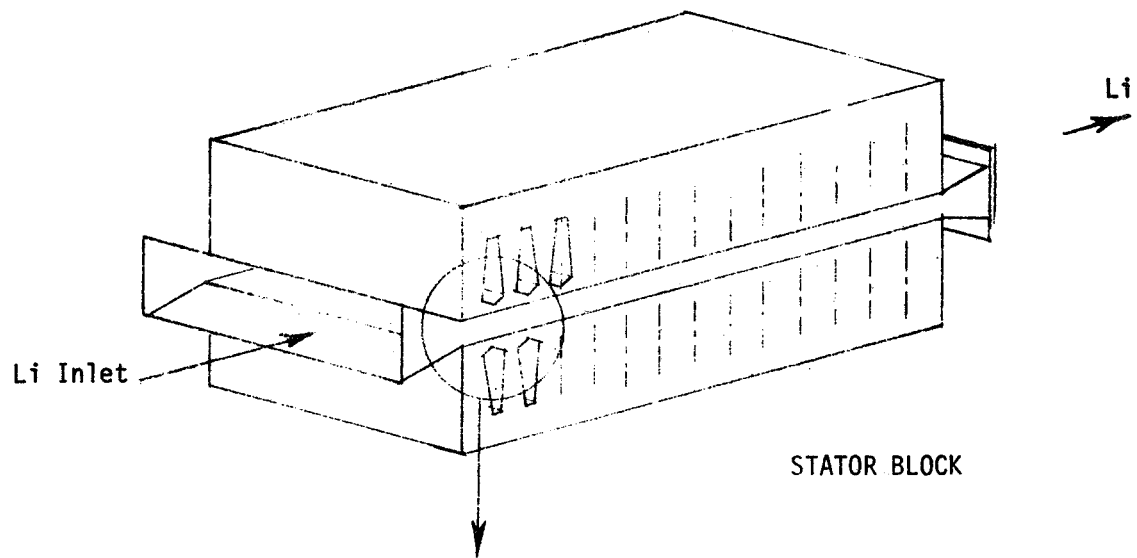


Figure 2-37. Proposed MHD Generator Duct

2.5.2.3.3 Core Loss - The core loss has been approximately evaluated with the use of experimental data for total core loss (eddy current plus hysteresis) in watts per pound for Hyperco 27 0.004 inch thick laminations as a function of flux density and frequency. At a frequency of 300 Hz, 20,000 gauss (2T) the core loss is of the order of 20 watts per pound. This corresponds to 3600 watts for the 180 pound core. This loss is small (but not negligible) compared to the I^2R loss in the windings. The temperature difference involved in conducting this loss through a Hyperco 27 stator is of the order of 150^oF assuming the core is cooled at the back. It may be noted, however, that 0.9 is a more realistic value of stacking factor for flame sprayed alumina interlaminar insulation type cores with 0.004 inch laminations.

2.5.2.3.4 Winding Loss - It has been found that large errors result from the calculation of the winding loss on the basis of applying an average current density and average ac/dc resistance (R_{ac}/R_{dc}) ratio, and an average space factor over the entire slot cross section. The reasons for this are the following:

1. The presence of a slotliner ground insulator, of turn to turn insulation, and of low conductivity nickel or Inconel coating in the silver (or copper) conductors affects the effective available conducting cross section of the various conductors stacked in the tapered slot quite non-uniformly. This causes inequality of the current density in slot conductors, at least with the present slot dimensions.
2. Since the slot leakage field flux density varies greatly from the top to bottom of the slot, the conductor eddy current density and the R_{ac}/R_{dc} ratio also vary greatly. Formulae for this effect available in the literature cover only the case of a constant width slot. The average value of the R_{ac}/R_{dc} ratio for 50 series conductors approximately 1.13 mm thick at 300 cps (silver at 700^oF) is approximately 1.4, but the ratio varies from essentially 1.0 for the bottom conductor to 2.2 for the top conductor (near the open end of the slot) (Reference 20).

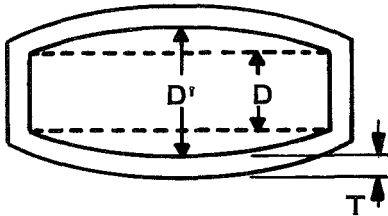
The following conclusions can be stated:

1. A 20 to 30 mil thick ceramic slot liner (smaller thicknesses being mechanically impractical), combined with wrap-around E or S glass serving turn to turn insulation, combined with several mils of nickel or Inconel coating results in prohibitively high current densities in the conductors placed near the bottom of the narrow slots. The design must be modified to widen some of the slots at the narrow end.
2. In conjunction with wider slots at the narrow end, design for non-uniform conductor thickness may be advantageous. The effect of thickness on R_{ac}/R_{dc} loss ratio is much smaller at the slot bottom than at the top. This would tend to equalize current density and loss per unit volume.
3. The winding loss calculation portion of the generator design computer program might be modified to calculate current density and R_{ac}/R_{dc} ratio for each individual conductor, taking into account the effects of varying conductor dimensions, leakage field flux density, and variation of temperature. This could be done in conjunction with a somewhat detailed design selection of the conductor and slot insulation system.

2.5.2.3.5 Heat Transfer. Because of extremely high current density in some of the slot conductors (region of the narrow end of slots 18 through 21) the conductor cooling mode based on heat conduction along the conductors in the slot portion to a cooled, out-of-stack region of the conductors is not adequate in this portion of the winding. Also, even the wide region of these same slots is somewhat marginal with respect to hot spot to coolant ΔT because of the high R_{ac}/R_{dc} ratio prevailing locally near the open end of the slots. As stated above, it is essential to reduce the peak local current density in some of the slots. Also, it appears that a more detailed calculation procedure for conductor temperature distribution is necessary. This procedure should account for intra conductor heat transfer across turn to turn insulation and associated interface thermal resistances and also for heat transfer into the stack across the slot insulator and associated interfacial thermal resistances. Some data is available (Reference 21) in the magnitude of such interfacial thermal resistances under vacuum conditions.

2.5.3 MHD NOZZLE ASSEMBLY

One key problem was investigated in the design of the MHD nozzle assembly, how to prevent unacceptable distortion of the nozzle geometry due to creep effects. The baseline system uses a nozzle with a very wide and shallow bore, 9 to 10 inches wide and only about an inch high in the throat. Made of Cb-1Zr and operating at $\sim 1800^{\circ}\text{F}$ for 10 to 20,000 hours, internal pressure can distort this rectangular flow passage to an elliptical shape. The pressure profile can be considered roughly the same as that reported in Reference 22 and illustrated in Figure 2-38. A calculation of design stresses and material thickness requirements was made using the nozzle geometry shown in Figure 2-39. It was assumed that the limit of acceptable distortion would be a 5 percent increase in the flow passage width or height, d



$$d' \leq 1.05 d$$

Thus, the beam (side) deflection, y , is 2.5 percent of the passage dimension, and the strain, ϵ , is

$$\epsilon = \frac{32C}{l^2} y = \frac{16t}{l^2} y$$

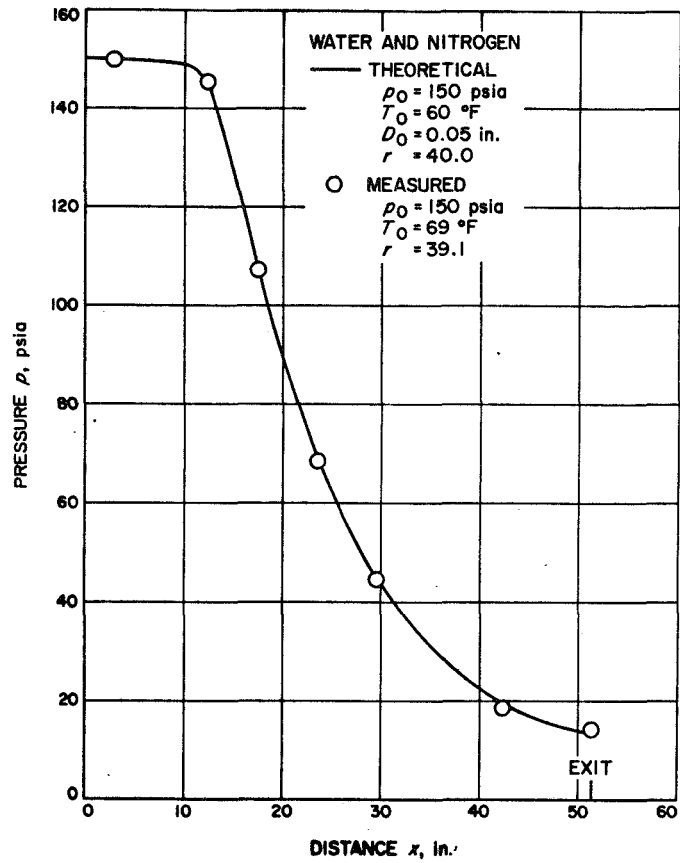


Figure 2-38. Comparison of Theoretical and Experimental Pressure Profiles in a Two-Phase Nozzle

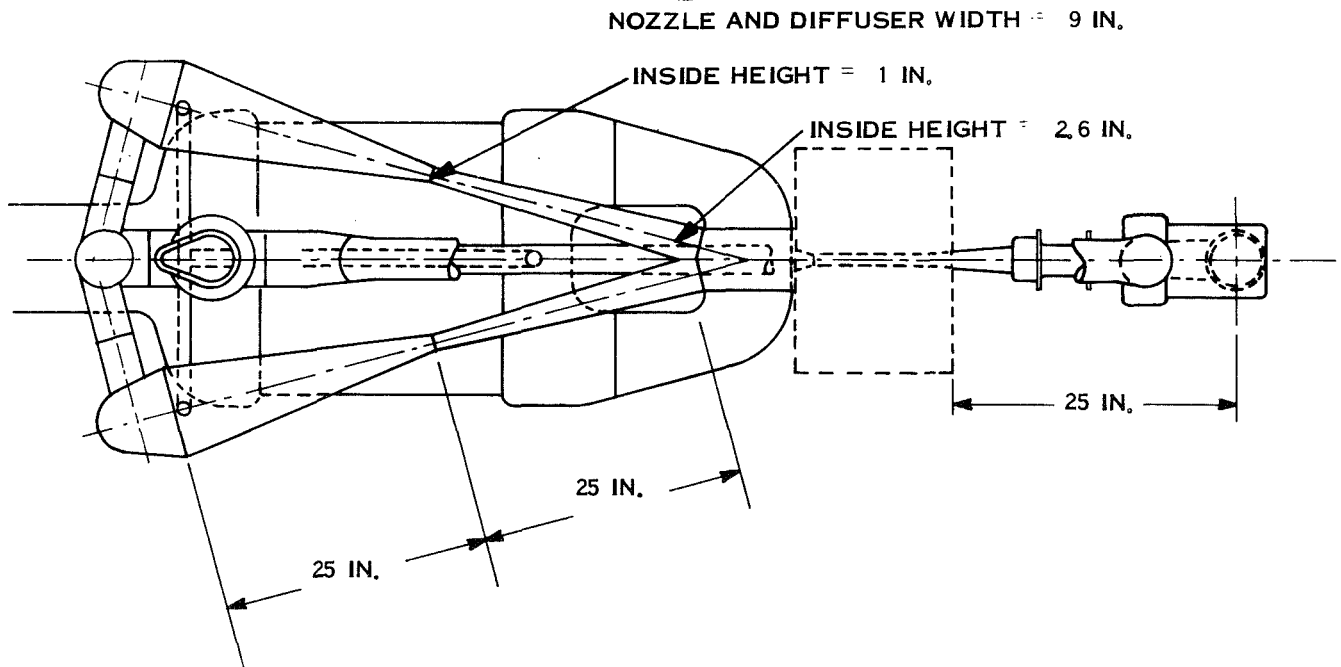


Figure 2-39. MHD Nozzle and Diffuser Size - Baseline Design

and the stress, σ , is

$$\sigma = \frac{Mc}{I} = \frac{Pl^2}{12} \times \frac{6}{t^2} = \frac{Pl^2}{2t^2}$$

where

t = the height or thickness of the beam

l = the beam length

c = distance from neutral axis to outermost fiber of the beam

M = the bending moment

I = the moment of inertia

P = internal pressure

For throat deflection

$$l = 9 \text{ in.}, l^2 = 81 \text{ in.}^2, d = 1 \text{ in.}$$

$$y = 0.025 \times 1.0 = 0.025 \text{ in.}$$

$$\% \epsilon = \frac{1600 t}{l^2} y = \frac{1600 \times 0.025}{81} t = 0.495 t$$

For outlet end deflection

$$l = 9 \text{ in.}, l^2 = 81 \text{ in.}^2, d = 2.6 \text{ in.}$$

$$y = 0.025 \times 2.6 = 0.065 \text{ in.}$$

$$\% \epsilon = \frac{1600 \times 0.065}{81} t = 1.28 t$$

It was assumed that the nozzle internal pressure is 100 psia at the throat and 10 psi at the outlet end. Therefore, for throat stress:

$$P = 100 \text{ psi}$$

$$\sigma = \frac{100 \times 81}{2t^2} = \frac{4050}{t^2}$$

For outlet end stress

$$P = 10 \text{ psi}$$

$$\sigma = \frac{10 \times 81}{2t^2} = \frac{405}{t^2}$$

To evaluate these stresses in terms of material thickness two materials Cb-1Zr and TZM, were considered and the following assumptions were made:

- a. Cb - 1Zr properties are taken from Reference 23, page 9-26, Figures 9-11 and 9-15 with the time scale of Figure 9-11 of Reference 23 increased by a factor of 1000 to take advantage of the improvements available through annealing. Figures 2-51 and 2-52 here are reproductions of Figures 9-11 and 9-15 of Reference 23. The 0.5 percent creep curve is estimated to be ~ 33 percent of the 1 percent curve (see Figure 2-40).
- b. TZM properties are taken from Reference 24 (page 479, Figure 7) indicating that $\sigma_{\text{TZM}} \approx 10 \times \sigma_{\text{Nb-1Zr}}$ at 1800° F. Consequently, the stress scale of Figure 2-40 can be multiplied by 10 and the figure used for TZM.
- c. The side of the nozzle acts as a fixed-fixed beam.
- d. No stress or load redistribution takes place due to creep.
- e. Five percent change in passage width allowed for creep over 15,000 hours,

Using these assumptions and the preceding relationships of stress and wall thickness, the wall thicknesses in Table 2-19 were calculated. The weights of the Cb-1Zr nozzle assembly and the TZM nozzle assembly were calculated by assuming that all of the nozzle upstream of the throat and the downstream diffuser are made of throat (100 psi) wall thickness, and that the nozzle downstream of the throat is made of the wall thickness calculated for the end (10 psi). This is an optimistic assumption if the pressure profile shown in Figure 2-38 is representative. The weight calculated for the Cb-1Zr nozzle was 1270 pounds; the weight of the TZM nozzle was calculated to be 850 pounds. The TZM nozzle

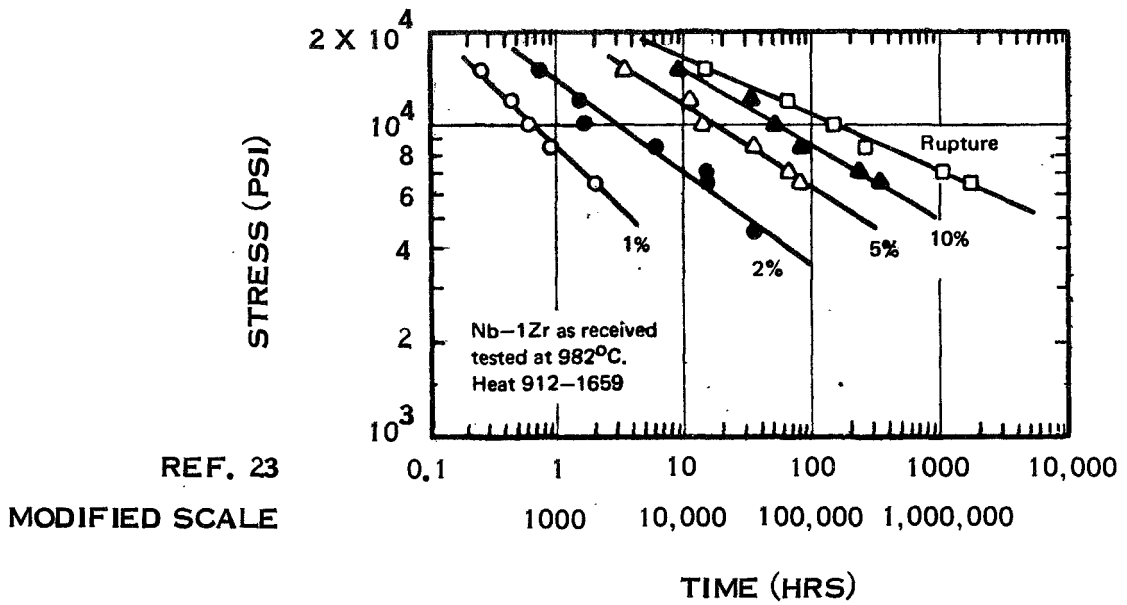


Figure 2-40. Creep Rupture Data for Nb-1Zr Alloy Sheet Tested in Vacuum at 982°C

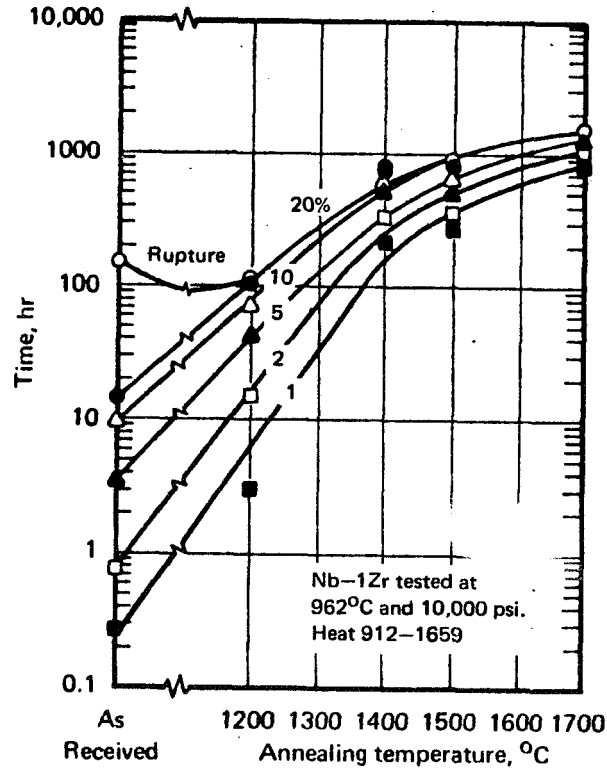
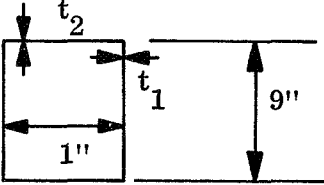
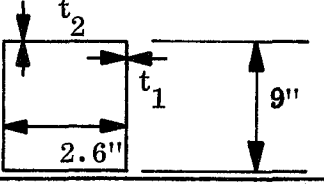


Figure 2-41. Effect of One Hour Pre-test Annealing Treatment on Creep Rupture Strength of Nb-1Zr Alloy Sheet Tested in Vacuum at 982°C

is used in the weight summary, realizing that a Cb-1Zr inner liner may be needed for chemical compatibility with the liquid metal streams.

TABLE 2-20. MHD NOZZLE WALL THICKNESSES

<u>THROAT</u>		T = 1800°F P = 100 psia	
	Material	t_1 (in)	t_2 (in)
	Nb-1Zr	1.3	0.9
	TZM	0.7	0.5
<u>END</u>		T = 1800°F P = 10 psia	
	Material	t_1 (in)	t_2 (in)
	Nb-1Zr	0.7	0.5
	TZM	0.3	0.25

The nozzle assembly design is under review by the JPL investigators for three reasons:

- a. The weight of this assembly is high as indicated by the preceding calculations.
- b. Lithium/cesium separation may require two-stage impingement; i.e., four nozzles might be used in two pairs with the combined streams from the pairs being impinged on one another for final separation (References 25 and 26). A four-nozzle assembly of this type is shown in Figure 2-42; it is sized for a 200 kWe system.
- c. Reoptimization of the generator design to eliminate vanes reduces nozzle width.

The nozzle assembly in Figure 2-42 was laid out using round nozzles, each fitted with a squared outlet. The purpose of making this layout was to estimate the weight of such an assembly and to check arrangement compatibility. Generous allowances were made for vapor flow area and wall thicknesses were calculated. The rectangular cross-section separator regions require a 0.16 inch wall; the round nozzles require from 0.091 to 0.007 inch walls. The weight was calculated using 0.090 inch wall thickness for the entire round nozzles and 0.16 inch wall thickness for the separator regions. A weight of only 250 pounds is estimated for the entire assembly including inlet headers, hangers, stiffeners, etc., using all Cb-1Zr. If this assembly, sized for a 200 kWe system, were sized up for a 275 kWe system like the baseline design, the nozzle assembly weight should increase at most in proportion, say, to 350 pounds. This compares to the previously calculated baseline nozzle weights of 980 pounds for Cb-1Zr and 650 pounds for TZM (in all cases, the MHD duct and downstream diffuser weights are excluded). The reduced weight is due to the use of the round cross-section throughout the high pressure regions where creep stresses required such great wall thickness in rectangular designs.

The use of this four-nozzle assembly, or its analog with one nozzle pair lying in a plane above the other, promises great design freedom with no weight penalty.

2.5.4 VALVES , PIPING AND PUMPS

2.5.4.1 Valves and Piping

For the MHD system, the temperature conditions are such that stainless steel can be used as the containment and piping material on the radiator side of the recuperator and Cb-1Zr for the recuperator and higher temperature sections. Table 2-21 lists the valves required in the MHD power system. It has been assumed that all of these valves can be variations of the high temperature alkali metal valve developed by General Electric-Nuclear Systems Programs under NASA Contract NAS 3-8514. This valve is shown in Figure 2-43. The motor-operated versions are assumed to have a NaK-cooled drive motor assembly on the pinion gear shaft. The estimated weights of the valves when dry are listed in Table 2-21 and are extrapolated from the one-inch size valve presently on test, which weighs 5.5 pounds dry, without a drive motor. For the 200 kWe or 400 kWe systems, the valve sizes may change but weight changes would be negligible.

MHD System Valves - Baseline Design

TABLE 2-21.

<u>Valve</u>	<u>Service</u>	<u>Size Inches</u>	<u>Type</u>	<u>Remarks</u>	<u>Estimated Weight Pounds</u>
LV-1	Lithium Nozzle Inlet	3.5	Motor-Oper. Globe		13
LV-2	Lithium Diffuser Outlet	3.5	Motor-Oper. Globe		13
LV-3	Startup Pump Bypass	2.6	Swing Check		5
LV-4	Lithium Accumulator Control	3.5	Motor-Oper. Globe	1/4-in. port above seat, closed when backseated	13
LV-5	Lithium Loop Drain	1/4	Globe	Seal Weld Cap	2
LV-6	Lithium Loop Vent	1/4	Globe	Seal Weld Cap	2
CV-1	Cesium Nozzle Inlet	1.5	Motor-Oper. Globe		9
CV-2	Radiator Loop Outlet	1.5	Motor-Oper. Globe		9
CV-3	Cesium Loop Drain	1/4	Globe	Seal Weld Cap	2
CV-4	Cesium Loop Vent	1/4	Globe	Seal Weld Cap	2

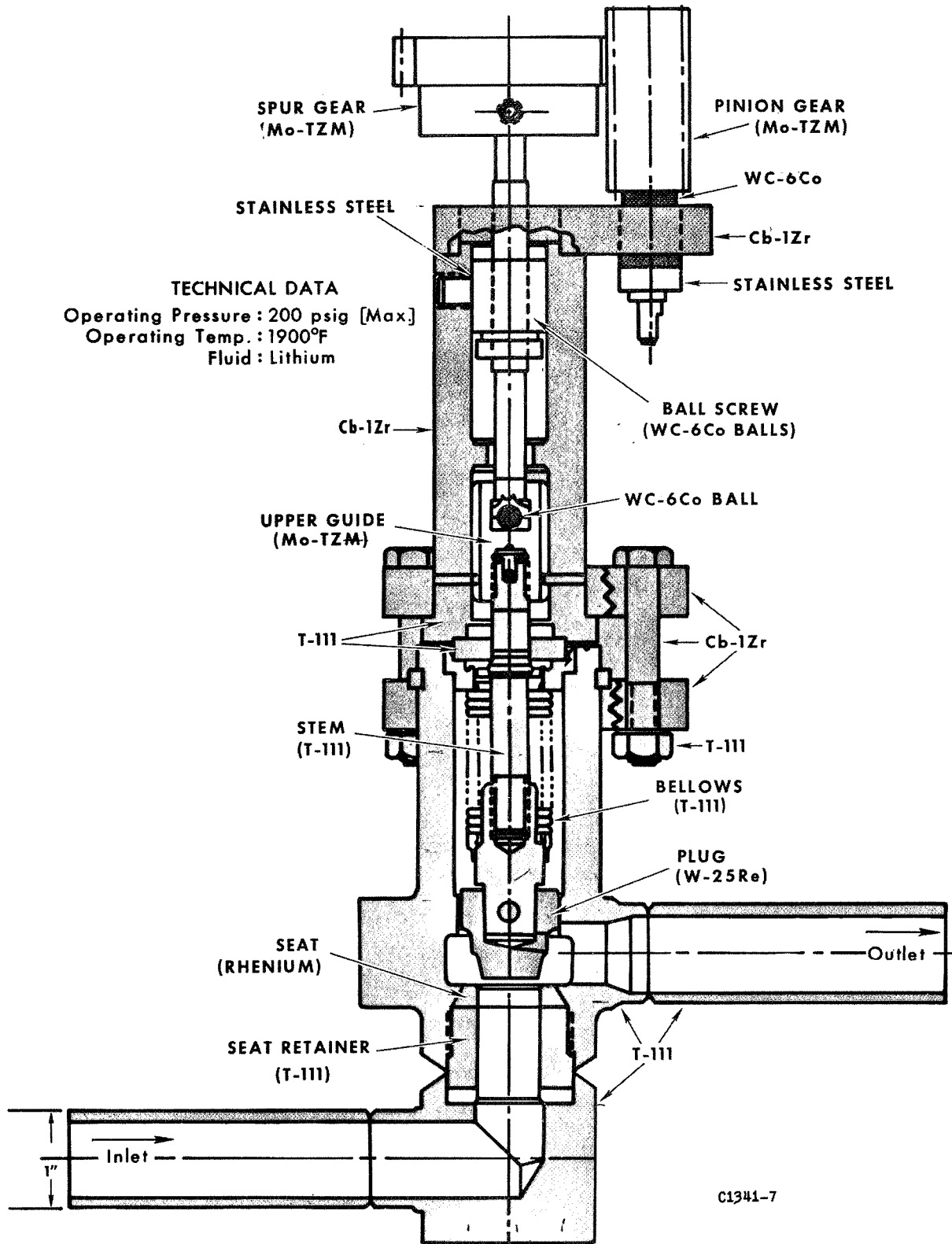


Figure 2- 43. Schematic View of High Temperature Alkali Metal Valve

All the valves except the check valve, LV-3, are assumed to be globe type as is the existing valve. There might be an incentive to make some of the valves, especially LV-1 and LV-2, gate valves to minimize pressure drop. Certainly, the development of the globe valve assumes the material technology to build a gate valve for this service; the problem would be in reconfiguration. The full-shut to full-open stroke of a gate valve is characteristically greater than that of a globe valve. As a consequence the bellows and other bonnet parts of the design shown in Figure 2-43 would have to lengthen appreciably. Configuration of such a gate type valve was considered briefly but dropped as not worth pursuit at this level of investigation.

The MHD system uses two accumulators for liquid metal inventory and pressure control, both are assumed to be cylindrical, gas-pressure-controlled, bellows type accumulators with a single outlet. The design parameters for the baseline sizes of these accumulators are listed in Tables 2-22 and 2-23. The lithium accumulator is designed to be exposed to the high (150 psia) lithium system pressure only during startup. Valved over to the cesium pump suction by closing Valve LV-4, the lithium accumulator would operate at much lower pressure through the mission and therefore would require less creep strength. A shell weight saving of up to 700 pounds is achieved by this approach.

2.5.4.2 Pumps

The MHD power system uses one very large EM pump and several small ones. Guidance for EM pump selection was taken from References 27 and 28 and experience with the potassium boiler feed pump built and being tested by GE-NSP under NASA Contract NAS3-9422 (see Figures 2-44 and 2-45).

Three small pumps are needed to circulate the high and low temperature NaK in the auxiliary radiators (see Paragraph 2.5.5) and to circulate lithium through the reactor during system warmup prior to initial start. Since the small pumps must operate on battery power during system warmup, and their small size makes power conditioning losses negligible, dc conduction pumps of the type illustrated in Figure 2-46 were chosen. The lithium startup pump was estimated to require 350 watts of power for eight hours at 0.7 volts dc to produce a lithium flow of 10 pounds per second at a head of 1 psi. The estimated weight of this pump is 6 pounds and its overall efficiency is 18 percent. Since the weight of this small pump is almost trivial, an assigned weight of 10 pounds for each of the three DC pumps is carried in the weight summary and no further analysis was made.

TABLE 2-22. LITHIUM ACCUMULATOR DESIGN PARAMETERS
BASELINE DESIGN

Fluid	Lithium
ΔV intake (warmup)	1100 in. ³
ΔV expel (startup)	2200 in. ³
Temperature	1800 ^o F
Pressure, startup, \leq 10 hours	150 psia
run, 10-20,000 hours	5 psia
Material	Cb-1Zr
Shell OD	14 in.
Wall Thickness	0.13 in.
Shell Length	48 in.
Bellows	2 ply, 0.010 in. thick
Bellows Length	34 in.
Number of Convolution	43
Length of One Convolution	0.786 in.
Bellows OD	13 in.
Bellows ID	10 in.
Dry Weight	132 lb
Wet Weight (at launch)	173 lb

TABLE 2-23. CESIUM ACCUMULATOR DESIGN PARAMETERS
BASELINE DESIGN

Fluid	Cesium
ΔV intake	160 in. ³
ΔV startup	3000 in. ³
Temperature	1100 ^o F
Pressure	10 psia
Material	Stainless Steel
Wall Thickness	0.040 in.
Shell Length	40 in.
Shell OD	18.5 in.
Bellows	2 ply, 0.010 in. thick
Bellows Length	26 in.
Number of Convolution	33
Length of Convolution	0.786 in.
Bellows OD	17.5 in.
Bellows ID	14.5 in.
Dry Weight	65 lb
Wet Weight (at launch)	270 lb

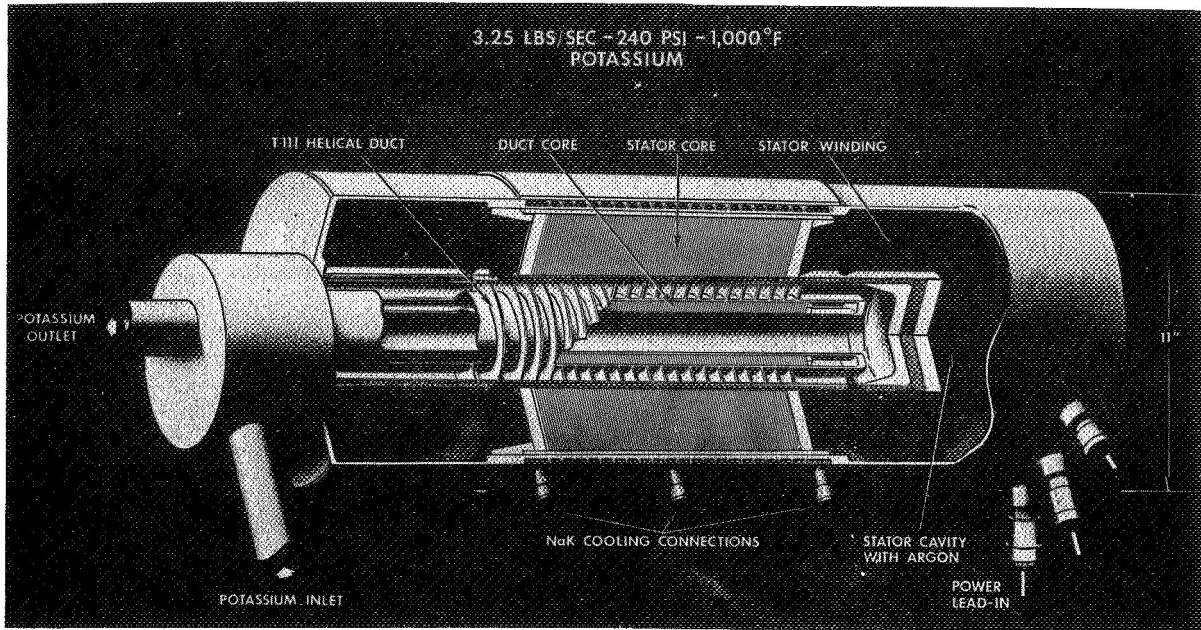


Figure 2-44. Potassium Boiler Feed Pump - Cutaway

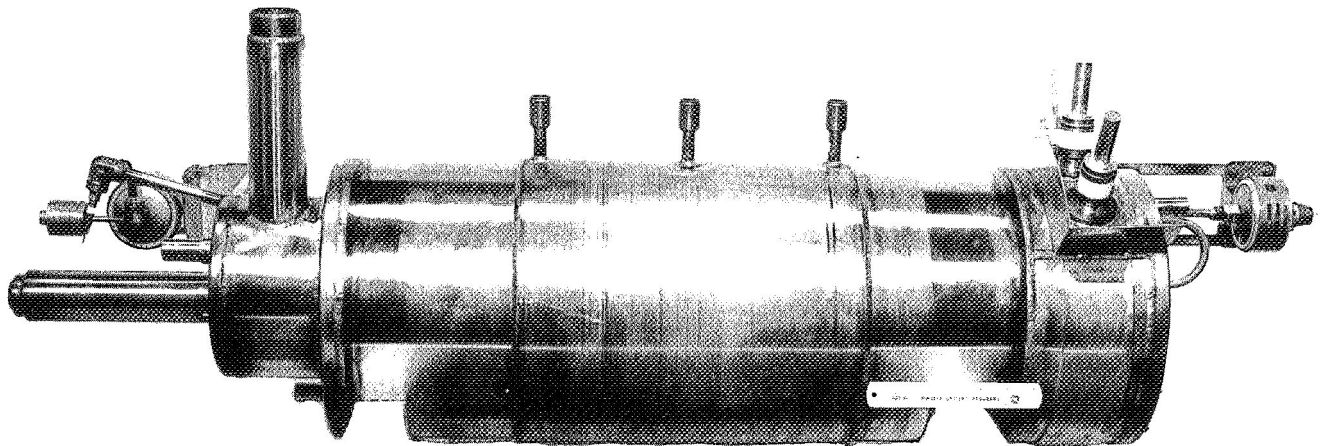


Figure 2-45. Potassium Boiler Feed Pump - Final Assembly

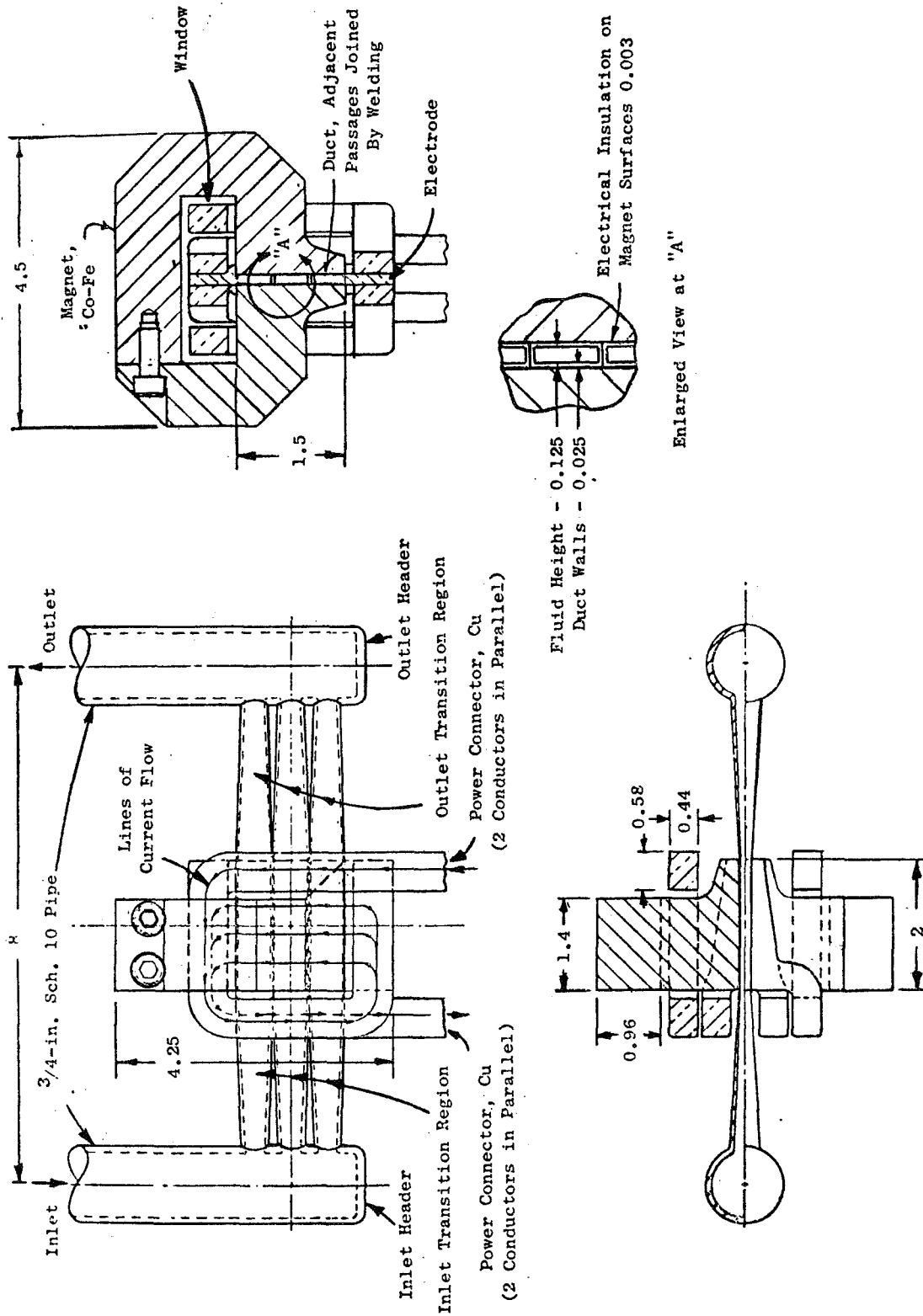


Figure 2-46. DC Conduction Pump

The cesium pump, on the other hand, is required to pump ~ 13 pounds per second of cesium at a head of 140 to 150 psi. The power required is of the order of 20 kWe. To develop such a high pumping head, the designer is usually inclined toward choice of the helical ac pump; the reliability of the ac pump is also an attractive advantage. In addition, the pump designs analyzed in Reference 27 indicate that the weight advantage enjoyed by dc pumps over ac pumps dwindles from 2.5:1 at low or average heads to as little as 1.5:1 at high heads. Since the MHD system produces ac power at relatively high voltage, it will be easier to supply power to an ac pump. A last, and important consideration, is that the development required for an ac pump would be much less than for a dc pump because of the experience already gained with pumps such as the one shown in Figure 2-45. Thus, it was decided that the cesium pump should be a 3 phase helical induction (ac) pump for the following reasons:

- a. Reliability
- b. High Head Capability
- c. Competitive Weight
- d. Minimum Power Conditioning
- e. Minimum Development Cost.

Using the Pump Capability Parameter (PCP) as explained in Reference 27, a design curve for the cesium pump was drawn up (Figure 2-47). The slope of the curve is consistent with the designs presented in Reference 27; two points on the curve represent the potassium boiler feed pump operating today and a design reported in Reference 28; the baseline design cesium pump falls between. One further assumption was made, however. It seems reasonable that continued development of this type pump can achieve improved efficiency at current weights or lower weight with current efficiency. It would be very optimistic to expect significant improvement in both simultaneously. The curve in Figure 2-47 represents current weight; current efficiency is just over 16 percent. Since the MHD power system is expected to weigh at least ~ 40 pounds/kWe output, an efficiency saving is considered more attractive than a weight saving. Consequently, cesium pump design is based on Figure 2-47 weight and an efficiency of 20 percent to reflect design available when the MHD system might be flight-ready. It should be acknowledged that the relatively high resistivity of cesium will make achievement of 20 percent pump efficiency a formidable task; a conservative approach would assume 15 percent efficiency.

2.5.5 RADIATOR DESIGN

The MHD power system employs a large, direct-condensing, vapor chamber main radiator to condense the cesium working fluid. The system also uses a number of smaller auxiliary radiators.

2.5.5.1 Main Radiator Design

Study guidelines for the MHD spacecraft specify the use of a triform vapor chamber fin radiator with condensing cesium as the primary fluid. As previously mentioned (Sub-section 2.4, Configuration Trade-offs) the cone/cylinder configuration was considered as a possible alternative. Various heat rejection system studies conducted at General Electric have indicated that consideration of radiator structural requirements often decreases the attractiveness of flat panel radiators. Although these conclusions have been based on conduction fin radiator analyses, they might be expected to be valid for vapor chamber fin radiators as well.

Work recently performed at General Electric under the Vapor Chamber Radiator Study, NAS 3-10615, included evaluation of four design concepts which are applicable to the MHD radiator. These concepts included:

- a. Cylindrical or elliptical tube/fin
- b. Rectangular channel
- c. Hexagonal honeycomb
- d. Rectangular channel/fin

These geometries were compared on the basis of utilization in a cone cylinder, load bearing radiator for the advanced Rankine cycle. Radiator inlet and outlet temperatures were 1200 and 980^oF, respectively. Vapor chamber construction was assumed to be stainless steel; wicking material was assumed to be 150 by 150 mesh screen. Sodium, potassium and cesium were the candidate fluids.

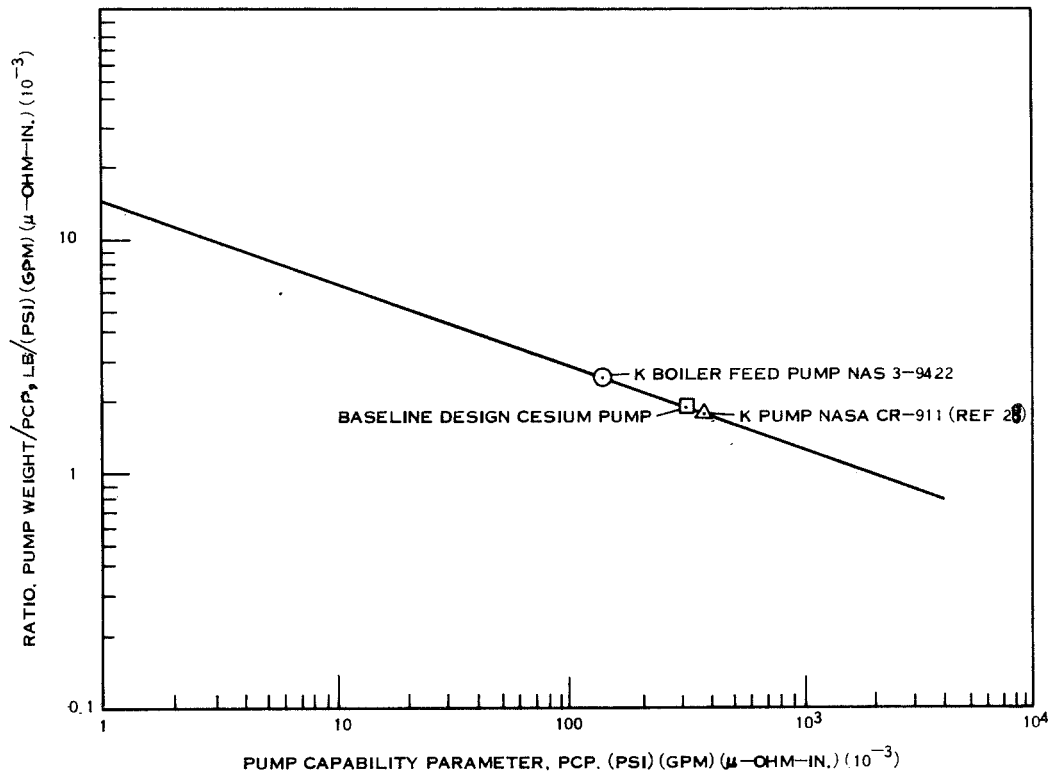


Figure 2-47. Specific Weight Relationship - Three Phase Helical Induction Pump

Radiator weights for each combination of geometries and fluids were calculated over a range of parameters as illustrated in Figures 2-48 through 2-51. A comparison of the vapor chamber fin specific weight versus vapor chamber condenser length is shown in Figure 2-52. The "A" and "C" designations refer to a 0.20 inch and 0.010 inch fin thickness, respectively. During this phase of the program potassium and cesium were excluded from further study due to sodium's superior performance (see Figure 2-53).

In order to obtain a more complete evaluation of the overall radiator weight the vapor chamber fin results were combined with an analysis of the primary ducts. Two duct geometries were examined as shown in Figures 2-54 and 2-55. Figure 2-54 shows an unpenetrated duct whereas the duct in Figure 2-55 is penetrated by the vapor chamber fin. A summary of the thermally optimum total radiator weights including primary ducts, vapor chambers, wicks, and fluid inventory is presented in Table 2-23.

PARAMETERS EVALUATED

LENGTH (L) = 0.50', 1.0', 1.5', 2.0'
 O. DIAMETER (O.D.) = 0.500", 0.750", 1.000"
 FIN THICKNESS (T_{FIN}) = 0.010", 0.020", 0.040"
 FIN LENGTH (L_{FIN}) = 0.000", 0.125", 0.250", 0.500"
 TUBE THICKNESS = 0.015

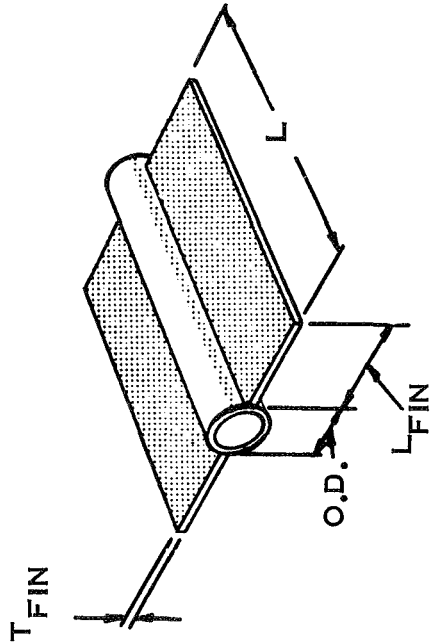


Figure 2-48. Concept 1, Cylindrical or Elliptical Tube Fin

PARAMETERS EVALUATED

LENGTH (L) = 0.500', 1.000', 1.500', 2.000'
 EQUIV. DIA. (D_E) = 0.250", 0.500", 0.750"
 CHANNEL WIDTH (W) = 0.250", 0.375", 0.500", 0.750"
 1.000", 1.500"
 PLATE THICKNESS (T_P) = 0.015" 0.023"
 INNER WALL THICKNESS (T_W) = 0.010"

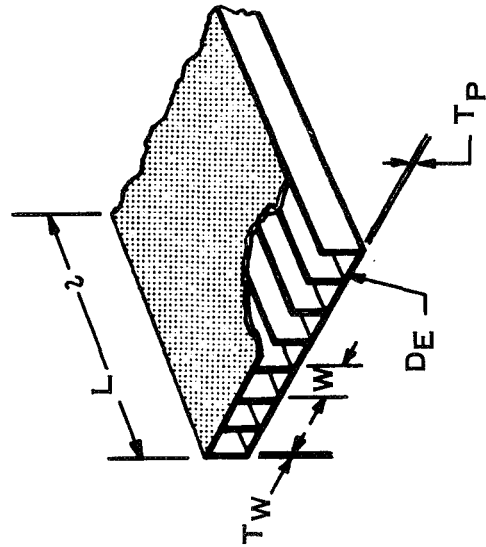
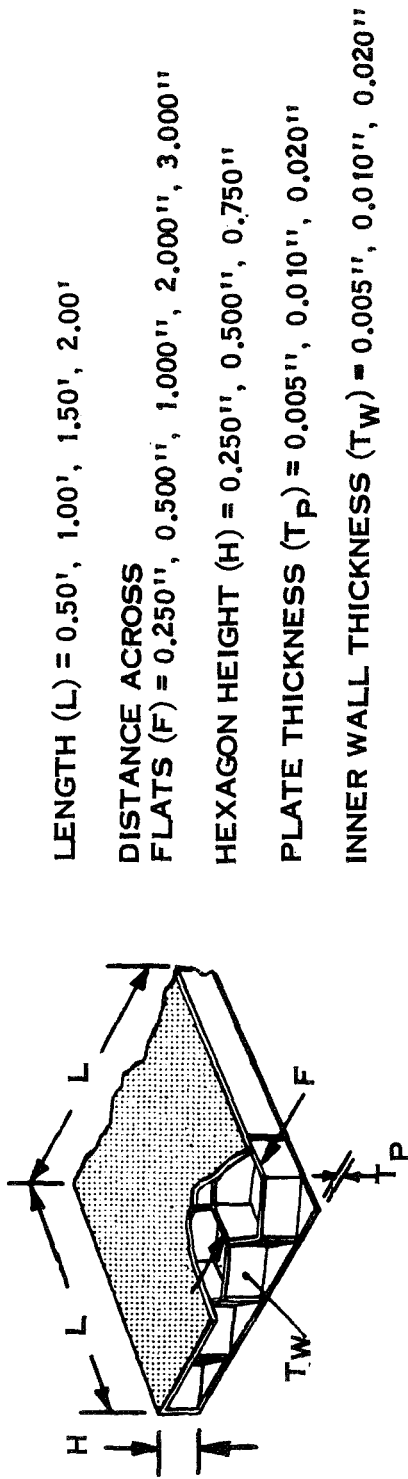


Figure 2-49. Concept 2, Rectangular Channel

PARAMETERS EVALUATED



LENGTH (L) = 0.50', 1.00', 1.50', 2.00'

DISTANCE ACROSS FLATS (F) = 0.250", 0.500", 1.000", 2.000", 3.000"

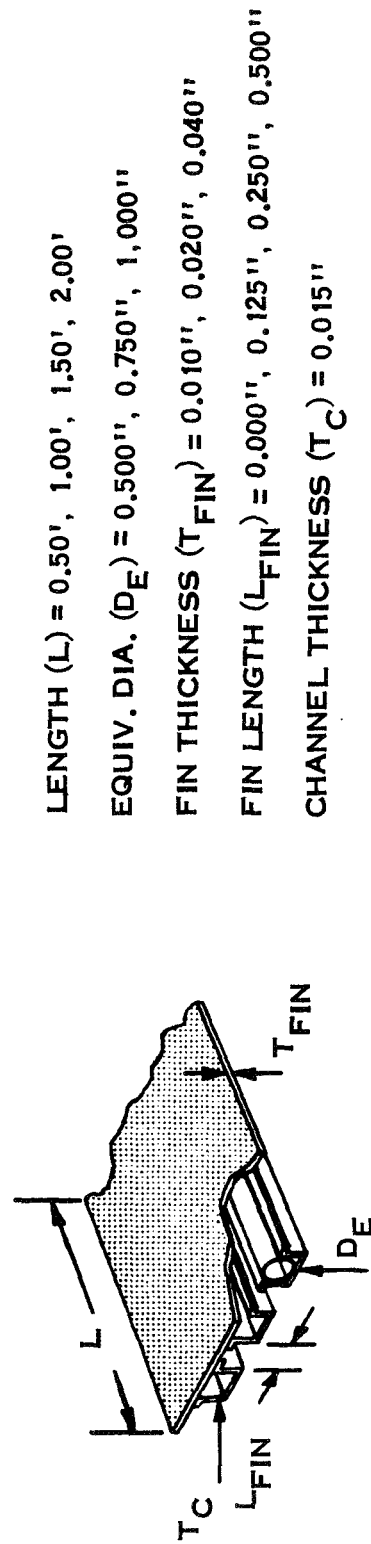
HEXAGON HEIGHT (H) = 0.250", 0.500", 0.750"

PLATE THICKNESS (T_P) = 0.005", 0.010", 0.020"

INNER WALL THICKNESS (T_W) = 0.005", 0.010", 0.020"

Figure 2-50. Concept 3, Hexagonal Honeycomb

PARAMETERS EVALUATED



LENGTH (L) = 0.50', 1.00', 1.50', 2.00'

EQUIV. DIA. (D_E) = 0.500", 0.750", 1.000"

FIN THICKNESS (T_{FIN}) = 0.010", 0.020", 0.040"

FIN LENGTH (L_{FIN}) = 0.000", 0.125", 0.250", 0.500"

CHANNEL THICKNESS (T_C) = 0.015"

Figure 2-51. Concept 4, Rectangular Channel Fin

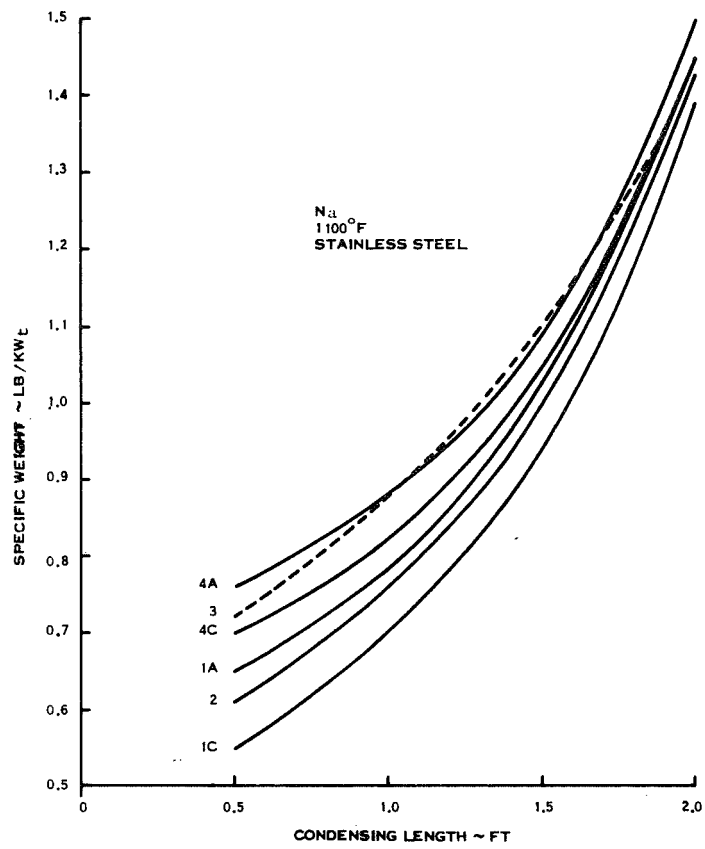


Figure 2-52. Comparison of Condensing Configuration

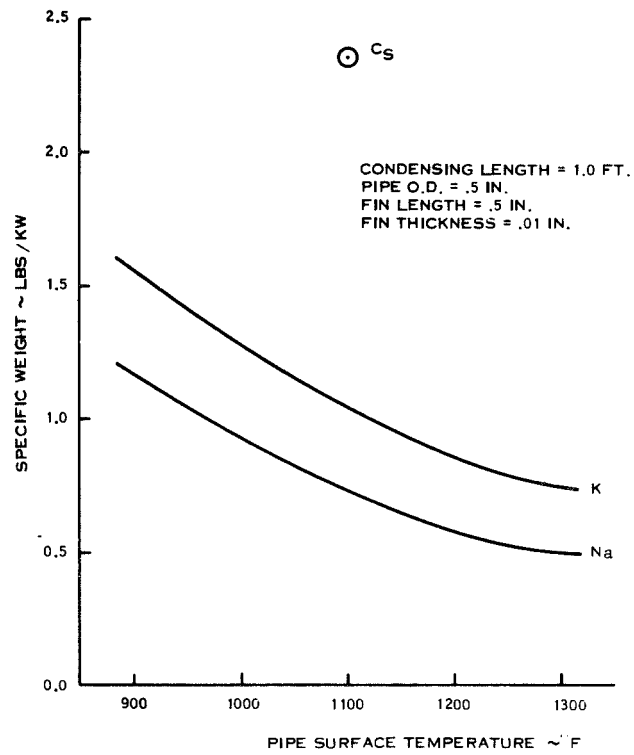


Figure 2- 53. Fluid Comparison Finned Cylinder Geometry

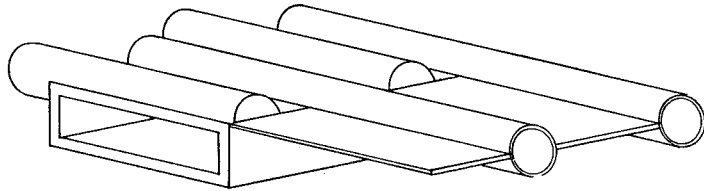
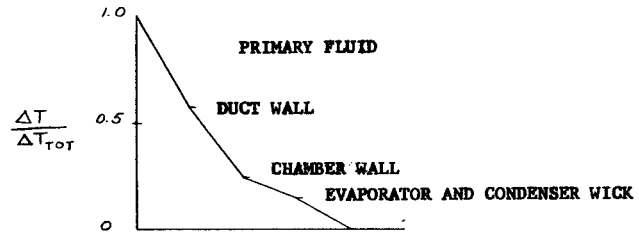
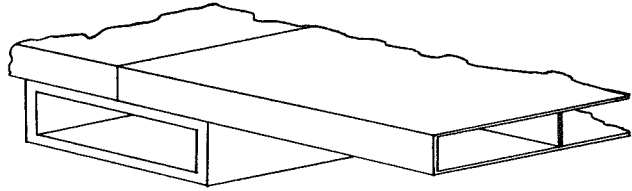


Figure 2-54. Dust-Chamber Concepts - Unpenetrated Duct

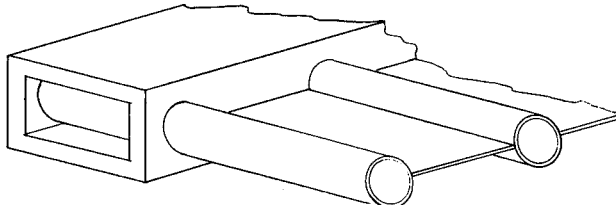
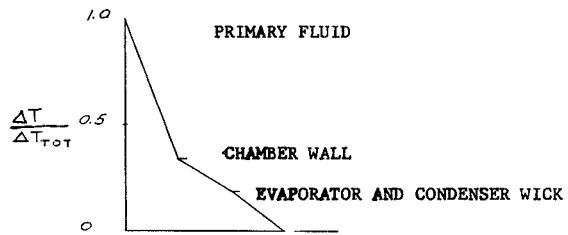
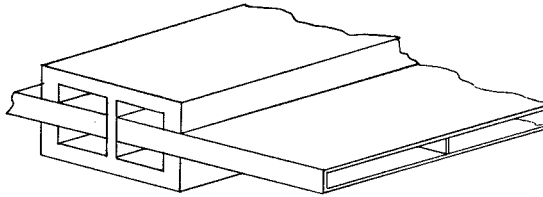
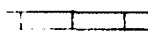
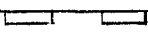
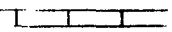


Figure 2-55. Duct-Chamber Concepts - Penetrated Duct

TABLE 2-24. SUMMARY OF RADIATOR WEIGHTS
(NO STRUCTURAL CONSIDERATIONS)

CONFIGURATION (OPEN DUCTS)	WEIGHT (LBS.)	AREA (FT ²)	NUMBER OF CHAMBERS
 1, 10 mil fins	1510	855	11,500
 2	1670	630	9,200
 1, 20 mil fins	1700	800	8,500
 4, 10 mil fins	1710	885	8,900
 4, 20 mil fins	1850	860	6,550
 3	2500	950	281,000
(CLOSED DUCTS)			
 2	1520	750	11,100
 1, 10 mil fins	1800	1000	12,800
 1, 20 mil fins	1950	950	9,050
 4, 10 mil fins	1980	990	8,950
 4, 20 mil fins	2075	950	7,700
 3	2850	1370	405,000

The next step in the radiator geometry evaluation was consideration of additional structural members required to support a 15,000 pound power-plant during a Saturn V launch where the radiator is the aerodynamic fairing. Table 2-25 summarizes the complete radiator system weight including structural weight. The lightest weight is obtained using Configuration No. 2 with an unpenetrated duct.

Fabricability of these concepts was also investigated. The easiest geometries to fabricate are cases 1 and 4, however, 2 was also felt to be possible. The fabrication of geometry 3 was judged to be extremely difficult since each honeycomb section must be sealed from adjacent cells.

A final comparison of the concepts on the basis of thermal, structural and fabrication considerations is presented in Figure 2-56. A rating has been assigned to each geometry under each criteria. In view of these results, the concepts, in order of preference, are: rectangular channel, cylindrical and rectangular channel/fin, and hexagonal honeycomb.

Using the rectangular vapor chamber fin geometry, a reference design for the vapor chamber fin radiator was formulated. Sodium was selected as the vapor chamber working fluid because of its high surface tension and latent heat of vaporization. The radiator material of construction was assumed to be stainless steel throughout.

The primary concern in ensuring a reliable vapor chamber design is to satisfy the following expression:

$$\Delta P_c \geq \Delta P_w + \Delta P_v$$

where

ΔP_c = capillary pump pressure rise

ΔP_w = wick frictional pressure drop

ΔP_v = vapor pressure drop

TABLE 2-25. SUMMARY OF RADIATOR WEIGHTS

CONFIGURATION (OPEN DUCTS)	AREA FT ²	NO. OF CHMB'S	WEIGHT RAD.	RINGS REQ'D	RING WT-LBS	REQ. SHEET THK.	SHEET WT.	TOTAL WT.
1, 10 mil fins	855	11,500	1510	6	303	.019	363	2176
2 15 mil plates	630	9,200	1670	4	195	.018	166	2031
1, 20 mil fins	800	8,500	1700	6	283	----	---	1983
4, 10 mil fins	885	8,900	1710	6	314	.019	375	2399
4, 20 mil fins	860	6,550	1850	6	305	----	---	2155
3 .5" cell (.0075")	950	281,000	2500	6	324	.0095	155	2979
(CLOSED DUCTS)								
2 15 mil plates	750	11,100	1520	4	232	.018	197	1949
1, 10 mil fins	1000	12,800	1800	10	560	.018	382	2742
1, 20 mil fins	950	9,050	1950	10	532	----	---	2482
4, 10 mil fins	990	8,950	1980	8	436	.023	470	2886
4, 20 mil fins	950	7,700	2075	8	418	----	---	2493
3 .5" cell (.0075")	1370	405,000	2850	8	464	.011	362	3676

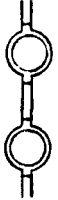
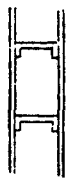
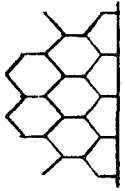
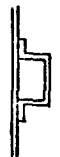
CONFIGURATION	THERMAL	STRUCTURAL	FABRICATION	TOTAL RATING (LOW IS GOOD)
<p>1</p> 	<p>1</p> <p>HIGH RATIO OF FLOW AREA TO HEAT PIPE CIRCUMFERENCE MINIMUM WEIGHT</p>	<p>4</p> <p>LOW LOAD AREA AND SMALLER PRIMARY DUCT RADIUS OF GYRATIONS CAUSE LOCAL AND PANEL INSTABILITIES</p>	<p>1</p> <p>CONSIDERED ON A PAR WITH (4) IF EXTRUSION IS USED</p>	<p>6</p>
<p>2</p> 	<p>1</p> <p>HIGH EFFECTIVE RADIATOR TEMP. GOOD EVAPORATOR INTERFACE MINIMUM RAD. AREA</p>	<p>1</p> <p>THERMALLY DEFINED GEOMETRY MORE CLOSELY MEETS LOCAL AND PANEL STABILITY REQUIREMENTS</p>	<p>2</p> <p>SOMEWHAT MORE DIFFICULT THAN (1) OR (4) BUT USE OF FLANGES PERMITS GOOD BRAZE</p>	<p>4</p>
<p>3</p> 	<p>3</p> <p>GOOD EVAPORATOR INTERFACE POOR HEAT TRANSFER</p>	<p>2</p> <p>INCREASED RADIATOR AREA REQUIREMENTS NECESSITATE LARGER BAYS ∴ THUS INCREASE PANEL INSTABILITY</p>	<p>3</p> <p>CONSIDERED VERY DIFFICULT IN THE CHARGING & SEALING OF CHAMBERS</p>	<p>8</p>
<p>4</p> 	<p>2</p> <p>GOOD METEOROID RESISTANCE AREA COMPARABLE TO (1), HIGHER WEIGHT</p>	<p>3</p> <p>LOW LOAD AREA AND SMALL PRIMARY DUCT RADIUS OF GYRATION CAUSE LOCAL AND PANEL INSTABILITIES</p>	<p>1</p> <p>CONSIDERED TO BE SIMPLE TO FABRICATE BY WELDING OR BRAZING</p>	<p>6</p>

Figure 2-56. Evaluation Summary and Recommendations

The capillary pump pressure rise can be estimated by the following expression:

$$\Delta P_c = \frac{2 \sigma}{\gamma_p \cos \theta}$$

where

σ = fluid surface tension

γ_p = effective pore radius of capillary wick

$\cos \theta$ = contact angle between the fluid and the wick

From a design standpoint, γ_p is the only degree of freedom in changing the capillary pressure rise, since σ and θ are functions of the fluid. In order to increase the capillary pressure rise, a fine mesh (200 by 200) stainless steel wire screen was selected. This choice provides a substantial pumping capability without imposing too high a frictional pressure drop.

The condenser fluid passage is designed with the following objectives in mind:

- a. Minimize the return fluid pressure drop
- b. Maintain the fluid in a predictable configuration.

An illustration of the condenser wick geometry is shown in Figure 2-57. The wire diameter is 0.020 inches in diameter and the mesh size is 150 by 150.

Due to the dependence of the sodium vapor temperature on pressure, it is necessary to design the vapor passage so as not to induce any discernible pressure drop in the vapor. The required cross sectional flow area of the vapor is primarily dependent upon the length, width and the temperature level of the heat pipe. Arrangement constraints fix the width of the the triform radiator panel at 64 inches. If one primary fluid duct were used, the condenser would be approximately 32 inches in length which past studies have shown to be far from optimum for this type of application. In order to maintain more reasonable condenser

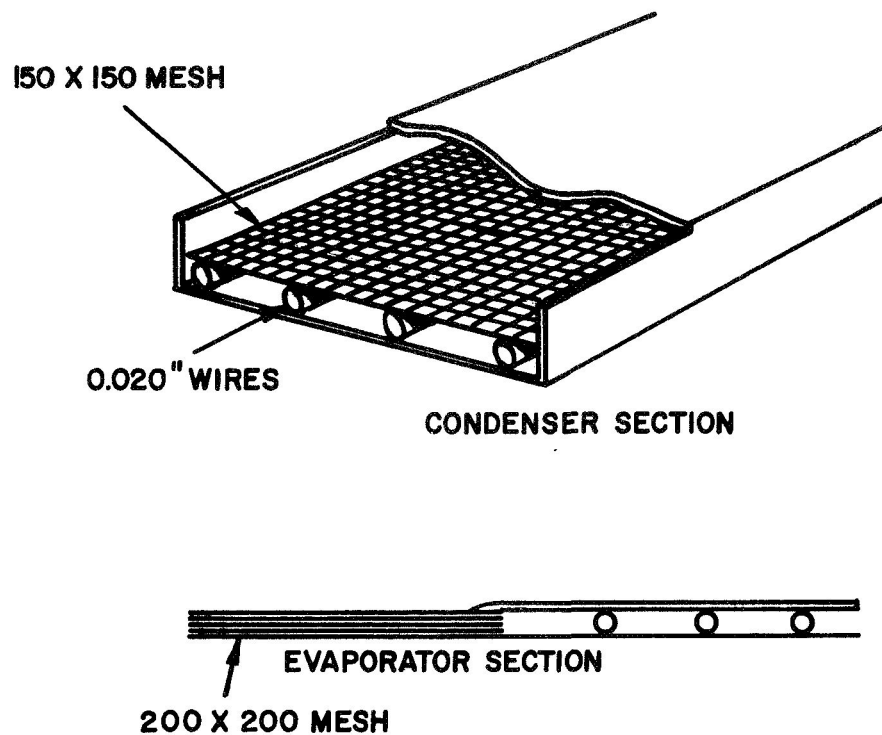


Figure 2-57. Vapor Chamber Wick Geometry

lengths (16 inches), two primary fluid ducts were used. The width of each vapor chamber was limited to 1.25 inches as a result of structural considerations arising from internal gas pressure. Under these conditions, the minimum allowable height necessary to allow vapor flow without an observable pressure drop is 0.300 inches.

The purpose of the primary fluid ducts is to transfer heat to the evaporator sections of the sodium heat pipes. If properly designed, the cesium fluid temperature can remain constant along the condensing length of the radiator panel. The design chosen which is attractive from the standpoint of fabrication, flow geometry and meteoroid protection is the half cylinder duct geometry. The duct was sized to limit inlet vapor velocity to <10 ft/sec. for stable flows; key details of the design are illustrated in Figure 2-58.

One design problem which remains with the baseline system is that the vapor entering the radiator, at 1642^oF, has too much superheat for good radiator design. With design iteration, the radiator should be sized to provide further subcooling and the recuperator size should be increased to reduce the superheat at the radiator inlet.

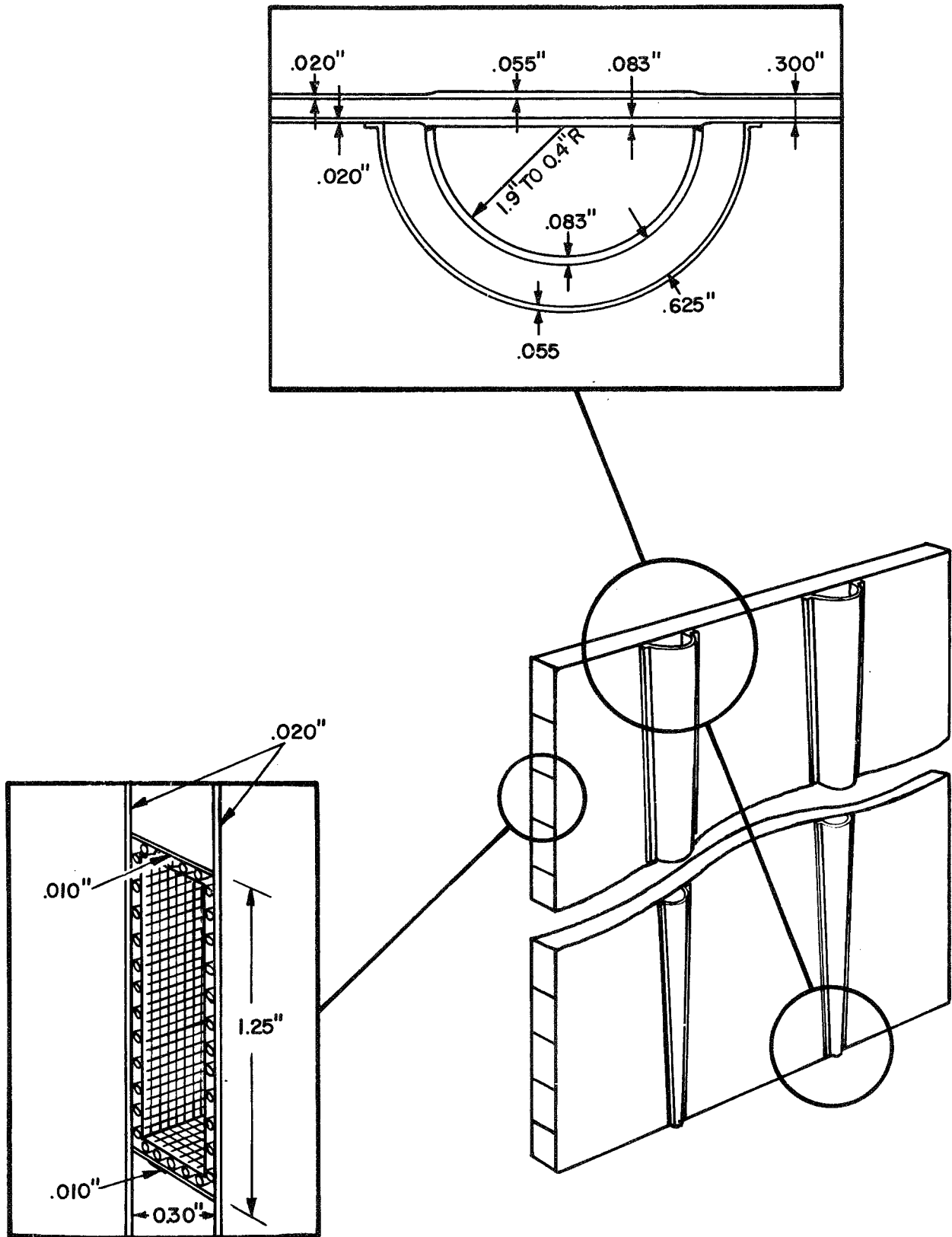


Figure 2-58. Main Radiator Panel Details

The load bearing capability and inherent stiffness provided by the relatively large cesium ducts makes them suitable as primary structural elements during the launch phases of the mission. In fact, this additional function of the primary coolant ducts is the principal reason for the attractiveness of the triform radiator configuration.

The results of NAS 3-10615 have indicated that the weight and area advantages of a VCF radiator may be tempered by the fabrication disadvantages associated with reliably sealing thousands of individual vapor chambers. In order to estimate the weight and area advantage offered by the VCF radiator, the reference design was compared to a condensing conduction fin radiator concept using both Be/SS and SS/Cu technology.

Replacement of vapor chamber fins with conduction fins results in reasonably effective fin lengths of only one to two inches; this greatly increases the number of primary coolant channels required. The resulting design is a panel with a large number of small coolant channels having a small radius of gyration, which reduces the effectiveness of the triform as a load bearing structure. As shown in References 29 and 30, the conduction fin heat rejection concept becomes a much more efficient component of the space power plant when used as the aerodynamic fairing and as the primary launch vehicle structure. The comparison provided by Reference 30 between a cruciform and conical radiator is illustrated in Figure 2-59.

Reference 31 calculated weights of Be/SS conduction fin radiators utilizing condensing potassium at various meteoroid survival requirements. Since the product of the latent heat of vaporization and vapor density for potassium is approximately equal to that of cesium, for the temperatures investigated, the results of this investigation can be directly compared to those of the MHD study. Ratioing the results of Reference 31 to account for power and a small temperature change, the basic weight of a Be/SS radiator (not including additional structure) is estimated to be 1850 pounds.

The use of a Be/SS radiator is contingent upon the successful development of a sound metallurgical bond between the stainless steel liner and beryllium armor (see Figure 2-60). Another conduction fin radiator concept whose technology is well within the present state-of-the-art is the SS/Cu copper design. An illustration of this concept is also shown in Figure 2-60. The stainless steel acts as the tube liner and meteoroid armor while the copper lamination serves to raise the fin effectiveness. A pure stainless steel radiator

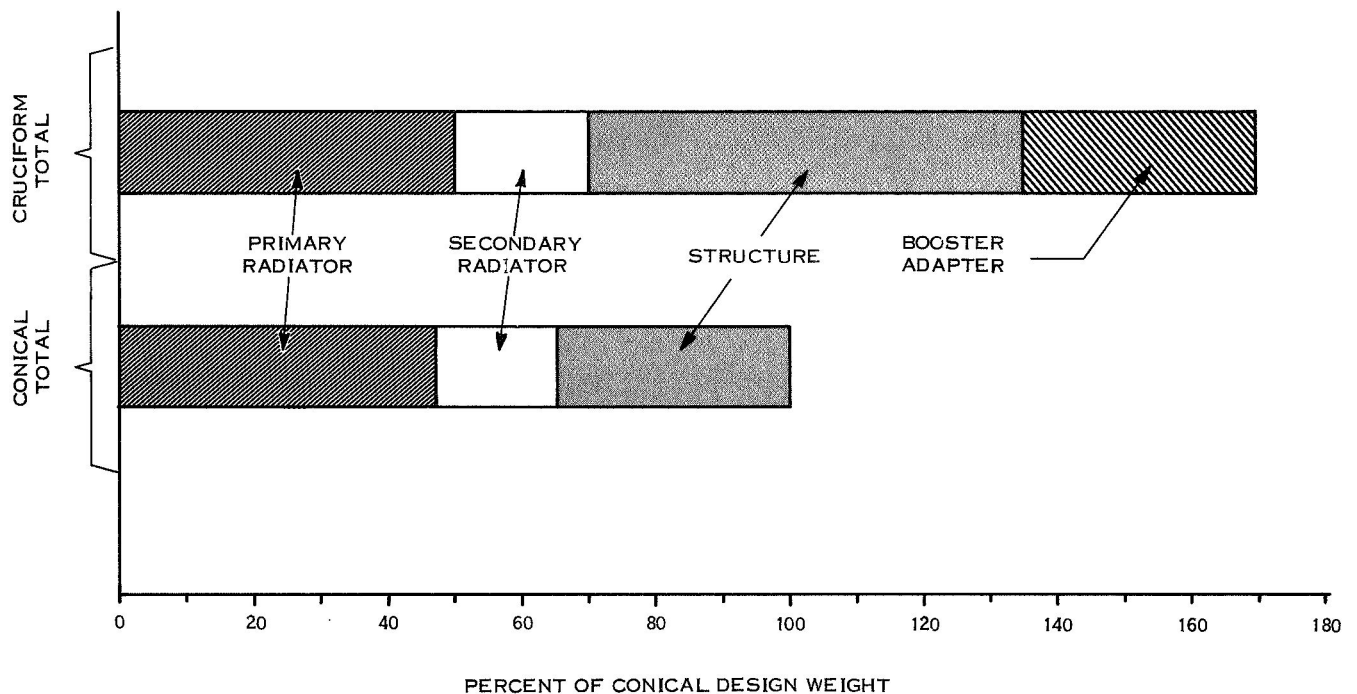


Figure 2-59. Cruciform and Conical Total Radiator Weight Comparison

is less attractive, since fin lengths must be shortened and meteoroid armor must be provided for the additional tubes. Referring again to the results of Reference 31, the estimated weight of a SS/Cu, condensing conduction fin radiator is 4100 pounds.

The cone-cylinder configuration considered for the conduction fin radiator must withstand g loading and aerodynamic forces during launch. In order to prevent buckling, additional stringers and stiffening rings must be added to the basic structure. Consideration of this factor results in a 700 and 560 pound weight addition for the SS/Cu and Be/SS radiators, respectively. A final weight comparison between the three direct condensing radiator concepts discussed is shown in Table 2-26. The Be/SS concept is considerably lighter than either the VCF or SS/Cu radiators. Of particular significance is the nominal weight penalty of the present state-of-the-art SS/Cu radiator over the VCF concept.

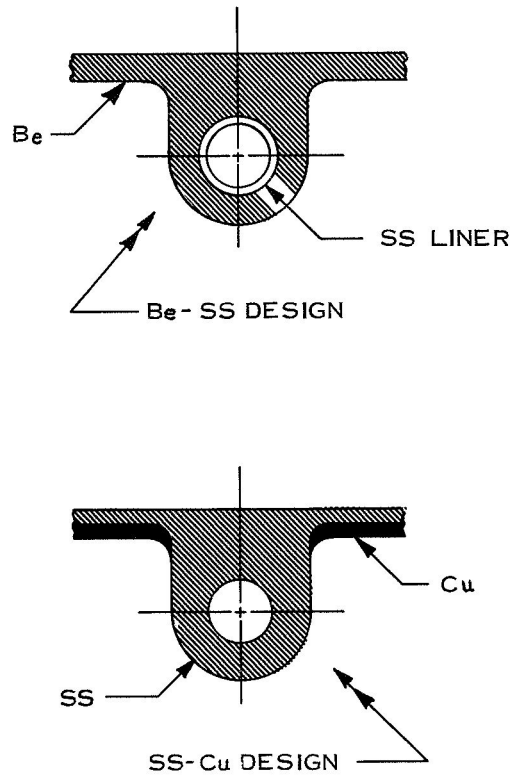


Figure 2-60. Offset Conduction Fin Radiator Geometry

2.5.5.2 Indirect Cycle

Examination of direct condensing radiator operation reveals a particular sensitivity to power load variations, flow maldistribution and external forces as well as formidable startup problems. Therefore, the operational reliability of the MHD flow system may be enhanced by the incorporation of a separate heat rejection loop.

At normal operating conditions the fluid enters condensing radiator tubes in a saturated condition. Condensation occurs under nearly isothermal conditions (depending upon the static pressure rise or loss) until the vapor is completely condensed. This point forms the vapor-liquid interface within the tube. The liquid must now be subcooled in order to prevent vaporization in the return lines. In the 1200^oF temperature range the fluid is subcooled approximately 300^oF per foot of radiator length. This is typical of condensing radiators because of the low mass flow rates required; the low flow rates are a consequence of the large amounts of energy transported per pound of fluid in the form of the latent heat of vaporization.

At part power operation less energy is being rejected so that the condensing tube length is reduced and the subcooled tube length is increased. This results in a change in the fluid inventory requirement due to the difference in the vapor and liquid mass densities. Failure to provide additional fluid to the loop would result in flow instability. Assuming that the additional fluid has been added, a second problem presents itself. As mentioned above, the subcooled liquid loses energy very rapidly due to the high temperature and low flow rate requirements of the system. Therefore, the radiator outlet temperature will be reduced to very low levels due to the increased subcooling length. The effect of this on the overall system deserves careful attention.

The rapid subcooling which occurs in the radiator tubes can produce disastrous results when flow maldistribution is present. Severe maldistribution can change the axial temperature drop from tube-to-tube or panel-to-panel to the extent where radiator buckling is caused by the induced thermal stresses. Direct condensing radiator tests using potassium, conducted at Oak Ridge National Laboratory by A.P. Fraas (Reference 32), exhibited maldistribution due to "sonic velocities in the manifold." A more successful series of investigations, performed by O. A. Gutierrez, et al. (Reference 33), also exhibited serious, if not catastrophic, flow maldistribution. It is improbable that any radiator system, liquid or two-phase, can be designed to be completely free of flow maldistribution; however, to a two-phase working fluid radiator, this characteristic is significantly more important.

The maintenance of a stable vapor-liquid interface during the steady state mode is necessary for proper operation. Movement of the interface under this condition produces flow instability, which can be damaging to the system's operation. Instabilities arise due to some imposed external force on the fluid such as those that might occur during spacecraft orientation. Design of the flow ducts, therefore, must consider any contingency during the mission which would tend to make the inertial forces acting on the liquid larger than the surface tension and adhesion forces. The problem of flow instabilities is not as severe to a liquid working fluid radiator since the fluid density is relatively constant throughout the system.

By using a separate heat rejection loop the condensing process occurs in a relatively compact heat exchanger volume where the startup and flow stability problems are more controllable. A discussion of the condenser design is included in Section 2.7.2.

The weight penalty incurred by incorporating a separate heat rejection loop into the system was evaluated for both vapor chamber and conduction fin concepts.

Addition of a separate heat rejection loop increases the weight of the system by:

1. Adding a pump to the system
2. Adding a heat exchanger to the system
3. Lowering the average radiator temperature by removal of the condensing fluid
4. Lowering the radiator fluid inlet temperature by introduction of the heat exchanger.

The results of this analysis, presented in Table 2-26, indicate the Be/SS conduction fin radiator to be significantly lighter than either the SS/Cu or vapor chamber fin radiator concepts. Of the two VCF concepts examined, flat panel triform and conical, the flat panel exhibited a 900 pound weight advantage. (Note that this comparison does not include the weight of structure on the flat panel triform.)

One important factor which should also be considered in comparing the direct and indirect systems is the redundant loop capability possible with the indirect cycle. Employing several independent fluid loops can be advantageous when high meteoroid survival probabilities are required. With this design approach one or more loops can be allowed to fail without loss of system capability.

The relationship between meteoroid survival probability, redundancy and overall radiator weight was examined by General Electric during work on Contract NASW-1440 for the advanced Rankine cycle. An illustration of these results is given in Figure 2-61 for Be/SS conduction fin radiators. As shown, a substantial weight advantage can be attained at higher meteoroid survival probabilities if one or more independent loops is allowed to fail. Obviously, the weight decrease arises from the lower meteoroid armor thickness associated with the redundant system.

The lower radiator weights which appear to be possible with Be/SS are contingent upon the ability to overcome several beryllium manufacturing obstacles. Much of the difficulty stems from the fact that for use with liquid metal coolants, a protective liner is required with beryllium. Reference 34, a comprehensive survey of materials compatibility with alkali metals, indicates that certain steels, and alloys of columbium or molybdenum, perform satisfactorily in contact with liquid alkali metals. This liner material must be in

TABLE 2-26. Radiator Comparisons

DIRECT CYCLE				
Radiator Type	Vapor Chamber Triform-SS	SS/Cu Conduction Fin - Conical	Be/SS Conduction Fin - Conical	
Radiator Area Ft ²	1440	1400	1400	
Radiator & Feedline Weight	2770	4100	1850	
Structural Weight	1000	700	560	
Total System Weight,* pounds	3770	4800	2410	
INDIRECT CYCLE				
	Vapor Chamber Fin Triform-SS	Conical/SS	Conical Conduction Fin SS/Cu	Be/SS
Radiator Area Ft ²	1730	1500	1800	1800
Radiator, Feedline, Power Plant Weight	3440	4800	5250	2600
Structural Weight	1200	740	890	710
Pump Weight	150	150	150	150
Heat Exchanger Weight	400	400	400	400
Total System Weight,* pounds	5190	6090	6690	3860

* In addition, a flight fairing weight penalty must be added to these weights.

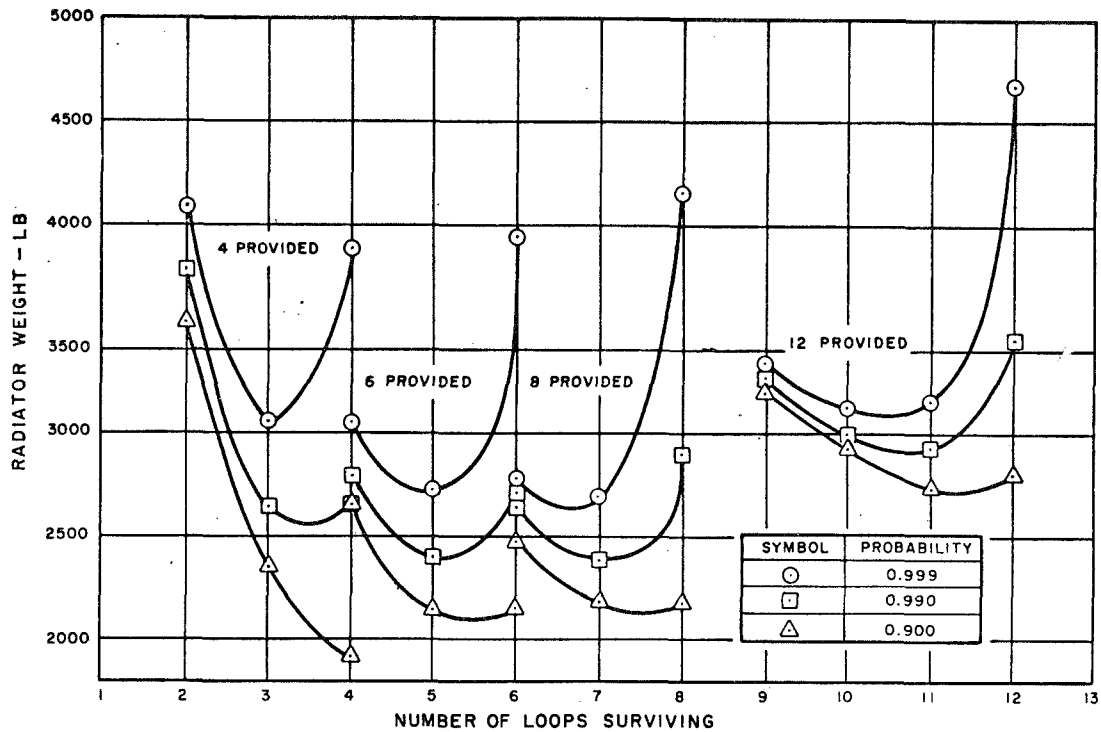


Figure 2-61. Effect of Redundancy on Radiator Weight for the Indirect Condensing System

intimate thermal contact with the beryllium to minimize temperature drops across the gaps. Unfortunately, the thermal expansivity for beryllium differs significantly from the candidate liner materials. Expansivities are compared in Figure 2-62. Other specific problem areas which must be resolved include the following:

- Techniques for brazing, braze welding or diffusion bonding beryllium to tube liner materials must be developed.
- Fabrication techniques for large panel segments must be developed.
- Techniques for making structural and mechanical joints in beryllium will require considerable development. Previous studies (Reference 35) on non-coplanar space frames made of beryllium indicate that "mechanical joints may comprise 80 percent of the truss weight."
- Specific coatings or surface control treatments require development.

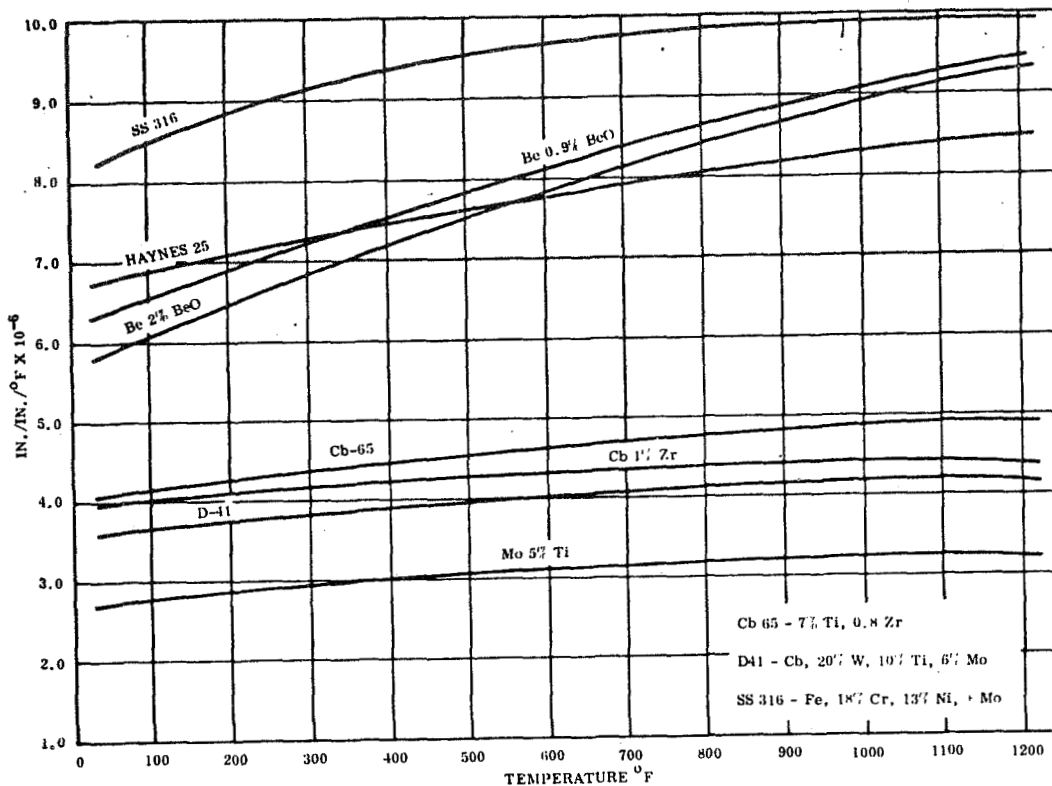


Figure 2-62. Coefficient of Thermal Expansion vs. Temperature for Various Radiator Materials

On the positive side, the following points can be made:

- Considerable fabrication experience exists with both hot pressed block and cross rolled sheet forms.
- The physical and mechanical properties for the forms of interest are sufficiently well documented for structural design of many mechanical components.
- Techniques for metal forming and machining are relatively well developed. Such operations as cutting, milling, forming, turning, drilling, routing, grinding, and chemical milling are carried out as a matter of routine.
- The quality and uniformity of fabricated beryllium products are satisfactory for design purposes where lower temperatures or shorter design lives are considered.

2.5.5.3 Summary

The MHD power system can be used with either a direct condensing or indirect condensing heat rejection loop. However, the indirect condensing heat rejection design offers greater reliability with only modest increases in system weight. The direct condensing system is susceptible to various flow problems and does not lend itself to redundant design.

Vapor Chamber Fin (VCF) radiators do not provide any significant system weight advantage over conventional SS/Cu conduction fin radiator technology. The development and fabrication problems associated with the VCF concept make the SS/Cu conduction fin radiator a logical choice at lower meteoroid survival probabilities (0.90 to 0.99). The redundant characteristics of the individual vapor chambers make this design approach valuable when higher meteoroid survival probabilities are required. Since the guideline value for non-puncture probability is 0.95 (see Section 2.2.4.1), it would appear to have been more prudent to have conducted this parametric design study with the conduction fin radiator. This was not done since use of the vapor chamber fin radiator was one of the specified guidelines and the comparison to an indirect condensing conduction fin design (the Alternate Baseline Design discussed in Section 2.7.2) was not made until late in the study.

The material combination offering the lightest radiator weight was Be/SS. The high strength to weight ratio of beryllium coupled with its high thermal conductivity results in a thermally efficient, lightweight radiator structure. However, before Be/SS radiators can be seriously considered, a significant amount of development work is required in the area of fabrication and meteoroid impact testing.

2.5.5.4 Auxiliary Radiators

The MHD power system auxiliary radiators are located on the surface of the MHD equipment bay. Table 2-27 lists the salient characteristics of the two active radiators which cool the MHD generator windings, stator, and the pump and valve motors in the MHD bay. The reactor, radiation shield, excitation capacitors, batteries, and the main power conditioning equipment are passively cooled by direct radiation to space.

2.5.6 STRUCTURE AND INSULATION

2.5.6.1 Structural Design

On the basis of the structural and arrangement trade-offs discussed in Section 2.4, the configuration chosen for the MHD spacecraft consists of two large assemblies connected by a long triform radiator structure. The large assembly at the head of the spacecraft includes the nuclear reactor, the radiation shield, and the MHD equipment bay. The reactor is mounted to the top of the radiation shield on short tubular struts.

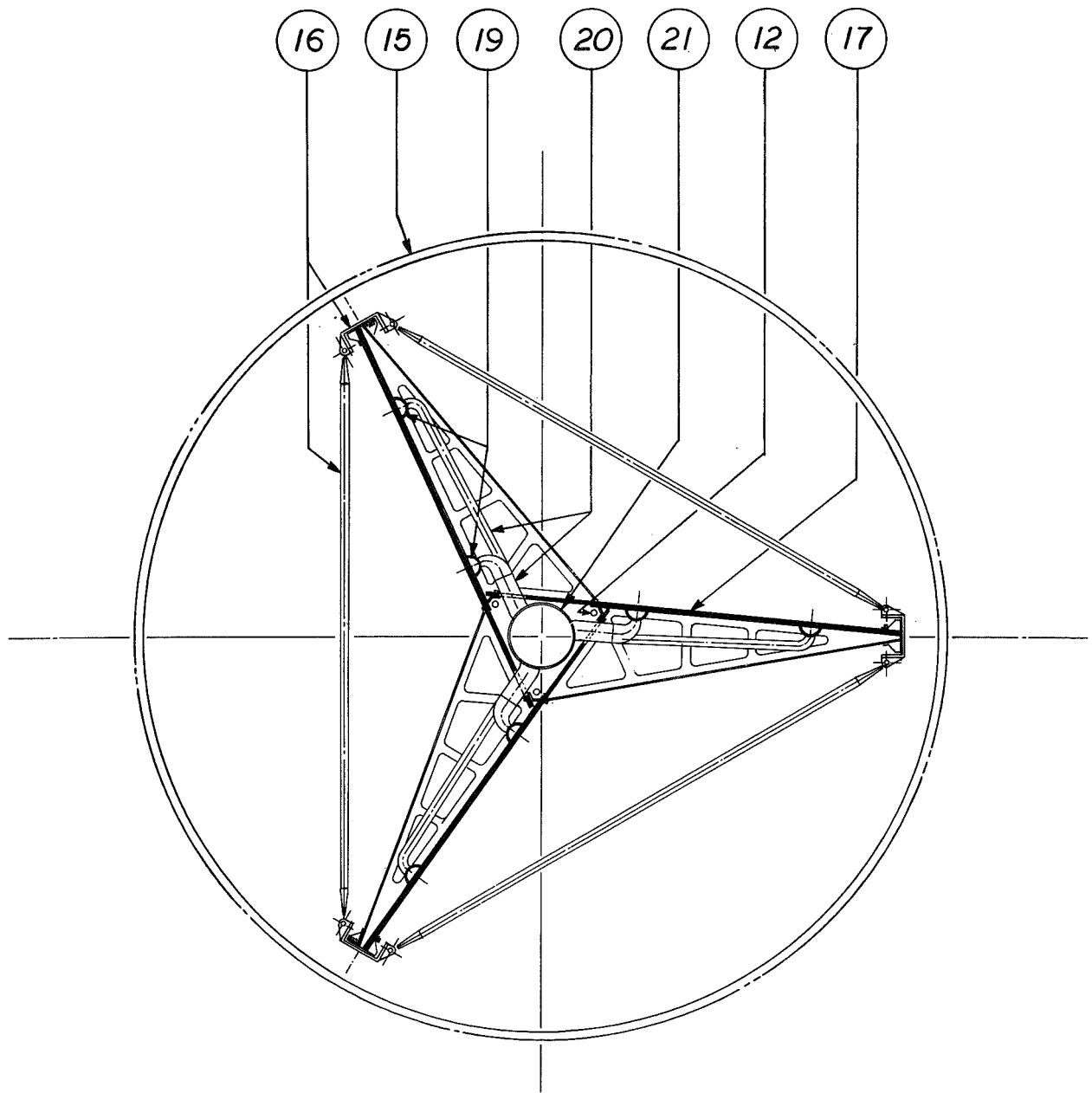
TABLE 2-27. AUXILIARY RADIATORS BASELINE DESIGN

Service	Winding Cooling	Stator Cooling
Heat Loads	P_{coil} , 12.2 kW	MHD Generator 35 kW Others 15 kW
Average Temperature	340° F	800° F
Tube Spacing	7.1 in.	3.5 in.
Fin Efficiency	0.88	0.9
Radiator Area	85 ft ²	50 ft ²
Specific Weight	0.97 lb/ft ²	1.9 lb/ft ²

The radiation shield is a stainless steel reinforced, solid lithium hydride block, stiffened both internally and externally. The MHD bay is a rib and skin structural shell extending from the bottom of the shield; internal trusses, ribs and ties carry component loads up to the shield or out to the stiffened shell.

The lower assembly of the spacecraft is a cylindrical body containing the main power conditioning equipment, the payload, the thruster system, and the mercury propellant tanks. All internal loads are carried on the shell structure of the lower assembly; additional trusses are used to take loads from the radiator spine out to the lower shell.

The main radiator is built up on a full-length stainless steel triangular boom. This boom is made up of three 1.5 x 1.5 x 0.050 inch thick channel beams which run full length to form the edges of the boom, and 16 x 1.5 x 0.040 inch welded cross bars are spanned by crossed tension ties which run from corner to corner. The vapor chamber panels of the radiator are hung on studs protruding from the channel beams and secured with washers and locknuts. The studs pass through sealed, reinforced holes in the vapor chamber panels. Torsional stiffness is provided by fitting tapered radial trusses between bays. These tapered trusses, shown in Figure 2-63, are made of 1.5 x 1 x 0.060 inch tee section and are welded to the central triangular boom. These radial trusses provide a good structural tie between the central boom and the stiffeners



ITEM	DESCRIPTION
12	CESIUM RETURN LINES
15	FLIGHT FAIRING
16	DISPOSABLE LAUNCH SUPPORT STRUCTURE
17	VAPOR CHAMBER PANEL - 12
19	CESIUM CONDENSING DUCT - 24
20	CESIUM VAPOR HEADERS
21	CESIUM VAPOR FEED DUCT

Figure 2-63. Main Radiator Assembly (Section)

running the full length of the radiator panel outer edges. In addition, they provide support for the feed and return pipes to the two vertical condensing ducts running down each radiator panel.

The outer edges of the radiator panels are fitted with permanent channel type stiffeners which link the panels together to form a light column at each edge of the radiator connecting the head and lower assemblies of the spacecraft. These channels also act as the wireways for all cabling connecting the two ends of the spacecraft.

Following the concept discussed in Paragraph 2.4.3, disposable structure is used to assist the triform radiator in carrying launch loads. Three channels weighing a total of 1970 pounds are fitted over the edge stiffeners of the radiator panels (see Figure 2-26). The size of these channels varies with elevation as is illustrated in Figure 2-64. The disposable structure also includes 320 pounds of stabilizing tubes as illustrated in Figure 2-27. A force and moment distribution diagram for the MHD baseline spacecraft is presented in Figure 2-65.

The weights of the structures which must be added to the main radiator bay to support the launch loads were calculated parametrically as a function of radiator length and reactor weight in order to determine structure weight of systems other than the baseline.

Figure 2-66 shows the weight of the required nondisposable structure as a function of the length of the main radiator and the weight of the reactor. This structure consists of longitudinal support members permanently attached to the outer edge of each of the three radiator panels. These members are formed from 0.06-inch thick sheet of 301 Stainless Steel in the half hard condition and are sized to support the loads associated with the Stage II burnout condition. Included in the weight is a seven percent factor for fittings.

Figure 2-67 shows the weight of the required disposable structure as a function of the length of the main radiator and the weight of the reactor. The disposable structure consists of longitudinal support members pinned to the outer edges of each of the three radiator panels, joined by diagonal tension members to provide lateral and torsional stability. The longitudinal members are channel sections and the diagonal tension members are thin wall cylindrical tubes, both formed from 301 SS in the half hard condition. The disposable structure members are sized to provide the additional strength necessary to support the loads associated with the Stage I burnout condition. Following Stage I burnout, they are ejected, reducing the weight of the spacecraft. Included in the weight is a 15 percent factor for fittings.

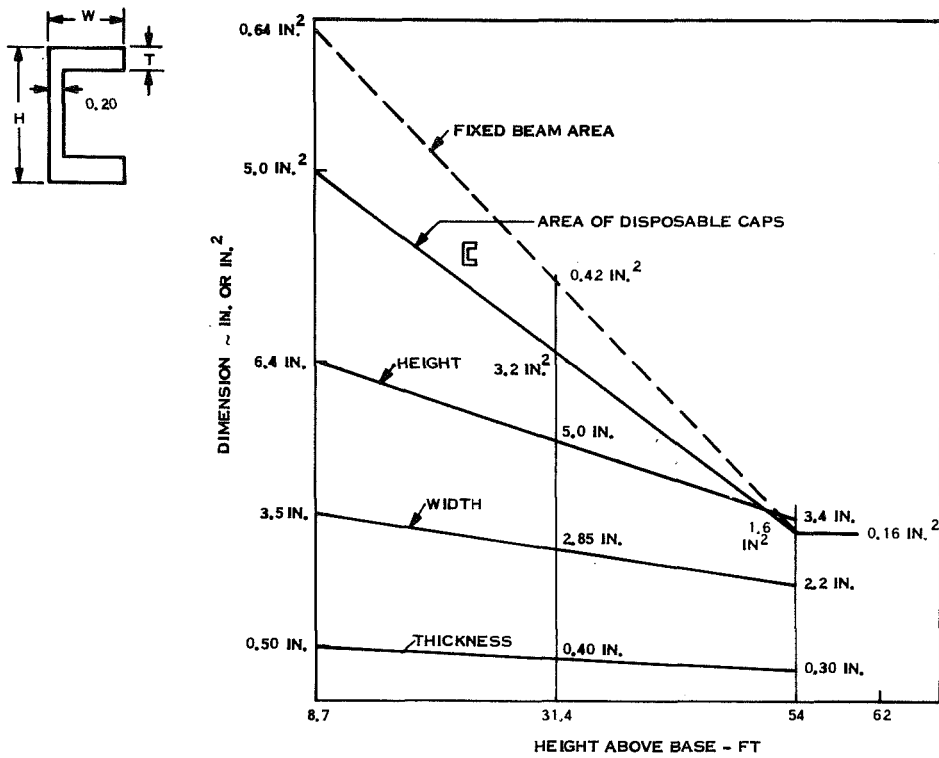


Figure 2-64. MHD - Size of Disposable Structure

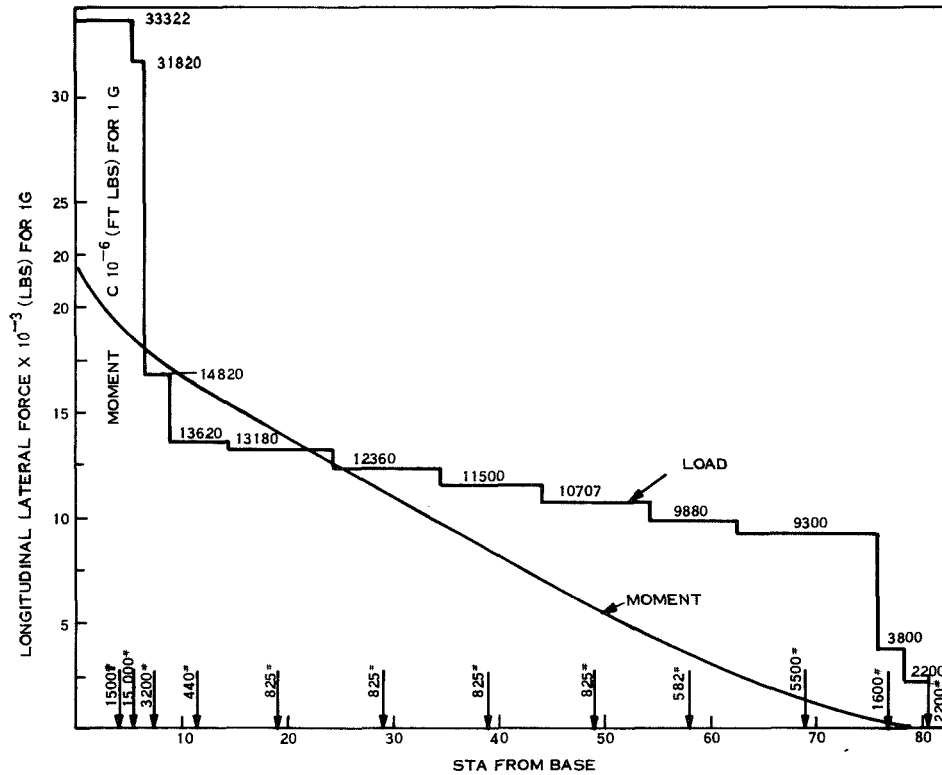


Figure 2-65. MHD - Spacecraft, Unit Force and Moment Distribution

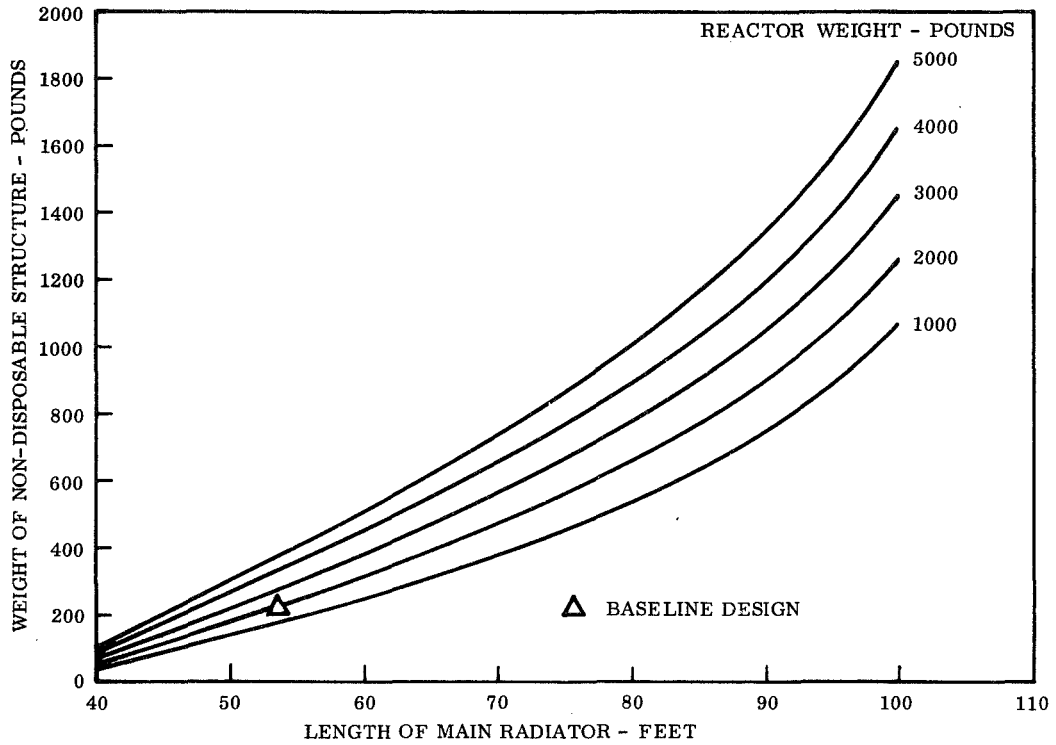


Figure 2-66. MHD Spacecraft Main Radiator Weight of Nondisposable Support Structure vs. Length of Radiator and Reactor Weight

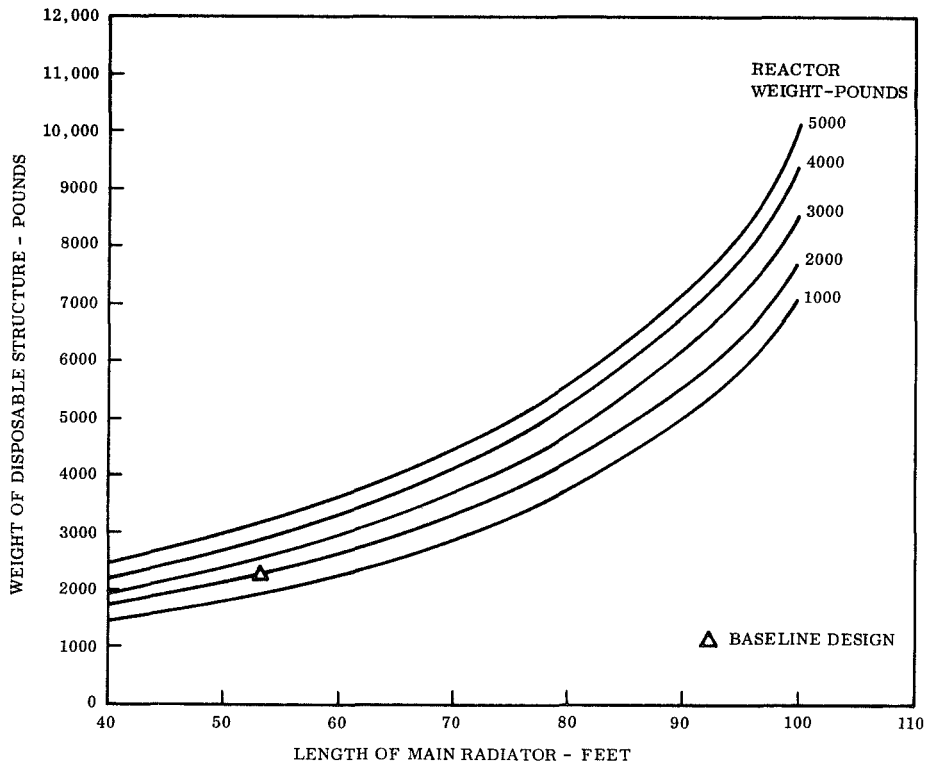


Figure 2-67. MHD Spacecraft Main Radiator Weight of Disposable Support Structure vs. Length of Radiator and Reactor Weight

Since the support structures have been sized for strength, without regard to lateral excursions of the tip or the frequency of the fundamental bending mode of vibration, the following studies are recommended if the longer spacecraft show promise from other considerations:

1. The maximum lateral deflection of the tip of the spacecraft should be calculated to determine if the dynamic envelope of the shroud is violated.
2. The fundamental frequency of the spacecraft in the lateral direction should be calculated to determine if it is low enough to cause severe coupling between the launch vehicle control system and the launch system structural dynamics.

Either of these considerations could require a significant increase in the weight of the support structure for the longer spacecraft.

2.5.6.2 Insulation

In the MHD spacecraft, an effective insulation system is needed to enclose the MHD bay and to isolate the lower assembly of the spacecraft from the main radiator's heat. A trade-off was made to select the insulation from two candidate systems. One is a molybdenum/nickel/copper/aluminum multifoil insulation system which has been successfully tested (Reference 36); the other is a single, thick layer of fibrous insulation, typically Johns-Manville MinK 2000, weighing 25 lb/ft³. The effective thermal conductance of the half-inch thick (55 layer) multifoil system was estimated to be 20 watts/ft² with the insulation weight running 2.2 lb/ft² including a 0.020 inch support sheet on the hot (high metal density) side. The conductance of MinK 2000 was estimated to vary with thickness, and were as follows:

<u>Conductance (watts/ft²)</u>	<u>Thickness (inches)</u>	<u>Weight* (lbs/ft²)</u>
20	4	8.25
40	2	4.125
80	1	2

* Does not include support sheeting

Assuming a 10 percent increase for a support sheet, the 80 watt/ft² fibrous insulation system is the same weight as the 20 watt/ft² multifoil system; consequently, the multifoil system was selected.

2.5.7 ELECTRICAL SYSTEM DESIGN

2.5.7.1 Introduction

The electrical power system and its components have been designed for use in an electrically propelled spacecraft with a nuclear reactor power plant and a liquid metal magnetohydrodynamic (MHD) generator as a power converter. The baseline 275 kWe (gross power) design resulted in an electrical system having an efficiency of 92.9 percent and a specific weight of 11.9 pounds/kilowatt. The MHD output inverters have an efficiency of 97.2 percent and a specific weight of 4.8 pounds/kilowatt. The following sections show the design detail.

The electrical system design is based upon considering each winding of the MHD as a separate phase which is individually transformed, rectified, filtered, and combined forming the dc high and low voltage electrical buses. The machine is self-excited by means of shunt capacitors.

2.5.7.2 Requirements/Characteristics

The primary requirements of the electrical system are to convert the electrical power developed by the magnetohydrodynamic (MHD) generator to forms suitable for use by the various electrical loads and to distribute the electrical power with proper protection and control.

2.5.7.2.1 Magnetohydrodynamic (MHD) Generator Characteristics - The MHD generator is similar in principle to the standard rotating induction generator; consequently, previous knowledge of the rotating machine can be applied to the MHD, with modification for the geometry differences. Whether an MHD machine acts as generator or motor depends solely upon its slip, which is the velocity difference between the moving magnetic field in the stator and the fluid velocity, divided by the field velocity:

$$s = \frac{U_{\text{fluid}} - U_{\text{field}}}{U_{\text{fluid}}}$$

The power factor of the generator is fixed by the machine and not by the load, and the generator can deliver power only at leading power factor. The MHD depends upon its quadrature leading current for excitation and unless the combined connected load requires this component, the MHD generator loses its excitation and voltage. Since loads are usually inductive, it is necessary to operate induction generators in parallel with another machine to supply the lagging current demanded by the load and sufficient lagging

current to neutralize the leading component of the current delivered by the MHD. To supply the reactive volt-amperes the paralleled machine may be either a synchronous converter or a set of capacitors. Use of synchronous machines in long term space application is not feasible because of inherent unreliability.

Hence, it is necessary to self-excite the generator by means of a bank of capacitors connected across the terminals of the generator. The leading current flowing through the capacitors provides the magnetizing magnetomotive force required to excite the generator.

With sufficient capacitance across the terminals of the generator, voltage will build up initiated by random electrical equilibrium disturbance. The startup phenomenon is known to occur in conventional rotating induction motors due to residual magnetism in the rotor; however, less is known about the initiation process in MHD machines. Laboratory tests have shown that MHD generators will build up voltage while self-excited (Reference 38).

There is a critical capacitance reactance, similar to the critical resistance in the field circuit of a dc shunt generator, which must be less than a certain value in order for the induction generator to build up.

In the MHD generator the "air" gap in the stator circuit is inherently very large, much larger than that of a rotating induction generator. This results in a very large exciting power requirement. These excitation kilovolt-amperes, reactive (kVAR) which the capacitors must supply are high compared to the kilowatt output of the generator. Experimental MHD induction generators described in the literature have exhibited power factors in the range of 8 to 22 percent. In the case of the 300 kWe baseline generator, power factor is 20.9 percent.

Considering the power factor for the baseline generator, the reactive kVA required for excitation is approximately 1400 kVAR total, or 50 kVAR per phase. In the travelling wave region these values have been used for estimating excitation system characteristics in the electrical system design. Additional capacitance may be required to compensate for transmission line reactance and for the inductive reactance exhibited by the power conditioning equipment. At an average phase voltage of 860 volts, the excitation current supplied by the capacitors is about 60 amperes per travelling wave phase, compared to a load current of 11 amperes per phase.

MHD electrical characteristics for the 300 kWe baseline system are shown in Table 2-28. Relative angles of the phase currents with respect to a reference are designated as current angle in Table 2-28; angle between the individual phase voltage and current is given as phase angle. The total power shown is 294.84 kWe, which is the theoretical output power based on perfect travelling wave form. As the analysis of Reference 6 indicates, the output of a generator with a finite number of slots will be lower. In this case, with 23 slots, the penalty is 3 percent, reducing the available power output of the baseline MHD generator to 286 kWe.

2.5.7.2.2 Load Requirements - A tabulation of the electrical requirements of the spacecraft loads is given in Table 2-29, and the mercury bombardment ion thruster power requirements are shown in Table 2-3. The main portion of the system electrical power is conditioned for the ion thruster screen grids which require about 80 percent of the generated power at 3100 volts dc. A total of 37 thrusters are on the spacecraft of which 31 are active and 6 are spares.

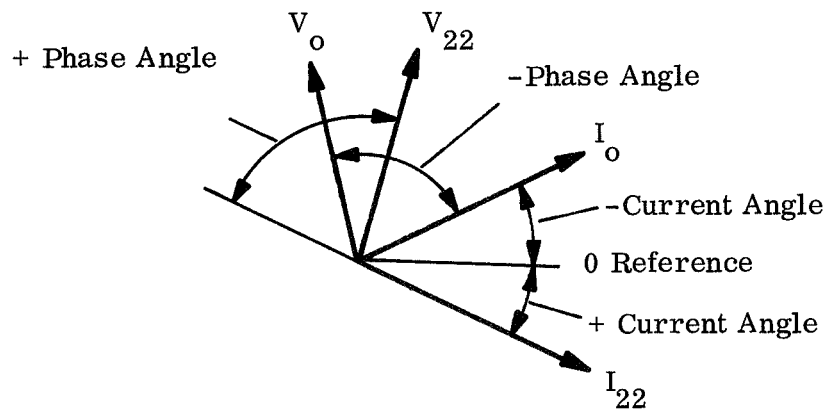
The ion engines, which represent the principal electrical load of the entire system, are known to arc frequently. When arcs occur, it is necessary to shut down the arcing engine to allow the arc to extinguish, then restart it. Analysis shows that even at the extreme arcing rate of 20 arcs per hour the reduction in average load is only about 3.5 percent. Since arcing frequency tends to diminish with time, the reduction in average load by thruster arcing may be neglected.

2.5.2.2.3 Mission Requirements - The electrical system must be designed to provide power to the loads under the following conditions during the flight:

- a. Full power operation (300 kW) from beginning of mission to the coast period.
- b. Part power operation during coast; the thrusters are inoperative and only hotel loads and payloads are connected.
- c. Full power operation (300 kW) from the end of the coast period to attainment of orbit around Jupiter.

TABLE 2-28. GENERATOR ELECTRICAL CHARACTERISTICS

Slot	RMS Voltage (Volts)	RMS Current (Amperes)	Current Angle* (Deg)	Phase Angle* (Deg)	Real Power (kW)	Reactive Power (KVAR)
0	704.4	244.5	-36.4	-61.8	-81.31	151.8
1	944.0	57.9	35.5	70.2	18.51	51.4
2	936.5	57.8	33.9	70.9	17.72	51.1
3	928.8	57.8	32.3	71.6	16.94	50.9
4	920.9	57.8	30.7	72.3	16.17	50.7
5	912.8	57.9	29.1	73.1	15.41	50.6
6	904.5	58.1	27.5	73.8	14.66	50.5
7	896.1	58.3	26.0	74.6	13.92	50.4
8	887.5	58.6	24.4	75.3	13.21	50.3
9	878.8	59.0	23.0	76.1	12.50	50.3
10	869.9	59.4	21.6	76.8	11.80	50.3
11	860.9	59.9	20.2	77.5	11.12	50.4
12	851.9	60.4	18.9	78.3	10.46	50.4
13	842.8	61.0	17.6	79.0	9.80	50.5
14	833.7	61.7	16.3	79.7	9.16	50.6
15	824.5	62.4	15.2	80.5	8.53	50.7
16	815.4	63.2	14.0	81.2	7.91	50.9
17	806.2	64.0	13.0	81.9	7.29	51.1
18	797.1	64.9	11.9	82.6	6.67	51.3
19	788.1	65.8	11.0	83.3	6.05	51.5
20	779.1	66.8	10.0	84.0	5.41	51.7
21	770.1	67.8	9.2	84.8	4.75	52.0
22	723.7	325.3	50.2	54.1	138.15	190.7
Total Power Generated					294.84	1410.2
Frequency: 326 Hz						



* Definition:

TABLE 2-29. SPACECRAFT ELECTRICAL LOAD REQUIREMENTS

Item	Function	Power Required - kW
Cesium Pump	Returns cesium condensate to MHD cycle	18.3
Auxiliary Pump	Cools MHD generator windings	0.35
Auxiliary Pump	Cools MHD generator stator, pumps, etc.	0.35
Startup Pump	Circulates Lithium for Startup	0.35
Reactor Controls	Controls reactivity of reactor	1.0
Thrusters	Propulsion	240.0
Payload, Science	Science and Communications	1.0
Guidance and Control	Thrust vector control - ion engines	0.5
System Controls	Protection, switching and control of electrical system	0.5

2.5.7.2 Electrical Power System Design

The electrical power system for the 300 kWe baseline spacecraft is shown in Figure 2-68. In this system, the electrical power output from each slot is considered as a separate phase with different output potential. To supply the two distribution buses, each phase is transformed to two standard secondary voltages, rectified, filtered and connected in parallel.

The potential of the high voltage output bus, which provides power to all of the screen electrodes of the ion thrusters, is established by the 3100 volt dc requirements of the screens. Regulation for the high voltage system is assumed to be provided by varying the input voltage to the cesium EM pump, which in turn affects the MHD generator output (see Section 2.5.7.2.7).

The 250 volt output provides power to the remaining spacecraft loads including the auxiliary power supplies required for each thruster, as well as the hotel loads and payloads. The 250 volt potential was selected for auxiliary power distribution being relatively high voltage for cable power loss minimization, but below most corona and arc-over levels regardless of atmospheric pressure and humidity.

The electrical power balance for the baseline system is presented in Table 2-30 and a summary of electrical component weights is presented in Table 2-31. As is shown in Table 2-30, the power capacity for the MHD generator is slightly in excess (5 kWe) of the electrical loads and losses.

The design resulted in an electrical system with an efficiency of 92.9 percent with a specific weight of 12 pounds/kilowatt. The output inverters have an efficiency of 97.2 percent with a specific weight of 4.8 pounds/kilowatt.

2.5.7.2.1 Inverter Design - MHD output characteristics and the load requirements lead to candidate circuits for inversion/conversion systems.

Considering the various phase angles, different power output capabilities of the phases, and the fact that 80 percent of the generator output is to be converted to 3100 vdc, the selected system design is to transform, rectify, filter and combine the outputs into a common bus. Details of the basic power inverter are shown schematically in Figure 2-69.

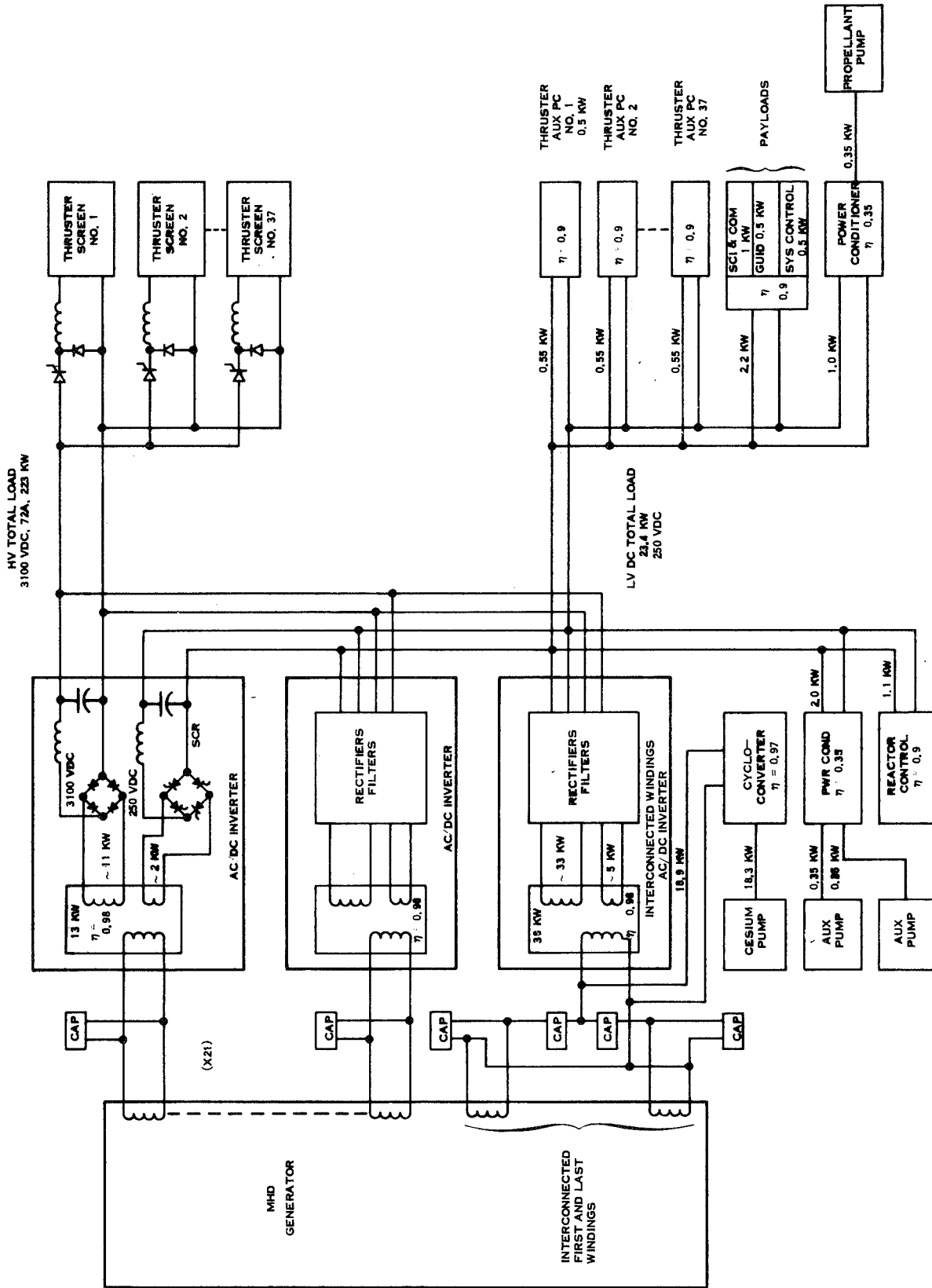


Figure 2-68. MHD Spacecraft Electrical Power System

TABLE 2-30. MHD BASELINE SYSTEM POWER BALANCE

	<u>WATTS</u>
LOSSES	
POWER TRANSFORMERS	5700
RECTIFIERS - HIGH VOLTAGE	528
- LOW VOLTAGE	220
FILTERS - HIGH VOLTAGE	1235
- LOW VOLTAGE	150
TRANSMISSION CABLES - INVERTER CABLE	270
- HIGH VOLTAGE CABLE	40
- LOW VOLTAGE, EM CABLE	150
- LOW VOLTAGE, AUXILIARY CABLE	40
EXCITATION CAPACITOR DISSIPATION (0.5% OF 1410 KVAR)	7000
SCREEN INTERRUPTERS	1250
THRUSTER AUXILIARY POWER COND. (15.5 KW, $\eta = 0.9$)	*
EM PUMP POWER COND. Cs (18.3 KW, $\eta = 0.97$)	550
AUXILIARY (1.05 KW, $\eta = 0.35$)	2950
PAYLOAD POWER COND. (2 KW, $\eta = 0.9$)	200
REACTOR CONTROLS POWER COND. (1 KW, $\eta = 0.9$)	100
TOTAL LOSSES	20,383
LOADS	
THRUSTER SCREENS	223,000
THRUSTER AUXILIARY POWER	15,500
PAYLOADS, SCIENCE AND COMMUNICATION	1,000
GUIDANCE	500
SYSTEM CONTROL	500
CESIUM PUMP	18,300
SMALL EM PUMPS	1,050
REACTOR CONTROL	1,000
TOTAL LOADS	260,850
TOTAL POWER REQUIRED	281,000
NET POWER FROM MHD GENERATOR	286,000
(SURPLUS POWER)	5,000
ELECTRICAL SYSTEM EFFICIENCY (261 KWE / 281 KWE)	92.9 %

* LOSSES ARE INCLUDED IN ION ENGINE EFFICIENCY.

TABLE 2-31. ELECTRICAL SYSTEM WEIGHT SUMMARY

COMPONENT	WEIGHT (POUNDS)
<u>Inverters</u>	
Transformers	737
Rectifiers - High Voltage Bus	4
- Low Voltage Bus	1
Filters - High Voltage Bus	170
- Low Voltage Bus	45
Wire, Brackets, Heat Paths, Control Logic	412
<u>Excitation Capacitors</u>	
Travelling Wave Region	379
Interconnected First and Last Winding	405
<u>Screen Supply Interrupters</u>	
	310
<u>Auxiliary Power Conversion</u>	
	372
<u>Power Distribution Cables</u>	
	320
<u>Startup Batteries</u>	
	<u>240</u>
TOTAL WEIGHT	3395
Electrical System Specific Weight (281,000 W Output)	12 lbs/kWe

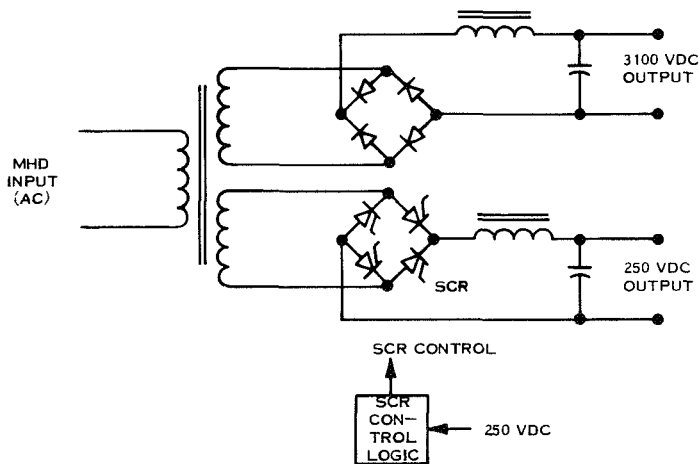


Figure 2-69. Power Inverter

The individual inverter design approach was used for equipment sizing for this study, since it results in the optimum design for a weight limited spacecraft. The power inversion equipment for the phases in the travelling wave length region was sized for average power output and average voltage, and the equipment for the interconnected phase 0 and 22 in the compensating region was sized individually. It should be remembered that some inverters may be larger and some smaller than average; however, with transformer taps to compensate for various output voltages, as few as seven inverter designs may be sufficient.

From the MHD Generator data shown in Table 2-28 an average power output of 11.3 kW and an average voltage output of 860 volts vac were selected as characteristic of the travelling wave region.

With disproportional larger power generated in Phase 22 and a power demand in Phase 0, these phases are interconnected. The remaining power is 56.84 kW. To further balance the power contributed to the common bus and to minimize transformation losses, the second largest power user, the 18.3 kW cesium pump is connected across the interconnected output via a single phase to three phase cycloconverter.

2.5.7.2.2 Transformer Design - Each transformer for the individual outputs must be unique in design because of different rms voltages and power generated. For sizing, however, an average design was calculated, acknowledging that some transformer may be larger and some may be smaller.

The average transformer design was based on a 10 kilowatt unit with 864 volts ac sine-wave input and the secondaries were assumed to be 3100 volts ac, 4 amperes, and 250 volts vac, 4 amperes. Frequency for the average transformer design was 326 Hz.

Because of the frequency, Silectron AH 4 mil thick core material was selected for the transformer. Magnetic flux density (B) was 12 kilogauss, and the design resulted in selection of an HA-320 core (Arnold Engineering Company).

Total weight was found to be 32 pounds with an electrical efficiency of 98 percent. The interconnected first and last phase generator outputs with the cesium pump connected required a transformer of 40 kilowatts at 730 volts ac.

Design of the interconnected output transformer resulted in selection of an Arnold Silectron AH 1207 core, which with the necessary wire and insulation, weighed 65 pounds with an electrical efficiency of 98 percent.

Total transformer characteristics are as follows:

<u>Weight</u>	<u>Power Loss</u>	<u>Volume</u>
737 pounds	5700 watts	3540 in. ³ (2.0 ft ³)

2.5.7.2.3 Rectifier Design - Rectification of the high voltage alternating current is performed at the output of each phase transformer through a bridge circuit. Three series 1N1348RA diodes rated at 600 volts Peak Reverse Voltage (PRV) are in each branch. The diodes are rated at 6 amperes maximum allowable forward current, weigh 0.25 ounces and have forward voltage drop of one volt and electrical loss of 4 watts each, for a total of 4.2 pounds and 528 watts loss.

Rectification and low voltage regulation is performed by phase controlled Silicon Controlled Rectifiers (SCR's). In an ac circuit, the SCR must be triggered into conduction at the desired instant of time during the half-cycle of the applied voltage wave during which the anode is positive. In the phase controlled circuit, initiation of conduction is delayed in time resulting that the SCR conducts for only a predetermined portion of the positive half-cycle. In this manner, the average power delivered to the load can be varied, and when coupled with a filter, the output results in a voltage regulated dc bus. When the line voltage reverses every half-cycle, the SCR will be automatically commutated off and consequently will not require special commutation circuits.

The unit selected for this application is the GE-SCR type C10 series 2N1777A, with a repetitive PRV of 400 volts and a 7.4 ampere rms limit. Total weight for the SCR's for the 250 volt bus is 1.1 pounds and electrical losses are 220 watts.

2.5.7.2.4 Filter Design - In both the high voltage and low voltage circuits, the output filters are used to lower the ripple factor after the transformer output has been rectified. The filters act as storage devices supplying power during periods when the transformer output is below the level of the common bus.

The problem was to design an LC filter which would reduce the pulsating full-wave rectified output to a 3100 volt dc level with 5 percent permissible ripple, with twenty-two parallel inverters providing power to the bus with fixed phase differences.

Analysis has shown that for the 3100 volt system, an inductor in each circuit should be at least 340 mh, with a capacitor on the common bus of 4.8 μ fd. For the low voltage system, the individual inductors should not be less than 25 mh with a common capacitor of 75 μ fd.

Inductor design resulted in selection of Silectron, 4 mil thick core material. Parameters for the inductors for the traveling wave outputs are as follows:

Bus	Core	Weight (each)	Power Loss (each)
250 volts	AH-223	1.6 pounds	6 watts
3100 volts	AH-188	7.2 pounds	53 watts

For the interconnected first and last outputs, the inductor for the high voltage has a weight of 16.5 pounds and a loss of 125 watts; the 250 volt bus inductor weighs 3.7 pounds with a loss of 15 watts.

Because of the common busses, individual filter capacitors are not necessary; single capacitors will suffice for each bus. Capacitors for the LC filters for the 250 and 3300 volt busses were appraised at minimum capacitance of 72.3 μfd and 4.8 μfd , respectively. The high voltage capacitor was selected to be 5.8 μfd - 7500 volts dc, GE catalog No. 14F1418, dc case style 70, weighing 10 pounds. The low voltage capacitor was selected to be 75 μfd , 1000 volts dc, GE catalog No. 23F1024, dc Case style 72, weighing 6.6 pounds.

2.5.7.2.5 Excitation Capacitor Selection - The function of the capacitors which are connected in parallel with the load to the MHD generator is to supply the excitation component of current in order for the generator to deliver the required power

The most difficult requirement is operating with a case temperature of $+200^{\circ}\text{C}$. A limited industry search has shown that no capacitor units are available without development which can work with reliability at these temperatures; however, the technology exists for designing a capacitor to meet the requirements. At these extremes, only dielectrics of mica, mica paper and perhaps teflon and kapton may be used with silicone oil-base impregnates. A mica paper marketed by 3M Corporation called Samica was used for the capacitor designs, shown in Table 2-32.

The value of capacitance required for a given reactive power is a function of phase output voltage current and frequency. The applicable equations are:

TABLE 2-32. CAPACITOR DESIGNS

kVAR	VRMS	C	LB/kVAR	IN ⁻³ /kVAR	STRESS	DIELECTRIC THICKNESS
20	250	127.4	2.58	34.3	139	1.8
20	480	34.6	0.71	9.4	267	1.8
20	850	27.6	0.38	5.1	354	2.4

Where

kVAR-Watts, VRMS-Volts, C-Microfarad, Stress-Volts/Mil, Dielectric Thickness-Mils. Other conditions are 400 Hertz, 200°C, 12-year life, high radiation.

$$C = \frac{I}{2 \pi f V}$$

$$\text{kVAR} = 2\pi f V^2 C$$

where f = frequency, Hertz

V = voltage, volts

C = capacitance, Farads

I = current, amperes

Capacitor specific weight (lb/kVAR), theoretically is constant regardless of voltage; however, because of dielectric material thickness limitation, the specific weights of the excitation capacitors are affected by voltage. Figure 2-70 illustrates the specific weight/voltage function derived from the capacitor designs of Table 2-32. The specific volume of capacitors in the range of interest is 13 cubic inches per pound.

In the regions where the fluid enters and leaves the travelling magnetic field, undesired voltages and currents are induced in the fluid, and these cause increased ohmic losses. In order to set up the proper boundary conditions so that the travelling field region acts like a segment out of an infinitely long machine, compensating poles are used. These set up a flux in the fluid to cancel the undesirable voltage due to the ends (References 4 and 5).

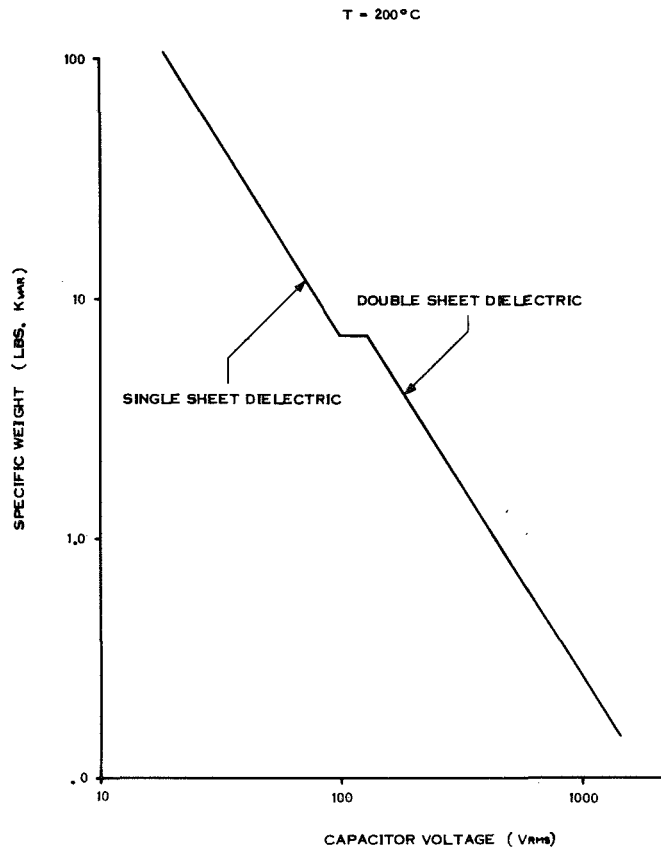


Figure 2-70. Capacitor Specific Weight

Note from Table 2-28 that the first winding is a real power load and a reactive power generator, whereas the last winding is a generator for real and reactive power. In order to supply the real power requirements of the first winding with a minimum of power conversion losses, the two compensating windings are connected together directly. Since the outputs operate at differing phase angles and voltage levels, correction is provided by capacitors.

The remaining real power is used to supply the ac cesium pump through a cycloconverter and to supply any unused power to the vehicle electrical power buses.

In determining the excitation capacitor requirement for interconnecting the compensating field windings, two approaches were considered and are shown in Figures 2-71.

The three capacitor method uses capacitors C_O and C_L to phase-angle correct the outputs of first and last winding, respectively. Capacitor C_E is used for supplying the remaining reactive power. In the five capacitor method, the primary reactive power component of

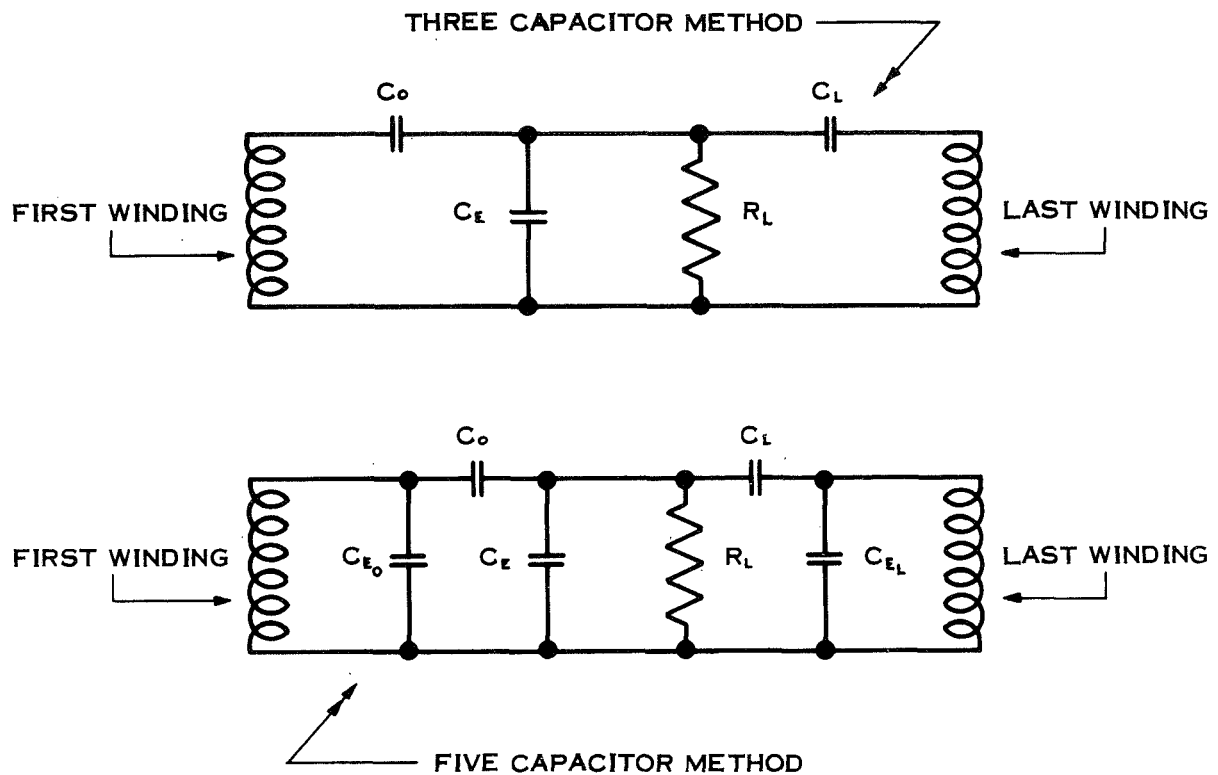


Figure 2-71. Interconnection, First and Last Winding

the outputs are supplied by the shunt capacitors C_{EO} and C_{EL} before phase-angle correction, reducing the current through the phase-angle correcting capacitors. The three MHD designs, 200 kWe, 300 kWe and 400 kWe, resulted in significantly less capacitor weight using the five capacitor method. Table 2-33 shows the comparison.

TABLE 2-33. COMPENSATING CAPACITANCE WEIGHT

MHD Output (kWe)	Three-Capacitor Method (lb)	Five-Capacitor Method (lb)
200	718	513
275	523	379
400	415	228

The travelling wave region capacitance weight for each system is shown in Table 2-34 along with the total weights using the five capacitor method for compensating winding interconnection.

TABLE 2-34. TOTAL CAPACITANCE WEIGHT

MHD OUTPUT (kWe)	TRAVELLING WAVE REGION (lb)	TOTALS* (lb)
200	122	635
275	405	784
400	326	554

* Five capacitor interconnection method.

The reason for the lower power systems requiring the heavier capacitors is that these systems have lower phase voltages. Lower output voltage increases the amount of capacitance, and with a lower limit on dielectric thickness, the capacitor group has a higher weight. These weights could change if a different number of conductor turns per coil were used in the generator; all the analysis here is based on 50 turns per coil.

2.5.7.2.6 Thruster Screen Interrupters - The high voltage electric system configured for the MHD generator is based on the use of a common thruster screen supply with individual static circuit interrupters for each thruster.

In order that a common screen supply be feasible several factors must be considered. If all screens are fed from a common supply, all are interconnected electrically. Hence, it is necessary that such interconnection be compatible with the complete electrical system, including the thruster auxiliary power conditioners. Also, it must be possible to isolate individual thrusters from the common supply in the event that the thrusters fail on momentary arc-over.

Each individual thruster screen is fed from the common high voltage bus at the thrusters through a series network consisting of a high speed electronic switch (SCR) and a series reactor (L). A simplified schematic diagram of the solid state static switch used as the screen circuit interrupter is shown in Figure 2-72. A number of SCR's are connected in series to withstand the high voltage of the screen supply and are connected in parallel with resistor-capacitor networks to provide for proper steady state and transient voltage division. Commutation of the main SCR's is provided by firing the auxiliary SCR, connecting the charged capacitor C across the main SCR's, providing a momentary reverse bias, shutting off the main SCR's.

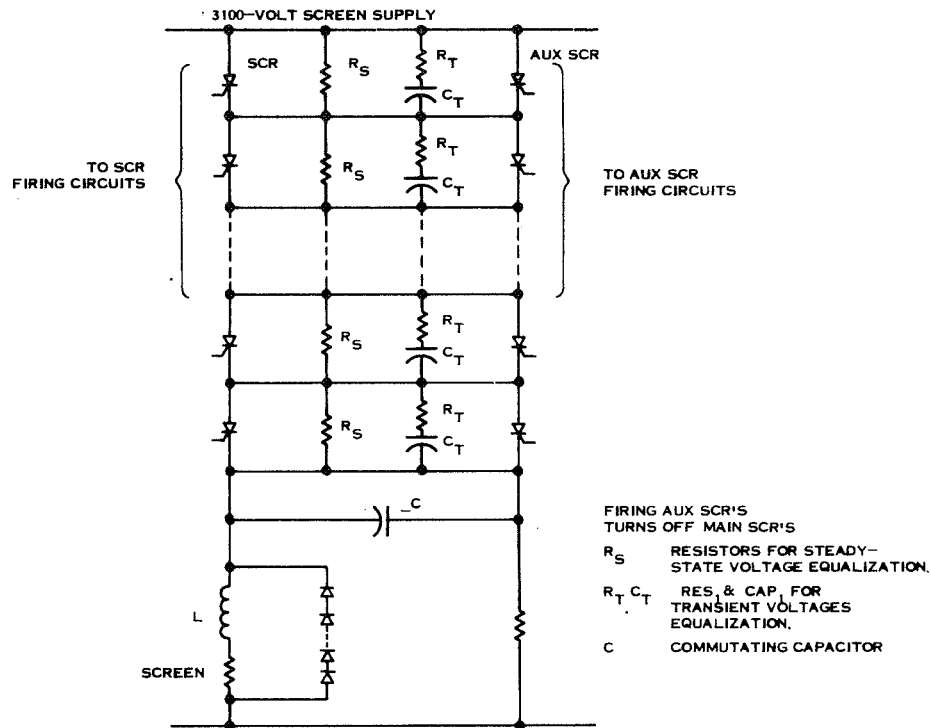


Figure 2-72. Circuit, Screen Circuit Interrupter

The interrupters operate immediately upon the development of a fault. The series inductors provide the energy necessary to clear the fault, as well as providing momentary, transient circuit isolation during faults.

The main SCR interrupts the circuit between screen and the power bus in the event of an arc within the thrusters, as detected by a sudden drop in voltage at the screen, the appearance of voltage across the series reactor, L, or a commanded signal. Following circuit interruption by the SCR, energy stored in the inductor L continues to supply power to the arc for a period of up to two milliseconds. The SCR remains off for a period of 0.2 seconds to allow time for the arc to clear and the thruster conditions to return to normal. After 0.2 seconds, the SCR is again switched on, reestablishing screen voltage and hopefully restoring full thruster operation. If the arc restrikes three times within ten seconds the screen supply to that thruster and the inputs to the auxiliary power supplies for that thruster are permanently disconnected. This thruster is considered disabled and one of the six spare thrusters is placed into operation.

During the spacecraft coast period when the thrusters are not required to operate, power to the thrusters is disconnected by the static switches in the screen supplies and by the contactors in the input circuits to the auxiliary thruster power supplies.

2.5.7.2.7 Auxiliary Power Conditioning - EM Pump Power Conditioning - There are five EM pumps in the system; four of which are used in the MHD power system. Largest is the cesium pump, being rated for 18.3 kW. The other pumps, which are two auxiliary pumps and a propellant pump, are rated at 0.35 kW each. Batteries supply the fifth pump, which is used only for MHD startup.

The cesium pump design requires three phase 60 Hz power for proper operation. Alternating current power was selected because of the power availability and because the development of high power ac pumps is more advanced than dc pumps.

For power conditioning for the cesium pump, a cycloconverter (synchronous static frequency divider) is selected, reducing the generator frequency of 326 Hz to the 60 Hz range suitable for the pump. A transformer may be necessary to reduce the generator output voltage to the voltage required by the pump; however, analysis is not complete.

Estimates of the characteristics of the cycloconverter are based upon a design reported in Reference 28; the weight is taken as 40 pounds, efficiency as 97 percent and the size 8 x 6 x 10 inch.

Control of the cesium pump and consequently control of the MHD generator output voltage, can be accomplished by electronically delaying the firing of the SCR's in the frequency divider to provide a lower rms voltage.

The auxiliary pumps and the propellant pumps are direct current conduction pumps and therefore require power at relatively low voltage, ≤ 1 volt dc. Using conventional power conversion techniques to transform the system's ac output to dc at such low voltage, efficiencies of less than 50 percent are encountered. With ac-dc conversion, the voltage drop in the output rectifiers approximates or exceeds the output voltage. Since these dc EM pumps are quite small, ~ 350 watts each, the penalty of even

low efficiency power conversion is negligible; therefore, it was assumed that all three normally operating pumps (two cooling pumps and the propellant pump) are provided with power from the low voltage dc bus with power conditioning efficiency assumed to be 0.35.

Auxiliary power conditioning is also required for the following operations:

- a. Reactor control
- b. Special ion engine units
- c. Spacecraft guidance control
- d. Payload

Table 2-35 shows the weight and efficiencies for the auxiliary power conditioners. The weights presented for the special ion thruster units are those provided by JPL. No losses are shown for the special ion engine units, since this power loss is already factored into the ion thruster efficiency used to calculate the beam power.

Table 2-35. Auxiliary Power Conditioning Characteristics

Component Application	Power Input kWe	Power Conditioning Efficiency, %	Weight Pounds	Losses Watts
Main EM Pump	18.9	97	40	550
Auxiliary EM Pumps, MHD bay	2.0	35	10	1300
Propellant Pump	1.0	35	5	650
Reactor Control	1.1	90	15	100
Auxiliary Ion Engine Unit	17.0	90	272	*
Payload Units				
Science	1.0	90	10	100
Guidance	0.5	90	10	50
Control	0.5	90	10	50

* Losses included in ion engine efficiency.

2.5.7.2.8 Startup Batteries - Three EM pumps are required for MHD power system startup and since the main electrical power is not yet available, the startup energy must be supplied by batteries. These startup pumps are the two auxiliary pumps for coolant circulation and a lithium circulation pump. The lithium startup pump requires 350 watts for 8 hours at about 0.7 volt dc, which is 2800 watt-hours of energy. The two auxiliary cooling pumps together are assumed to require similar energy, and will double the battery requirements.

To supply the necessary energy, 18 silver cadmium cells are connected in parallel, supplying 2800 ampere-hours at one volt. Each cell has 150 ampere-hour capacity, measuring 1.7 x 5.5 x 7.6 inch, and weighing 5.8 pounds. Total weight for each of the two sets is 120 pounds with 14 pounds allowed for mounting, casing, and potting. Total size is 12.6 x 18.3 x 8.6 inch each set.

2.5.7.2.9 Electrical Cable Design - Five major sets of power distribution cables are required for the MHD electrical system. Cables conduct power from the generator to the transformer/inverters in the thrusters section, excitation cables from generator to capacitors, from the inverters forward to the EM pumps, from the inverters to the high voltage ion engines, from the inverters to the engine auxiliary power conditioners and payloads.

Cable power loss and weight estimates for the baseline design are as follows:

<u>Cable Designation</u>	<u>Weight Pounds</u>	<u>Power Loss Watts</u>
Inverter Cable	100	270
Excitation Cables	150	---
High Voltage Cables	5	40
Low Voltage - EM Pumps	50	150
Low Voltage - Engine Aux, Payloads	15	40

2.5.8 RELIABILITY AND REDUNDANCY

The reliability of any power system may be enhanced by the selection of components and operating conditions which offer the greatest reliability and by the addition of redundant devices. The liquid metal MHD power system is quite simple and promises good reliability, but it, too, can enjoy improvements in reliability.

2.5.8.1 Reliability

The electrical system used in the MHD system, employing ac to dc conversion, is relatively reliable when compared to dc to dc conversion. The oscillator stage of the dc converter is not necessary and the remaining transformers have inherently high reliability.

Capacitor reliability operating at 200°C is unknown, as no systems have been developed and tested for that condition. In fact, life data at 150°C is not available. The specification of the dielectrics and oils show that these materials are good to 200°C , and consequently were selected for use. A development program will be necessary, with sufficient lead time for life testing, in order to validate the selected designs. Once reliability data has been acquired, spare capacitance (if necessary) can be designed into the excitation system.

Thruster power conditioning has the high reliability resulting from the use of individual power conditioners for each thruster. A loss of a single power conditioner would require activation of one of the six spare thruster assemblies.

From the standpoint of improving the reliability of the MHD power system a number of approaches stand out. First is the selection of system design parameters. As part of the design selection trade-offs the cycle temperature level is varied (see Section 2.6.4) the overall range of interest is 1600°F to 2200°F , but interest focuses on the narrower range of 1800° to 2000°F . It does appear that the system size and weight might enjoy nominal reductions if a cycle temperature of about 1950°F were chosen. However, the 1800°F cycle temperature is considered far more attractive because a 150°F reduction in material operating temperature offers significant improvements in creep, corrosion and erosion resistance.

The design approach selected for a system or one of its major components can greatly enhance the system's reliability. The MHD generator in this system produces relatively high voltage alternating current in some two dozen stator coils. As was shown in Reference 6 a reduction from, say, 24 to 23 coils has only a negligible effect on the generator output or efficiency. Proceeding, one can conclude that if an MHD generator is built with 24 coils, all feeding a common load in some way, and one coil is cut, the other 23 coils can assume the load of the lost coil. Therefore, reliability considerations influence the choice of main power conditioning approach, the choice between one polyphase transformer and many single phase transformers (see Section 2.5.7). By choosing many single phase transformers, the reliability of the system was enhanced. The open circuit failure of any coil in the travelling wave region would result in only a slight degradation of system performance. The same cannot be said for the end coils; operation of these coils is vital to the system. However, these coils are really pairs, consisting of two equal and opposite coils at each end of the generator (see Figure 2-34). Only one of these coils in a pair is necessary to serve the generator provided it can carry the necessary electrical current. Therefore, if each of these end coils is made with double size conductors, a failure of one would have little effect on generator performance.

2.5.8.2 Redundancy

A common method of improving the reliability of a system is the inclusion of redundant or alternate components and subsystems to serve vital functions. This method may be used with the MHD power system. Considering the makeup of the MHD power system (a schematic diagram is shown in Figure 2-90) many types of redundancy are possible. First, at the system level, two complete MHD power systems could be used in a spacecraft. Since almost everything in the power system is resistant to radiation, these two systems could be arranged in simple tandem order. System weight per kilowatt at full power would probably be greater than for one of the half systems alone. The unit at the nose end of the spacecraft would have a smaller radiation shield but the unit closer to the payload would require much heavier structure and radiation from the lower reactor could scatter off the radiator of the upper system, possibly requiring more shielding.

As an alternate, the systems could be mounted in congruent parallel, that is, two reactors in tandem, a single radiation shield, two MHD bays in tandem and two radiators in parallel or tandem order. Although one radiation shield could be eliminated and many structural members might be combined, the specific weight would not be reduced. One penalty of significance with direct condensing main radiators would be an increase in the vapor flow pressure drop between the MHD bay and the radiator, if parallel or tandem main radiators are used. The resulting lower radiator temperature can significantly increase the radiator size and weight. With NaK-cooled condensers and conduction fin radiators (see the Alternate Baseline Design, Section 2.7.2), genuine weight savings might be achieved by using two parallel fluid systems using a single reinforced shell as a shared fin.

It is probably more reasonable to approach reliability improvement through redundancy on a more restrained component basis. When enough failure rate data is available for the various components a detailed reliability analysis of the system can reveal the critical components. The use of redundant small components can be assessed on a pound for pound basis using current weights. Even the addition of an extra cesium pump would not change structural and piping weights significantly, needing only a few pounds for structure, pipe connections and a check valve. Redundancy in the larger components such as the reactor and main radiator is not so easy to assess, in that arrangement choices such as side by side or tandem order are possible, as discussed for system redundancy. In any case, redundancy does not necessarily improve reliability. The complexities entailed in the use of redundant components, the extra valves, pipes, switches, etc. can frequently lead to reduced system reliability.

2.6 PARAMETRIC ANALYSIS

The parametric analysis of the MHD power system and spacecraft designs involved the conduct of certain detailed analyses needed to establish design approach, selection of a baseline system design for comparison purposes, and then parametric system analysis to evaluate the variation of system efficiency, operating temperature, and output power level.

2.6.1 SPECIAL DETAILED ANALYSES

In addition to the parameters calculated in the generator and cycle programs as originally written (described in Reference 2), there is a need to calculate other parameters which are of significant concern to the spacecraft designer. Modifications to the computer programs were made to calculate these values on the bases described below.

2.6.1.1 MHD Stator Iron Weight

In the present generator analysis the stator slot height, D_o , is calculated but the total iron height is not. This total height can be identified as D_s and set equal to the sum of $D_o + D^*$ where D^* is the height of unslotted iron. D^* can be calculated explicitly since the net magnetic flux in this region is equal to the compensating pole flux (Reference 4). The iron cross-sectional area can therefore be calculated by setting

$$B_S \cong \frac{\sqrt{2} \phi_c}{A} \quad (1)$$

where

B_S = saturation flux for iron, T

ϕ_c = compensating pole flux, W_b

A = iron area, m^2

B_S is an input to the program; ϕ is calculated by the program; and A is the product of c (channel/stator width, a program input) and D^* , the dimension sought. Therefore, total stator iron height is

$$D_S = D_o + D^*$$

$$D_S = D_o + \frac{\sqrt{2} \phi_c}{c B_S} \quad (2)$$

The length of the stator block is

$$L_{Tot} = L_{TW} + L_{IN} + L_{OUT} \quad (3)$$

where

L_{TOT} = total length

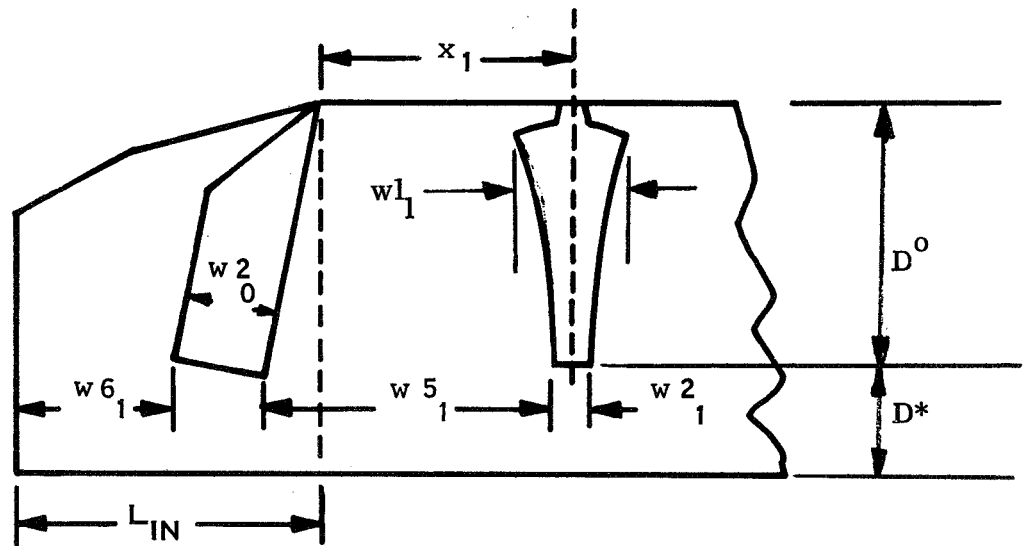
L_{TW} = length of travelling wave section

L_{IN} = length of upstream compensating pole section

L_{OUT} = length of downstream compensating pole section

From the arguments developed in Reference 2 L_{IN} and L_{OUT} can be estimated quite closely as

$$L_{IN} = w_{5_1} - \left(x_1 - \frac{w_{2_1}}{2} \right) + w_{2_0} + w_{6_1} \quad (4)$$

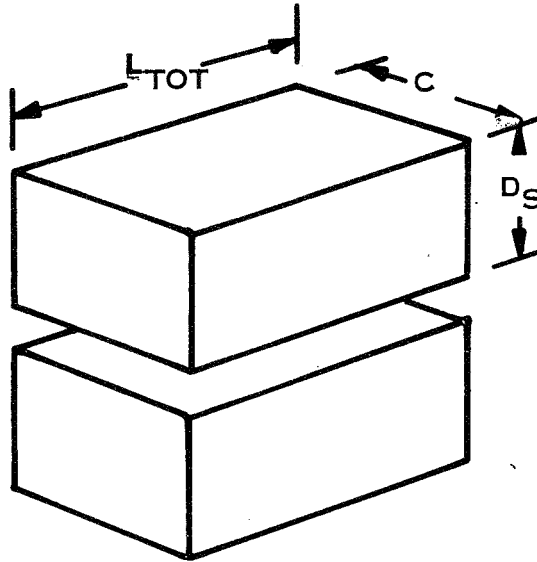


By the same technique

$$L_{OUT} = w_{5_2} - \left(L - x_{K-1} - \frac{w_{2_{K-1}}}{2} \right) + w_{2_K} + w_{6_2} \quad (5)$$

The total stator volume then can be estimated by multiplying

$$V_{St} = 2 \times D_S \times c \times L_{TOT} \quad (6)$$



The generator program already calculates the slot area and the slot volume can be calculated by

$$V_{slot} = c \sum_{n=1}^{n=N-1} [w_1 D_n - w_2 (D_n - D_o)] / 3 \quad (7)$$

for the travelling wave region and

$$V_{end\ slot} = c 4 w_A D_o$$

for all four compensating pole slots (assuming a pair at each end of the generator) where

$$w_A = 1/2 (w_0^2 + w_N^2)$$

$$w_{2_o} = L_1, \text{ if } L_1 < D_o$$

$$w_{2_o} = D_o, \text{ if } L_1 > D_o$$

$$w_{2_N} = L_2, \text{ if } L_2 < D_o$$

and

L_1 = length of upstream compensating pole

L_2 = length of downstream compensating pole

The iron weight can then be calculated

$$\text{Weight } F_e = \rho F_e [V_{st} - V_{slot} - V_{end\ slot}]$$

2.6.1.2 MHD Generator Winding Weight

In the calculation of MHD generator performance, winding losses are calculated by the use of a winding loss factor, α , which is defined:

$$\alpha = \frac{\text{actual winding loss (including iron loss)}}{\text{solid fill DC loss of slot portion of coils}}$$

The numerical value of α has been assumed to be 3 as a typical value. Since the copper coil windings of the MHD generator are estimated to weigh more than 1000 pounds (Reference 1), an explicit relationship between copper weight and actual winding loss is needed in order that a tradeoff between copper weight and auxiliary cooling system weight can be made. In Reference 4 the coil loss factor, α , was broken down as follows:

- a. slot filling factor: 0.8
- b. ac/dc resistance ratio: 1.4
- c. external conductor dc resistance is equal to slot dc resistance
- d. The iron core loss is assumed to be negligible.

Thus,

$$R_{\text{eff}} = \alpha R_i = 1.4 \frac{R_i}{0.8} + 1.0 \frac{R_i}{0.8} = 3 R_i$$

where R_i is the solid-fill slot dc resistance.

If the total current is I , then the total winding loss is calculated as $\alpha I^2 R_i$. With α broken down it is possible to determine the external conductor resistance penalty when reducing the conductor weight as follows. Let resistance of external copper be γ times the above-assumed value so that $\gamma = 1$ corresponds to $\alpha = 3$ with the values assumed under items a and b above retained unchanged. Then:

$$\alpha = 1.75 + \frac{\gamma}{0.8}$$

which is plotted in Figure 2-73.

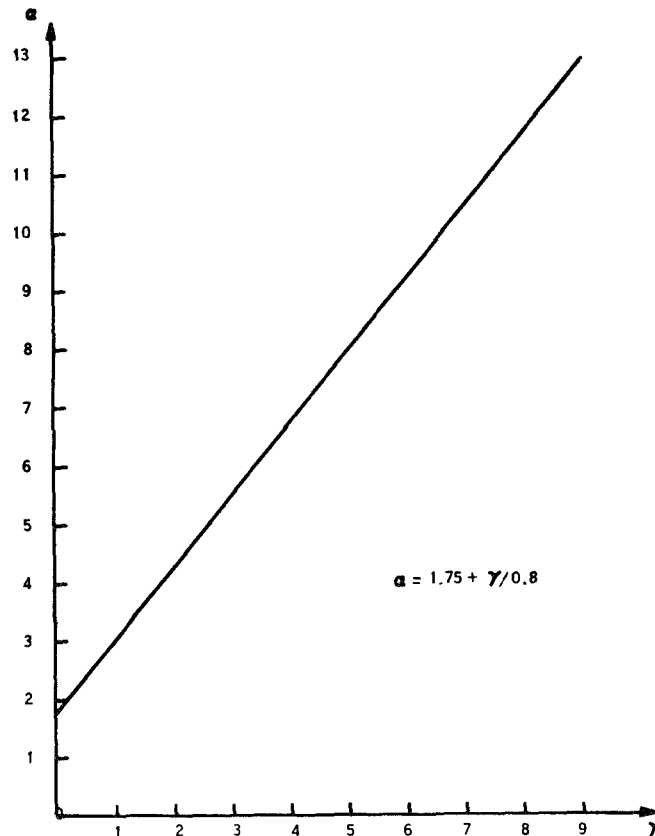


Figure 2-73. Relation Between Coil Loss Factor, α , and External Conductor Resistance Factor, γ

We now wish to express copper weight as a function of γ . Since resistance

$$R = \rho \frac{\ell}{A}$$

where

ρ is copper resistivity

ℓ is conductor length

A is conductor area

It will be necessary to determine ℓ and A for the slot conductor and for the external conductor. For the slot conductor the volume of the copper and hence the weight can be obtained explicitly in the program. The cross sectional area of a particular slot is given by

$$A = \left[W1 \cdot D - W2 \cdot (D - D_o) \right] / 3 \quad (8)$$

where

$$D_o = 0.75 D_{k-1}$$

and

D_{k-1} is the sharp point depth of the last inboard slot (see Figure 2-74)

and since the length is c , the volume for the travelling wave region slots is given by

$$\text{Vol}_{\text{cu}} = \frac{.8c}{3} \sum_{n=1}^{n=N-1} W1_n \cdot D_n - W2_n (D_n - D_o) \quad (9)$$

The copper volume for the compensating pole slots is calculated

$$V_{\text{end Cu}} = 0.8 c 4W_A D_o$$

where

$$w_a = \frac{w_o^2 + w_N^2}{2}$$

and

$$w_o^2 = L_1, \text{ if } L_1 < D_o$$

$$w_o^2 = D_o, \text{ if } L_1 > D_o$$

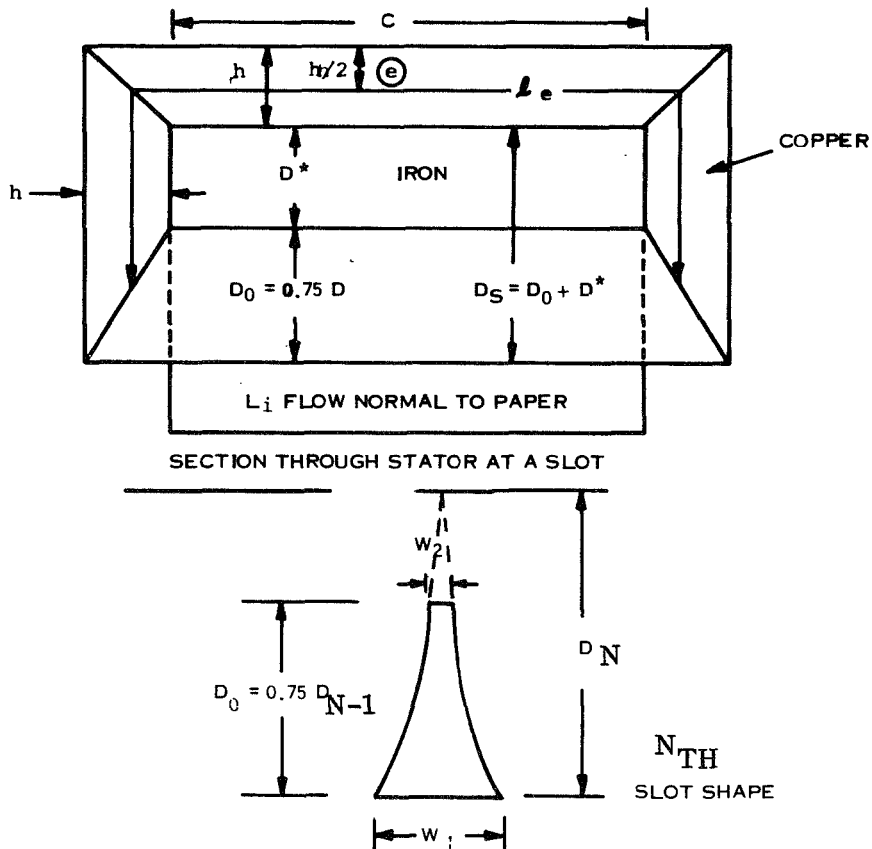


Figure 2-74. MHD Stator Winding Geometry

$$w_{2N}^2 = L_1, \text{ if } L_2 < D_o$$

$$w_{2N}^2 = D_o, \text{ if } L_2 < D_o$$

and

L_1 = length of upstream compensating pole

L_2 = length of downstream compensating pole

In both cases the sum is multiplied by 0.8 as this is the packing fraction of copper in a slot

We can express the volume of the copper external to a particular slot as

$$\text{Vol}_{\text{cu}} = W_e \ell_e h \tag{10}$$

where

W_e is the external width of the copper winding

ℓ_e is the external length of the copper winding

h is the height of the copper winding

By inspection of the generator program results, it appears reasonable to set

$$W_e = 5/3 W_1 \tag{11}$$

(a better approach might be to set W_e equal to the corresponding sector width, but this requires more inspection). This will reasonably fill the outside face of the stator block with copper.

We can estimate the length of the copper as

$$l_e = c + 2 (1/2 D_o + D^* + h/2 + h/2)$$

$$l_e = c + D_s + D^* + 2h \tag{12}$$

The first term $(1/2 D_o)$ in the bracket is considered a reasonable estimate in the cross-section shape-changing region on leaving the slot.

We can now write the cross-sectional area as

$$A_e = 5/3 W1 \cdot h$$

and since

$$\frac{l_e}{A_e} = \gamma \frac{l_s}{A_s} = \gamma \frac{c}{A_s}$$

We can now write

$$\gamma \frac{c}{A_s} = \frac{c + D_s + D^* + 2h}{5/3 W1 h}$$

solving for h yields

$$h = \frac{A_s [c + D_s + D^*]}{5/3 W1 \cdot \gamma c - 2A_s} \tag{13}$$

Putting (11), (12) and (13) into (10) yields

$$\text{Vol}_{cu_n} = (c + D_s + D^* + 2h_n) (5/3 W1_n) \left[\frac{A_{s_n} (c + D_s + D^*)}{5/3 W1_n \gamma c - 2A_{s_n}} \right] \tag{14}$$

This equation yields the volume of the copper external, to the nth slot.

The total volume of copper is then

$$\text{Vol}_{\text{cu}} = \text{Vol}_{\text{cu}_0} + \text{Vol}_{\text{cu}_N} + \sum_{n=0}^{n=N} \text{Vol}_{\text{cu}_n} \quad (14)$$

The first two terms are necessary to include all compensating pole slot copper for the case of two compensating pole slots at each end.

These equations will be used in programming the weight calculations into the generator code.

2.6.1.3 Coil Coolant Requirement

In the calculation of coil dissipation losses, an average coil temperature, T_C , is specified and used to evaluate the resistance which is temperature dependent. This temperature must be maintained by cooling the coil external to the generator. The coolant supply temperature i. e., auxiliary-radiator outlet temperature, T_{out} , required will be a function of T_C , coil dissipation and coil dimensions. The following technique has been used to evaluate T_{out} . The result is then used to size the auxiliary radiator.

Half of a coil is shown schematically in Figure 2-75 which also indicates some of the non-enclature. Volume 1 is inside the stator, Volumes 2 and 3 are outside with Volume 3 being in contact with the fin structure of Figure 2-76. Coil dissipation, P_{coil} , is divided on a volumetric basis. For example, the dissipation in 1 is

$$Q_1 = \frac{P_{\text{coil}} \text{Vol}_1}{2 (\text{Vol}_1 + \text{Vol}_2 + \text{Vol}_3)}$$

where

Vol_1 is the volume of 1.

Assuming uniform dissipation and a one dimensional temperature distribution in Volumes 1 and 2 the temperature drops are given by

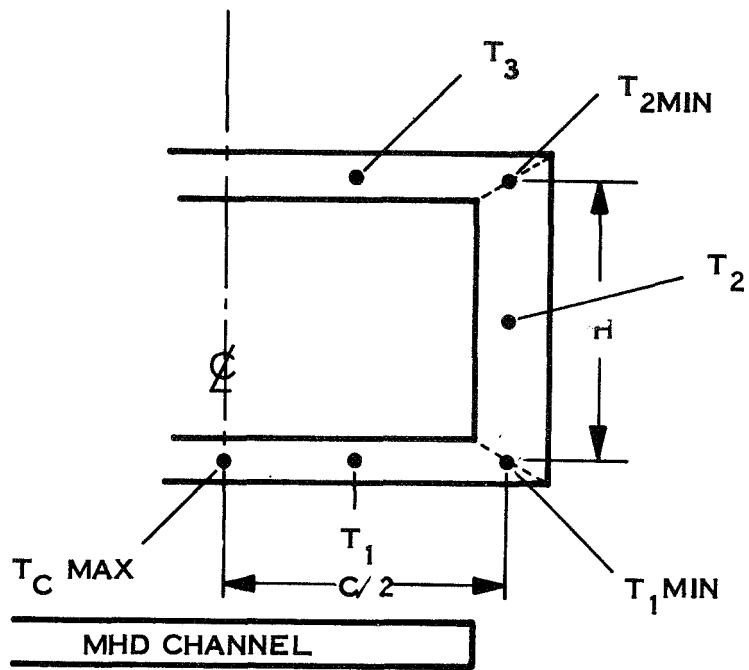


Figure 2-75. Coil Geometry and Temperatures

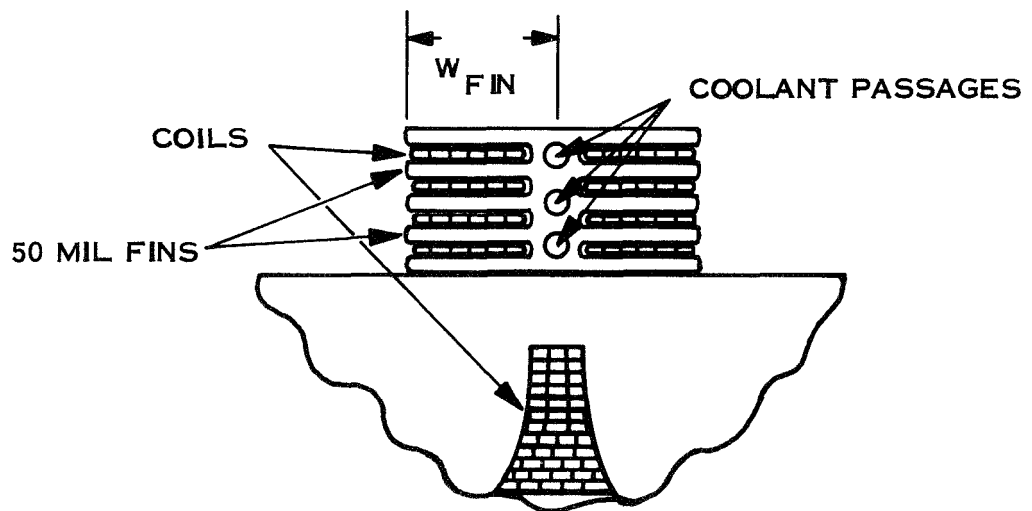


Figure 2-76. Coil Cooling Fins

$$\Delta T_1 = T_{c \max} - T_{1 \min} = \frac{Q_1}{\text{Vol}_1} \left[\frac{1}{2} (c/2)^2 \right] \quad (1)$$

$$\Delta T_2 = T_{1 \min} - T_{2 \min} = \frac{Q_2}{\text{Vol}_2} \left[\frac{1}{2} h^2 \right] + \frac{Q_1 h}{A_2 K} \quad (2)$$

A_2 is the cross sectional area of volume 2. Copper thermal conductivity K is taken as constant with the value 9.4 watts/in. $^{\circ}\text{C}$ which is correct at 200°C . The variation in K between 100°C and 400°C is from 9.7 to 8.95 watts in. $^{\circ}\text{C}$. Temperature gradients in volume 3 are neglected since this volume is being cooled.

Since the coil average temperature, T_C , is used to calculate resistance from

$$R = \rho l/A,$$

T_C is calculated as a weighted average as follows:

$$T_C \left(\frac{C}{2A_1} + \frac{h}{A_2} + \frac{C}{2A_3} \right) = T_1 \frac{C}{2A_1} + T_2 \frac{h}{A_2} + T_3 \frac{C}{2A_3} \quad (3)$$

where

$$T_1 = T_{c \max} - \frac{1}{2} \Delta T_1$$

$$T_2 = T_{c \max} - \Delta T_1 - \frac{1}{2} \Delta T_2$$

$$T_3 = T_{2 \min} = T_{c \max} - \Delta T_1 - \Delta T_2$$

With ΔT_1 and ΔT_2 given by (1) and (2) and T_C specified, equation (3) can be solved for $T_{c \max}$. The temperature drops are thus determined with the dissipation and geometry while the temperature level is determined by average coil temperature.

Fluid temperature T_{out} is given by

$$T_{out} = T_3 - \Delta T_{ins} - \Delta T_{fin}$$

ΔT_{ins} = gradient across insulation

ΔT_{fin} = gradient along length of fin

$$\Delta T_{ins} = \frac{P_{coil/24} \Delta L}{K_{ins} A_{fin}}$$

$$\Delta T_{fin} = \frac{P_{coil/12}}{Vol_{fin}} \left(\frac{1}{2} W_{fin}^2 \right)$$

The insulation gradient is based on heat transfer to 24 fin surfaces (Figure 2-14) of area $A_{fin} = W_{fin} \times C$. The fin width W_{fin} is just $1/2 W_e = 5/6 W_l$. ΔL , the insulation thickness is assumed to be 6 mils and $K_{ins} = 0.109 \text{ Btu/hr Ft}^2 \text{ } ^\circ\text{F}$.

The fin gradient assumes one dimensional temperature and uniform heat addition over the surface.

In the computer program, this procedure is followed for only the last coil. Since this coil has the largest dissipation per unit volume, the ΔT_1 , ΔT_2 , and T_C values which are calculated are maximum. The T_{out} value is thus smaller than required for all coils except the last one and the resultant radiator area is conservative.

2.6.1.4 Conditions at Recuperator Exit

The energy exchange, Q_r , in the recuperator is determined by an energy balance for the liquid cesium between points 12 and 13 of Figure 2-8. With given recuperator inlet conditions (at point 8), a given pressure drop and a calculated Q_r , the conditions at the recuperator exit (point 9) can be determined.

This is done by an iterative process assuming for a starting point that all the lithium is condensed at point 9, i. e., $\beta_9^{(0)} = 0$. An energy balance between points 8 and 9 then yields a first value for $T_9^{(1)}$ which is larger than the correct value. With $T_9^{(1)}$ and p_9 an equilibrium value of β , $\beta_9^{(1)}$, is calculated. A new heat balance produces $T_9^{(2)} < T_9^{(1)}$, since not all of the lithium is condensed. This $T_9^{(2)}$ corresponds to an equilibrium value $\beta_9^{(2)} > \beta_9^{(1)}$. The iteration is continued until T_9 doesn't change significantly.

2.6.1.5 Secondary Radiators

The secondary radiator is modeled using test data obtained with a NaK 78 radiator operating with T_{inlet} between 300 and 700°F, $\Delta T = 50$ to 200°F and $Q < 10$ kW. The geometry is shown in Figure 2-77.

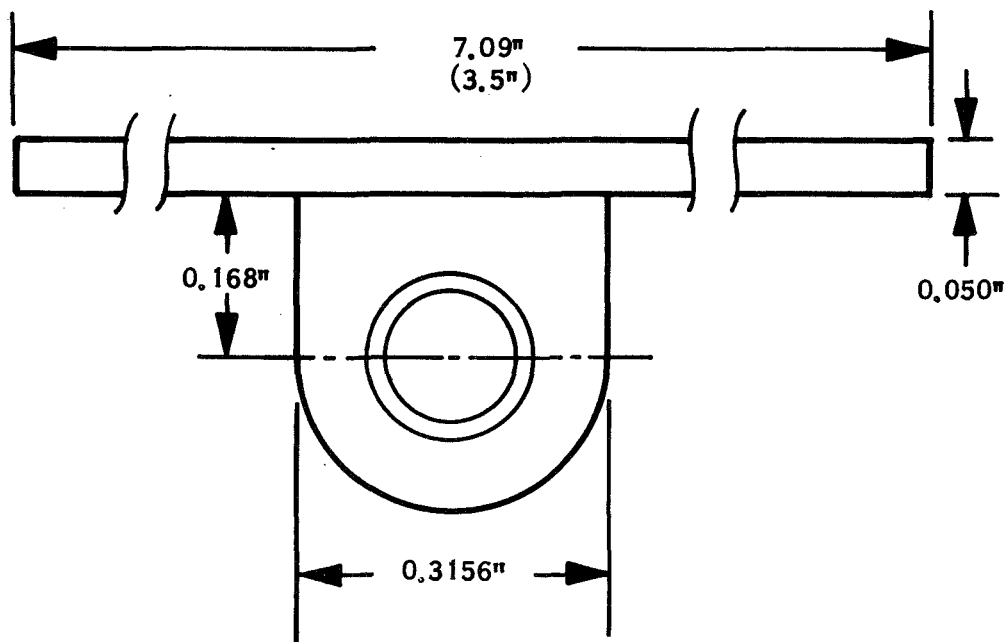


Figure 2-77. Auxiliary Radiator Geometry

An effective temperature is defined

$$T_{eff}^4 = T_s^4 + \frac{4 T_s^3 (T_{in} - T_{out})}{\ln \left[\frac{(T_{in} - T_s)(T_{out} + T_s)}{(T_{in} + T_s)(T_{out} - T_s)} \right] + 2 \left[\tan^{-1} \left(\frac{T_{out}}{T_s} \right) - \tan^{-1} \left(\frac{T_{in}}{T_s} \right) \right]}$$

$$\begin{aligned}
T_{\text{eff}} &= \text{effective temperature } ^{\circ}\text{R} \\
T_{\text{s}} &= \text{sink temperature} = 460^{\circ}\text{R} \\
T_{\text{in}} &= \text{radiator inlet temperature } ^{\circ}\text{R} \\
T_{\text{out}} &= \text{radiator outlet temperature } ^{\circ}\text{R}
\end{aligned}$$

A curve fit for fin efficiency is

$$\eta = 0.983 + 8.5 \times 10^{-5} T_{\text{eff}} - 2.56 \times 10^{-7} T_{\text{eff}}^2$$

The required radiator area for coil cooling is thus

$$A_{\text{c}} = \frac{P_{\text{coil}}}{\eta \epsilon \sigma (T_{\text{eff}}^4 - T_{\text{s}}^4)}$$

$$\epsilon = \text{emissivity of radiator} = 0.85$$

Radiator weight for coil cooling is given by

$$\text{WT (lb)} = 0.968 A_{\text{c}} (\text{ft}^2)$$

For the coil radiator, a negligible radiator ΔT is assumed i. e., $T_{\text{in}} \approx T_{\text{out}} = T_3$. Cooling of the stator, valve motors and pump may be done at an 800°F temperature level. The radiator model above is used with $T_{\text{eff}} = 800^{\circ}\text{F}$. The tube spacing is cut from 7.09 to 3.5 inch to raise η to 0.9 and a weight multiplier of 1.55 is applied to reflect a material change to Cu/SS for the higher temperature. The higher temperature secondary radiator weight is then given by

$$\text{WT (lb)} = 1.91A (\text{ft}^2)$$

2.6.1.6 Capacitor Cooling

The large reactive power characteristic of the MHD generator means that dissipative losses in the excitation capacitors can be an appreciable heat rejection load. No off-the-shelf capacitor suitable for the MHD spacecraft has been

identified but conversation with manufacturers indicate that a mica/silicone oil type would offer the high temperature and high radiation resistance desired with relatively low dissipative losses. The size of a typical unit of 5 μ fd capacitance was estimated to be 6 by 4 by 3-inch with dissipation loss perhaps as high as 1 percent if the capacitor operating temperature were $\sim 400^{\circ}\text{F}$. At lower temperatures the dissipative loss would be reduced. In order to provide adequate heat rejection by the capacitors, they were arranged broad-side to space, over a panel area of 60 square feet. This area was chosen as being sufficient to reject 1 percent dissipative loss at 400°F , 0.61 percent at 300°F , or 0.35 percent at 200°F (see Figure 2-78). It is believed that the dissipation versus temperature curve for the capacitor will have a more shallow slope and that the 60 square foot panel area will assure stable operation at some temperature less than or equal to 400°F .

2.6.2 SELECTION OF BASELINE DESIGN PARAMETERS

The baseline design was selected by comparing results of several calculations made with the combined cycle and generator programs. An initial set of calculations was made with the parameters in Table 2-36.

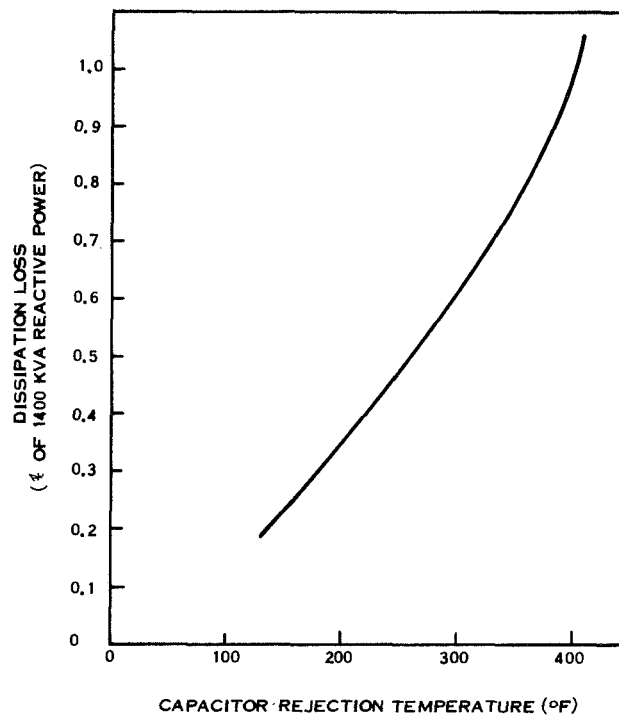


Figure 2-78. Capacitor Heat Rejection

TABLE 2-36. PARAMETERS VARIED IN DESIGN SELECTION
(RUNS 1 TO 11)

Run No.	Coil Ratio γ	Coil Temperature T_c ($^{\circ}\text{C}$)	Nozzle Exit/ Throat Area Ratio AR	Separator to Condenser ΔP (N/M) ²	Inlet Field B_o Wb/M ²
1 (Base)	1.0	200	3.0	2×10^4	0.48
2	1.0	200	3.0	<u>1.5×10^4</u>	0.48
3	1.0	200	3.0	<u>2.5×10^4</u>	0.48
4	1.0	<u>250</u>	3.0	2.0×10^4	0.48
5	1.0	<u>300</u>	3.0	2.0×10^4	0.48
6	1.0	200	<u>2.75</u>	2.0×10^4	0.48
7	1.0	200	<u>3.25</u>	2.0×10^4	0.48
8	<u>0.8</u>	200	3.0	2.0×10^4	0.48
9	<u>1.2</u>	200	3.0	2.0×10^4	0.48
10	1.0	200	3.0	2.0×10^4	<u>0.46</u>
11	1.0	200	3.0	2.0×10^4	<u>0.50</u>

Parameters held fixed were:

Wall thickness = 4 mm (fluid to stator gap)

Power output = 275 KW

Pump efficiency = 20%

Nozzle Case = 4 (Li/C_s mass flow ratio = 14:1)

Nozzle Exit W/H = 3.5

THETA = 0.262 Radians (impinging half-angle)

Velocity Factor = 1

Gas vol. flow rate ÷ Liq vol. flow rate = 3, at the capture slot

Upstream Diffuser L/W = 0.2

Downstream Vane $L/W = 0.2$

No. of upstream vanes 18

No. of downstream vanes 28

Heat source $\Delta P = 7 \times 10^4 \text{ N/M}^2$

Recuperator $\Delta P = 4 \times 10^3 \text{ N/M}^2$

Condensor $\Delta P = 2 \times 10^4 \text{ N/M}^2$

Results are presented in Table 2-37 and Figures 2-79, 2-80, and 2-81. Design parameters are sought which will minimize weight and radiator area. Preliminary radiator area is reflected in the weight calculation only on a pounds per square foot basis; there really should be a multiplier applied to reflect the increase in flight fairing and structure weight which accompanies increases in primary radiator area and length.

There is an incentive to limit the secondary radiator area. The spacecraft configuration provides about 200 square feet of surface on the outside of the MHD equipment bay. About 60 square feet of this surface is needed for mounting the excitation capacitors and the rest is available for secondary radiator area with no increase in spacecraft length. Thus, if the secondary radiator area is less than 140 square feet, the weight of one pound per square feet is realistic since the radiator panels can be hung on the MHD bay. However, if the area exceeds 140 square feet a structural extension of the MHD bay will be required, with attendant increases in structure and flight fairing weight.

The weight trends indicated in Figure 2-79 indicate choice of low separator to condenser Δp , B_o and γ but high nozzle area ratio and coil temperature. Figure 2-80 also indicates choice of low γ and B_o and high coil temperature and area ratio. The secondary radiator area is insensitive to variation in separator to condenser pressure drop. Figure 2-81 shows that to minimize primary radiator area, it is important to have low Δp and area ratio and that primary radiator area is much less sensitive to the other variables. Consequently, an area ratio of 3.25 and a Δp of $1.5 \times 10^4 \text{ N/M}^2$ were selected and further investigation was made with the γ , B_o and T_c parameters. The parameter variations are given in Table 2-38 and the results are listed in Table 2-39. Inspection of the results shows that Run No. 19 gives a near minimum total weight and primary radiator area with a secondary radiator area of 129 square feet a bit less than the desired limit of ~ 140 square feet. The parameters of Run No. 19 were therefor chosen for the baseline design.

TABLE 2-37. PARAMETRIC WEIGHTS AND AREAS (RUNS 1 TO 11)

Run No.	Weight - Pounds						Areas - ft ²	
	Generator	Capacitors	Primary Radiator	Secondary * Radiator	Total	Primary Radiator	Secondary** Radiator	
1	618	1197	2818	653	5286	1395	665	
2	618	1197	2718	653	5186	1346	665	
3	618	1197	2930	653	5398	1450	665	
4	621	1196	2833	428	5078	1402	436	
5	623	1197	2848	308	4976	1410	314	
6	626	1376	2760	798	5560	1368	814	
7	616	1053	2942	560	5171	1458	530	
8	794	1195	2807	324	5120	1390	320	
9	528	1196	2829	2488	7044	1399	2530	
10	916	1244	2811	162	5129	1390	166	
11	430	1146	2848	***	-	1410	-	

* Includes 48.5 pounds for stator cooling

** Includes 50 ft² for stator cooling

*** Required radiator temperature was less than sink temperature

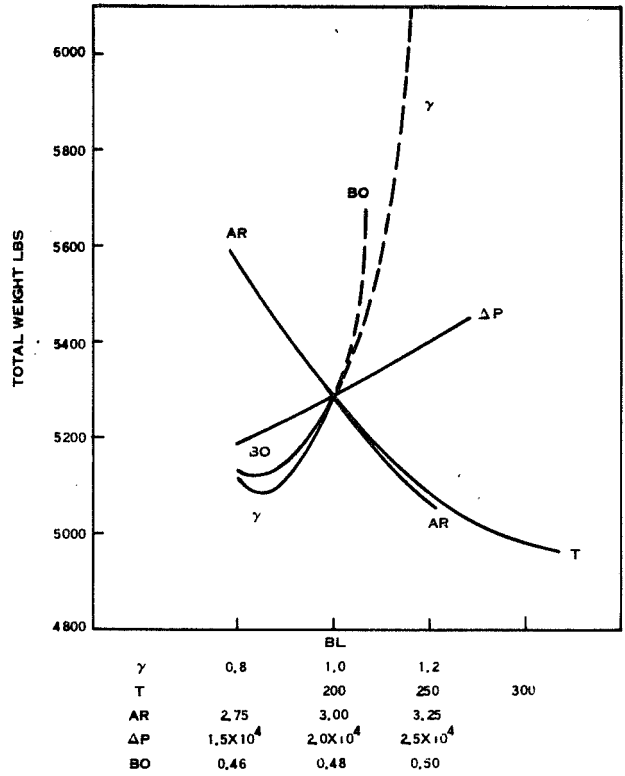


Figure 2-79. Total Weight Variation

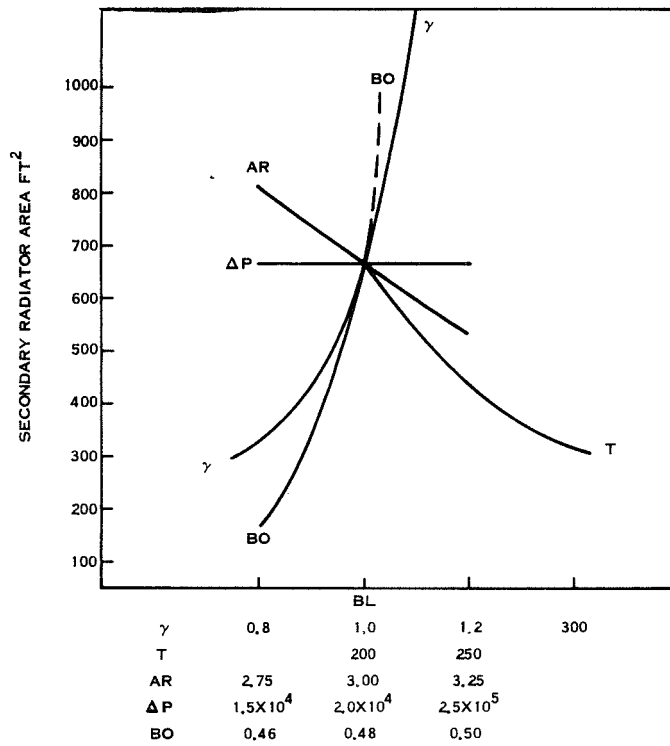


Figure 2-80. Secondary Radiator Area Variation

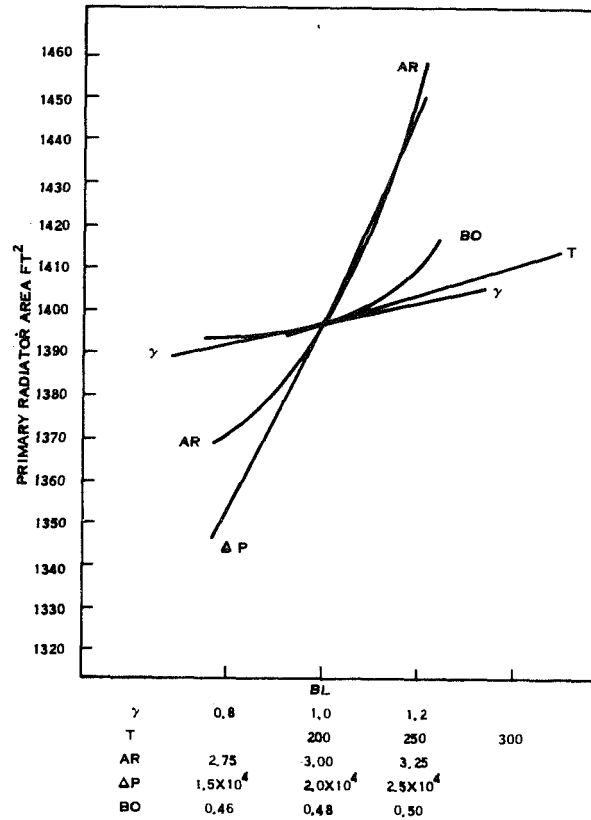


Figure 2-81. Primary Radiator Area Variation

TABLE 2-38. PARAMETERS VARIED IN DESIGN SELECTION
(RUNS 12 TO 20)

Run No.	Coil Ratio γ	Coil Temperature T_c ($^{\circ}\text{C}$)	Inlet Field B_o (Wb/M^2)
12	0.8	200	0.46
13	0.8	250	0.46
14	0.8	300	0.46
15	0.9	300	0.46
16	1.0	300	0.46
17	0.9	250	0.47
18	1.0	250	0.47
19	0.9	300	0.47
20	1.0	300	0.47

TABLE 2-39. PARAMETRIC WEIGHTS AND AREAS (RUNS 12 TO 20)

Run No.	Generator	Weight - Pounds				Areas - Ft ²		
		Capacitor	Primary Radiator	Secondary* Radiator	Total	Primary Radiator	Secondary** Radiator	
12	1259	1097	2814	128	5298	1392	131	
13	1261	1098	2823	107	5289	1398	109	
14	1263	1098	2832	95	5288	1400	97	
15	1052	1098	2837	100	5087	1405	103	
16	915	1099	2841	109	4964	1406	111	
17	841	1075	2828	156	4900	1399	160	
18	744	1075	2833	189	4841	1400	193	
19	843	1076	2840	126	4885	1406	129	
20	747	1076	2845	154	8422	1410	158	

* Includes 48.5 pounds for stator cooling

** Includes 50⁰ ft² for stator cooling

2.6.3 CYCLE EFFICIENCY VARIATION

2.6.3.1 Velocity Factor Definition

In the MHD cycle and generator calculations a velocity factor, K_V , is used as a multiplier on the generator inlet velocity; K_V is discussed in Appendix II of Reference 2. This velocity factor is a user input which can account for non-ideal behavior of the lithium/cesium separator. In the baseline design the factor was taken as 1.0, representing ideal separator performance. Friction losses in the separator can be reflected by a decreasing K_V ; in that sense $K_V \times 100$ may be considered separator efficiency. From an analytical standpoint K_V can be greater than one if it is used to represent two other fluid mechanisms as well as friction loss. The calculation of the generator inlet velocity involves an assessment of vapor/liquid slip in the two-phase nozzles and calculation of the amount of cesium dissolved in the lithium stream. If one desires to be less conservative in these two respects than the baseline design, a velocity factor of greater than one is a convenient analytical tool to do so.

2.6.3.2 Velocity Factor Calculations

A set of runs were made with Run No. 19 (the baseline design) as the standard and the velocity factor varied from the baseline value of 1.0 down to 0.8; Table 2-40 lists the runs. Generator and system quantities normalized by the values calculated in Run 19 are shown in Figure 2-82 as a function of velocity factor. Decreased velocity factor causes decreased system efficiency with the resultant increase in primary radiator size, coil loss and reactor weight. Secondary radiator temperatures are low so the calculated areas are large or in some runs the radiator temperature is below the sink temperature. For this reason, coil loss is given as more meaningful information than secondary radiator area.

TABLE 2-40. RUNS WITH VELOCITY FACTOR VARIED

Run No.	Vel. Factor K_V	Nozzle Area Ratio	Gamma Coil Ratio γ	ΔP Sep. to Cond. (N/M ²)	Inlet Field (Wb/M ²)	
19	1.0	3.25	0.9	0.15×10^5	0.47	
20	0.95	↓	↓	↓	↓	
21	0.9					
22	0.85					
23	0.8					
24	0.85					
25	↓	3.75	↓	↓	↓	
26	↓	3.25				
27	↓	↓				0.2×10^5
28	↓	↓				0.15×10^5
29	↓	↓				1.0
					0.45	
					0.47	

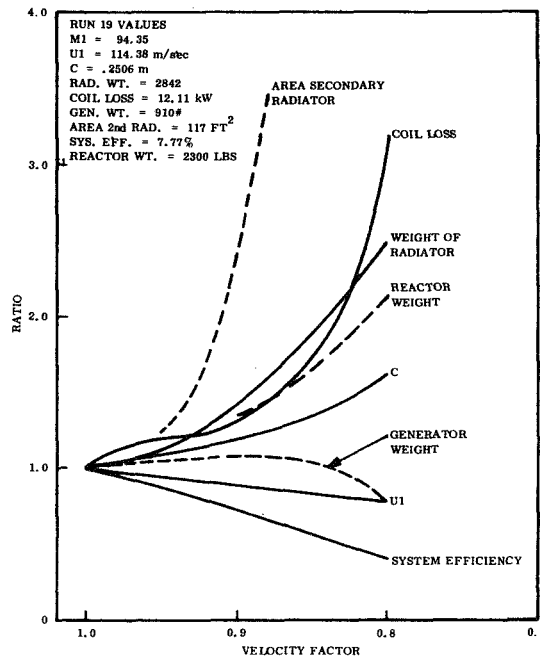


Figure 2-82. Effect of Velocity Factor Variation

The velocity factor = 0.85 case, Run 22, was investigated in Runs 23 to 29 for sensitivity to various parameters to check the possibility for optimization. Increasing area ratio, Run 25, produced the most favorable results but could not increase efficiency appreciably. Therefore, the trends evidenced in Runs 19 through 23 are considered representative of optimized systems.

As can be seen in Figure 2-82, only the secondary (coil cooling) radiator area gets out of hand in the range of velocity factor from 1.0 to 0.9. This is not a severe problem since manual reoptimization of coil loss, coil ratio, coil temperature and radiator fin efficiency can produce an acceptably low radiator area. This is, in fact, what is done to translate a computer generated MHD spacecraft design to a detailed layout.

Table 2-41 lists the calculated parameters for these runs; the efficiency, reactor weight, generator weight, primary radiator weight, and coil loss are direct computer program outputs. The other weights and corrections, which are calculated manually, include the corrections for changes in structural weight, shield weight and piping weight. All weights are then normalized to the baseline design (Run 19) weight. Taking the calculated power plant weight fractions from Table 2-41 and plotting them against efficiency, one obtains the curve shown in Figure 2-83. It is evident that the power plant weight does not increase rapidly until the efficiency falls below 5 percent; in the range from 7.77 percent down to 5 percent the weight increase is roughly proportioned to efficiency decrease with a 32 percent weight increase at 5 percent efficiency. The consequences of such weight increase may be related to mission performance by referring to Section 2.8.2, Mission Analysis.

2.6.4 CYCLE TEMPERATURE VARIATION

The lithium/cesium MHD cycle used in this study does not respond to system temperature change in the same way as typical Rankine cycle systems. As system temperature increases, the heat rejection temperature can be increased, thereby reducing radiator size and weight. However, offsetting this advantage, the increased temperature will cause more cesium to dissolve in the lithium stream requiring the use of proportionately more cesium; the cycle calculations assume equilibrium solution of cesium in lithium for conservatism.

TABLE 2-41. EFFECT OF EFFICIENCY VARIATION

Run	Efficiency %	Reactor Weight lbs.	Generator Weight lbs.	Primary Radiator Weight lbs.	Coil Loss kW	Structural Weight Increase lbs.	Shield Weight Increase lbs.	Piping Weight Increase lbs.	Weight Increase Over Baseline lbs.	Fraction of Baseline Power Plant Weight (15,810 lbs.)
19	7.77	2300	910	2842	12.1	0	0	0	0	1.0
20	6.68	2650	958	3347	13.3	372	140	100	1515	1.095
21	5.55	3120	974	4070	15.8	970	310	210	3602	1.23
22	4.40	3850	946	5202	21.12	2650	580	410	7586	1.48
23	3.15	5200	739	7353	38.49					
24	4.57	3700	957	5257	19.05					
25	4.74	3600	966	5358	17.40					
26	4.39	3850	946	5419	21.12					
27	4.31	3900	647	5311	30.34					
28	4.44	3800	1341	5147	15.02					
29	4.38	3850	859	5217	22.09					

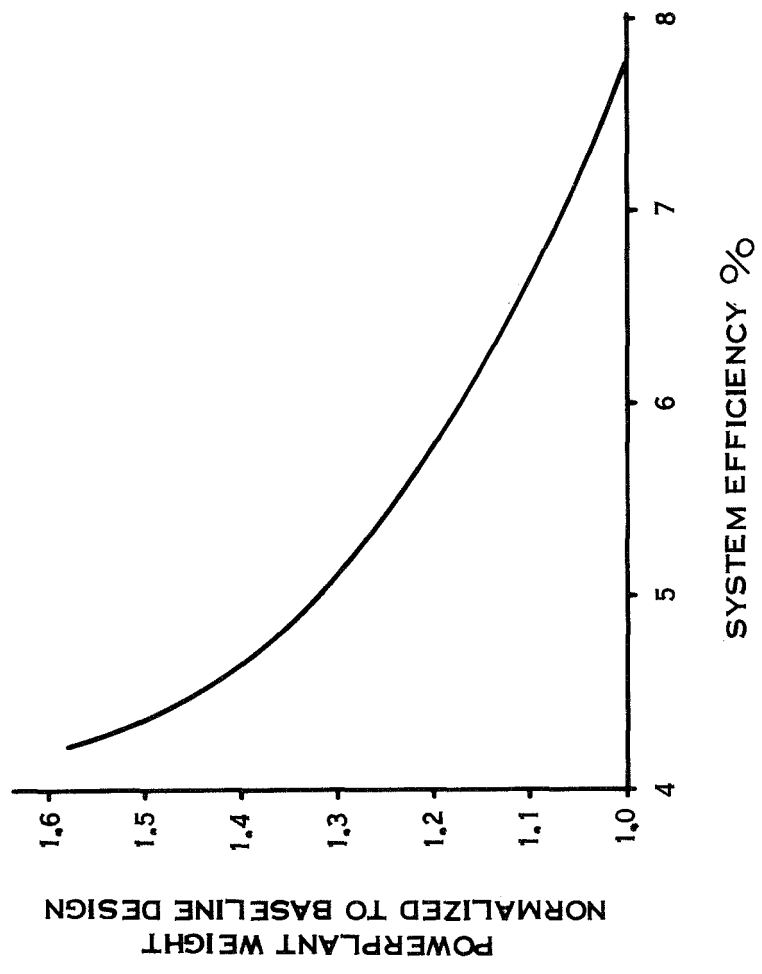


Figure 2-83. Variation of Power Plant Weight with System Efficiency

2.6.4.1 Calculations

The next effort was directed toward determining the effect of different temperature levels. Runs 30 to 43 studied the effects of temperature and lithium to cesium mass ratio. Parameters and results are given in Table 2-42 and the results are also shown in Figures 2-84 and 2-85.

It can be seen from Figure 2-84 that increased temperature causes the maximum efficiency condition to occur at a lower Li/Cs ratio, and that maximum efficiency decreases as temperature is increased above 1800°F. The parameter of greater interest is weight; Figure 2-85 shows the sum of reactor, generator and radiator weight as a function of cycle temperature; the curve is set by the baseline design and optimum weights for 1900° and 2000°F taken from the calculations listed in Table 2-43.

The only variable except temperature in these results is lithium to cesium mass ratio and the system is not optimum as indicated by the generator weights. A series of runs were made to optimize the cases Li/Cs = 11, T = 1900°F and Li/Cs = 8, T = 2000°F with Runs No. 35 and 42 as the baselines, respectively. The variables are given in Table 2-43.

Considering the Li/Cs = 11, T = 1900°F case first, Figure 2-86 shows little variation in system efficiency, therefore, reactor weight is constant. The optimum generator design (from a weight viewpoint) has a higher inlet field, near 0.49, compared to results at 1800°F. Comparing Run 47 to Run 35, the generator weight is reduced more than the increase in secondary radiator weight increase. Higher fields produce large secondary radiator weight or the need for secondary radiator temperature lower than sink temperature.

The Li/Cs = 8, T = 2000°F case is optimized with inlet field only. Results are shown in Figure 2-87 illustrating optimization at higher inlet field as temperature is increased.

Weights from optimized runs; Run 19 for T = 1800°F, Run 47 for T = 1900°F, and Run 52 for T = 2000°F are shown in Figure 2-85. From a system weight viewpoint there is no incentive to go to the higher temperature levels. This conclusion is re-enforced when one considers unaccounted for weight increases in piping, nozzles, etc., at high temperature levels. Results shown in Figures 2-86 and 2-87 are also given in Table 2-44.

TABLE 2-42. Effect of Temperature and Li/Cs Ratio

Run No.	Temperature OF	Li/Cs Ratio	System Efficiency %	Generator Weight lb	Reactor Weight lb	Primary Radiator Weight lb	Secondary Radiator Weight lb	Total
19	1800	14	7.77	910	2300	2842	12	6064
30	1800	11	7.65	916	2500	2876	93	6385
31	1850	14	7.56	1003	2600	2638	79	6320
32	1850	11	7.61	1103	2700	2611	46	6460
34	1900	14	7.19	1036	2900	2505	63	6504
35	1900	11	5.97	1328	2800	2402	32	6562
36	1900	8	7.17	1022	2900	2520	35	6477
37	1900	5	5.97	519	3500	3098	274	7391
38	1950	14	6.51	930	3600	2503	75	7108
39	1950	11	7.14	1206	3300	2276	34	6816
40	1950	8	7.11	1386	3300	2300	23	7009
41	2000	11	6.56	1182	4150	2239	36	7607
42	2000	8	6.9	1848	3900	2144	19	7911
43	2000	5	6.06	974	4430	2504	25	7933

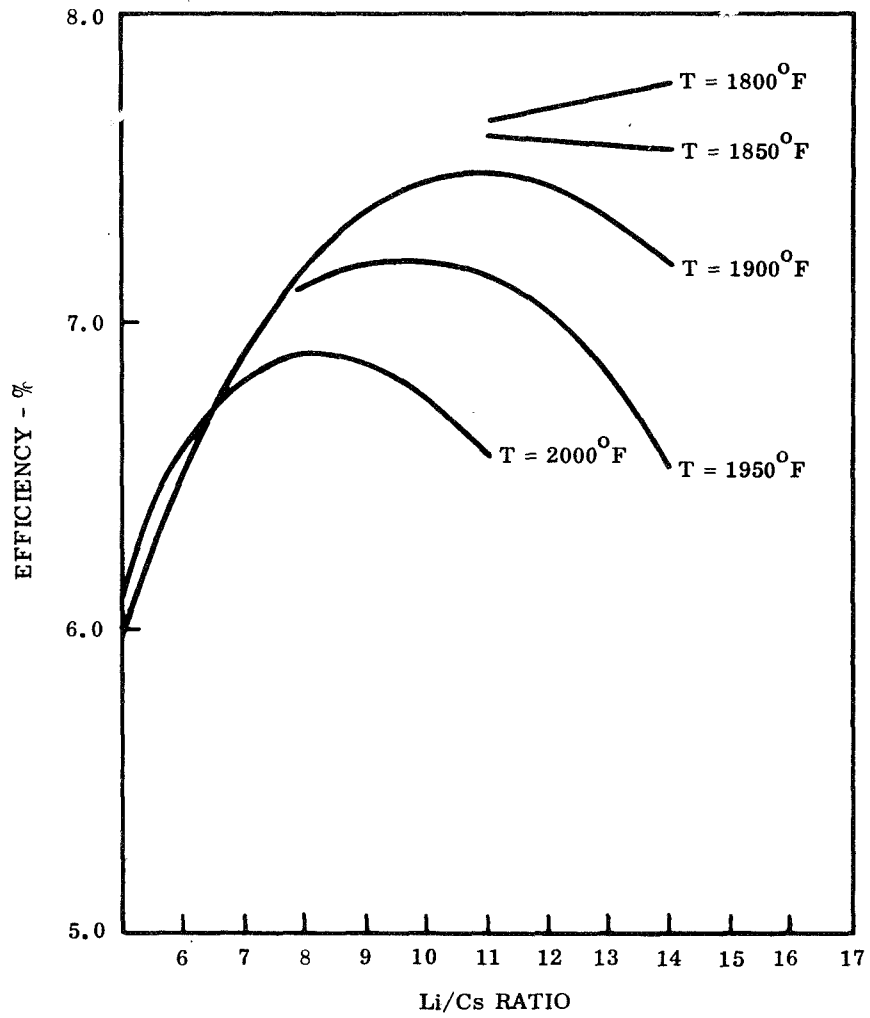


Figure 2-84. Effect of Temperature and Li/Cs Mass Ratio on Efficiency

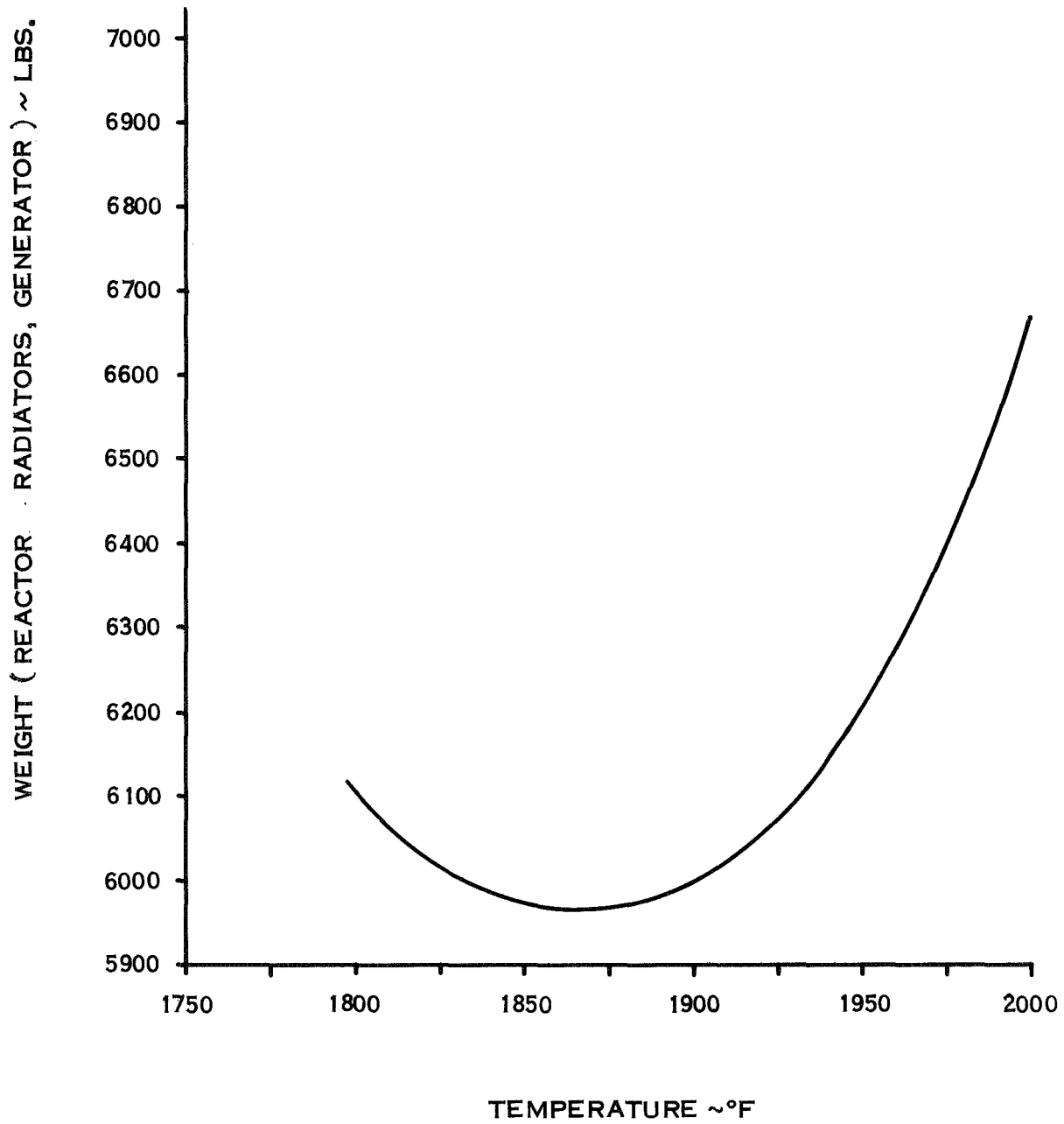


Figure 2-85. Effect of Temperature on Weight

TABLE 2-43. RUNS FOR OPTIMIZATION AT 1900°F AND 2000°F

Run No.	Case		Nozzle Area Ratio	Inlet Field Wb/M ²	N Upstream Vanes	N Downstream Vanes
	Li/Cs Ratio	T °F				
35	11	1900	3.25	0.47	18	28
44	11	1900	3.0	0.47	18	28
45	11	1900	3.5	0.47	18	28
46	11	1900	3.25	0.45	18	28
47	11	1900	3.25	0.49	18	28
48	11	1900	3.25	0.47	22	34
49	11	1900	3.25	0.47	14	22
50	11	1900	3.25	0.49	22	34
42	8	2000	32.5	0.47	22	34
51	8	2000	3.25	0.49	22	34
52	8	2000	3.25	0.51	22	34
53	8	2000	3.25	0.53	22	34

TABLE 2-44. WEIGHTS FOR OPTIMIZATION AT 1900°F AND 2000°F

Run No.	Generator Weight Pounds	Primary Radiator Weight Pounds	Secondary Radiator Weight Pounds	Reactor Weight Pounds	Total
35	1328	2402	32	2800	6562
44	1365	2338	34	2800	6537
45	1292	2476	30	2800	6598
46	2706	2419	18	2800	7943
47	652	2403	145	2800	6000
48	1062	2429	43	2800	6334
49	1327	2406	32	2800	6565
50	656	2422	140	2800	6018
42	1848	2144	19	3900	7911
51	920	2139	34	3900	6993
52	546	2126	85	3900	6657
53	308	2138	*	3900	----

*Radiator temperature below sink temperature

It appears from Figure 2-85 that the minimum weight system may fall anywhere in the 1800-1950°F range. However, the curve is so flat in this region that weight savings of no more than about 100 pounds seem attainable; this is not considered a sufficient cause to increase cycle temperature above the 1800°F level of the baseline system.

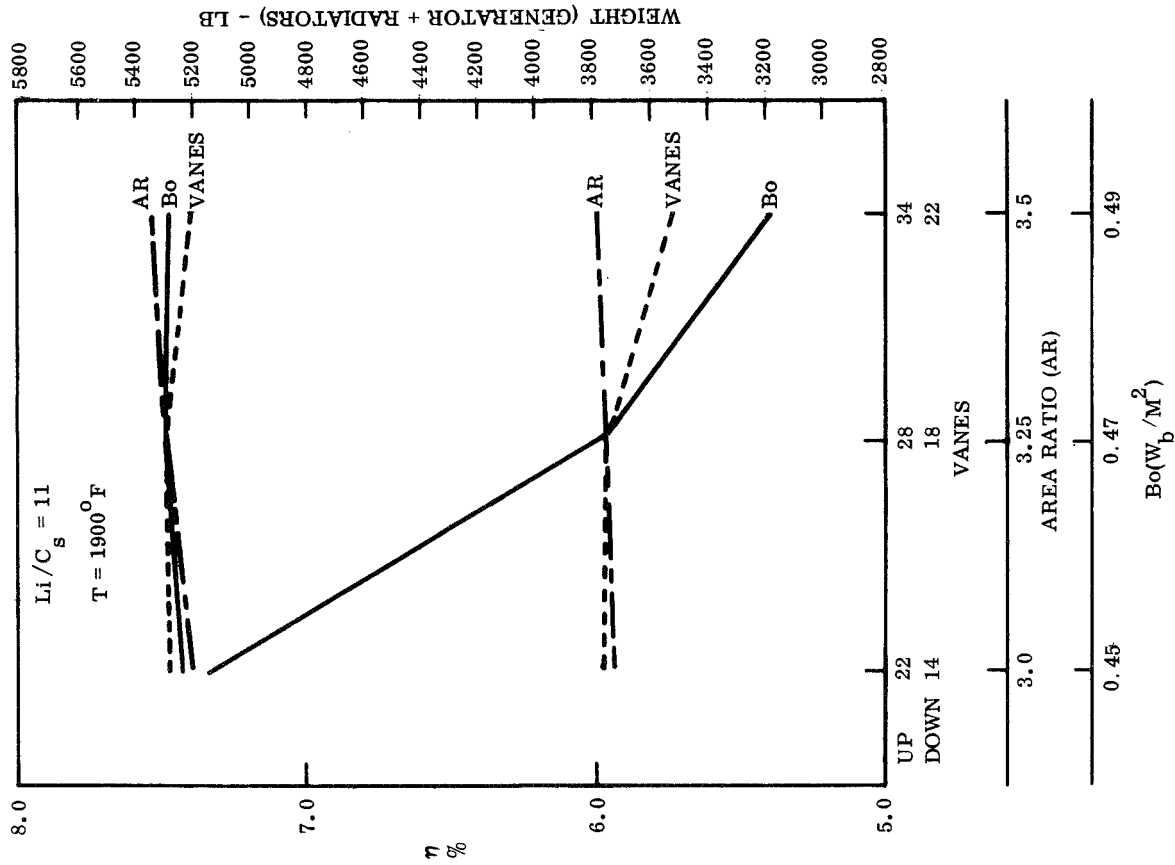


Figure 2-86. Optimization of Case 11 (Run 35)

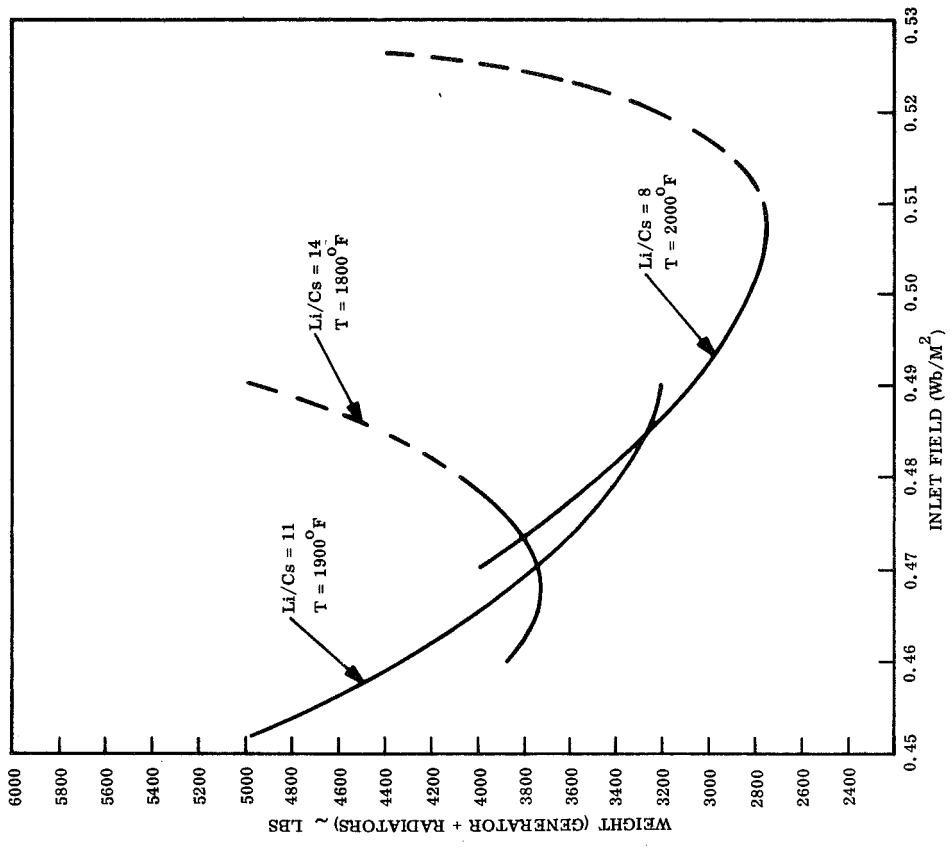


Figure 2-87. Effect of Inlet Field on Weight

2.6.5. OUTPUT POWER VARIATION

A series of MHD power systems, ranging in gross power output from 100 kWe to 3MWe, were investigated to explore the effects of output power variation. In general, a power system is designated here by its gross output power, the raw unconditioned power. Figure 2-88 depicts the relationship between gross output power and net output power using the baseline design system values for example. The eight specific power levels considered are listed with their most basic parameters in Table 2-45. Three of these systems, the 200 kWe, 275 kWe, and 400 kWe, have been considered in detail with specific spacecraft designs as described in the following sections of this report.

2.6.5.1 Selection of High Power Spacecraft Size

In selecting the basic configuration of the 275 kWe baseline design, two design methods were chosen which significantly affect the variability of the system over a broad power range. These two methods are the generator coil cooling approach and the general arrangement of auxiliary radiators only around the MHD bay.

The generator coil cooling approach and analysis are described in detail in Section 2.6.1.3. Basically, the portion of the coil on the outside face of the stator block is clamped to a heat sink assembly which is cooled by a circulating fluid. Since the I^2R heating takes place throughout the coil, and especially in the higher resistance stator interior section, there is an appreciable temperature drop between the center of the coil in the stator and the center of the coil in the heat sink. This temperature drop increases with decreasing coil cross section and with increasing stator width. With the methods of generator analysis used, the optimum generator is fairly wide; as a result, for a 500 kWe system, the optimum channel was calculated to be more than a foot wide (32.7 centimeters). With this width the effective temperature of the auxiliary coil cooling radiator must be below 200⁰F in order to maintain the coil peak temperature to 750⁰F. With large auxiliary radiator areas and judicious design, these 500 kWe values might be attainable. However, we concluded that spacecraft designs of the baseline type should not be taken up much higher in power than 400 kWe. We therefore selected 400 kWe as a higher power spacecraft design point. This is not to say that MHD generators of greater than 400 to 500 kWe cannot be used; current studies of narrower, constant slip generators at JPL (see Section 2.5.2) can provide efficient generator

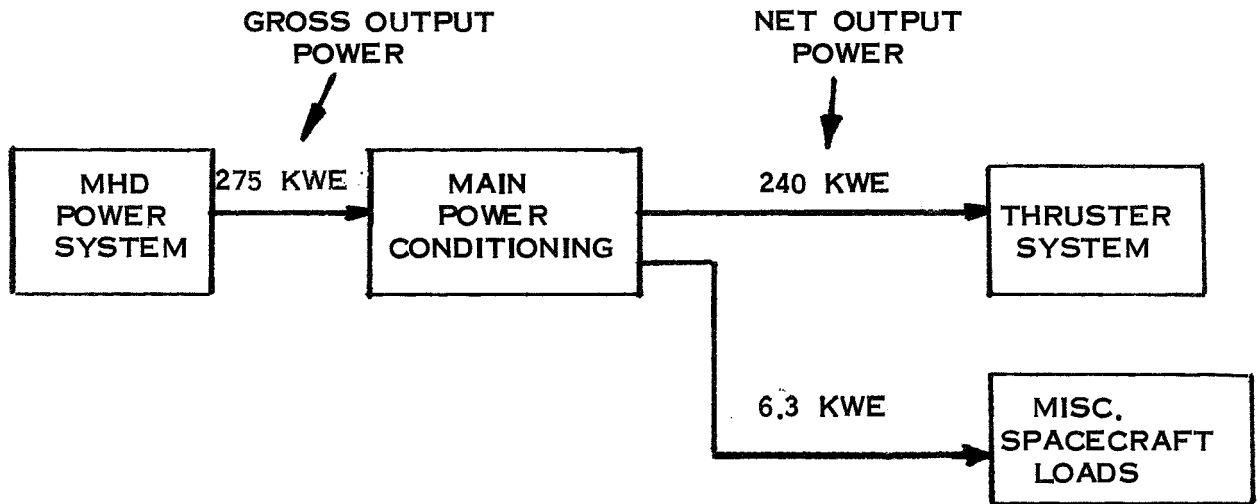


Figure 2-88. Power Output Definition

designs with reduced widths, thereby raising this coil-cooling power ceiling. Moreover, this limit really derives from the coil cooling method chosen in this study; an alternate cooling technique might eliminate this sort of limit altogether.

2.6.5.2 Selection of Low Power Spacecraft Size

At the lower end of the power spectrum, one expects the specific weight of the power plant to increase as the relatively fixed weights begin to dominate, or one expects to reach power levels which are too low to be of interest from the mission analysis standpoint. The specific weights of the 400 kWe, 275 kWe and 200 kWe propulsion systems were calculated as listed in Table 2-46. One can see no dramatic increase in specific weight as power is reduced over this range. In fact, the differences in specific weight shown are not considered meaningful since modest changes in design or configuration might cancel them. Below 200 kWe, the spacecraft concept seems far less attractive from a mission utility point of view, especially in competition with all-chemical thrust (see Section 2.8.2). The 200 kWe system was therefore chosen as the lower bound of spacecraft size.

TABLE 2-45. OUTPUT POWER VARIATION

GROSS POWER RATING (KWE)	REACTOR THERMAL POWER (MW)	SYSTEM EFFICIENCY (%)	PRIMARY RADIATOR AREA (FT ²)
100	1.5	6.8	570
200	2.5	7.8	985
275 BASELINE	3.5	7.8	1400
300	3.8	7.8	1520
400	5.0	8.1	2000
500	6.1	8.2	2480
1000	11.6	8.6	4810
3000	32.9	9.1	14000

TABLE 2-46. SPECIFIC POWER COMPARISON

GROSS POWER (KWE)	NET POWER (KWE)	PROPULSION SYSTEM WEIGHT (LBS)	GROSS SPECIFIC WEIGHT (LBS/KW GROSS)	NET SPECIFIC WEIGHT (LBS/KW NET)
200	175	14,760	73	84
275	240	18,140	66	76
400	350	24,110	60	69

2.7 SPACECRAFT DESIGNS

This section describes the various spacecraft designs developed in this study. The first design discussed is the baseline design, a 275 kWe system selected to match a thrust system requiring a net input of 240 kWe. The other designs discussed here include an alternate baseline design which uses a NaK-cooled condenser with a conduction fin radiator, and baseline design variants of 200 kWe and 400 kWe output.

2.7.1 BASELINE SYSTEM DESIGN

The baseline design cycle conditions are given in Figure 2-89, the fluid system schematic diagram is shown in Figure 2-90, and the spacecraft inboard profile is shown in Figure 2-91. Table 2-47 gives the weight summary and breakdown for the baseline design spacecraft. The detailed design parameters for the baseline design MHD generator are in Tables 2-14, 2-15 and 2-16, which are presented in Section 2.5.2.

2.7.1.1 Arrangement

The arrangement of the baseline design spacecraft is based on Configuration No. 4 discussed in Section 2.4.4. The reactor and the payload are situated at opposite ends of the spacecraft to minimize shielding; the narrow angle radiation shield is located immediately beneath the reactor.

2.7.1.1.1 MHD Bay - The MHD power system equipment is located in a three-sided tapered bay (Figure 2-92) which extends from the bottom edges of the radiation shield; the surface panels of this bay and the surface panels of the radiation shield form continuous planes and provide sufficient area to reject the following loads to space:

- a. Neutron and gamma heating of the shield
- b. Dissipation losses from the excitation capacitors
- c. Winding losses from the MHD generator
- d. Heat transferred to the MHD generator stators from the MHD duct
- e. Miscellaneous heat loads from MHD equipment such as pumps and valves.

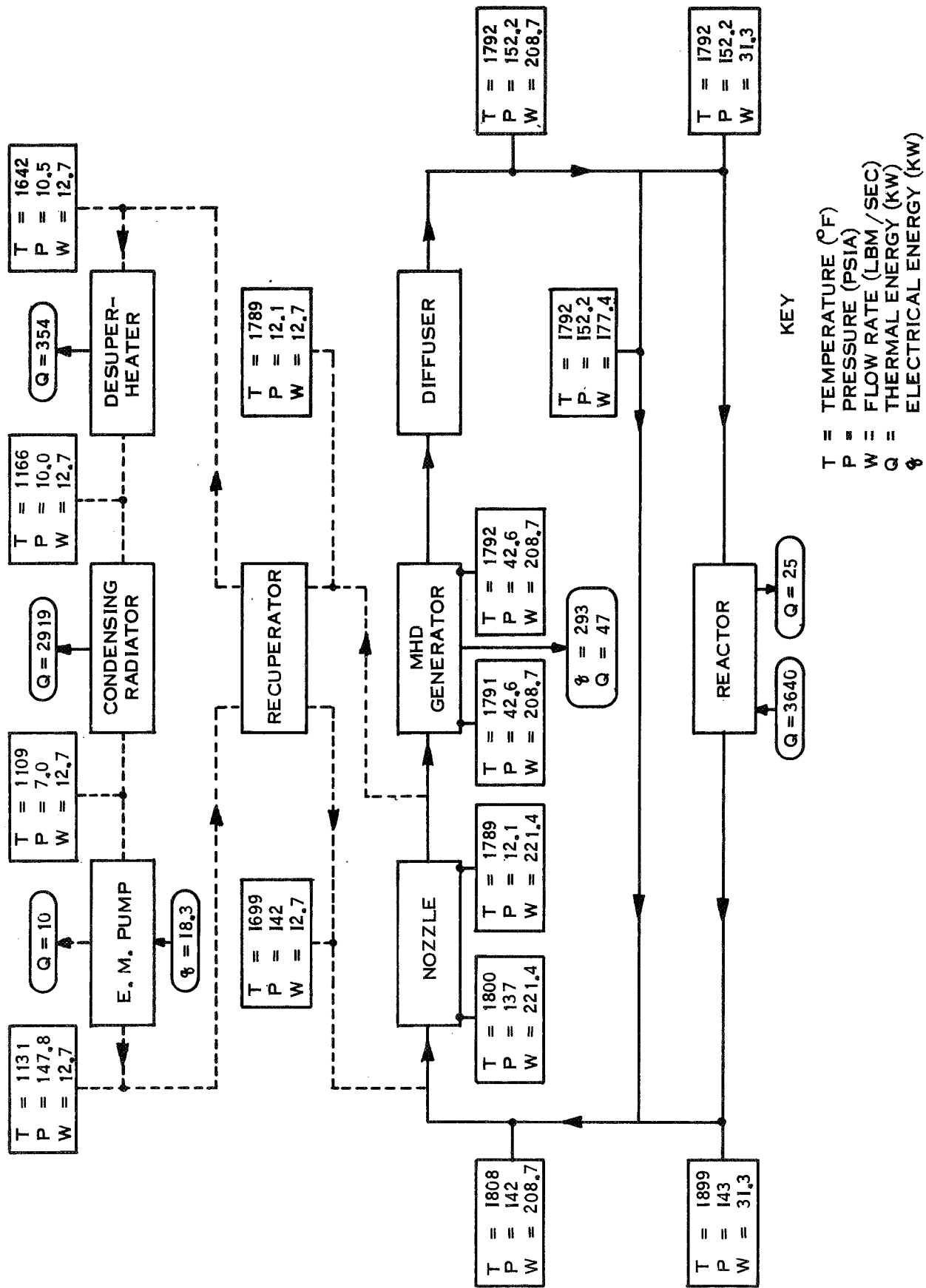


Figure 2-89. Cycle Conditions, MHD Power System Baseline Design

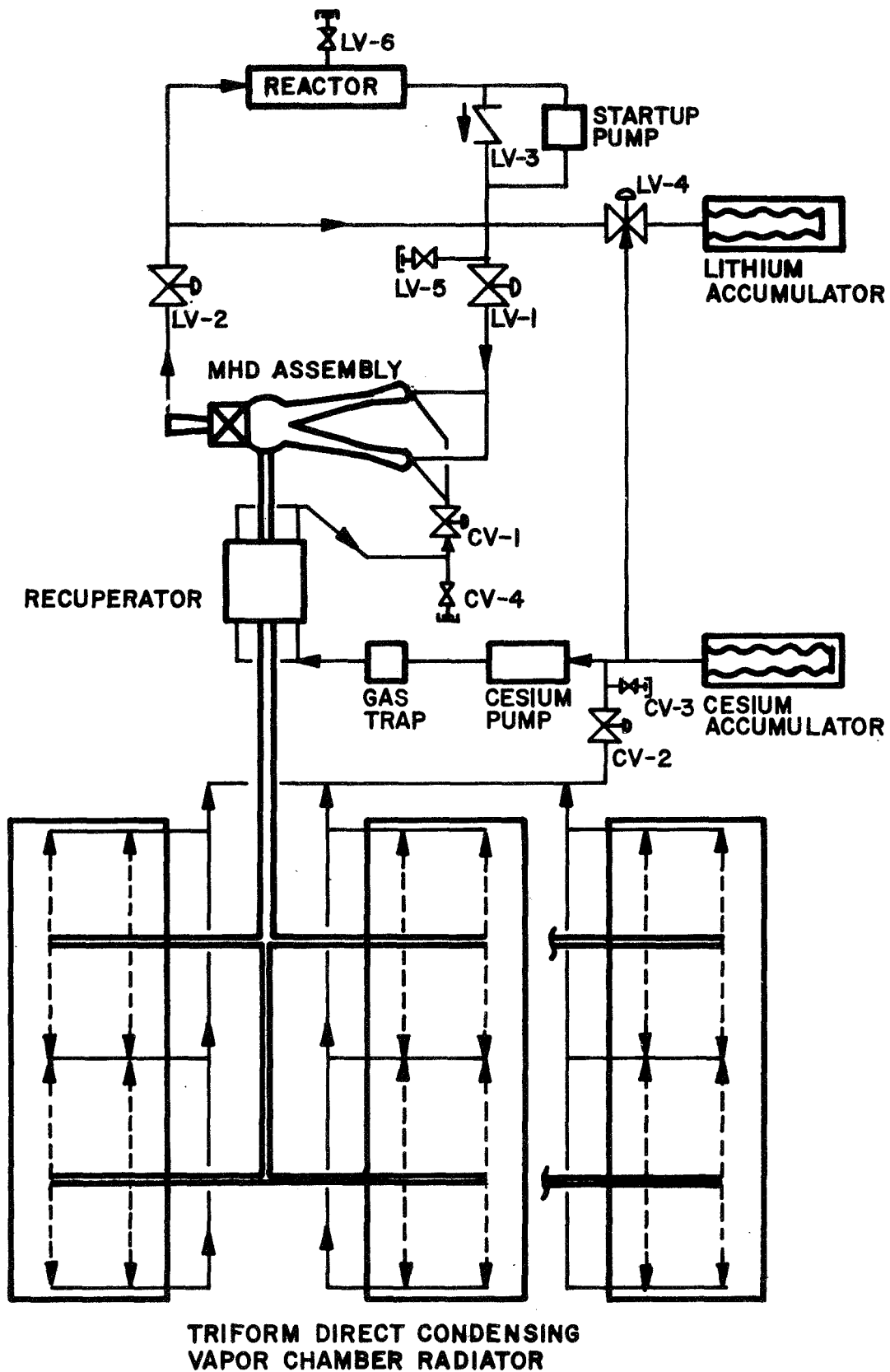
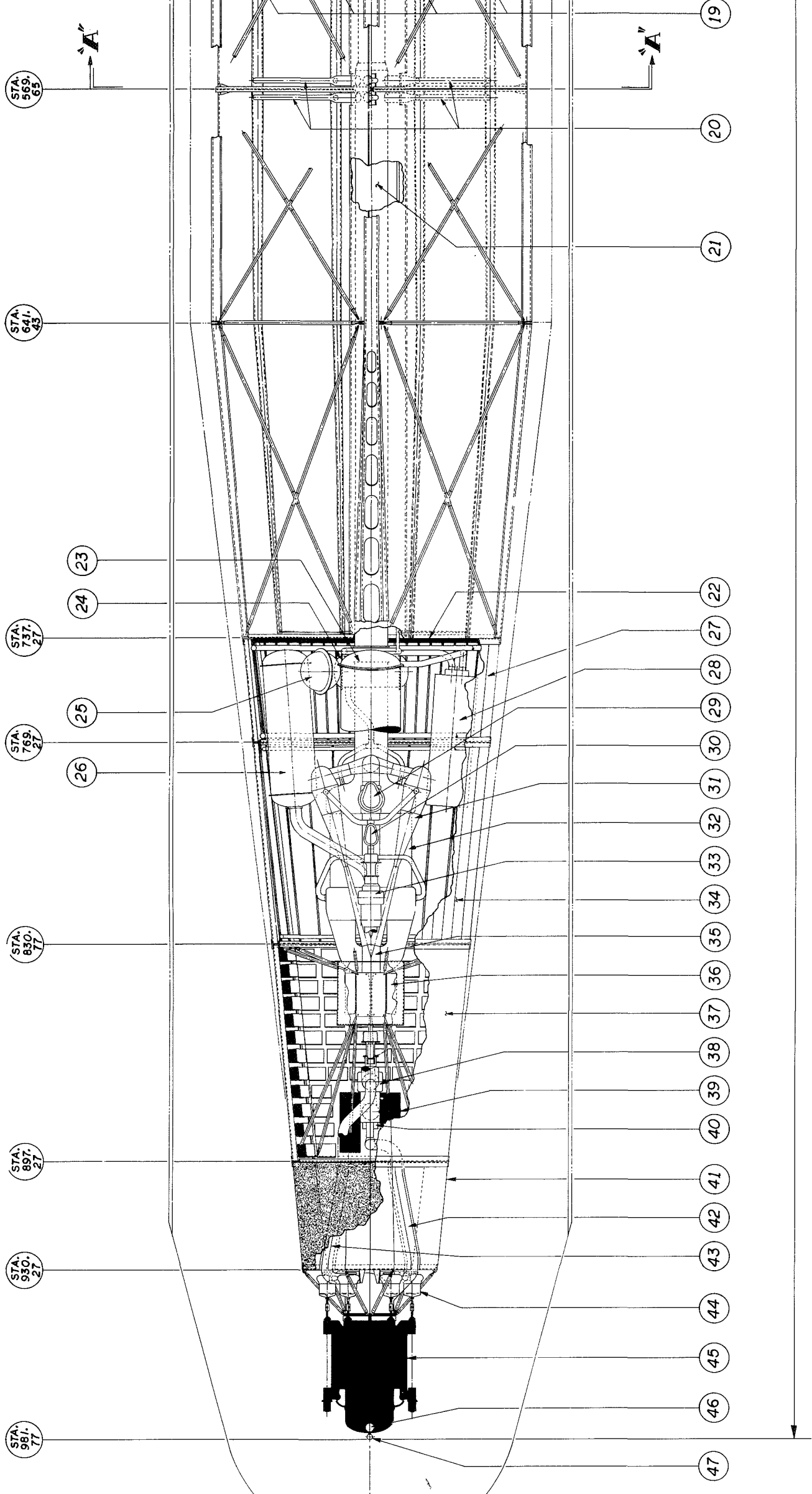
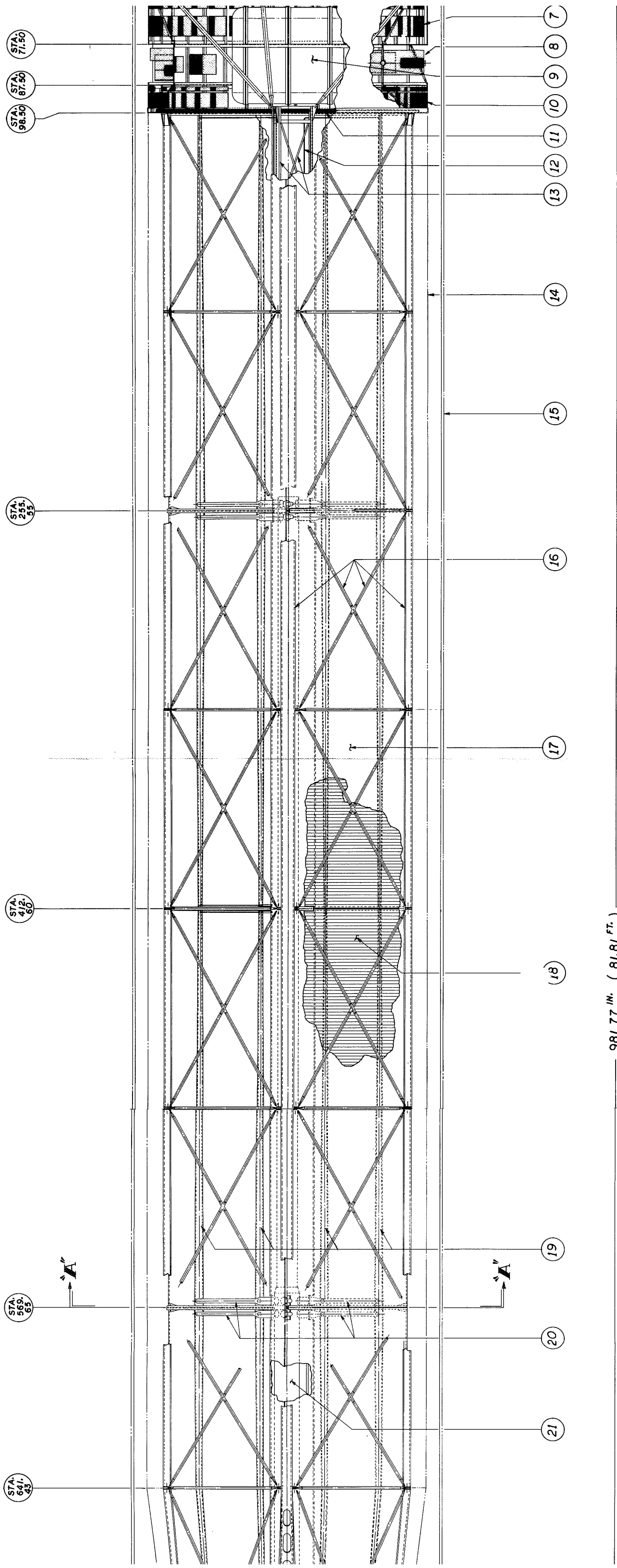


Figure 2-90. Fluid Schematic Diagram, MHD Power System



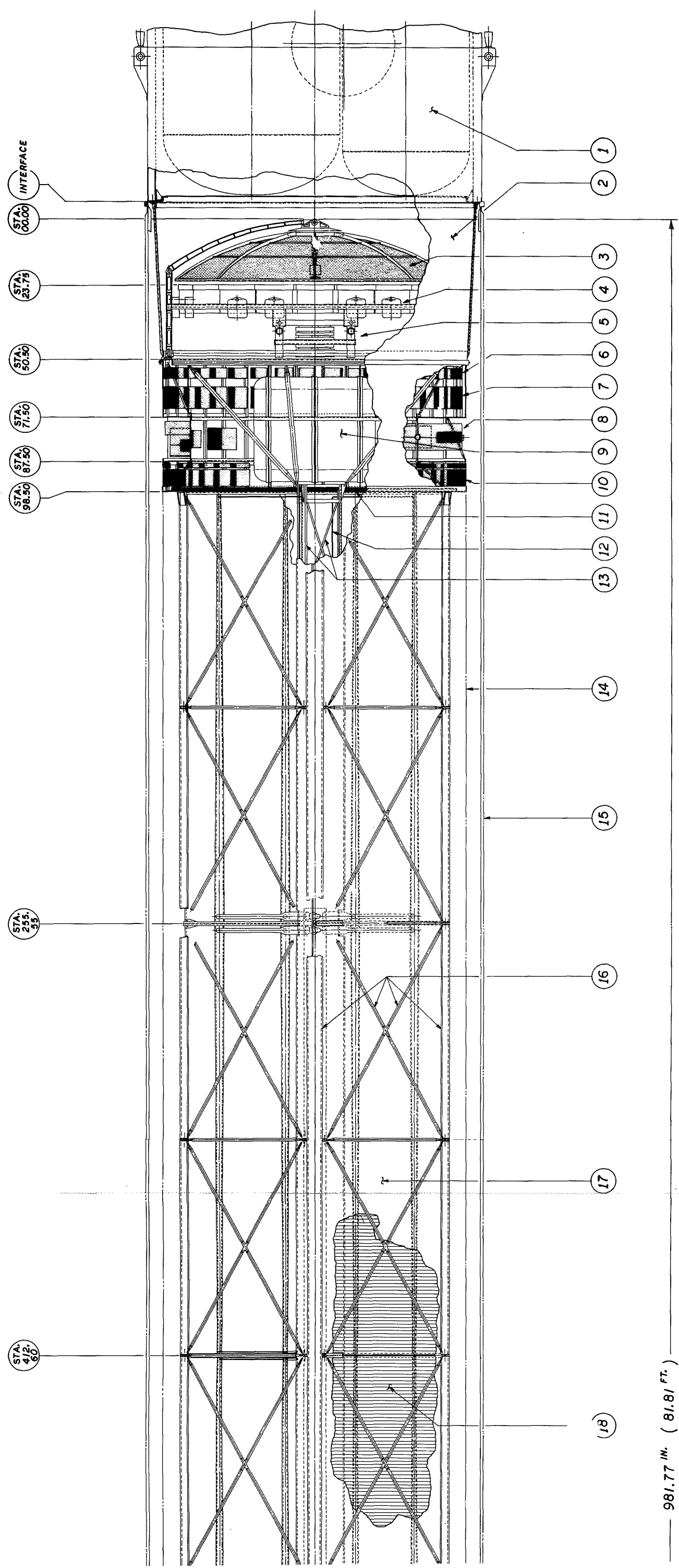
- | ITEM | DESCRIPTION |
|------|---|
| 1 | LAUNCH VEHICLE |
| 2 | PAYLOAD ADAPTER |
| 3 | COMMUNICATIONS ANTENNA |
| 4 | THRUSTER PLATFORM 37 MERCURY ION ENGINES |
| 5 | TVC SYSTEM |
| 6 | THRUSTER ISOLATION UNITS |
| 7 | SPECIAL THRUSTER POWER CONDITIONING UNITS |
| 8 | PAYLOAD EQUIPMENT BAY |
| 9 | MERCURY PROPELLANT TANKS |
| 10 | TRANSFORMER AND RECTIFIER BAY |
| 11 | THERMAL BULKHEAD - AFT |
| 12 | CESIUM RETURN LINES |
| 13 | RADIATOR CENTRAL TRUSS ASSEMBLY |
| 14 | SPACECRAFT PERIMETER ENVELOPE |
| 15 | FLIGHT FAIRING |
| 16 | DISPOSABLE LAUNCH SUPPORT STRUCTURE |
| 17 | VAPOR CHAMBER PANEL - 12 |
| 18 | VAPOR CHAMBERS |
| 19 | CESIUM CONDENSING DUCT - 24 |
| 20 | CESIUM VAPOR HEADERS |
| 21 | CESIUM VAPOR FEED DUCT |
| 22 | THERMAL BULKHEAD - FORWARD |
| 23 | CESIUM ACCUMULATOR |
| 24 | GAS TRAP |
| 25 | CONTROL GAS STORAGE TANK |
| 26 | LITHIUM ACCUMULATOR |
| 27 | HIGH TEMP. AUXILIARY RADIATOR |
| 28 | CESIUM PUMP |
| 29 | VALVE LV - 1 |
| 30 | VALVE CV - 1 |
| 31 | NOZZLE ASSEMBLY |
| 32 | RECUPERATOR |
| 33 | VALVE LV - 4 |
| 34 | LOW TEMP. AUXILIARY RADIATOR |
| 35 | SEPARATOR |
| 36 | MHD GENERATOR |
| 37 | EXCITATION CAPACITOR BAY |
| 38 | VALVE LV - 2 |
| 39 | BATTERIES |
| 40 | START UP PUMP |
| 41 | SHIELD ASSEMBLY |
| 42 | REACTOR OUTLET LINES |
| 43 | REACTOR INLET LINES |
| 44 | ACTUATORS |
| 45 | REACTOR |
| 46 | HEATING JACKET INLET |
| 47 | VALVE LV - 6 |
| 48 | VENTS AND DRAINS LV 5 CV 3 CV 4 |
| 49 | VALVE CV 2 |

2



240 KW_e(NET) MHD SPACECRAFT

Figure 2-91.



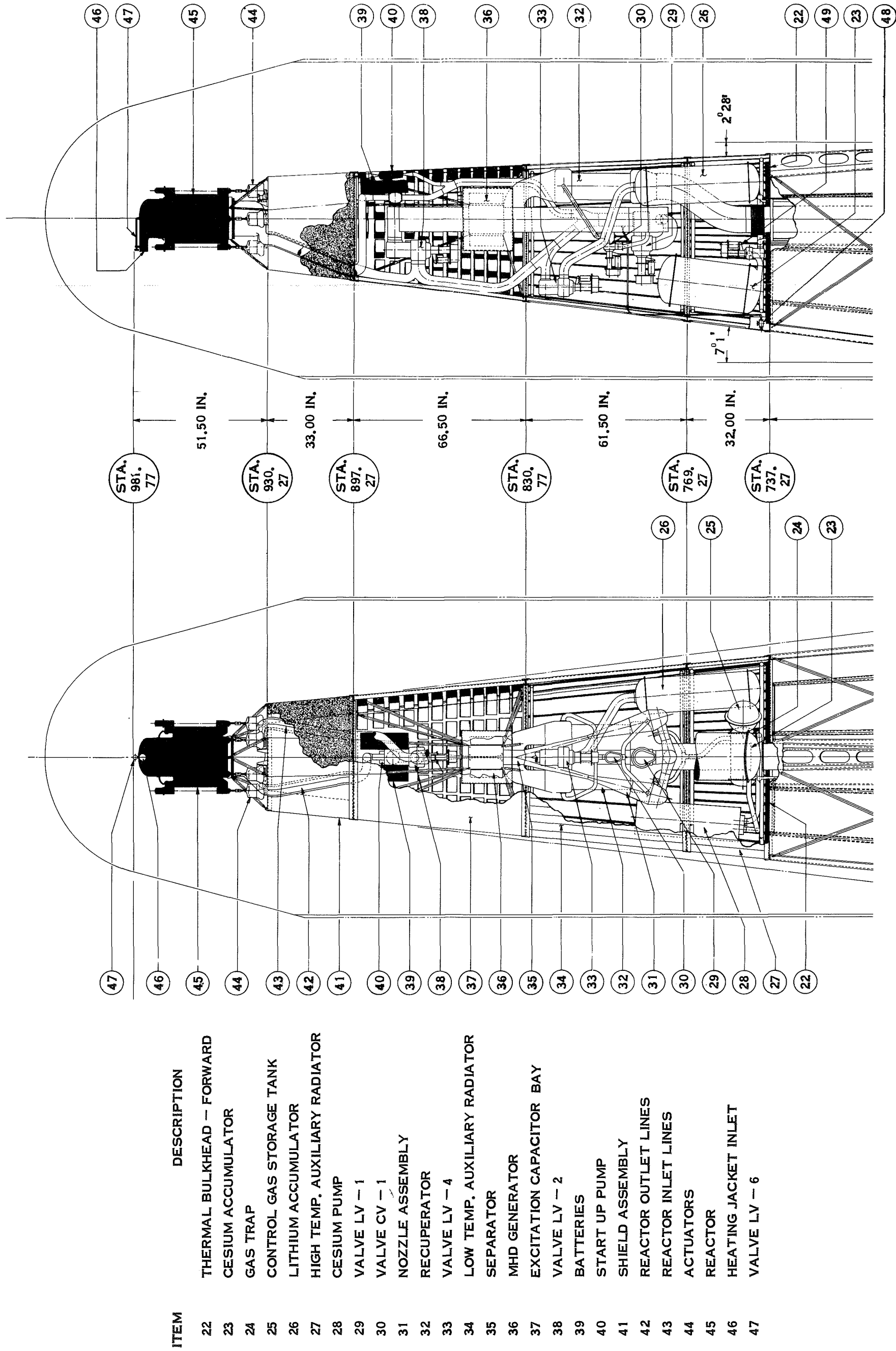
981.77 IN. (81.81 FT.)

40 KWe (NET) MHD SPACECRAFT

Figure 2-91. MHD Baseline Spacecraft, In-Board Profile

Table 2-47. MHD Baseline Spacecraft Weight Summary

Component		Weight - Pounds		
Propulsion System				18,140
Power Plant Subsystem			15,350	
Reactor Subsystem			2190	
Reactor Dry		2070		
Actuators		120		
Shield			1470	
Neutron		1470		
Permanent Gamma		None		
Power Conversion			7510	
Lithium Loop			550	
Piping	210			
Accumulator	130			
Valves (6)	50			
Startup E. M.				
Pump (1)	10			
Fluid	150			
MHD Flow Assembly			850	
Inlet Headers (2)	70			
Mixers (2)	20			
Nozzles (2)	470			
Separator	90			
MHD Duct	50			
Diffuser	150			
MHD Generator			840	
Stator Fe (2)	180			
Windings	660			
Cesium Loop			2130	
Piping	720			
Accumulator	60			
Valves (4)	20			
EM Pump	640			
Gas Trap	10			
Recuperator	400			
Fluid	280			
Main Radiator			2940	
Vapor Panels	1790			
Ducts and Piping	980			
Insul. Bulkheads	170			
Auxiliary Radiator			200	
Piping	60			
Pumps	20			
Fin Panels	110			
Coolant	10			
Electrical Power & Control System			2890	
Excitation System			930	
Capacitors	780			
Cabling	150			
Main Power Cond.			1480	
Transformers	740			
Rectifiers	10			
Filters	220			
Distr. Cabling	100			
Ass'y Hardware, Control Logic, Etc,	410			
Hotel Load			170	
Power Condit.	100			
Radiator	20			
Distr. Cabling	50			
Power Plant Control			70	
Startup Batteries			240	
Structure			1290	
Reactor Support	60			
Neutron Shield (ext)	120			
MHD Bay Structure	660			
Shell	220			
Internal	30			
Insulation	410			
Radiator Structure	450			
Internal Truss	160			
Bay Bulkheads	60			
Permanent External	230			
Thruster Subsystem			2790	
Ion Engine Subsystem			1235	
Ion Engine Units	585			
TVC Unit	550			
Miscellaneous	100			
Power Cond. Electron.			580	
Special Ion Eng. PC	270			
Thruster Isolation	310			
Power Cond. Radiators			890	
HV Power Supply	770			
Special Ion Engine Units	70			
Thruster Isolation	50			
High Voltage Power Cables			20	
3100 Volt Cables	5			
250 Volt Cables	15			
Structure			65	
Special PC Bay	65			
Propellant System				14,730
Propellant			14500	
Tanks & Distr.			220	
Structure			10	
Net Spacecraft				2340
Guidance & Control			50	
Communications			60	
Science			2,065	
Radiator			25	
Structure			35	
Gross Spacecraft in Earth Orbit			35,210	
Launch Vehicle Adapter			250	
Launch Shroud Payload Weight Penalty (4400 lb fairing)			1,060	
Disposable Structure Weight Penalty (2290 lb structure)			550	
Launch Vehicle Payload Requirement			37,070	



ITEM	DESCRIPTION
22	THERMAL BULKHEAD - FORWARD
23	CESIUM ACCUMULATOR
24	GAS TRAP
25	CONTROL GAS STORAGE TANK
26	LITHIUM ACCUMULATOR
27	HIGH TEMP. AUXILIARY RADIATOR
28	CESIUM PUMP
29	VALVE LV - 1
30	VALVE CV - 1
31	NOZZLE ASSEMBLY
32	RECUPERATOR
33	VALVE LV - 4
34	LOW TEMP. AUXILIARY RADIATOR
35	SEPARATOR
36	MHD GENERATOR
37	EXCITATION CAPACITOR BAY
38	VALVE LV - 2
39	BATTERIES
40	START UP PUMP
41	SHIELD ASSEMBLY
42	REACTOR OUTLET LINES
43	REACTOR INLET LINES
44	ACTUATORS
45	REACTOR
46	HEATING JACKET INLET
47	VALVE LV - 6

Figure 2-92. MHD Bay Arrangement

The shield surfaces are used only for passive cooling of the shield itself. The MHD bay surface is divided into three major sections; the uppermost section is used for mounting the excitation capacitors. The middle section is devoted to the auxiliary radiator which rejects MHD generator winding losses; the average temperature of this radiator is about 340^oF. The lowest section of the bay surface is devoted to the auxiliary radiator which rejects heat from the MHD stators pumps and valve motors; the average temperature of this radiator is about 800^oF. In addition, the surfaces of the MHD bay provide mounting, heat rejection, or access area from the following auxiliary equipment:

- a. Two startup battery sets (one for the lithium startup flow and one for auxiliary cooling startup flow)
- b. Storage tank and regulators for control gas used to pressurize lithium and cesium accumulators
- c. Valves for evacuating, filling and draining the lithium and cesium systems

To prevent excessive backheating of the excitation capacitors, batteries, gas tank, and auxiliary radiators, the ~1800^oF nozzle assembly and fluid equipment in the MHD bay is enveloped in a teepee-shaped envelope of multifoil insulation sized to hold heat leakage to approximately 20 watts per square foot at normal operating temperatures. The use of this overall insulation wrap eliminates the need for insulation on any of the individual pipes and equipment except the reactor and its feed and return lines connecting it to the MHD bay. The MHD bay insulation also runs across the bottom face of the MHD bay to prevent thermal interference with radiator operation. The multifoil insulation and skin of the MHD bay provides micrometeoroid impact protection for equipment in the bay.

The MHD nozzle assembly is arranged vertically in the bay and attached to the MHD stator blocks which are suspended on tubular trusses from the outside structure of the MHD bay at the shield interface. In this way, by making the basic structural attachments of both ends of the nozzle assembly to the stator blocks, the delicate MHD duct between the stator blocks is isolated from loads and given maximum support. Lateral supports at the stator blocks and at the nozzle inlets restrain the entire assembly. The structural supports for the MHD generator and nozzle assembly are assumed to be simple tubular trusses; no attempt was made to isolate vibrations induced by the high velocity two-phase flow in the nozzles.

The pressure recovery or lithium-pumping diffuser is mounted in the upper center of the MHD bay with its outlet line feeding through an isolation valve (LV-2) and branching into the reactor inlet line leaving the bay and the bypass line which swings down toward the inlet end of the nozzle assembly. The reactor return line enters high in the MHD bay and, feeding through a check valve (LV-3), combines with the bypass line to supply the lithium flow to the nozzles. A small dc electromagnetic pump is connected in bypass around the check valve, mounted at the surface of the MHD bay adjacent to the batteries which power it. This pump is used to circulate lithium through the reactor and the bypass line for system warmup.

The cesium condensate enters the MHD bay near the center of the bottom panel, three return pipes feeding a ring header. Flow from the header goes to the cesium pump, through the gas trap, and branches to feed cesium through the recuperator to the nozzle inlets. The two cesium lines between the recuperator and the nozzles are recombined briefly in order to use only one isolation valve in that location (CV-1). The other cesium isolation valve (CV-2) is located between the ring header and the pump suction.

The accumulators and the cesium pump are mounted to the outer shell of the MHD bay. The insulation envelope includes the accumulators, permitting them to be warmed up by the startup flow in the lithium bypass line. One arrangement fault which is still carried in the MHD bay design is that the lithium accumulator is mounted upside down, with its outlet pipe pointed toward the reactor. This means that the accumulator, once filled, cannot be drained. The most that could be done would be to maintain the lithium molten by circulating hot gas around the accumulator bellows. In a final spacecraft design, this accumulator should be inverted and the piping rerouted.

2.7.1.1.2 Radiator Assembly - The main radiator assembly is shown in Figure 2-91 and in section in Figure 2-63. The radiator is divided into four bays of equal area three of which are made up with rectangular panels a little less than 13 feet tall. The fourth and uppermost bay is somewhat taller, its greater height needed to compensate for the diagonal breakback of the panel's outer edge which is necessary to stay within the shield shadow. This shield angle was chosen as the one which resulted in minimum shield weight.

If the radiator bays are numbered 1 to 4 from top to bottom, the vapor inlets are located at the bottom of bays 1 and 3 and the tops of bays 2 and 4. Conversely, the condensate outlets are at the tops of bays 1 and 3 and the bottom of bays 2 and 4. In this way, during warmup or at operating temperature, the material in any plane normal to the spacecraft axis will be essentially isothermal and thermal stresses will be minimized. The vapor feed duct runs down inside the central truss, 10-inch diameter to the bottom of bay 1, and 8.5-inch diameter from there to the bottom of bay 3. There are three condensate return lines, one running inside each corner of the central truss.

The vapor chamber panels, each with two vertical condensing ducts, are mounted individually on studs protruding from the central truss. Of course, that area of the panel which overlaps the central truss does not view space and, consequently, rejects no heat. This configuration was chosen for three main reasons. First, the overlapping triangle center gives each panel an exposed radiating area equal to that it would have if it could run on a true radius line right to the spacecraft centerline; this keeps the radiator length to a minimum by maximizing radiating area per unit length. Secondly, this arrangement eliminates the need for separate micrometeoroid armor for the long vapor feed and condensate return lines, the radiator panels and trusswork serving instead. Third, this arrangement facilitates field assembly and test; individual panels can be shop fabricated and tested. They are assembled by bolting to the central truss and making field welds at the vapor and condensate headers. With the exception of the tapered panels in the top bay, all panels are identical and interchangeable; the three top panels are identical.

2.7.1.1.3 Spacecraft Lower Assembly - The spacecraft lower assembly is a compound cylindrical section which contains, in descending order, the main power transformers and rectifiers, the science and communications equipment, and the thruster system. The propellant is stored in two saddle tanks in this bay, and the deployable main antenna is tucked under the thrusters within the perimeter of the launch vehicle payload adapter. After reaching earth orbit, the adapter is jettisoned and the antenna moves out to one side clearing the thrusters.

The single phase transformers and rectifiers which are used to convert the output of each MHD generator phase were mounted here rather than in the MHD bay to minimize the weight near the top of the spacecraft, to enjoy the cooler environment of the lower assembly and to keep the rectifiers in a lower radiation environment for added reliability. This choice relies on the fact that high slot voltage (700 to 950 volts) permits separate connection for each slot to run the full length of the radiator without severe cable weight penalty. The cables are radiatively cooled, running in wireways in the permanent structures at the outside edges of the radiator panels.

2.7.2 ALTERNATE BASELINE DESIGN

In the baseline design described in the preceding section, the main radiator is a vapor fin direct condensing type. As is discussed in Section 2.5.5 of this report, there are serious design problems associated with a design of this sort. These problems include flow instabilities, and thermal shock at startup. A more conservative spacecraft design approach is to provide a NaK-cooled heat exchanger to condense the cesium vapor, using pumped circulation through a conduction fin radiator to cool the NaK. The alternate baseline design was therefore drawn up on this basis; the NaK-cooled condenser replacing the recuperator, and no other changes to the system except those necessitated by this change. Figure 2-93 is the fluid schematic diagram for this alternate system, Figure 2-94 shows the inboard profile of this spacecraft design, and Table 2-48 is a repetition of the baseline design weight summary marked with the changes associated with conversion to the alternate design. As Table 2-48 shows, the spacecraft weight goes up by only 2000 pounds, and that with the most conservative radiator type, the copper/stainless steel. The condenser is arranged in the spacecraft (see Figure 2-94) to minimize the cesium vapor pressure drop and thereby permit the highest possible NaK and radiator temperatures. This, in turn, minimizes radiator area and weight. There was another reason for locating the condenser, and the NaK pump as well, entirely within the MHD bay; this enhances the modularity of the system, thereby simplifying manufacture and test. The MHD bay, for example, can thus be tested by using only four fluid connections, the lithium inlet and outlet and the NaK inlet and outlet.

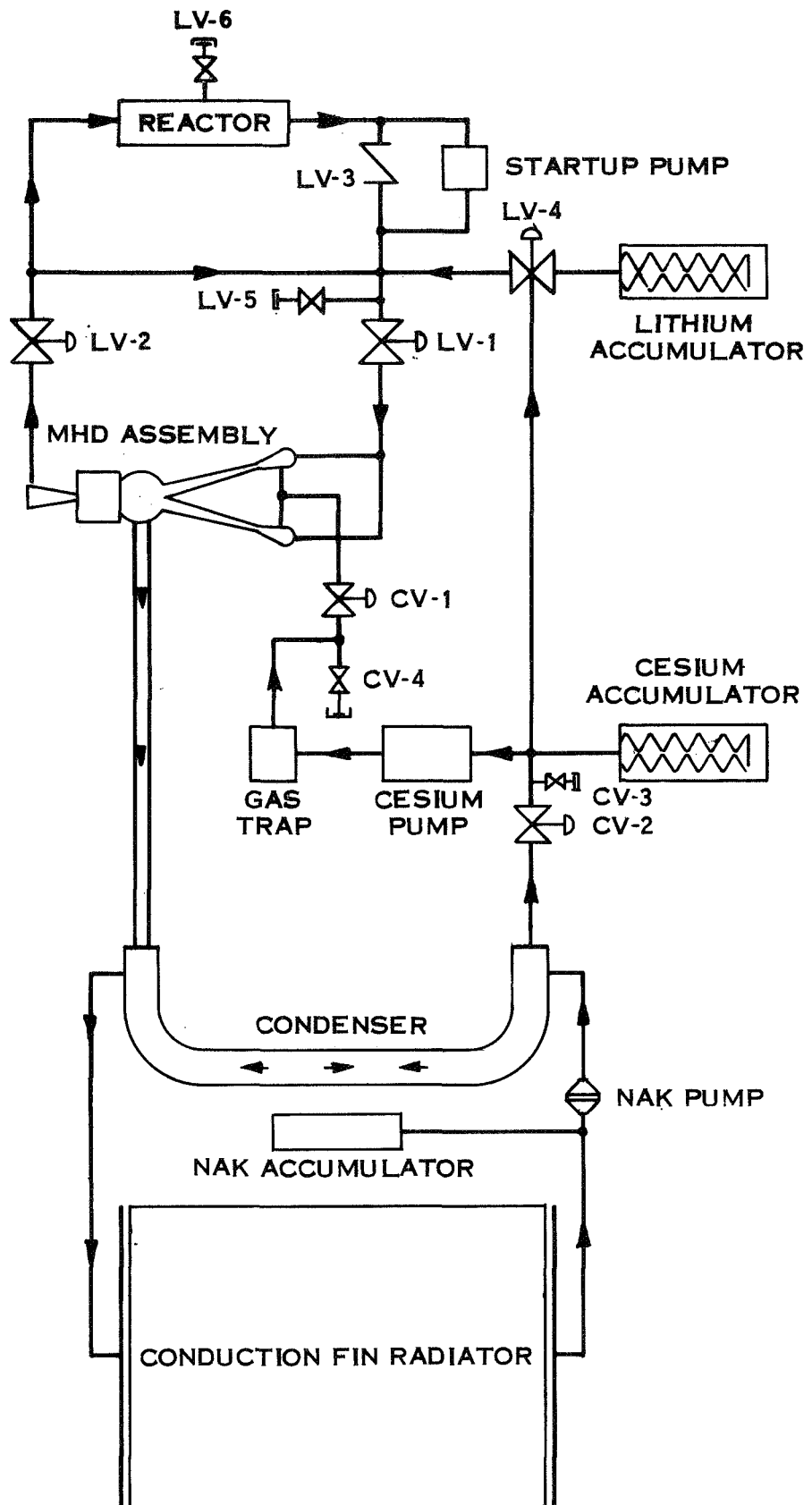
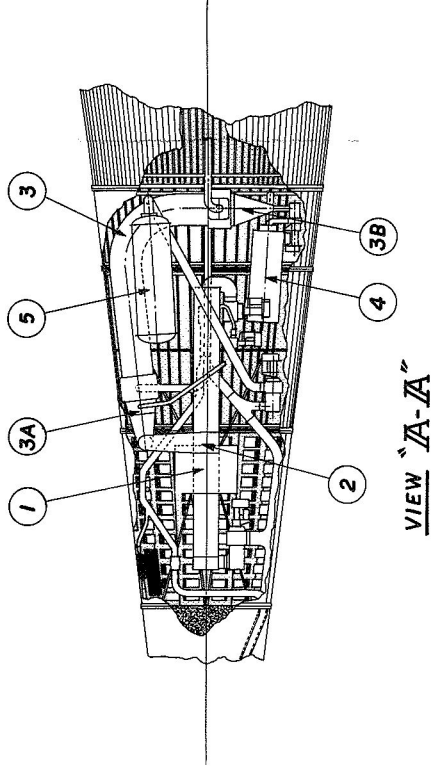


Figure 2-93. Fluid Schematic Diagram Alternate MHD Power System

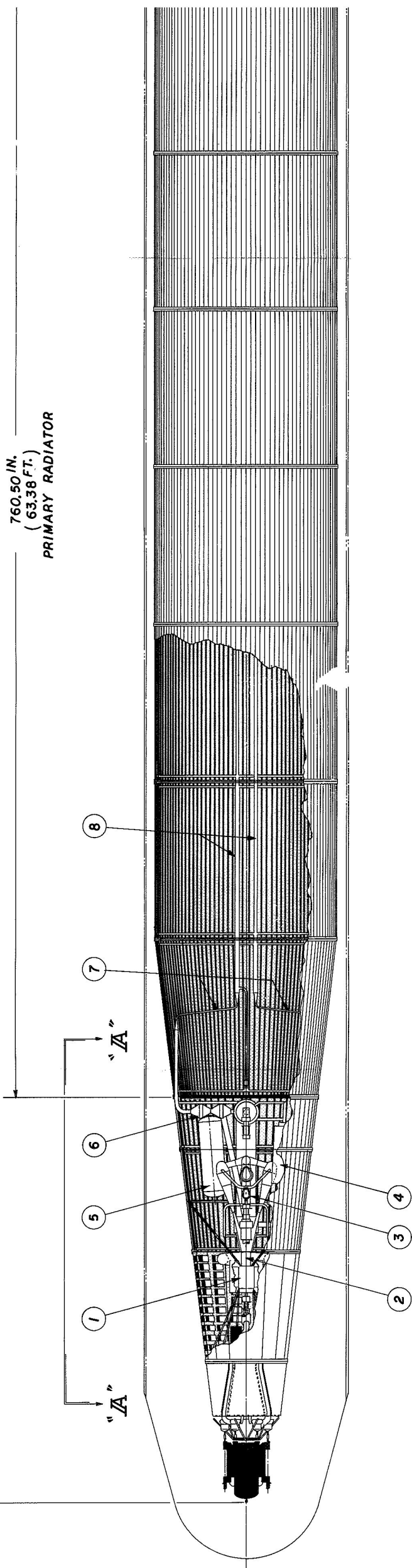


ITEM DESCRIPTION	
1	MHD GENERATOR
2	MHD NOZZLE ASSEMBLY
3	CONDENSER ASSEMBLY
3A	VAPOR INLET
3B	CONDENSATE OUTLET
4	CESIUM PUMP
5	CESIUM ACCUMULATOR
6	NAK PUMPS
7	POTENTIAL EXPANSION
8	RADIATOR FEED AND RETURN DUCTS

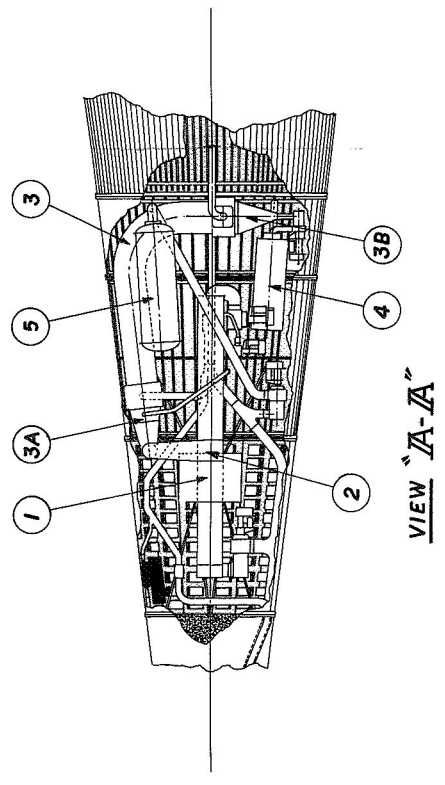
1103.50 IN.
(91.96 FT.)

OVERALL VEHICLE LENGTH

760.50 IN.
(63.38 FT.)
PRIMARY RADIATOR



2



ITEM DESCRIPTION	
1	MHD GENERATOR
2	MHD NOZZLE ASSEMBLY
3	CONDENSER ASSEMBLY
3A	VAPOR INLET
3B	CONDENSATE OUTLET
4	CESIUM PUMP
5	CESIUM ACCUMULATOR
6	NAK PUMPS
7	POTENTIAL EXPANSION
8	RADIATOR FEED AND RETURN DUCTS

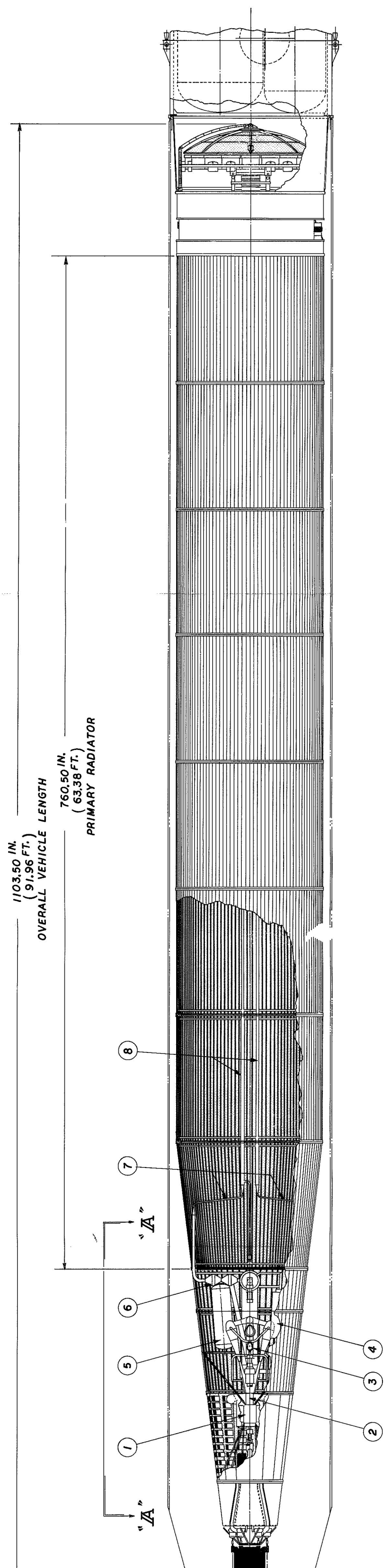


Figure 2-94. Inboard Profile, Alternate Baseline Design with Cylindrical Radiator

TABLE 2-48. MHD BASELINE SPACECRAFT WEIGHT SUMMARY CORRECTED FOR CONVERSION TO ALTERNATE DESIGN

Component	Weight - Pounds		
Propulsion System			18,140
Power Plant Subsystem			15,350
Reactor Subsystem	2220	2190	+150
Reactor Dry	2070		
Actuators	120		
Shield	1840	1470	+370
Neutron	1470		
Permanent Gamma	None		
Power Conversion		7510	
Lithium Loop	550		
Piping	210		
Accumulator	130		
Valves (6)	50		
Startup E. M. Pump (1)	10		
Fluid	150		
MHD Flow Assembly		850	
Inlet Headers (2)	70		
Mixers (2)	20		
Nozzles (2)	470		
Separator	90		
MHD Duct	50		
Diffuser	150		
MHD Generator		840	
Stator Fe (2)	180		
Windings	660		
Cesium Loop	40	2130	-850
Piping	720		
Accumulator	60		
Valves (4)	20		
EM Pump	640		
Gas Trap	10		
Recuperator	400		
Fluid	280		
Main Radiator	4450	2940	+2470
Vapor Panels	1790		
Ducts and Piping	980		
Insul. Bulkheads	170		
Auxiliary Radiator		200	
Piping	60		
Pumps	20		
Fin Panels	110		
Coolant	10		
Electrical Power & Control System		2890	
Excitation System		930	
Capacitors	780		
Cabling	150		
Main Power Cond.		1480	
Transformers	740		
Rectifiers	10		
Filters	220		
Distr. Cabling	100		
Ass'y Hardware, Control Logic, Etc,	410		
Hotel Load		170	
Power Condit.	100		
Radiator	20		
Distr. Cabling	50		
Power Plant Control		70	
Startup Batteries		240	
Structure		1290	
Reactor Support		60	
Neutron Shield (ext)		120	
MHD Bay Structure		660	
Shell	220		
Internal	30		
Insulation	410		
Radiator Structure		450	-450
Internal Truss	160		
Bay Bulkheads	60		
Permanent External	230		
Thruster Subsystem			2790
Ion Engine Subsystem		1235	
Ion Engine Units	585		
TVC Unit	550		
Miscellaneous	100		
Power Cond. Electron.		580	
Special Ion Eng. PC	270		
Thruster Isolation	310		
Power Cond. Radiators		890	
HV Power Supply	770		
Special Ion Engine Units	70		
Thruster Isolation	50		
High Voltage Power Cables		20	
3100 Volt Cables	5		
250 Volt Cables	15		
Structure		65	
Special PC Bay	65		
Propellant System			14,730
Propellant			14500
Tanks & Distr.			220
Structure			10
Net Spacecraft			2340
Guidance & Control			50
Communications			60
Science			2,065
Radiator			25
Structure			35

Gross Spacecraft in Earth Orbit	35,210		
INCREASED POWER	+860	(13kW @ 66#/KW)	+860
Launch Vehicle Adapter	250		
Launch Shroud Payload Weight Penalty (4400 lb fairing)	1,060		
Disposable Structure Weight Penalty (2290 lb structure)	550		-550
Launch Vehicle Payload Requirement	37,070	39,070	Δ = +2000

The use of the conical/cylindrical radiator form offers the best structural shape but does require rounding out the radiation shield. If the radiator were made in a three-sided deltoid configuration as shown in Figure 2-95, the spacecraft would be lengthened by about 12 feet, but the radiation shield weight could be reduced by about 500 pounds. In addition, the flat panels might make the radiator easier to build and less expensive. Further analysis is required before one design could be chosen over the other.

2.7.2.2 Design Details

2.7.2.2.1 Condenser - The condenser to be used in the MHD system is shown in Figure 2-96 and its design characteristics are tabulated in Table 2-49. The design type selected promises maximum flow stability in zero-G operation with minimum fluid inventory changes as power is varied.

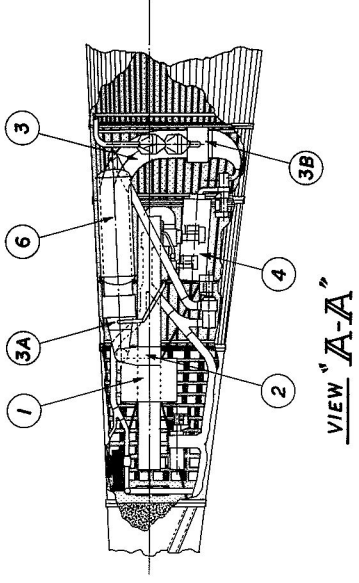
2.7.2.2.2 Separate NaK Heat Rejection Loop - The conditions of interest used to define the characteristics of the radiator with associated feed lines and pumps were:

1. Heat rejection rate = 3530 kW (system using no recuperator)
2. NaK coolant conditions:
 - Flow rate = 82.5 lb/sec
 - Maximum temperature = 1180^oF
 - Temperature drop = 200^oF
3. Condenser ΔP = 1.65 psi

A copper-stainless steel radiator model developed for the Thermionic Spacecraft Study (Reference 10) was used to estimate the radiator characteristics, which are:

1. An area of 1800 square feet
2. A weight of 4450 pounds
3. A coolant pressure drop of 2.9 psi

The optimum radiator feed line size was determined by computing the total equivalent weight per foot of pipe length as a function of pipe diameter. The total equivalent weight of the pipe is the sum of its actual weight and the weight equivalent of the required pumping power. Figure 2-97 presents the variation of actual weight, pumping power equivalent weight and total equivalent weight of piping, with pipe diameter, along with pertinent input conditions. As shown, the optimum feed line pipe diameter is 5.5 inches.

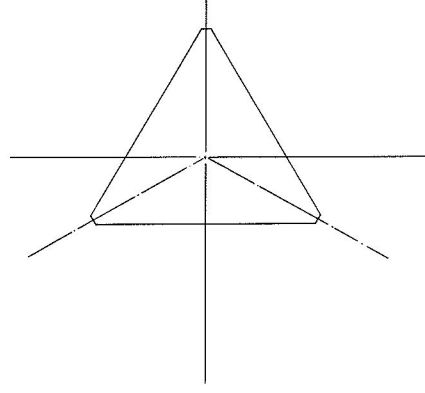
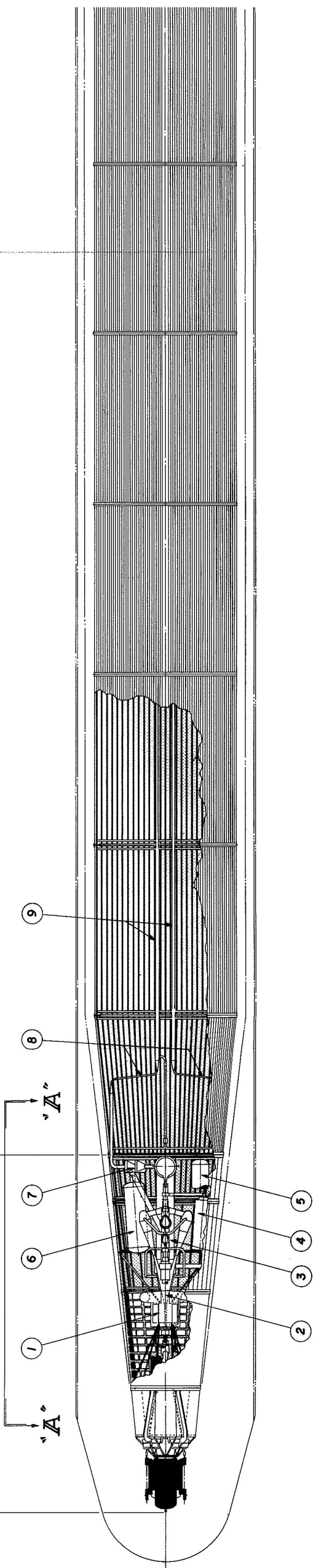


ITEM DESCRIPTION	
1	MHD GENERATOR
2	MHD NOZZLE ASSEMBLY
3	CONDENSER ASSEMBLY
3A	VAPOR INLET
3B	C. CONDENSATE OUTLET
4	CESIUM PUMP
5	LITHIUM ACCUMULATOR
6	CESIUM ACCUMULATOR
7	NAK PUMPS
8	DIFFERENTIAL EXPANSION COMPENSATION
9	RADIATOR FEED AND RETURN DUCTS

1252.36 IN.
(104.36 FT.)

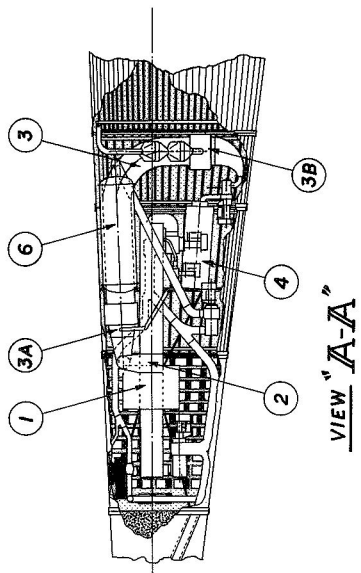
OVERALL VEHICLE LENGTH
909.36 IN.
(75.78 FT.)

PRIMARY RADIATOR



2

ITEM DESCRIPTION
1 MHD GENERATOR
2 MHD NOZZLE ASSEMBLY
3 CONDENSER ASSEMBLY
3A C. VAPOR INLET
3B C. CONDENSATE OUTLET
4 CESIUM PUMP
5 CESIUM ACCUMULATOR
6 LITHIUM ACCUMULATOR
7 NAK PUMPS
8 DIFFERENTIAL EXPANSION COMPENSATION
9 RADIATOR FEED AND RETURN DUCTS



1252.36 IN.
(104.36 FT.)

OVERALL VEHICLE LENGTH

909.36 IN.
(75.78 FT.)

PRIMARY RADIATOR

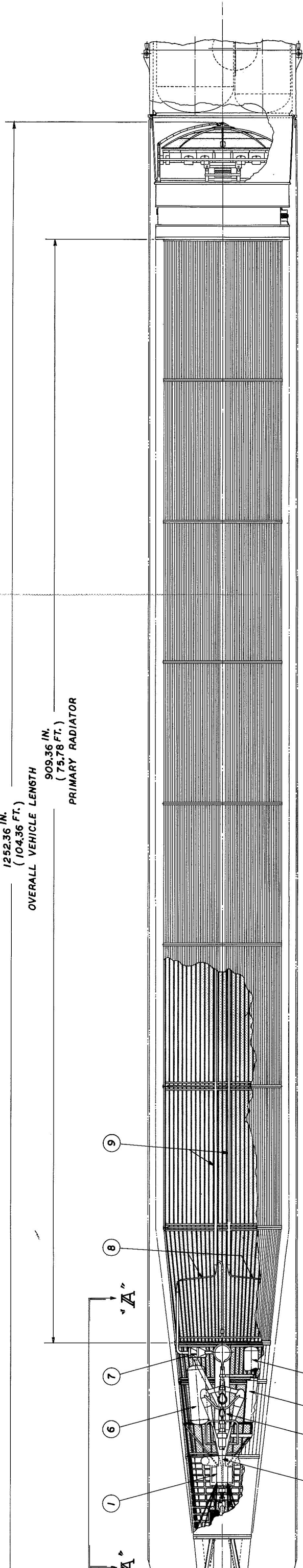


Figure 2-95. Inboard P Profile, Alternate Baseline Design with Tripanel Radiator

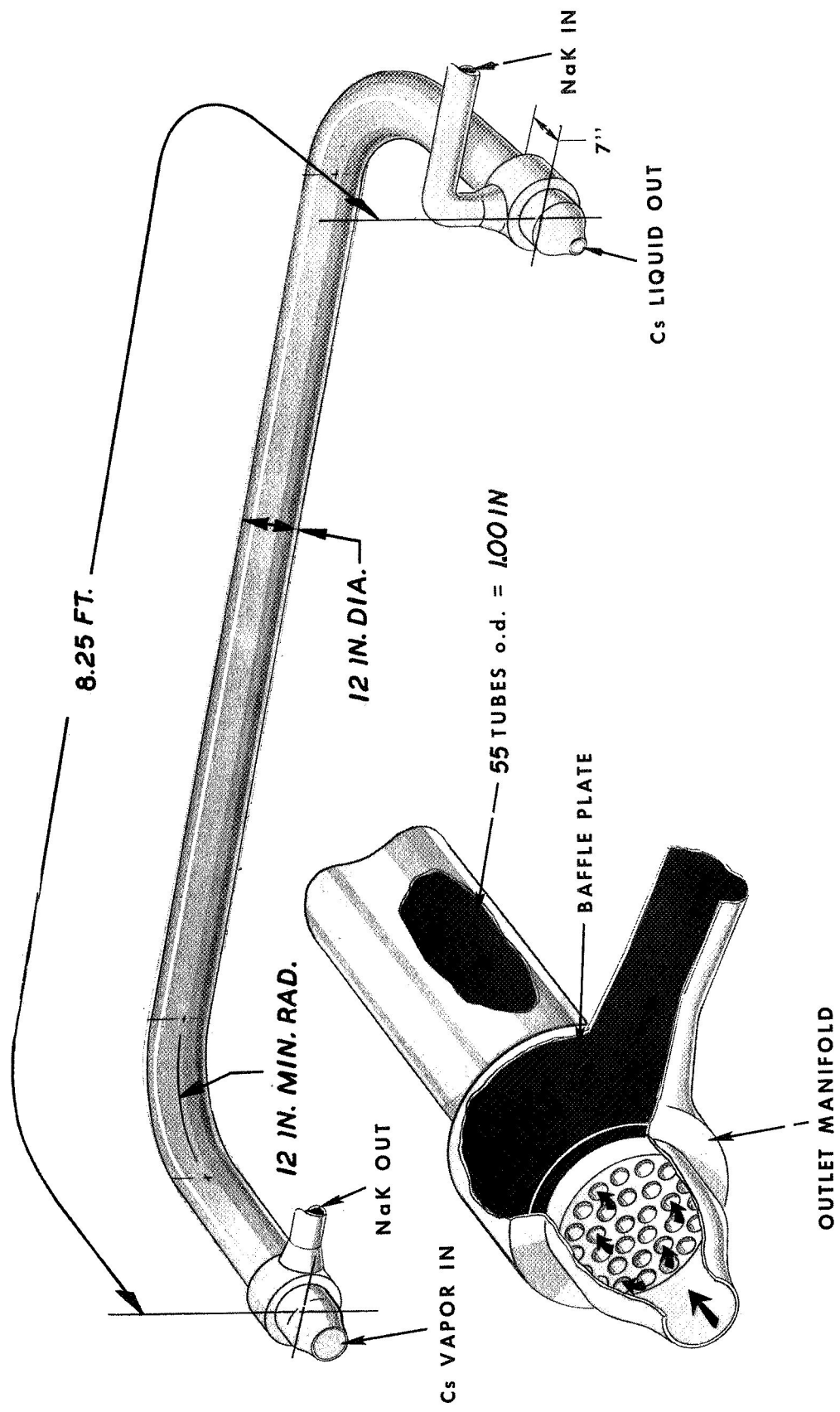


Figure 2-96. NaK-Cooled Cesium Condenser

TABLE 2-49. NaK-COOLED CESIUM CONDENSER DESIGN CHARACTERISTICS

Heat Load	3460 BTU/sec
Cesium Flow Rate	12.7 LBM/sec
Cesium Saturation Temperature	1200°F
Cesium Inlet Temperature	1800°F
Inlet Vapor Velocity	725 ft/sec
Number of Tubes	55
Condenser Tube O.D.	1.0 inch
Tube Wall Thickness	0.030 inch
Pitch to Diameter Ratio	1.5
Tube Matrix Geometry	Equilateral Triangular Arrangement
Shell Minimum I.D.	11.65 inches
Shell Wall Thickness	0.090 inch
ΔT_{NaK}	200°F
$\Delta T_{pinch\ point}$	20°F
NaK Average Temperature	1100°F
Required Condensing Length	6.25 feet
Total Length	8.25 feet
Overall Heat Transfer Coefficient	1770 BTU/hr ft ² °F
Cesium Side Total Pressure Drop	4.18 psi
NaK Side Total Pressure Drop	1.65 psi
Total Weight	400 lbs.

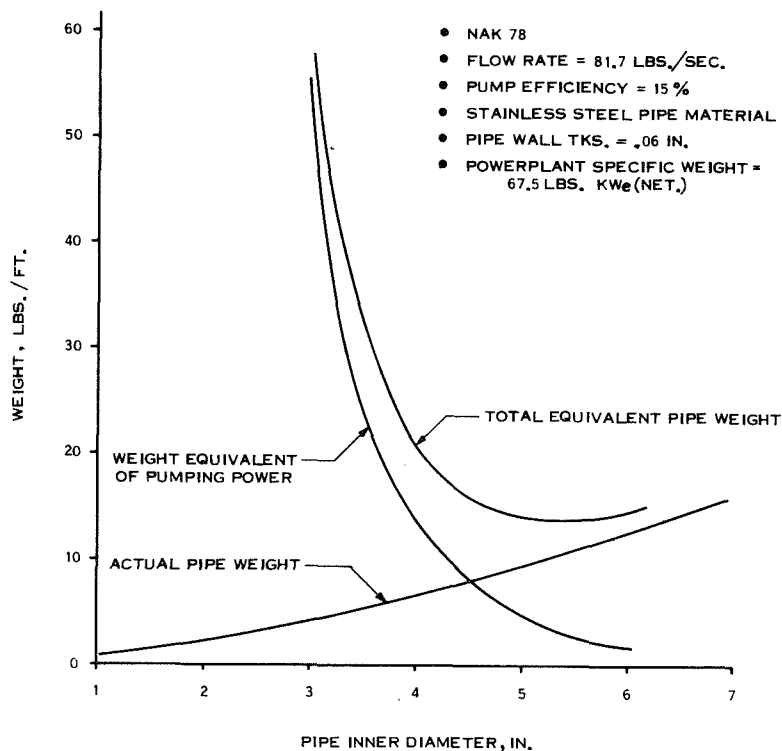


Figure 2-97. Equivalent Weight of Radiator Feed Pipe vs. Pipe Diameter

The total length of the radiator feed line is approximately 64 feet and its weight is 704 pounds. The pressure drop corresponding to the pipe length and diameter, and to the specified NaK flow rate, is 1.14 psi.

The total radiator loop pressure drop is the sum of the following ΔP increments:

- Condenser $\Delta P = 1.65$ psi
 - Radiator $\Delta P = 2.9$
 - Feed Line $\Delta P = \underline{1.14}$
- Total $\Delta P \quad 5.69$ psi

The required radiator loop pumping power, based on the above total ΔP and a pump efficiency of 15 percent, is 13 kW.

The weight of a dc EM pump providing the required NaK flow rate and pressure head was determined to be 90 pounds from the model developed in the Thermionic Spacecraft Study.

2.7.3 200 kWe SPACECRAFT

The cycle conditions for the 200 kWe power system are shown in Figure 2-98; the spacecraft is shown in Figure 2-99. This spacecraft is more than 16 feet shorter and about 3500 pounds lighter than the baseline design. Abbreviated weight summaries for the 200 kWe and baseline spacecraft are given in Tables 2-50 and 2-51. Note that about one-third of the reduction in propulsion system weight is in the reactor and main radiator weight reductions. The tendency of the weight of the rest of the system to be less responsive to reduction in power level is expected. Note that the reactor power level for the 200 kWe system, 2.6 MWt, from Figure 98, is nearing the point where reductions in reactor output would not reduce reactor size and weight. It is difficult to set the lower size limit without a firm reactor design, but a reactor of about 2 MWt rating is probably the minimum size.

The principal characteristics of the 200 kWe MHD generator are listed in Tables 2-52, 2-53, 2-54 and 2-55. The calculated weight of this 16.1 cm wide generator is 683 pounds, 545 pounds of copper and 138 pounds of iron. The weight optimization at this lower power level resulted in lower copper weight with higher coil losses because the outside surface area of the MHD bay provided almost 80 square feet for the coil cooling radiator, almost as much as in the baseline design.

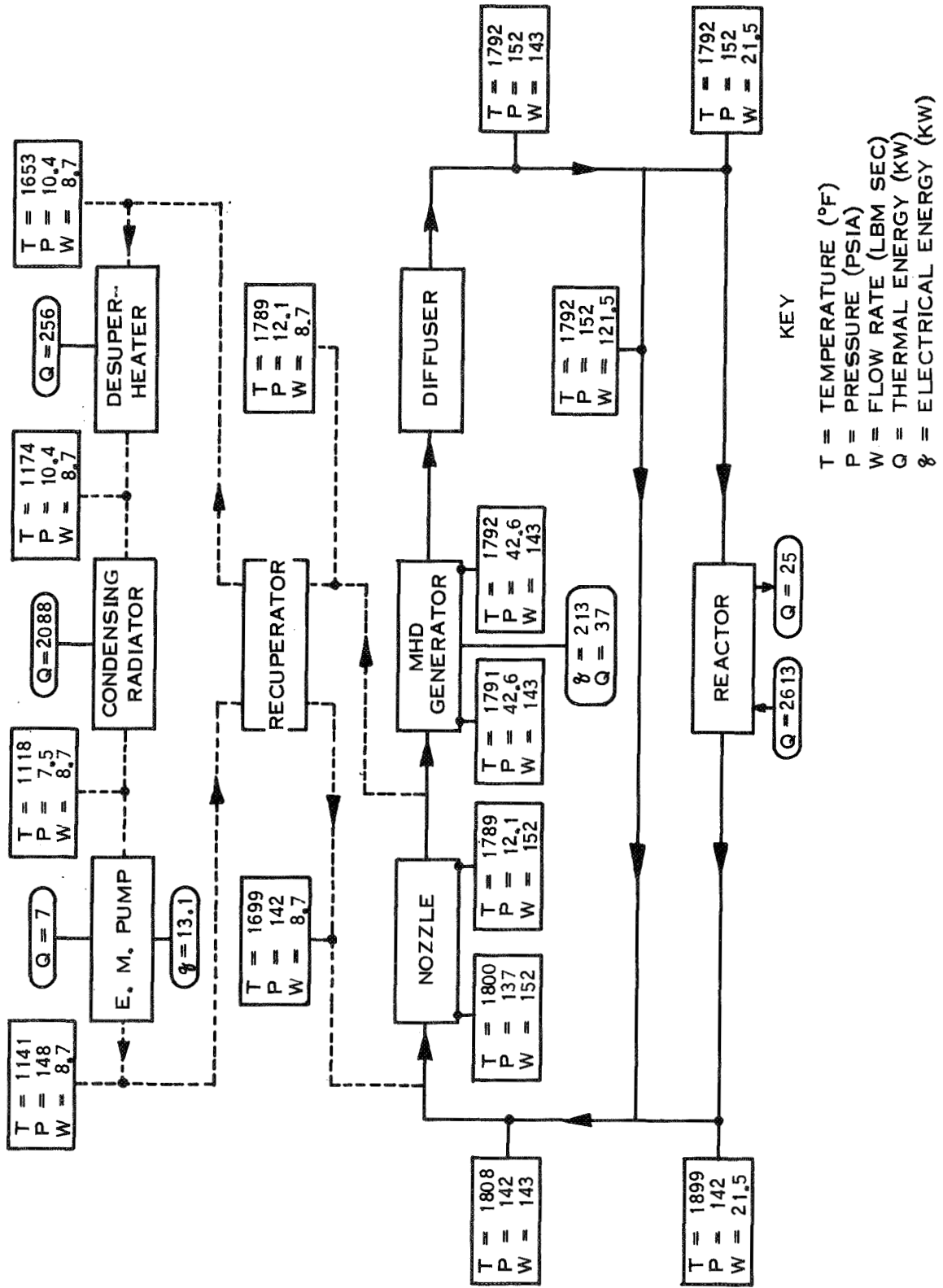


Figure 2-98. Cycle Conditions, 200 kWe MHD Power System

ITEM DESCRIPTION	
1	EXCITATION CAPACITOR BAY
2	LOW TEMP. AUXILIARY RADIATOR
3	HIGH TEMP. AUXILIARY RADIATOR
4	PRIMARY RADIATOR VAPOR CHAMBER

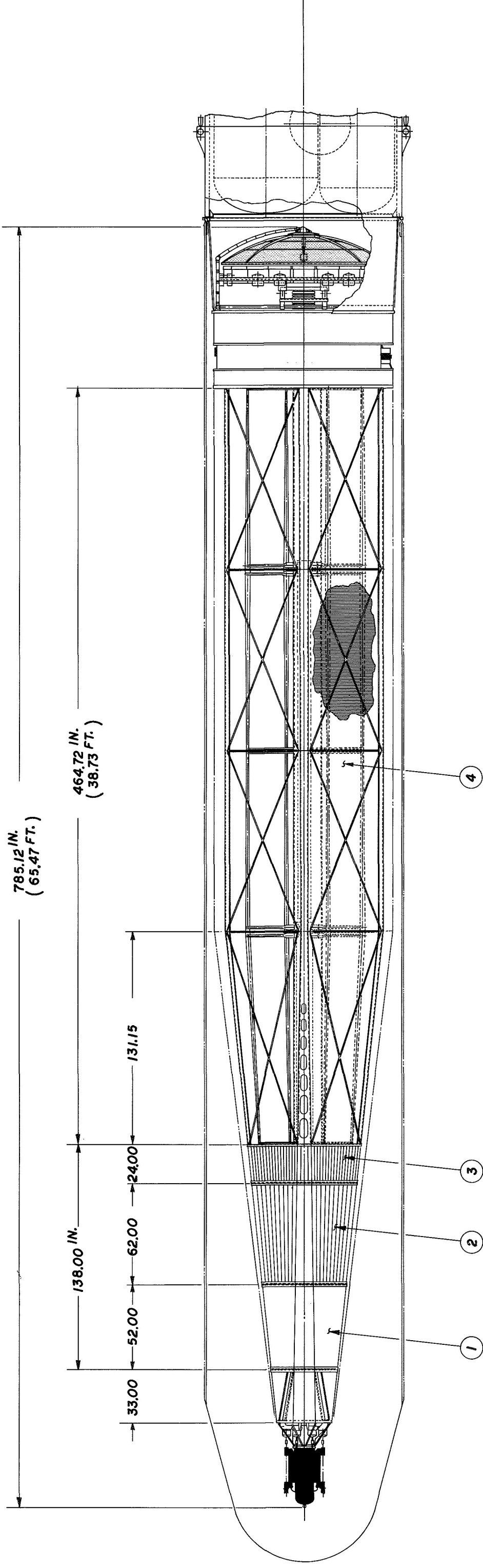


Figure 2-99. Inboard Profile, 200 kWe
MHD Spacecraft

TABLE 2-50. WEIGHTS - 200 kWe MHD SPACECRAFT

<u>ITEM</u>	<u>WEIGHT - LBS</u>
• PROPULSION SYSTEM	
• POWER SYSTEM	14,670
REACTOR	
SHIELD	1710
POWER CONVERSION	1390
GENERATOR	6150
LITHIUM LOOP	
MHD FLOW ASSEMBLY	
CESIUM LOOP	680
RADIATORS	530
ELECTRIC POWER & CONTROL SYSTEM	620
EXCITATION	1930
HOTEL LOAD POWER CONDITIONING	2390
MISCELLANEOUS	780
STRUCTURE & INSULATION	130
REACTOR & SHIELD	290
MHD BAY	130
MAIN RADIATOR	660
THRUSTER SYSTEM	320
ION ENGINES SUBSYSTEM	
MAIN POWER CONDITIONING	
ELECTRONICS, RADIATORS, ETC.	
• PROPELLANT & TANKAGE	10,800
• NET SPACECRAFT	2,340
SCIENCE	
OTHER	
• INITIAL MASS IN EARTH ORBIT	27,810

TABLE 2-51. WEIGHTS - MHD BASELINE DESIGN SPACECRAFT

<u>ITEM</u>	<u>WEIGHT - LBS</u>
•PROPULSION SYSTEM	18, 140
• POWER SYSTEM	13, 870
REACTOR	2190
SHIELD	1470
POWER CONVERSION	7510
GENERATOR	840
LITHIUM LOOP	550
MHD FLOW ASSEMBLY	850
CESIUM LOOP	2130
RADIATORS	3140
ELECTRIC POWER & CONTROL SYSTEM	1410
EXCITATION	930
HOTEL LOAD POWER CONDITIONING	170
MISCELLANEOUS	310
STRUCTURE & INSULATION	1290
REACTOR & SHIELD	180
MHD BAY	660
MAIN RADIATOR	450
•THRUSTER SYSTEM	4, 270
ION ENGINES SUBSYSTEM	1235
MAIN POWER CONDITIONING	1480
ELECTRONICS, RADIATORS, ETC.	1555
•PROPELLANT & TANKAGE	14, 730
•NET SPACECRAFT	2, 340
SCIENCE	2065
OTHER	275
•INITIAL MASS IN EARTH ORBIT	35, 210

TABLE 2-52. 200 kWe MHD GENERATOR DIMENSIONS

Slot No.	Distance from Beginning of Travelling Wave Region (cm)	Flow Channel Height at Slot Pole Piece (cm)	Width of Slot at Widest Point Neat Point Piece (cm)	Width of Slot at Narrowest Point, Opposite Pole Piece (cm)
0	0.00	0.843	3.212	3.212
1	1.40	0.865	1.831	1.342
2	2.77	0.888	1.778	1.278
3	4.11	0.912	1.725	1.213
4	5.43	0.936	1.672	1.147
5	6.72	0.960	1.619	1.080
6	7.99	0.985	1.567	1.012
7	9.22	1.011	1.514	0.944
8	10.43	1.038	1.462	0.874
9	11.62	1.064	1.410	0.804
10	12.77	1.092	1.360	0.735
11	13.90	1.120	1.310	0.664
12	15.00	1.149	1.261	0.594
13	16.08	1.178	1.212	0.525
14	17.13	1.208	1.165	0.456
15	18.16	1.239	1.118	0.389
16	19.16	1.270	1.073	0.323
17	20.14	1.302	1.029	0.260
18	21.09	1.335	0.985	0.200
19	22.02	1.368	0.943	0.145
20	22.93	1.403	0.901	0.095
21	23.82	1.438	0.861	0.053
22	24.69	1.473	3.212	3.212
Slot Depth			=	6.60 cm
Wall Thickness (Stator-to-Fluid)			=	0.4 cm
Li Channel Width			=	16.1 cm
<u>Compensating Pole</u>	<u>Length (cm)</u>	<u>Duct Avg. Height (cm)</u>	<u>No. of Vanes</u>	
Upstream	3.21	1.94	14	
Downstream	3.21	1.69	23	

TABLE 2-53. 200 kWe MHD GENERATOR DYNAMIC CHARACTERISTICS

Slot No.	Slip	Fluid Velocity (M/sec)	Wave Velocity (M/sec)	Field Strength (TESLA)
0	0.202	114.61	95.32	0.470
1	0.194	111.65	93.53	0.479
2	0.184	108.77	91.75	0.488
3	0.178	105.97	90.00	0.498
4	0.170	103.25	88.26	0.508
5	0.162	100.61	86.54	0.518
6	0.155	98.04	84.85	0.528
7	0.149	95.54	83.18	0.539
8	0.142	93.11	81.53	0.550
9	0.136	90.76	79.90	0.561
10	0.130	88.47	78.30	0.572
11	0.124	86.25	76.72	0.584
12	0.119	84.08	75.16	0.596
13	0.113	81.99	73.63	0.608
14	0.108	79.95	72.13	0.621
15	0.104	77.97	70.65	0.634
16	0.099	76.04	69.19	0.647
17	0.095	74.17	67.76	0.661
18	0.090	72.36	66.36	0.675
19	0.086	70.59	64.98	0.689
20	0.083	68.88	63.62	0.704
21	0.079	67.21	62.29	0.719
22	0.075	65.58	60.98	0.735

TABLE 2-54. 200 kWe MHD GENERATOR POWER SUMMARY

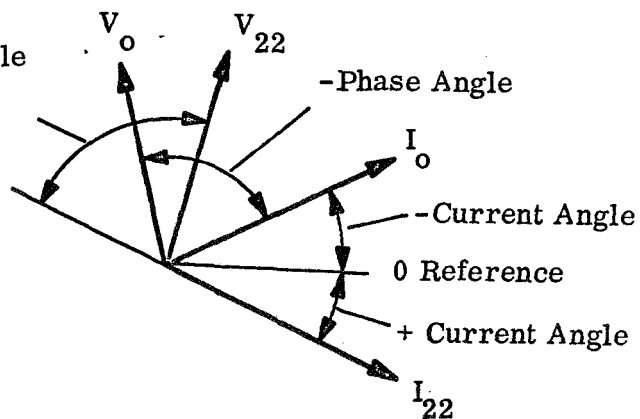
Sector	Input Power (Kinetic Energy) (kW)	Winding Loss (kW)	Net Power (kW)	Reactive Power (KVA)
0	11.56	1.44	-57.06	211.68
1	22.10	0.18	13.60	36.06
2	20.94	0.18	13.02	35.85
3	19.84	0.19	12.45	35.68
4	18.79	0.20	11.88	35.52
5	17.79	0.20	11.32	35.40
6	16.85	0.22	10.77	35.30
7	15.96	0.23	10.22	35.22
8	15.11	0.24	9.69	35.17
9	14.30	0.26	9.16	35.12
10	13.54	0.28	8.66	35.13
11	12.82	0.30	8.16	35.14
12	12.14	0.33	7.66	35.16
13	11.50	0.36	7.18	35.21
14	10.90	0.39	6.71	35.28
15	10.32	0.43	6.25	35.36
16	9.78	0.48	5.79	35.46
17	9.28	0.55	5.33	35.58
18	8.79	0.62	4.87	35.70
19	8.34	0.72	4.41	35.85
20	7.91	0.83	3.94	36.02
21	7.51	0.98	3.45	36.20
22	3.61	1.85	94.87	232.15
TOTAL	299.68	11.46	212.34	1189.26

TABLE 2-55. 200 kWe GENERATOR ELECTRICAL CHARACTERISTICS

Slot	Voltage (Volts)	Current (Amperes)	Current Angle* (Deg)	Phase Angle* (Deg)	Real Power (kW)	Reactive Power (KVAR)
0	597.4	366.96	-24.9	-74.9	-57.06	211.68
1	607.1	63.47	37.1	69.3	13.60	36.06
2	602.4	63.31	35.4	70.0	13.02	35.85
3	597.6	63.22	33.7	70.8	12.45	35.68
4	592.7	63.20	32.1	71.5	11.88	35.52
5	587.6	63.26	30.4	72.3	11.32	35.40
6	582.3	63.38	28.8	73.0	10.77	35.30
7	577.0	63.57	27.2	73.8	10.22	35.22
8	571.5	63.83	25.6	74.6	9.69	35.17
9	566.0	64.14	24.1	75.4	9.16	35.12
10	560.3	64.57	22.6	76.2	8.66	35.13
11	554.6	65.04	21.2	76.9	8.16	35.14
12	548.8	65.58	19.8	77.7	7.66	35.16
13	543.0	66.18	18.4	78.5	7.18	35.21
14	537.1	66.86	17.2	79.2	6.71	35.28
15	531.2	67.59	15.9	80.0	6.25	35.36
16	525.3	68.39	14.8	80.7	5.79	35.46
17	519.4	69.26	13.6	81.5	5.33	35.58
18	513.5	70.17	12.6	82.2	4.87	35.70
19	507.7	71.16	11.6	83.0	4.41	35.85
20	501.9	72.20	10.6	83.8	3.94	36.02
21	496.1	73.30	9.7	84.6	3.45	36.20
22	603.2	415.78	40.3	67.8	94.87	232.15
Total Power Generated					212.34	1189.26
Frequency: 314 Hz						

* Definition:

+ Phase Angle



The most noteworthy characteristic of the 200 kWe spacecraft is its compact size. Its 65-foot length could be handled in present launch facilities. However, with a net specific weight of 84 lb/kWe it may be difficult to compete with chemical propulsion for mission utility (see Section 2.8.2).

2.7.4 400 kWe SPACECRAFT

The cycle conditions for the 400 kWe power system are shown in Figure 2-100; the spacecraft is shown in Figure 2-101. This spacecraft is 30 feet longer and 6000 pounds heavier than the baseline design. An abbreviated weight summary is contained in Table 2-56; for comparison, the baseline spacecraft weights are given in Table 2-51. The reactor, power conversion system and structure all increase but note that the electrical system does not. The reason for this is that the excitation capacitor weight goes down with the higher voltage \sim 1000 volts ac average coil voltage versus \sim 800 volts ac in the baseline design.

The principal characteristics of the 400 kWe MHD generator are listed in Tables 2-57 through 2-60. The calculated weight of the 29.6 cm wide generator is 1353 pounds, 1067 pounds of copper and 286 pounds of iron. In order to avoid higher coil temperatures and higher coil weights, the coil cooling radiator in this design was expanded to an area twice as large as the one used in the baseline design.

The specific weight of the 400 kWe spacecraft is nominally 10 percent lower than the specific weight of the baseline spacecraft. At 60 lbs/kWe net a spacecraft of this size may be attractive for more ambitious payloads of several thousand pounds or more (see Section 2.8.2).

2.8 MISSION ENGINEERING

2.8.1 SPACECRAFT GUIDANCE AND CONTROL

A preliminary investigation of the guidance and control system has been completed. This investigation was concentrated mainly upon the control mechanism, of which four types were considered:

1. Cold gas jets
2. Hot gas jets
3. Ion engines
4. Momentum transfer devices (flywheels).

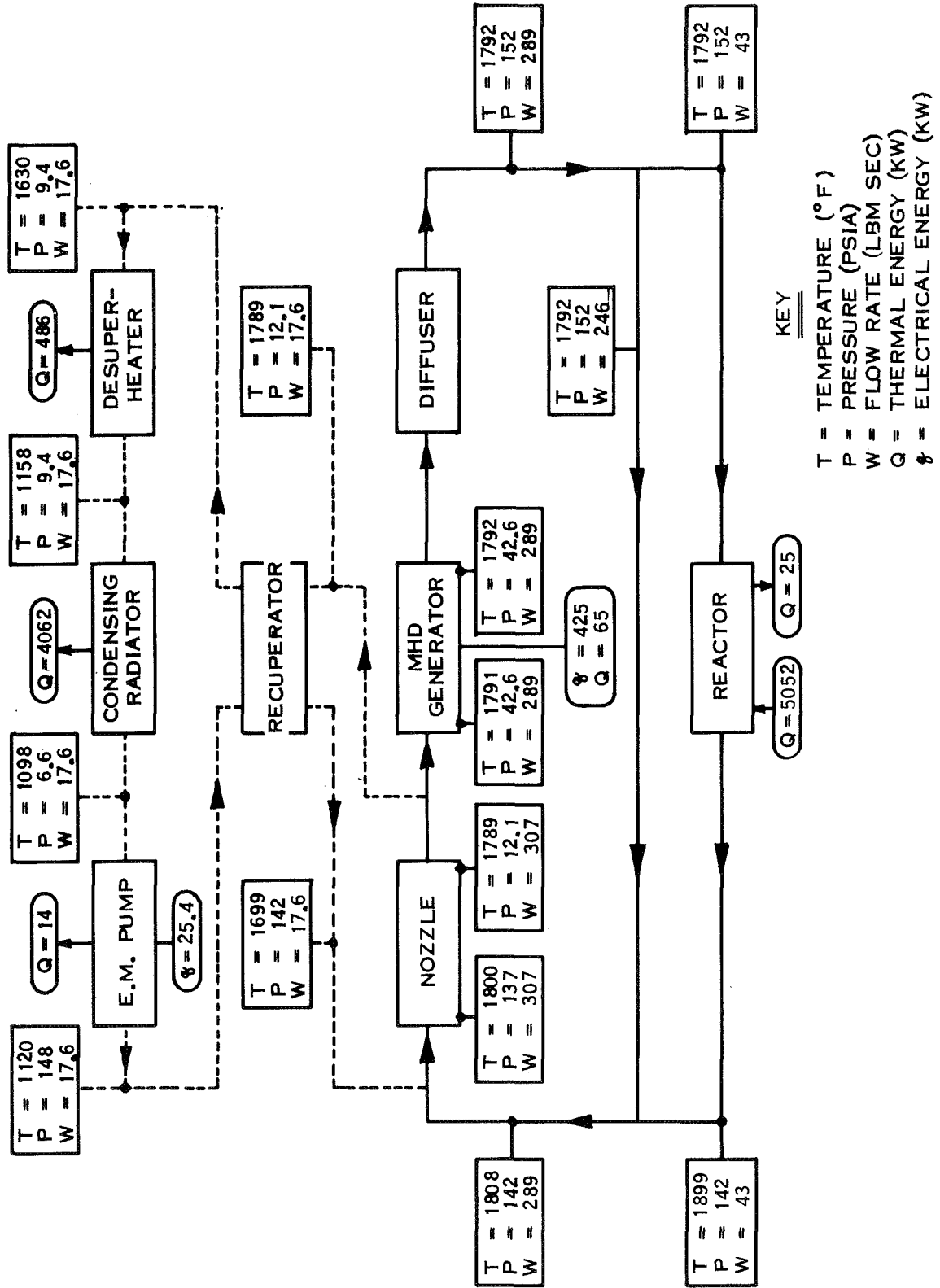
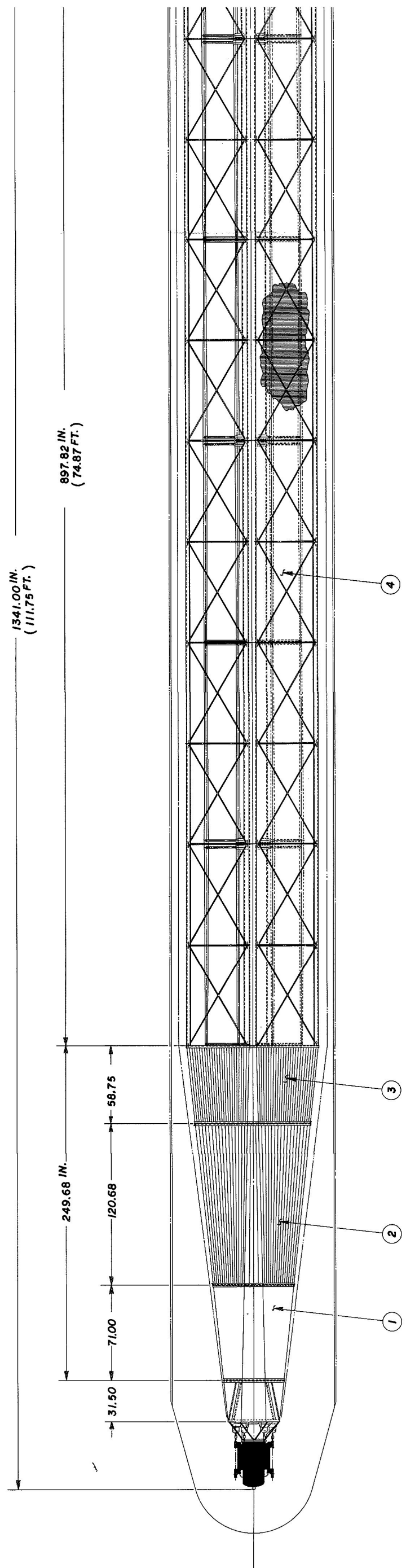


Figure 2-100. Cycle Conditions - 400 kWe MHD Power System

ITEM DESCRIPTION	
1	EXCITATION CAPACITOR BAY
2	LOW TEMP. AUXILIARY RADIATOR
3	HIGH TEMP. AUXILIARY RADIATOR
4	PRIMARY RADIATOR VAPOR CHAMBER
5	DEPLOYABLE ION ENGINE PLATFORM (4)



2

ITEM DESCRIPTION	
1	EXCITATION CAPACITOR BAY
2	LOW TEMP. AUXILIARY RADIATOR
3	HIGH TEMP. AUXILIARY RADIATOR
4	PRIMARY RADIATOR VAPOR CHAMBER
5	DEPLOYABLE ION ENGINE PLATFORM (4)

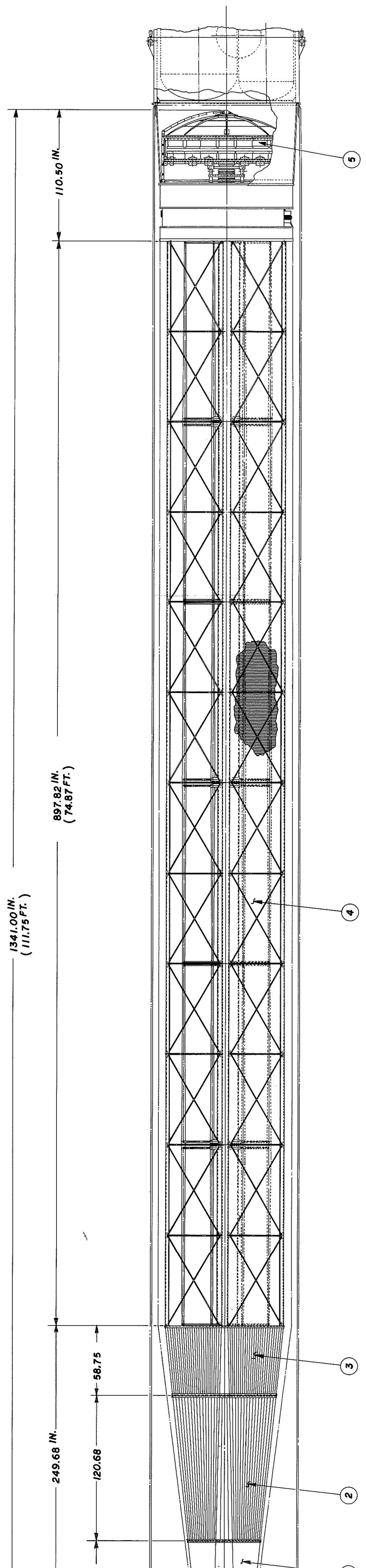


Figure 2-101. Inboard Profile, 400 kWe
MHD Spacecraft

TABLE 2-56. WEIGHTS - 400 kWe MHD SYSTEM

<u>ITEM</u>	<u>WEIGHT - LBS</u>
• PROPULSION SYSTEM	24,110
• POWER SYSTEM	18,130
REACTOR	3110
SHIELD	1630
POWER CONVERSION	10,310
GENERATOR	
LITHIUM LOOP	1350
MHD FLOW ASSEMBLY	580
CESIUM LOOP	1240
RADIATORS	2740
ELECTRIC POWER & CONTROL SYSTEM	4400
EXCITATION	700
HOTEL LOAD POWER CONDITIONING	200
MISCELLANEOUS	320
STRUCTURE & INSULATION	260
REACTOR & SHIELD	660
MHD BAY	940
MAIN RADIATOR	
• THRUSTER SYSTEM	5,980
ION ENGINES SUBSYSTEM	1800
MAIN POWER CONDITIONING	1910
ELECTRONICS, RADIATORS, ETC.	2270
• PROPELLANT & TANKAGE	21,500
• NET SPACECRAFT	2,340
SCIENCE	2065
OTHER	275
• INITIAL MASS IN EARTH ORBIT	47,950

TABLE 2-57. 400 kWe MHD GENERATOR DIMENSIONS

Slot No.	Distance From Beginning Of Travelling Wave Region (CM)	Flow Channel Height At Slot Pole Piece (CM)	Width of Slot At Widest Point Near Point Piece (CM)	Width of Slot At Narrowest Point, Opposite Pole Piece (CM)
0	0.00	0.887	5.916	5.916
1	1.48	0.911	1.935	1.379
2	2.93	0.935	1.879	1.311
3	4.35	0.960	1.822	1.241
4	5.74	0.985	1.765	1.169
5	7.10	1.012	1.708	1.097
6	8.44	1.038	1.651	1.023
7	9.74	1.066	1.595	0.949
8	11.02	1.094	1.539	0.874
9	12.27	1.122	1.484	0.798
10	13.48	1.152	1.428	0.722
11	14.67	1.182	1.375	0.647
12	15.83	1.212	1.322	0.571
13	16.97	1.244	1.270	0.497
14	18.07	1.276	1.219	0.423
15	19.15	1.308	1.169	0.352
16	20.20	1.342	1.121	0.283
17	21.23	1.376	1.073	0.218
18	22.23	1.411	1.027	0.158
19	23.21	1.446	0.981	0.104
20	24.16	1.483	0.937	0.058
21	25.95	1.556	5.916	5.916
Slot Depth = 7.60 cm Wall Thickness (Stator-to-Fluid) = 0.4 cm Li Channel Width = 29.6 cm				
<u>Compensating Pole</u>	<u>Length (cm)</u>	<u>Duct Avg. Height (cm)</u>	<u>No. of Vanes</u>	
Upstream	5.92	2.04	18	
Downstream	5.92	1.96	28	

TABLE 2-58. 400 kWe MHD GENERATOR DYNAMIC CHARACTERISTICS

Slot No.	Slip	Fluid Velocity (M/sec)	Wave Velocity (M/sec)	Field Strength (TESLA)
0	0.194	114.62	96.02	0.470
1	0.185	111.64	94.18	0.479
2	0.177	108.73	92.36	0.489
3	0.170	105.91	90.56	0.498
4	0.162	103.17	88.77	0.508
5	0.155	100.50	87.01	0.519
6	0.148	97.91	85.28	0.529
7	0.142	95.39	83.56	0.540
8	0.135	92.94	81.87	0.551
9	0.129	90.57	80.20	0.563
10	0.123	88.26	78.56	0.574
11	0.118	86.02	76.95	0.586
12	0.113	83.85	75.36	0.599
13	0.108	81.74	73.80	0.612
14	0.103	79.68	72.26	0.624
15	0.098	77.69	70.75	0.638
16	0.094	75.76	69.27	0.652
17	0.090	73.88	67.81	0.666
18	0.085	72.05	66.38	0.680
19	0.082	70.28	64.97	0.694
20	0.078	68.56	63.60	0.710
21	0.071	65.34	60.99	0.740

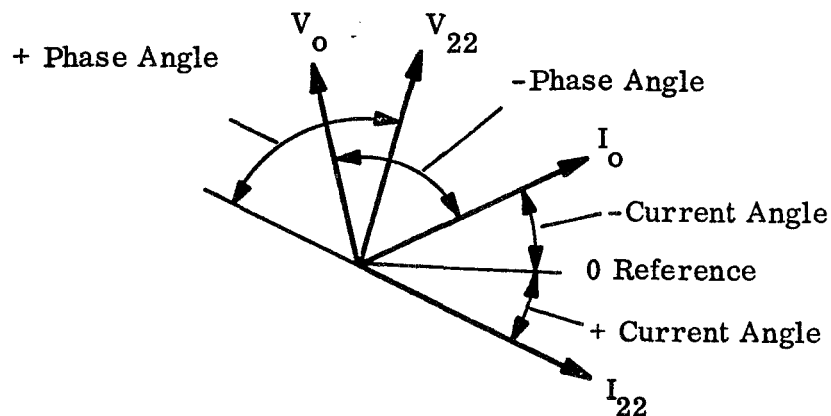
TABLE 2-59. 400 kWe MHD GENERATOR POWER SUMMARY

Sector	Input Power (Kinetic Energy) (kW)	Winding Loss (kW)	Net Power (kW)	Reactive Power (KVA)
0	22.59	0.59	-107.60	191.16
1	43.19	0.27	27.16	69.94
2	40.92	0.28	25.99	69.50
3	38.75	0.29	24.83	69.12
4	36.70	0.31	23.68	68.80
5	34.74	0.32	22.55	68.53
6	32.88	0.34	21.44	68.31
7	31.12	0.36	20.34	68.14
8	29.45	0.38	19.27	68.02
9	27.87	0.41	18.22	67.94
10	26.37	0.44	17.19	67.87
11	24.96	0.47	16.20	67.90
12	23.63	0.52	15.22	67.95
13	22.36	0.57	14.26	68.02
14	21.17	0.63	13.32	68.14
15	20.05	0.70	12.40	68.30
16	18.99	0.79	11.50	68.48
17	17.99	0.90	10.61	68.72
18	17.04	1.03	9.71	68.96
19	16.16	1.20	8.81	69.25
20	15.32	1.41	7.89	69.56
21	20.62	1.45	192.80	320.80
TOTAL	582.89	13.66	425.81	1883.44

TABLE 2-60. 400 kWe GENERATOR ELECTRICAL CHARACTERISTICS

Slot	Voltage (volts)	Current (amperes)	Current Angle* (Deg)	Phase Angle* (Deg)	Real Power (kW)	Reactive Power (KVAR)
0	833.8	263.09	-37.5	-60.6	-107.60	191.16
1	1123.5	66.78	38.0	68.8	27.16	69.94
2	1114.8	66.56	36.2	69.5	25.99	69.50
3	1105.9	66.41	34.5	70.2	24.83	69.12
4	1096.7	66.34	32.8	71.0	23.68	68.80
5	1087.3	66.35	31.1	71.8	22.55	68.53
6	1077.6	66.44	29.4	72.6	21.44	68.31
7	1067.7	66.61	27.7	73.4	20.34	68.14
8	1057.5	66.85	26.1	74.2	19.27	68.02
9	1047.1	67.17	24.5	75.0	18.22	67.94
10	1036.6	67.54	23.0	75.8	17.19	67.87
11	1025.9	68.05	21.5	76.6	16.20	67.90
12	1015.1	68.60	20.1	77.4	15.22	67.95
13	1004.1	69.22	18.7	78.2	14.26	68.02
14	993.2	69.91	17.4	78.9	13.32	68.14
15	982.1	70.68	16.1	79.7	12.40	68.30
16	971.1	71.51	14.9	80.5	11.50	68.48
17	960.1	72.42	13.8	81.2	10.61	68.72
18	949.1	73.38	12.7	82.0	9.71	68.96
19	938.1	74.41	11.6	82.7	8.81	69.25
20	927.2	75.51	10.6	83.5	7.89	69.56
21	910.1	411.23	45.0	59.0	192.80	320.80
Total Power Generated					425.81	1883.44
Frequency: 300 Hz						

* Definition:



2.8.1.1 Attitude Control Requirements

The vehicle inertias, power plant unbalance momentums, and disturbance momentums caused by gravity gradient and aerodynamic forces on the vehicle while in earth orbit have been estimated for a nuclear electric spacecraft. The control mechanism least costly in weight and size, and the one most easily integrated into the present vehicle configuration, appears to be ion engines. Since ion engines are already planned for the vehicle, the use of ion engines for attitude control requires the addition of only about 550 pounds for an inertial platform and associated electronics. It is estimated that the gas systems would require a total of approximately 800 pounds, and fluid flywheels, approximately 1000 pounds. Because the inertias are large, the disturbance velocities are small, and low thrusts can be used with negligible increase in position error.

Attitude control of the vehicle is required during the thrusting periods and for proper orientation in earth orbit. The vehicle configuration can be such that fluid loop momentums are approximately balanced. In addition to correcting the initial disturbances during startup and the momentum unbalances in the fluid loops, the attitude control system must be capable of correcting disturbances caused by power plant shutdown.

In addition to maintaining vehicle stability, there may be a requirement for the vehicle to pitch at the orbital rate to keep the antennas pointing toward earth or the planet around which the vehicle is orbiting. This requires a large amount of impulse to establish the required orbital rate. For example, for a 100-mile earth orbit approximately 1.9×10^3 lb-ft-sec of angular impulse is required to establish a pitch orbital rate of 0.067 deg/sec. This corresponds to an impulse of 38 lb-sec assuming a 50-foot pitch moment arm.

It is possible to provide this impulse with the ion engines. For example, by gimbaling and firing only certain engines, sufficient pitch torque can be developed.

2.8.1.2 Control by Mass Expulsion Devices

A mass expulsion type control system is characterized by a limit cycle about the desired attitude. The velocity of this limit cycle is determined by the control system time delays, slope of the switching lines, and magnitude of correction thrust available. The maximum excursions of this cycle are approximately determined by the position deadband. The thrust is sized to maintain the pointing accuracy during maximum disturbances. Correction

torques can be much smaller than the disturbance torques, with negligible effect on pointing accuracy, if the disturbance torques are of short duration. To keep deadband overshoot to a minimum with small correction torques, the magnitude of the slope of the switching line may be decreased.

Assuming that total impulse requirements, startup, disturbance and limit cycle are approximately 2.8×10^3 lb-sec, the amounts of propellant needed to provide the impulse for each system cold gas, hot gas and ion engines, are shown in the following table:

<u>System</u>	<u>I (sec)</u>	<u>Propellant (lb)</u>	<u>Thrust/Axis (lb)</u>
Cold gas	80	70	1
Hot gas	200	30	1
Ion Engine	5000	5	0.5

The jet control system may be idle for long periods of time but must still be capable of operating when called upon. The storage problems involved with gas systems, leakage and valve self-welding, make the ion engine system more appealing, particularly since ion engines are already located on the vehicle.

A thrust of 0.5 pound results in correction torques of 25 lb-ft in pitch and yaw and 5 lb-ft in roll. These are thought to be adequate for correcting any disturbances expected. The large disturbances during startup and power plant shutdown result in small changes in velocity, and therefore small correction torques can be used with minimum position overshoot. If larger disturbances can be expected, then the use of gas systems should be considered because of the low thrust capabilities of ion engines.

2.8.1.3 Control by Momentum Transfer

Momentum transfer devices may also be used for attitude control. In addition to the momentum transfer devices some kind of discrete impulse device will be necessary to unload the momentum devices. For long life, a fluid flywheel using an EM pump is probably the best momentum transfer mechanism since this eliminates bearing problems associated with motor driven flywheels. The estimated total weight of the guidance and control system using fluid flywheels for control is 1000 pounds. In order to handle larger disturbance and to unload the fluid flywheels, some sort of reaction device (cold or hot gas jets ion engines or solid propellant jets) is needed. These jets should have an

angular impulse capability of 3696 lb-sec in pitch and 184 lb-ft-sec in yaw and 2816 lb-ft-sec on roll. Assuming a moment arm of 40 feet in pitch and yaw and 20 feet in roll, an impulse capability of 295 lb-sec is required for disturbances. The jets need be used only to reduce the impulse to a level that can be handled by the flywheel. If the flywheels can handle the maximum momentum unbalance, the impulse jets can be sized for discrete impulse steps of 116 lb-ft-sec.

Impulse jets can be either cold gas, hot gas, ion engine or solid propellant. Since the jet impulse system may be unused for long periods before it is called upon to work, reliability considerations indicate that an ion engine or solid propellant jet impulse system should be used. The ion engine or solid propellant systems are not subject to the storage problems and valve freeze up problems of the gas systems.

It may be possible to use some sort of short duration device, similar to the firing of CO₂ cartridge, for these discrete impulse steps.

2.8.1.4 Attitude Control Using Existing Ion Engines

Ion engine control can be mechanized by a combination of gimbaling and translating the existing ion engines on the vehicle; the baseline ion engine system (Reference 9) has such capability. With this arrangement the additional weight required for attitude control is minimized. However, using ion engines means that power must be available instantaneously for simultaneous firing of the ion engines. Thus, if vehicle attitude must be controlled during coast periods, power cutback could be only a portion of ion engine power instead of the total ion engine power cutback possible using other mechanisms for attitude control. For the types of missions considered, the amount of time required to make attitude corrections may not be critical. Since communications will be received from the vehicle at infrequent intervals, attitude corrections can take several minutes (perhaps hours). With several minutes available for attitude corrections, individual ion engines rather than total propulsion can be used for attitude control, thus reducing peak power requirements drastically.

If large disturbances are expected during power plant cutback, it might be desirable to carry a cold gas system to correct these large disturbances in a shorter time than can be obtained with the ion engines. A cold gas system could also be used to provide attitude

control for initial stabilization before startup, although the final stage of the launch vehicle (e.g., the Titan Transtage) could provide this function. The backup cold gas system for correcting the large disturbance during startup and power plant cutback would have to be capable of approximately 500 lb-sec of impulse. This would require a cold gas subsystem weight, including tanks and plumbing, of approximately 100 pounds. The control system must then be capable of automatically switching to the cold gas system whenever position errors or vehicle rates become larger than a specified amount. The low peak power requirements and high degree of reliability attainable with this scheme of attitude control would make it a desirable system. The requirement for a cold gas system to correct for large disturbances does not detract from the system.

If quicker correction response and complete power plant cutback are desired, a gas system may be used. Since there is a possibility of an explosion due to leaks with a hot gas system and only a limited number of restarts are possible with a hot gas engine, a cold gas system, though heavier, is probably more practical. The cold gas system requires propellant tanks and eight attitude control valves, plus pressure regulators and associated plumbing. Weight is estimated at approximately 250 pounds for the gas system and 550 pounds for the inertial platform and electronics. This total weight of 800 pounds for the guidance and control system is still considerably less than that required for a fluid flywheel system. In any case, a weight of 550 pounds for the inertial platform should be included in spacecraft weights for any future analysis.

2.8.2 MISSION ANALYSIS

An investigation of various propulsion modes for accomplishing a Jupiter orbiter mission was conducted to make a general appraisal of the mission capabilities of MHD-powered spacecraft. The propulsion modes that were compared are as follows:

1. Low thrust earth escape, interplanetary transfer, and Jovian capture
2. High thrust earth escape followed by low thrust interplanetary transfer and Jovian capture
3. High thrust propulsion supplied by the launch vehicle to achieve earth escape and interplanetary transfer. (This mode implies a spacecraft which is neither MHD-powered nor electric-propelled; it was considered only for rough comparison.)

The following assumptions were made for all cases that were considered:

1. Spacecraft would be launched from Cape Kennedy during the early 1980's
2. Launch windows of a few days are acceptable
3. The specific impulse of the low thrust propulsion system is 5000 seconds
4. The electrical input power-to-thrust ratio of the low thrust propulsion system is 154 kWe/lb thrust
5. The terminal Jovian orbit is 1.17×10^6 miles radius (the orbit of the moon Callisto).

2.8.2.1 Launch Vehicles

Table 2-5, which was presented earlier in this section, lists eight candidate launch vehicles with some of their principal characteristics. Ranging from the Titan IIC-7 up to the Saturn V, they are divided into two categories, four vehicles which have a high energy terminal stage useful for interplanetary injection, and four which are more suited to placing a large payload in a selected earth orbit. The latter are those boosters which would be used with an all low thrust propulsion mission; the former would be used for high thrust escape from earth.

2.8.2.2 All Low Thrust Propulsion

We consider first the case where earth escape, interplanetary transfer, and Jovian capture are achieved using the low thrust propulsion system. Figure 2-102 shows the relationship of gross payload, or dry spacecraft weight, to trip time for various power plant ratings and various Initial Masses in Earth Orbit (IMEO). The gross payload includes the MHD power and propulsion system as well as the science payload. The trip time as presented in Figure 2-102 includes earth escape and interplanetary transfer (flight in heliocentric orbit) time but does not include Jovian capture time. The additional time needed to attain Jupiter orbit can be determined from the parametric plot of Figure 2-103; typical capture times are in the range of 1500 to 2000 hours, or 60 to 90 days.

Turning back to Figure 2-102, the three IMEO values represent three different launch vehicle requirements; IMEO = 30,000 pounds is the capability of the Titan IIC-7 launch vehicle; IMEO = 35,670 pounds is the value calculated for the baseline design MHD spacecraft (275 kWe gross power); and IMEO = 50,000 pounds is the capability of a Titan IIL-2 launch vehicle. In order to determine the net payload capability of an MHD-powered spacecraft, one must calculate the propulsion system weight and subtract it from the gross

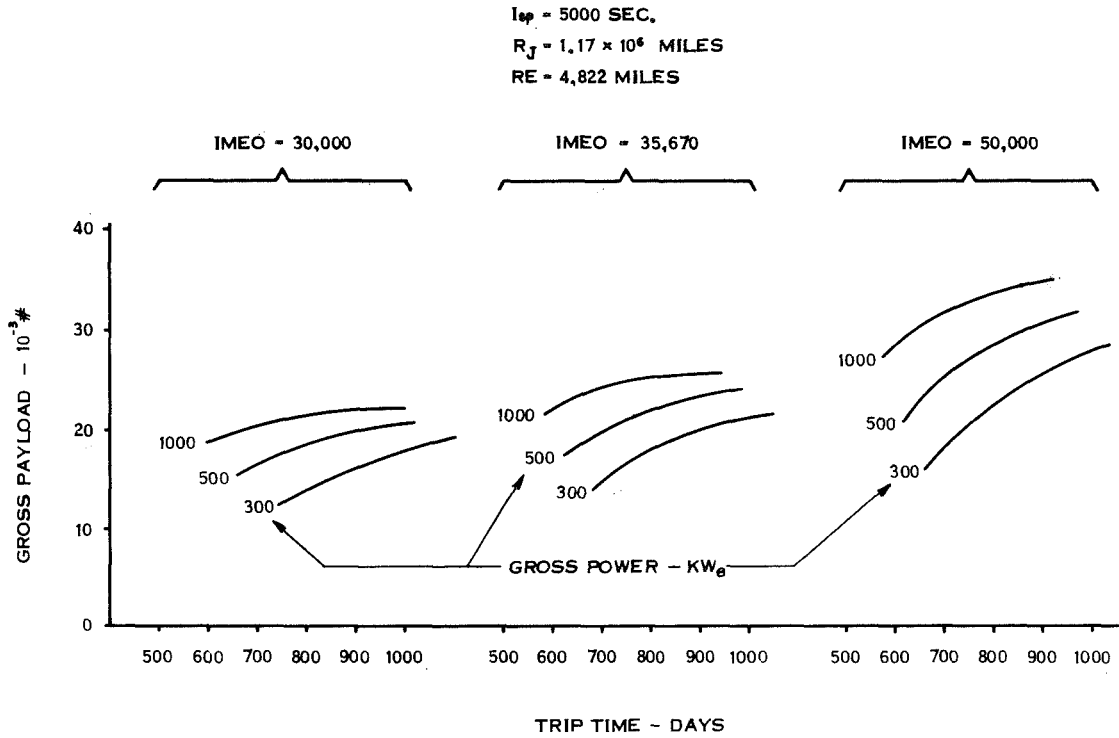


Figure 2-102. Jupiter Orbiter - All Low Thrust

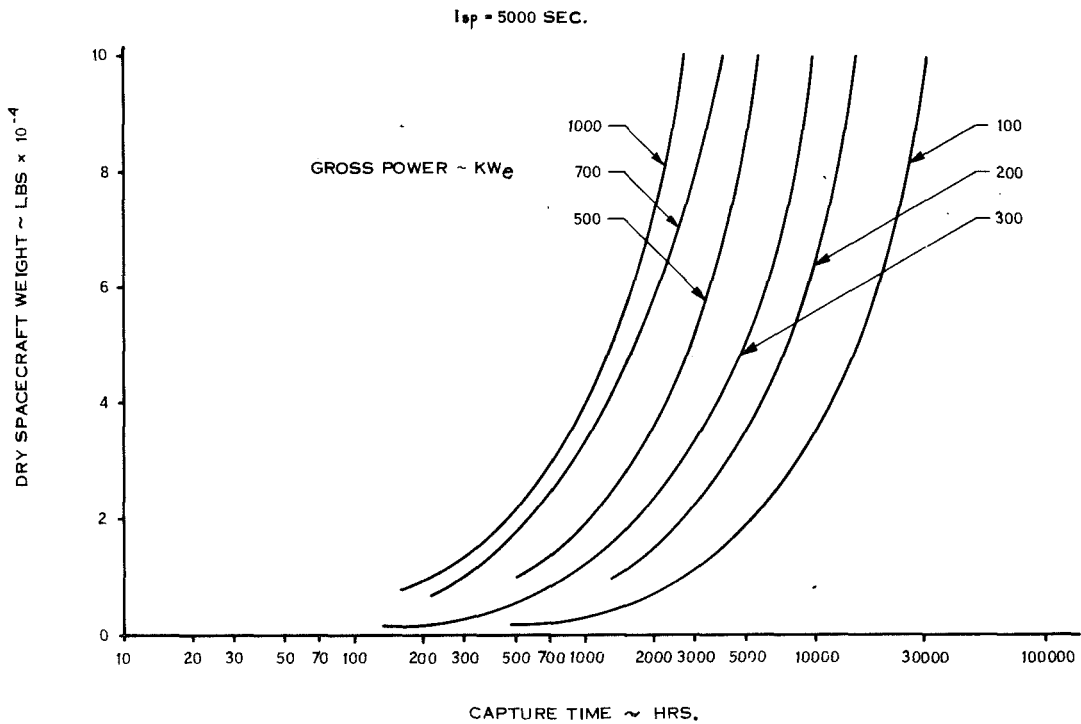


Figure 2-103. Capture Time to Achieve Jovian Orbit of 1.17×10 Miles

payload shown in Figure 2-102. Table 2-61 lists the propulsion system weights used in the mission analysis. These values of specific weight were used, the 77.5 lb/kWe representing the baseline design system and the other values selected to probe the sensitivity of the analysis to changes in propulsion system specific weight. System specific weight was not varied rigorously with power level because such a relationship is too sensitive to the weight variations associated with incompletely defined portions of the system, for example, the radiation and structure design.

TABLE 2-61. PROPULSION SYSTEM WEIGHTS USED FOR MISSION ANALYSIS (POUNDS)

Specific Weight, α , #/kWe	Power ~ kWe			
	200	300	500	1000
60	9600	14400	24000	48000
77.5	12400	18600	31000	62000
85	13600	20400	34000	68000

Using these three values of specific weight and the three values of IMEO previously identified, a set of net payload values was calculated for 300 kWe and 500 kWe propulsion systems assuming a 900 day trip time. Table 2-62 lists these net payload values. One can see that a propulsion system of approximately 300 kWe rating can carry payloads of up to several tons to Jupiter orbit in about 900 days using one of the Titan family launch vehicles. Heavier, more powerful systems demand more powerful launch vehicles. Shorter trip times may be obtained at the expense of reduced payload; note the slopes of the curves in Figure 2-102 to see that even modest reductions in trip time require severe reductions in net payload. One can then take the transport of a two to four ton payload to a one million mile orbit around Jupiter in about 900 days as typical of the MHD-powered spacecraft capability, using the all low thrust mode.

TABLE 2-62. JUPITER ORBITER PAYLOADS, ALL LOW THRUST

$$I_{SP} = 5000 \text{ SEC.}$$

$$R_E = 4822 \text{ MILES}$$

$$R_J = 1.17 \times 10^6 \text{ MILES}$$

$$T_T = 900 \text{ DAYS}$$

NET PAYLOAD ~ LB.

IMEO ~ LB.	GROSS POWER = 300 KWE			GROSS POWER = 500 KWE		
	$\alpha = 60\# / \text{KWE}$	$\alpha = 77.5\# / \text{KWE}$	$\alpha = 85\# / \text{KWE}$	$\alpha = 60\# / \text{KWE}$	$\alpha = 77.5\# / \text{KWE}$	$\alpha = 85\# / \text{KWE}$
30,000	4800	400	-1400	-3450	-10,450	-13,450
35,670	7400	3200	1400	- 100	- 7100	-11,000
50,000	13,800	9600	7800	7700	700	- 2300

2.8.2.3 High Thrust Escape - Low Thrust Transfer and Capture

In order to achieve shorter trip times than the 900 days deemed characteristic of the all low thrust mission, hybrid thrust missions were considered. In these the launch vehicle provides high energy thrust escape from earth and the MHD propulsion system provides low thrust for interplanetary transfer and Jupiter capture. Two launch vehicles were considered here, the Saturn V and the Titan III-L4/Centaur. Figure 2-104 shows the variation of net payload with trip time and system power level for the Saturn V launch vehicle. For any of the specific weights considered there is an increase in net payload with decreasing plant power in the range from 1000 kWe down to about 500 kWe. This occurs because at these high specific weights (60 to 85 lb/kWe) the weight of an incremental power increase in the low thrust system reduces the velocity attained by the initial chemical thrust by more than can be made up during the flight by that power increment. Consequently, either the trip is lengthened or the payload must be reduced. However, somewhere in the 200 to 500 kWe region, depending on α , an optimum is reached where the net payload for a given trip time is a maximum. With the Saturn V launch vehicle, truly large payloads can be sent to Jupiter in acceptably short times, 20,000 to 40,000 pounds in 450 to 800 days. The Saturn V provides a desirable shortening of trip time compared to the all low thrust cases considered but the payload mass is so greatly

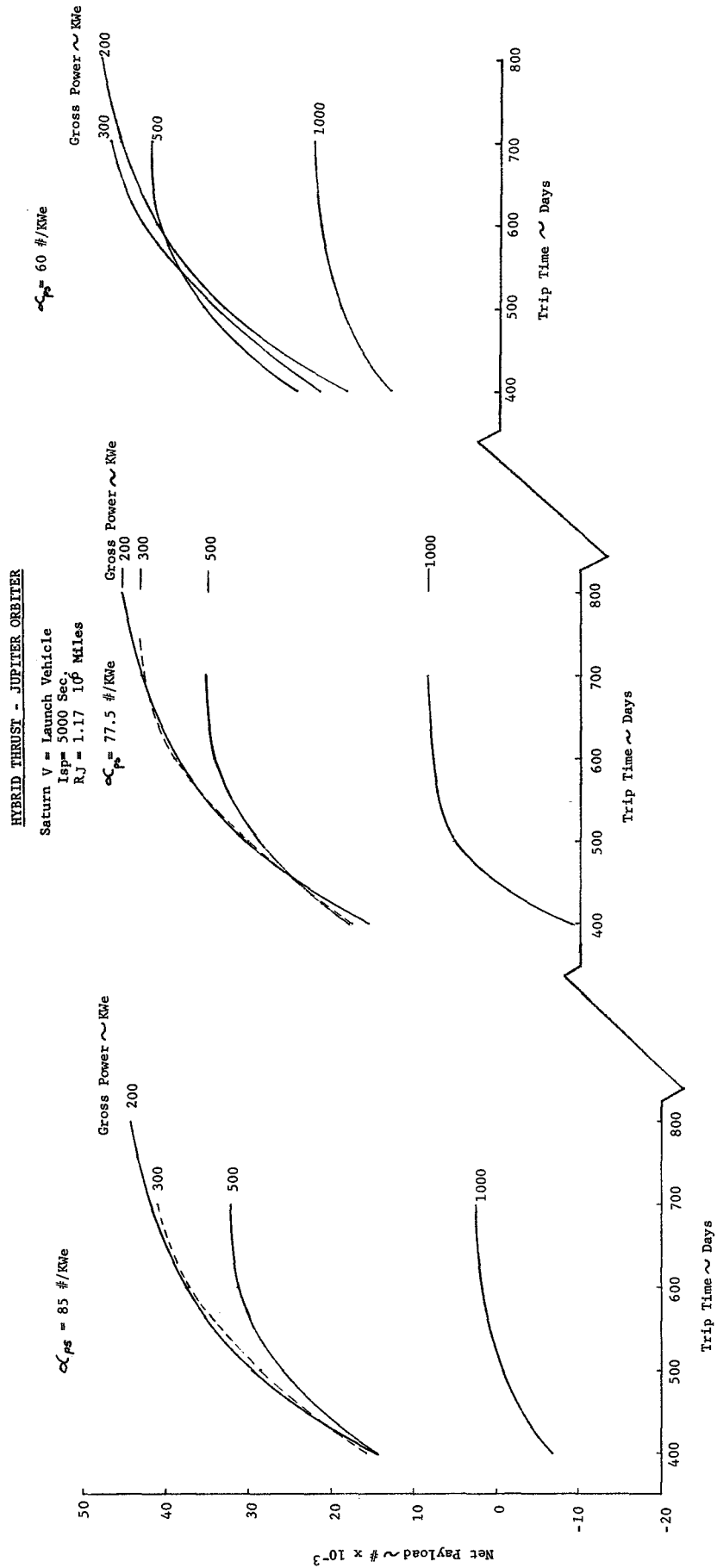


Figure 2-104. Net Payload vs. Trip Time - Saturn V Hybrid Thrust

increased that the two mission choices are not truly comparable. The Titan III-L-4/Centaur launch vehicle was also considered for hybrid thrust missions. Figure 2-105 shows the net payload to trip time relationships for this launch vehicle. Again, we see payload increasing with decreasing power as was the case with the Saturn V. Here the optimum power level does not appear as clearly as it does in Figure 2-104. Power levels below 200 kWe were not included in the analysis because the system specific weight is expected to increase quite rapidly as power is reduced below 200 kWe. As a consequence, it is not considered realistic to plot a 100 kWe or 150 kWe curve for any of the three α values shown in Figure 2-105.

As Figure 2-105 shows, if the Titan III-L-4/Centaur is used to launch an MHD-powered hybrid thrust mission, a several ton payload might be brought to Jupiter in about 500 days. This payload is comparable to that for a Titan-launched low thrust mission but the trip time is cut almost in half.

2.8.2.4 All High Thrust

For general comparison, it is useful to consider the payload/trip time possibilities of an all high thrust mission. Figure 2-106 shows the payload capabilities for intermediate class launch vehicles and Figure 2-107 shows this data for high energy class launch vehicles. It is important to note that these curves present payload values for flyby missions. In order to compare these payloads to the payloads of the MHD-powered spacecraft some allowance must be made for a payload electrical power system and for a retropropulsion system to bring the spacecraft into Jupiter orbit.

As far as an electrical power system is concerned, the most likely is a Radioisotope Thermoelectric Generator (RTG). Current RTG's provide only about one watt per pound of weight but systems under active development now should provide at least two watts per pound. Thus, a 1 kWe power system would weigh about 500 pounds.

A retropropulsion system would be far heavier. A chemical propulsion system large enough to bring the payload down into a 1.17 million mile orbit around Jupiter would take up almost all the payload weight allowance. However, some calculations were made which indicated that if about one-half of the payload weight were given over to the retropropulsion system, the spacecraft could attain a highly elliptical orbit with a periapsis as low as the

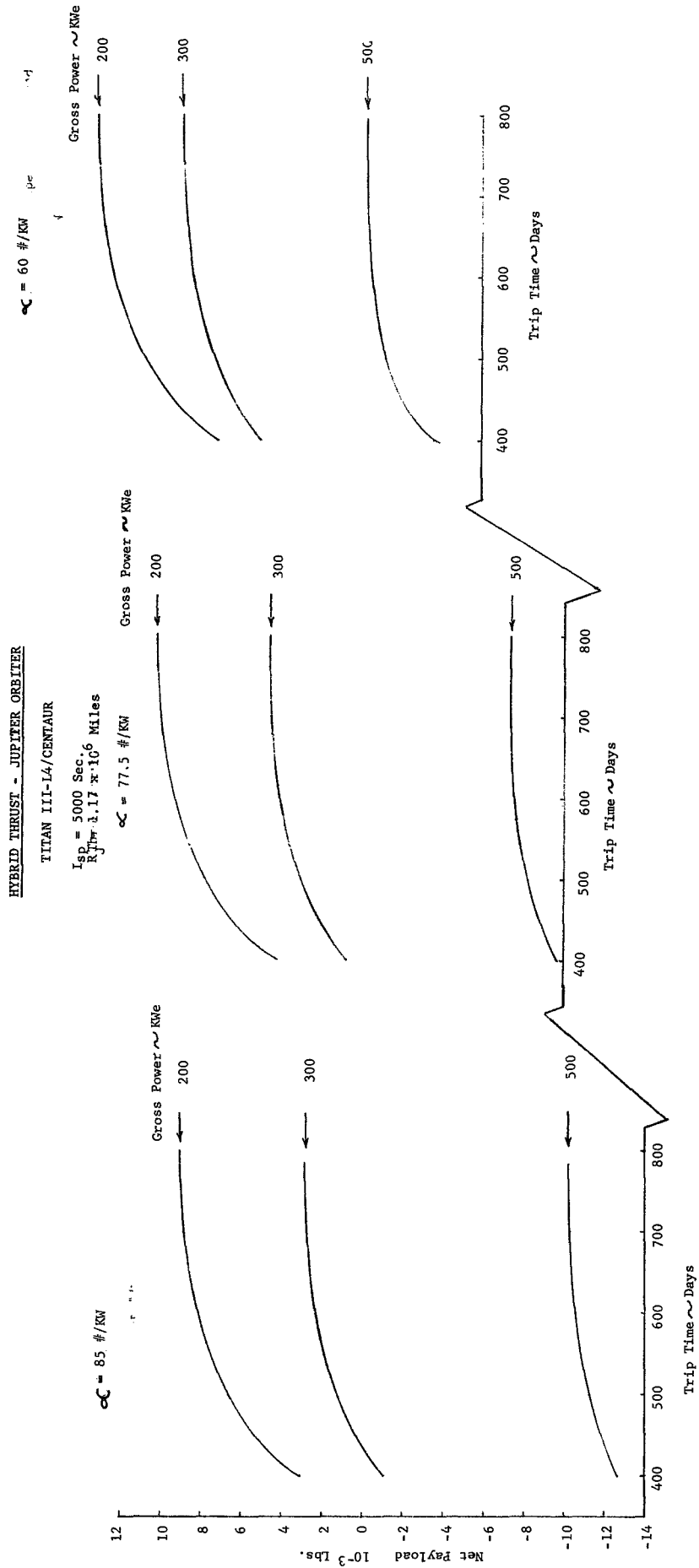


Figure 2-105. Net Payload vs. Trip Time - Titan III-L4/Centaur Hybrid Thrust

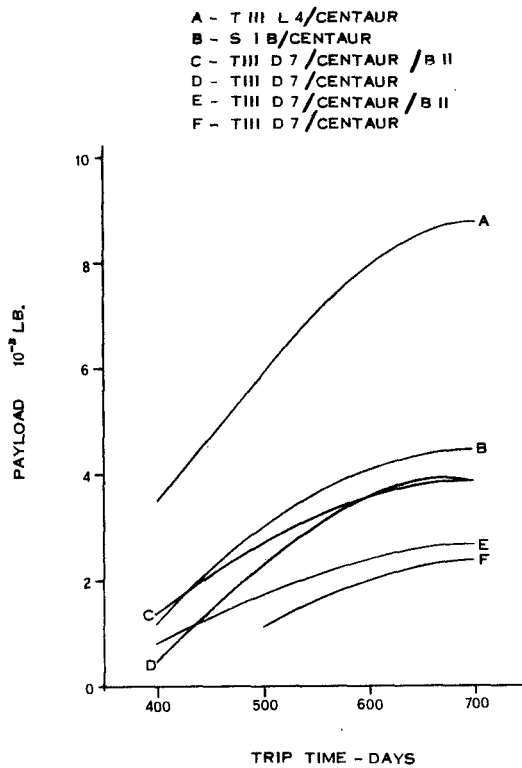


Figure 2-106. Launch Vehicle Payload Capability - Intermediate Class

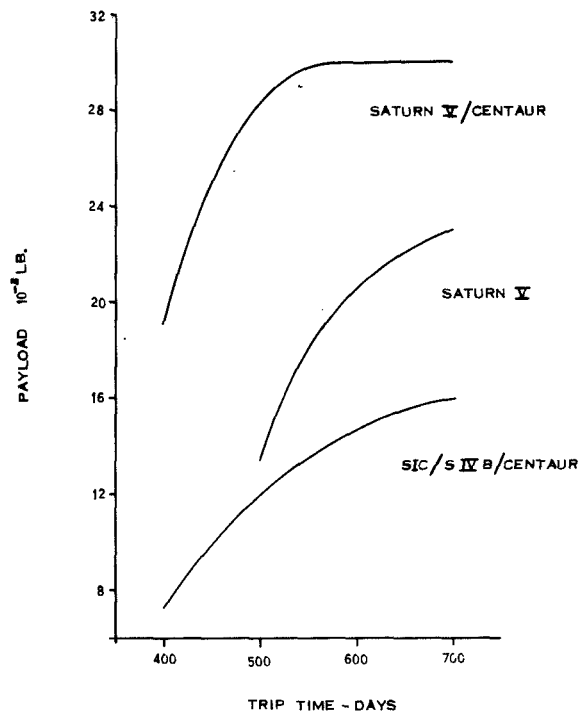


Figure 2-107. Launch Vehicle Payload Capability - High Energy Class

1.17 million mile radius of the Callisto orbit. From such an elliptical orbit the spacecraft might be able to obtain scientific data at least comparable to that attainable in a one million mile circular orbit.

If one assumes a 50 percent reduction for retropropulsion and 500 to 1000 pounds for an electrical power system, the payloads shown in Figures 2-106 and 2-107 indicate that only the largest launch vehicles can compete with the MHD-propelled spacecraft. However, if interest is confined to payloads of one ton or less requiring only about 1 kWe of power, the all high thrust mission, using one of the Titan launch vehicles, might be the most attractive choice.

2.8.3 OPERATIONS

In this study, prelaunch ground flow, in-orbit startup, and flight operations were considered. Startup, power operation and shutdown are discussed in Section 2.3; this section discusses ground flow operations using a basic ground flow plan.

The ground flow plan presents a typical profile which deals with the various stages of testing, transportation, and handling of the spacecraft subsystems, shipping segments, and totally assembled vehicle from the time of initial assembly at an aerospace facility to the vehicle liftoff at the launch pad. A number of engineering safeguards above normal spacecraft handling precautions are required due to the special problems encountered with nuclear reactors and liquid metals. It is recommended that the reactor coolants be purged from the liquid loops after conducting the subsystems and system tests. The reactor will be shipped separately and maintained at a remote launch site facility until very late in the final assembly schedule where it then moves to the Vertical Integration Building (VIB) for mating to the MHD module. Figure 2-108 shows the various sections of the total MHD powered spacecraft.

2.8.3.1 Special Problems for MHD Spacecraft Ground Flow

There are a number of special problems associated with the assembly, checkout and launch of an MHD-powered spacecraft. These include:

1. Nuclear reactor handling
2. Liquid metal handling
3. System preheating.

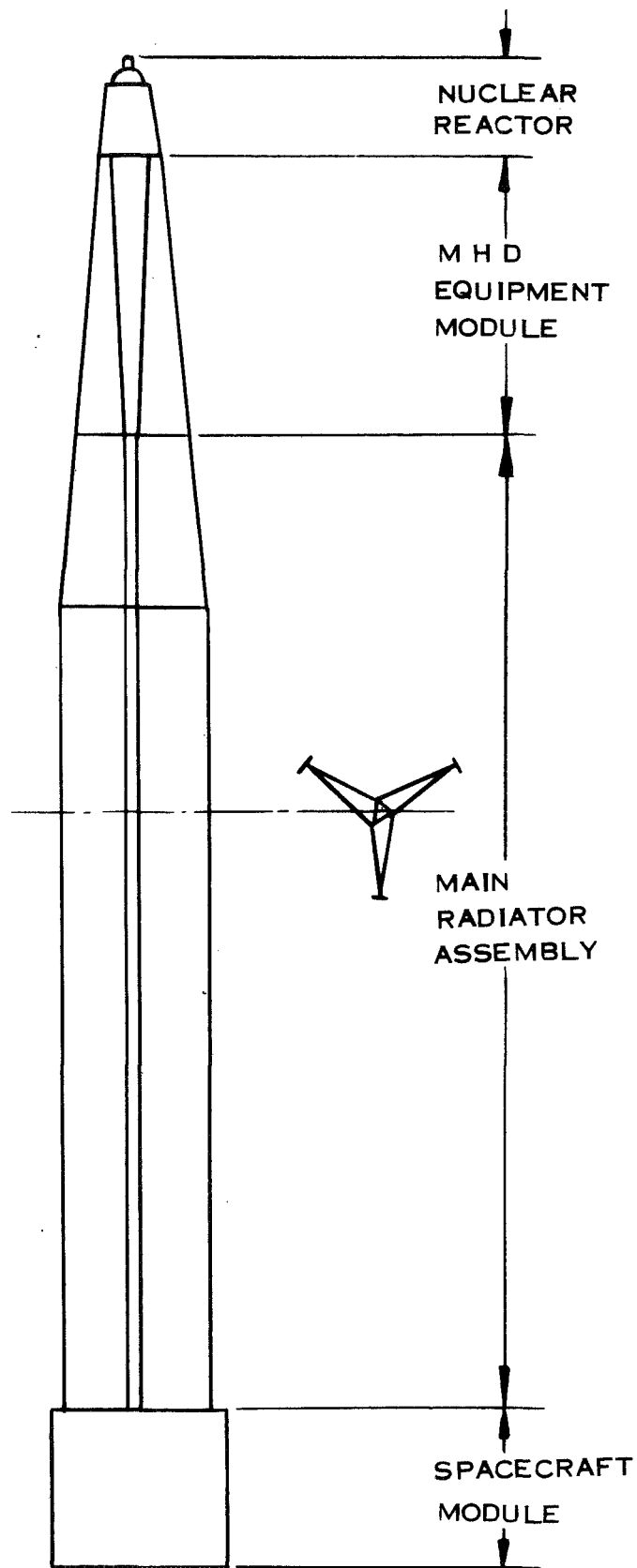


Figure 2-108. MHD-Powered Spacecraft Modules

2.8.3.1.1 Nuclear Reactor Handling - The basic approach in flight reactor operation is to withhold reactor startup until an acceptably high, long life, orbit is achieved. Thus, if the reactor is broken up or burned in a launch abort, little radioactivity is released to the environment. To minimize the amount of fission products in the reactor fuel, the reactor should receive little or no critical test before flight. It is possible to conduct all reactor critical testing on a qualification reactor and launch a duplicate reactor, which has never achieved criticality, with full confidence that it can be taken critical once in orbit. On the other hand, it may be preferable to conduct at least some low power critical testing of the flight reactor early in the ground flow, leaving sufficient time before launch for fission product decay to acceptably low levels. With either choice of approach it does not seem reasonable to perform any sort of MHD system operating test using the flight reactor as a heat source. The power-time required would probably generate far too many fission products for reasonable decay periods.

The nuclear reactor also requires special handling to preclude inadvertent criticality during shipment or storage. This may be done by fitting the reactor with special locks to prevent control drum, rod, or reflector operation, installing neutron poisons or fillers in or around the core, and sealing the reactor in special shipping containers to prevent the admission of neutron moderating materials such as water. It is therefore likely that the reactor would be shipped separate from the rest of MHD power system and spacecraft.

2.8.3.1.2 Liquid Metal Handling - The MHD power system uses two liquid metals, lithium and cesium, in relatively large quantities. Since both of these metals react readily with air, water, and other common materials, special precautions are required for their safe handling. Systems must be cleaned and evacuated before filling; a fire retardant atmosphere must be maintained while testing or filling, and special purification facilities are needed for system fluid inventories. None of these pose insurmountable problems, but they all do complicate ground flow.

2.8.3.1.3 System Preheating - The MHD working fluids, lithium and cesium, melt at 357^oF and 84^oF, respectively. As a consequence, they may freeze and plug system flow passages during handling or filling. To assure complete filling of the system and to

prevent flow blockage during reactor startup in orbit, the lithium system will be preheated to 500^oF before filling and maintained at 500^oF until launch. The system is provided with a heating jacket to allow heating by pumped inert gas. The high specific heat of lithium and system insulation provides enough thermal inertia to prevent excessive cool down in orbit before startup.

2.8.3.2 Ground Flow Plan

The overall ground flow plan is schematically presented in Figure 2-109. The plan is designed to permit standard assembly, testing, and shipping operations with a minimum interference resulting from the presence of the nuclear reactor heat source and the liquid metals. Redundant liquid metal facilities are required at the aerospace assembly and testing facility and at Cape Kennedy. Also, a nuclear storage facility is required at the Cape. With safety being of utmost importance, every effort will be made to minimize hazards and protect personnel and property from injury.

The procurement, fabrication, and assembly of subsystems will take place at the aerospace facility. Each subsystem will be subjected to the engineering, qualification, and final acceptance tests. As early as possible in the program schedule, the nuclear reactor will be subjected to a series of tests which culminate with removal of the mechanical interlocks and a short duration startup. This early testing program would allow sufficient time for the generated fission products to decay to safe levels prior to the reactor shipment to Cape Kennedy. The low power critical tests can verify many of the nuclear design parameters.

Upon completion of all subsystem level tests, the MHD spacecraft is assembled and readied for combined system tests. The assembled spacecraft could be tested at the NASA Plumbrook Space Power Facility where short term power operation of the reactor and MHD power plant could be performed. It should be noted that the short term criticality will prevent the MHD generator from producing power. However, in place of utilizing the reactor as a heat source, the MHD power system could be tested for longer time periods using the 5 megawatt heat source/heat sink facility at JPL where sufficient electrical power would provide the thermal energy for the required liquid metal heatup, as well as a large condenser for waste heat rejection.

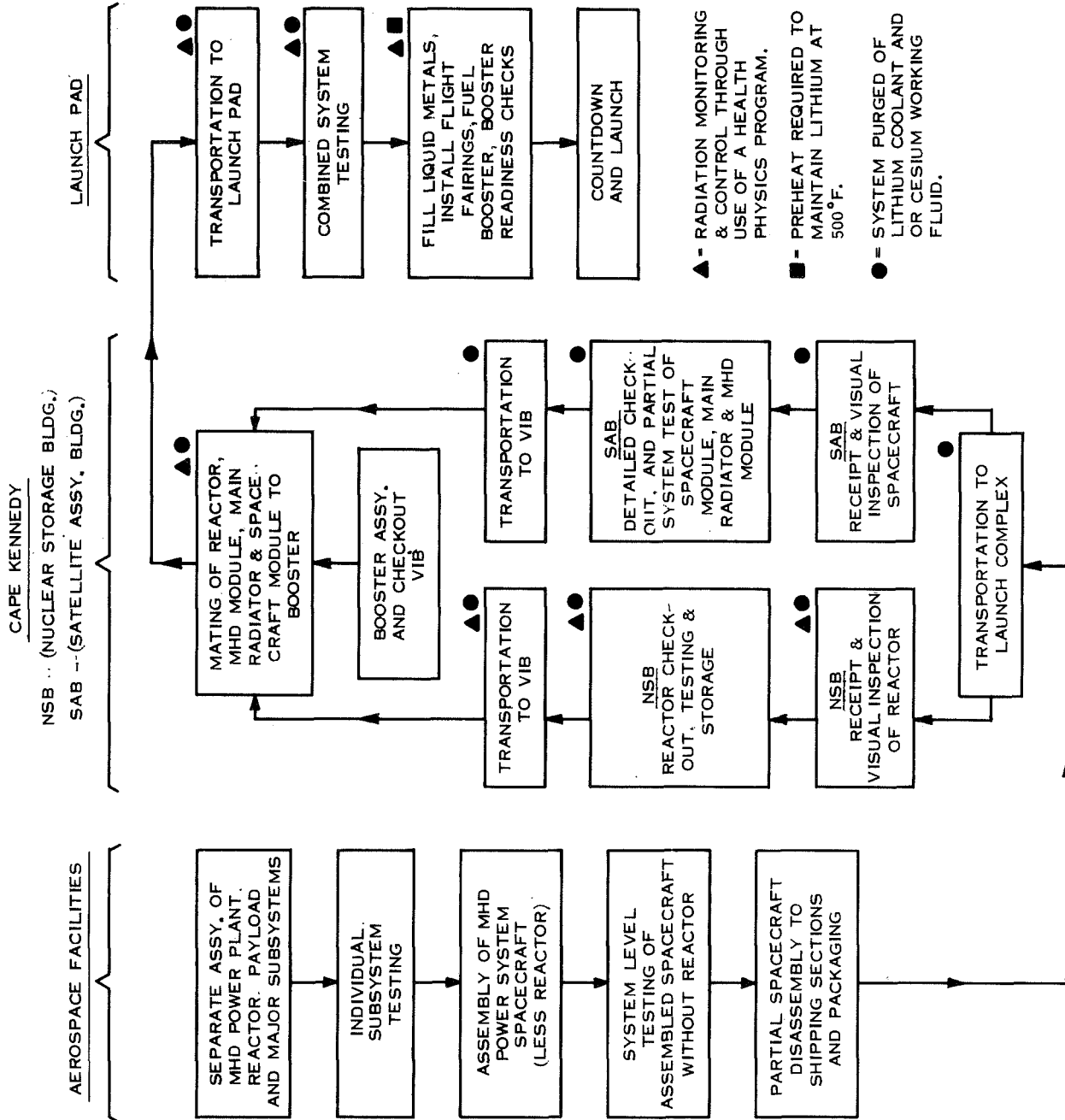


Figure 2-109. Overall Ground Flow Plan

The distinct advantage of testing at JPL is the elimination of additional fission products whose decay time would hinder the program schedules. Upon successful conclusion of this test, the power system would be purged of all liquid metals, and assembled to the rest of the spacecraft for checkout. The reactor would require individual handling requirements as mentioned later.

Upon arrival at the launch complex, the reactor is shipped directly to a Nuclear Storage Building (NSB) where it is inspected for assurances as to its operational readiness including individual reflector drum rotations. It is then stored in this radiation-controlled area for shipment late in the schedule from the NSB directly to the VIB. In the meantime, all other vehicle segments are shipped directly to the Spacecraft Assembly Building (SAB) where additional acceptance testing is performed. The spacecraft MHD Equipment Bay, Radiator, and Spacecraft Module are assembled without the reactor. All liquid and vapor lines are welded together except the reactor connections. Further inspections and testing are performed on the power conditioning components, the payload experiments, the liquid metal pumps, the radiator and interconnecting plumbing, telemetry checkouts, continuity of all electrical circuits, etc.

In parallel with the work being accomplished in the SAB, the booster is erected in the Vertical Integration Building (VIB) and standard launch vehicle flight readiness operations and checkouts are performed. The spacecraft minus the reactor is transported to the VIB and mated to the booster where additional checks are made. Final reactor installation preparations are readied in the VIB. The reactor arrives at the VIB as late in the countdown as possible. All possible safeguards will be incorporated to protect and train launch site personnel to the hazards associated with transportation, handling, and installing the reactor. The reactor inlet and outlet plumbing is welded to the mating hardware in the MHD Equipment Bay. Final leak detection tests are performed. The booster/spacecraft assembly then moves to the launch pad. The liquid loops will then be evacuated and the preheated liquid metals will be pumped into the accumulators and piping. After the system is filled the vent and drain valve connections are seal welded. As mentioned previously, the lithium metal within the vehicle will require 500⁰F temperatures to assure that freezing will not occur. These temperatures will be maintained up to the time of the launch by circulating hot helium gases through the coolant loop and

reactor heating jackets. The booster is fueled and all final system checkouts are performed.

The nuclear reactor "void-filler blocks" or mechanical interlocks are then removed. As these safeguards are removed, rapid shutdown devices will be activated. All vehicle flight fairings are buttoned up, and the terminal phase of the launch countdown progresses until actual liftoff.

During all phases of the vehicle assembly where the reactor is involved, a health physics program will be in operation to maintain personnel radiation exposure to prescribed limits.

2.8.3.3 Shipment Techniques

There are a number of different forms of land, air and sea transportation available for the expeditious and safe movement of the spacecraft segments to Cape Kennedy, such as trucking, railroad, aircraft, and barge. Shipment of the reactor requires special care. If the reactor were shipped assembled to the spacecraft, the load would be 10 feet in diameter and ~ 80 feet long. Consequently, it is much easier to design a reactor shipping container for the smaller package; this container should:

1. Prevent compaction of the reactor core
2. Prevent entrance of neutron moderating materials
3. Protect the reactor from fire or mechanical damage
4. Protect the reactor from contamination by dirt, metal, etc.

The rest of the spacecraft requires the usual type of protection during shipment; this shipment is greatly simplified if the liquid metals are shipped in separate containers. This would eliminate from the spacecraft shipment the problems associated with the reactivity and toxicity of the three liquid metals, lithium, cesium and mercury. The mercury propellant would be particularly troublesome because of its very large quantity, 10,000 to 20,000 pounds, and the troublesome inertial characteristics which result from mercury's exceptionally low viscosity and high density.

With the spacecraft segmented for shipment, the small reactor assembly, weighing only one to two tons, could be shipped portal-to-portal by AEC truck as is the present practice with isotope heat sources for space use. An escort guard can be provided as is the usual practice with reactor shipments. Liquid metal shipment could be by best chemical industry practices, and shipment of the other spacecraft modules or sections (see Figure 2-108) can be planned by ordinary ground flow practices.

3. CONCLUSIONS

4. RECOMMENDATIONS

5. NEW TECHNOLOGY

6. REFERENCES

3. CONCLUSIONS

The following conclusions are based on the past year's review of liquid metal MHD technology and the spacecraft study reported in the preceding sections. These conclusions are placed in two general categories, those relating to Li/Cs MHD technology and those relating more directly to unmanned spacecraft design.

3.1 Li/Cs MHD TECHNOLOGY

Although some promising results have been obtained, the Li/Cs MHD technology is still in a very early stage of development. Aside from some erosion test work, no Li/Cs MHD system has yet been run. The NaK/N₂ analog system described in Section 2.1 has not generated power yet; however, the difficulties encountered are not directly related to the magnetohydrodynamic design but rather associated with the specific experiment design. The startup runs that have been attempted, and the most recent work of Pierson (Reference 38) indicate the soundness of the electromagnetic theory. The real tests for the Li/Cs MHD system will be in the attainment of those design goals and assumptions which are vital to producing a useful power system; in general, these are:

1. CAN LOSSES - Current analyses assume no eddy current losses in the MHD duct walls facing the stators. A design must be developed which achieves this goal or which at least limits electrical losses to acceptable levels; unless such a design is developed the system just won't work (See Section 2.5.2).
2. Li/CS SEPARATION - Current analyses assume that impinging nozzle separation can effectively separate the liquid lithium from cesium vapor with little pressure loss. The nozzle performance predictions are based on tests with water and nitrogen gas. If lithium carryover is excessive, the extra heat load on the radiator will require a significant increase in its size. Moreover, inefficiency in the separator reflects directly in system inefficiency; if the system efficiency falls below 5 percent the weight penalties can be prohibitive (See Section 2.6.3).

3. SIDE CONDUCTORS - The electromagnetic analysis assumes that copper side bars in the MHD generator duct can be installed in such a way that no ohmic losses are suffered in completing the fluid current loop (See Section 2.1.2.1.1). Containing these conductors at 1800°F and minimizing the electrical resistance between the fluid and the conductors is a design problem which requires development work.
4. VANES - Those MHD generator designs which use vanes in the compensating pole sections of the duct are unattractive from a reliability standpoint. However, current generator design efforts at JPL are already directed toward elimination of these vanes.
5. Li CONTAINMENT - The system must contain 1800°F lithium flowing at high velocity for long periods. Aside from the special problems associated with the separator and the compensating pole vanes, the present state of refractory alloy technology seems adequate to solve this problem.
6. EM PUMP - The system needs a large cesium pump. Presently available electromagnetic pump designs might even be used. The analyses in this study have assumed a 20 percent efficiency for this pump; the high electrical resistivity of cesium makes this an optimistic goal. However, even if a pump efficiency of only 10 percent were achieved, the overall system efficiency would be reduced by only ~0.5 percent.

3.2 SPACECRAFT DESIGN

A number of conclusions can be drawn about the utility of the MHD power system in un-manned spacecraft design:

1. Specific Weight - The MHD power system is not attractive for use in spacecraft which carry modest payloads, i. e., up to two or three thousand pounds with power requirements of less than about 2 kWe, because of its relatively high specific weight. For payloads of such size the use of all chemical propulsion and other electrical power supplies appears more attractive. However, for payloads of greater weight and greater power requirements the MHD power system may be attractive. The mission analysis in this report is based on specific weights in the range of 60 to 85 lb/kWe. Achievement of specific weight as low as 60 lb/kWe is extremely doubtful; with successful development about 80 lb/kWe may be achieved.
2. Radiator - A NaK-cooled cesium condenser with a simple conduction fin radiator is far more attractive than the direct-condensing vapor chamber radiator. Weights are comparable and the conduction fin NaK radiator gives greater design freedom.

3. Reactor - At present there is no reactor suitable for use with the MHD power system. However, the same can be said for any of the space power systems which seek a nuclear heat source in the 1500° to 2200° F temperature range. The results of the SNAP-50 program and the test and design efforts since then at centers such as Oak Ridge National Laboratory, NASA-Lewis Research Center, and others suggest that when there is a clear need for a fast spectrum, lithium-cooled reactor for this temperature range it can be developed. The greatest obstacle to development of this reactor is not technical but financial. To gather another team of people like those who did the SNAP-50 work, and to develop this reactor would take many years and massive funding. At this time there are no public plans to undertake this reactor development.
4. Control and Reliability - It is easy to generate argument about the controllability and reliability of a flight MHD power system. However, such argument is better left until the general operating characteristics are demonstrated by an operating test system. The work of this study indicates that there are engineering solutions to the basic startup and control problems. As for reliability, the basic concept of the system, nothing moves but fluid, offers reliability through simplicity. It would be ill-advised to pop in redundant components at this time; too little is known of the system. With elimination of the MHD generator duct vanes, there is no one system locus or component that appears particularly vulnerable or less reliable than the rest. The durability of the system hangs or falls on the ability of the designer to cope with the forces of creep, corrosion and erosion for the expected life of the plant.
5. Configuration - If one chooses to use one of the larger MHD powerplants with a NaK conduction fin radiator as advised, one of the larger launch vehicles is needed, such as the Titan III L/4 or the Saturn V. If the 10-foot diameter limit is imposed, as was the case in the designs in the report, the spacecraft length will exceed 100 feet. It may be much better to use designs which flare out to approximately 20 feet in diameter, the reactor and shield sitting on a large conical/cylindrical radiator with the MHD equipment suspended within. The 22-foot SIVB diameter or bulbous flight fairings on the Titan can accommodate such configurations.

4. RECOMMENDATIONS

In light of the study results and the conclusions drawn in the preceding section, the following recommendations are offered.

1. Concentrate any efforts in the near future on development of the MHD technology itself; do not spend more on spacecraft studies at this time. The Phase II (FY 71) study postulated at the start of this study should be confined to MHD technology work.
2. Attack the most obvious technical problems of the system first and individually; in particular, seek a credible design for the MHD generator duct. The work described in Appendix A of this report is recommended as part of the follow-on effort.
3. When the MHD technology is better developed, i. e. , after at least some test of a hot Li/Cs ground system, begin again to study spacecraft application of the system.

5. TECHNOLOGY

No new technology items have been identified.

6. REFERENCES

1. Elliott, David G. , "Variable-Velocity MHD Induction Generator With Rotating-Machine Internal Electrical Efficiency," AIAA Journal, Volume 6, Number 9, pp. 1695-1702, September 1968.
2. GESP-7017, A Design Study for a Magnetohydrodynamic Power System for a Nuclear Electric Propelled Unmanned Spacecraft, Quarterly Progress Report No. 1, September 1969.
3. Pierson, E. S. and Jackson, W. D. , "The MHD Induction Machine," TR AFAPL-TR-107, May 1966, Air Force Aero-Propulsion Laboratory, Weight-Patterson Air Force Base, Ohio.
4. Elliott, D. G. et al. , "Theoretical and Experimental Investigation of Liquid Metal MHD Power Generation," Electricity from MHD, Vol. II, International Atomic Energy Agency, Vienna, 1966, pp. 995-1018.
5. Cerini, D. J. and Elliott, D. G. , "Performance Characteristics of a Single-Wavelength Liquid-Metal MHD Induction Generator with End-Loss Compensation," AIAA Journal, Vol. 6, No. 3, March 1968, pp. 503-510.
6. Elliott, D. G. , "Effect of Slots on MHD Induction Generator Efficiency," Tenth Symposium of Engineering Aspects of Magnetohydrodynamics, pp. 51-52, Cambridge, Massachusetts, March 1969.
7. Elliott, D. G. , and Weinberg, E. , "Acceleration of Liquids in Two-Phase Nozzles," Technical Report 32-987, Jet Propulsion Laboratory, Pasadena, California, July 1, 1968.
8. Reneau, L. R. , Johnston, J. P. , and Kline, S. J. , "Performance and Design of St Straight, Two-Dimensional Diffusers," Report PD-8, Department of Mechanical Engineering, Stanford, California, September 1964.
9. Thrust Subsystem Design for Thermionic-Electric Spacecraft Study, JPL Memo T. Masek to N. Simon, February 20, 1969.
10. GESP-7013, A Design Study for a Thermionic Reactor Power System for a Nuclear Electric Propelled Unmanned Spacecraft, Quarterly Progress Report No. 2, August 1969.
11. GE-PIR No. U-1K25-072, J. Garrity, J. Cokonis to W. Z. Prickett Addendum to Structural/Dynamic Analysis of Thermionic Spacecraft Configurations, August 4, 1969.

12. PWAC-445, Preliminary Design of the 2 MWT Reactor and Shield (PWAR-20) for the SNAP-50/SPUR Power Plant, December 30, 1964.
13. PWAC-643, SNAP-50/SPUR Program Engineering Progress Report, July 1, 1964 to September 30, 1964.
14. PWAC-457, 35 and 300 kWe SNAP-50/SPUR Power Plants for the Manned Orbiting Space Station Application.
15. NASA Lewis Research Center Internal Memorandum, Information on Nuclear Space Power Systems, October 1969.
16. Letter from F. R. Mynatt (ORNL) to W. Z. Prickett (GE) dated September 23, 1969.
17. Hays, L. G., and Cerini, D. J., Liquid Metal Magnetohydrodynamic Power Conversion NASA-JPL Space Programs Summary, Vol. III, 37-49 and 37-50, February 1968 and April 1968.
18. Calculations of Can Losses in Canned Motors, R. C. Robinson, I. Rowe, L. E. Donelan, Paper 57-134, AIEE Winter General Meeting, New York, January 1957.
19. General Electric Medium A. C. Motor Department Design Data Curve No. 144 HA 406 revised, R. G. Rhudy/G. Angst.
20. Performance and Design of Alternating Current Machines, M. G. Say and E. N. Pink, Pitman and Sons, London, 1936.
21. Final Report - Potassium Turboalternator Design Study, Contract NAS 3-10933, November 1969.
22. Elliott, D. G. and Weinberg, E., JPL Technical Report 32-987, "Acceleration of Liquids in Two-Phase Nozzles," July 1, 1968.
23. GEMP-685, R-68-NSP-9, Creep-Rupture Data for the Refractory Metals to High Temperature, March 1969.
24. Heller, J. A., Moss, T. A. and Barna, G. J., 4th Intersociety Energy Conversion Engineering Conference, pp. 465-483, Washington, D. C., September 1969.
25. Bogdanoff, D., "Liquid-Gas Separation Using Impinging Two-Phase Jets," Eleventh Symposium on Engineering Aspects of Magnetohydrodynamics, pp. 149-153, Pasadena, California, March 1970.
26. Personal Communication, D. G. Elliott to R. M. Bernero, March 27, 1970.

27. R 65SD3010, Electromagnetic Alkali Metal Pump Research Program, R. G. Rhudy and J. P. Verkamp, September 1965.
28. NASA CR-911, Design of Two Electromagnetic Pumps, G. E. Diedrich and J. W. Gahan, November 1967.
29. Cockfield, R. D., "Comparison of Load Bearing and Non-Load Bearing Radiators for Nuclear Rankine Systems," CR-72307, May 6, 1967, NASA.
30. Hagen, Kenneth G., "Integration of Large Radiators with Nuclear Electric Spacecraft Systems," Air Transport and Space Meeting, New York, New York, April 1964.
31. Cockfield, R. D. and Killen, R. E., "Comparison of Direct Condensing and Indirect Radiators for Nuclear Rankine Systems," NASA CR-72318, July 26, 1967.
32. Fraas, A. P., "Design and Development Tests on Direct Condensing Potassium Radiators," AIAA Specialists Conference on Rankine Space Power Systems, October 1964.
33. Gutierrez, O. A., Sekas, N. F., Acker, L. W., and Fenn, D. B., "Potassium Condensing Tests of Horizontal Multitube Convection and Radiative Condensers Operating at Vapor Temperatures of 1250 to 1500°F," AIAA Specialists Conference on Rankine Space Power Systems, CONF-651026, October 1965.
34. "Compatibility of Liquid and Vapor Alkali Metals with Construction Materials," DMIC Report 227, Battelle Memorial Institute, April 1966.
35. "Sixth Progress Report by the Committee on Beryllium Metallurgy of the Materials Advisory Board," Publication MAB 199-M(6), National Academy of Sciences, National Research Council, Washington, D. C., April 1966.
36. ALO 3632-39, UC-33, Union Carbide Corporation Linde Division, Quarterly Progress Report of Research and Development in a Thermal Insulation Study, December 1968 to February 1969.
37. Pierson, E. S., Brown, G. S., and Jackson, W. D., Liquid Metal MHD AFAPL-69-33, May, 1969.
38. Pierson, E. S., "Preliminary Experimental Results from a One-Wavelength MHD Induction Generator", Eleventh Symposium on Engineering Aspects of Magnetohydrodynamics, pp. 161-164, Pasadena, Calif. March 1970.

A P P E N D I X A
PROPOSED DESIGN CONSIDERATIONS
FOR CHANNEL OF MHD INDUCTION
GENERATOR

PROPOSED DESIGN CONSIDERATIONS FOR CHANNEL OF
MHD INDUCTION GENERATOR

Introduction

The liquid metal MHD induction generator being developed at JPL was reviewed from the Mid-term Report No. GESP-7025, December 1969, entitled "A Design Study for Magnetohydrodynamic Power System for a Nuclear Electric Propelled Unmanned Space Craft".

In its simplest concept, the JPL MHD induction generator consists of two parallel insulator walls sandwiched between two opposing magnets. The walls are separated on opposite sides by two electrical conducting electrodes forming an open rectangular channel. Electrical currents are generated by the movement of hot liquid lithium through the channel cutting the magnetic field. This system has a number of interesting attributes that could contribute to a highly reliable long-life power system. The proposed cycle with an upper temperature of 2300°R and a lower temperature range of $\sim 1300^{\circ}\text{R}$ certainly is not too demanding from a materials standpoint. The selection of Cb-1Zr for piping, reactor structures and channel housing is in all probability is the best choices based on today's liquid metals technology. (1,2,3)

There are a number of materials problems associated with this system and one of the most difficult is associated with the electrical insulator used in the channel housing. Non-metallics, which are electrical insulators, are all severely attacked by hot lithium. Those materials which may resist lithium corrosion at moderate temperatures become unsatisfactory or useless at temperatures in excess of 1000°C . (4) Therefore, the only immediate

solution is to clad those ceramic surfaces exposed to hot flowing lithium. This is made possible by recent technical advances in hot-gas-isostatic pressure bonding technology for bonding thin metallic sheaths to ceramics. For example, Cb-1Zr can be mechanically and chemically bonded to high density Al_2O_3 . When bonded, these structures are capable of being thermal cycled many times at temperatures ranging from room temperature to 1600°C without loss of bond integrity. Bonding of Cb-1Zr to Al_2O_3 is proposed as a direct approach eliminating lithium attack on ceramics.

The side electrical conductor bars designed to carry heavy shunting currents should be constructed of excellent electrical conducting material. Commonly used materials such as copper, aluminum, and silver all will become very weak at the normal operating temperatures of the system, and furthermore, none of these metals are resistant to the corrosion action in lithium for any substantial length of time. Corrosion resistance can only be insured by cladding each conductor bar with Cb-1Zr.

The stator blocks are temperature sensitive and must be kept below 1400°F, the curie temperature of iron. In addition, the copper winding must be kept cool as practical to minimize I^2R losses. This requires the use of metal coolants or thermal insulation blankets between the channel and the stator blocks to keep the transfer of heat from the channel at its lowest possible level. It is proposed that a zirconia textile cloth be incorporated into the generator system in the area between the stator and the channel. Calculations show that a 50 mil layer of zirconia cloth can reduce the heat transfers from the channel into the stator to only about 1/2 KW/hr. The use of thermal insulators becomes quite attractive as it eliminates the need for dynamic coolants between the channel and the stator.

Proposed Configuration

The proposed design of the MHD induction generator lithium channel is shown in Figure 1. The design is a simple non-rigid structure with built-in flexibility to minimize thermal and mechanical stresses that are prone to develop by temperature differences. Because techniques are well developed for cladding of Cb-1Zr on to Al_2O_3 , alumina has been selected to be the ceramic member. In addition, alumina is also one of the strongest and most shock resistant of the potentially useful ceramics that can be considered. Included for comparative purposes are a family of curves showing the modulus of rigidity. These data, shown in Figure 2, illustrate the superiority of Al_2O_3 over other oxide systems. As a thermal insulator Al_2O_3 , although not the best, is much better than BeO for example and almost equivalent to ThO_2 and ZrO_2 . Figure 3 has been included to depict the thermal conductive relationship of Al_2O_3 with other ceramics. Generally speaking, alumina appears to be one of the best possible choices for use as a construction material for the MHD generator.

The size of the MHD channel will conform to the recent established dimension by JPL.⁽⁶⁾ The ceramic structure will consist of a single plate of Al_2O_3 measuring 4.56 inches wide by 12.8 inches long. Without any attempt to optimize the thickness (1/8" - 1/4" thick) Al_2O_3 appears to be suitable for fabrication and cladding evaluation. These thicknesses are commercially available and have sufficient strength to withstand the internal lithium pressure. This is especially true if the channel is firmly backed by the stator.

The metal sheath selected to clad the Al_2O_3 should be as thin as practical (~.005"). Greater thickness will result in unacceptable power losses from

eddy currents. Using present hot isostatic bonding techniques, full size 4.5" x 13" plates with required tabs and auxiliary fixturing for attachment to the side shunt electrodes and headers can be fabricated as a single unit. Depending upon the materials and thermal expansion characteristics of each component, the interface may or may not be graded.. Grading is only useful where major differences in thermal expansion exist. The bond interface developed between the Al_2O_3 and Cb-1Zr after hot isostatic pressure bonding if ungraded, will be typical of that shown in Figure 4. The photomicrograph shows the structure at the interface formed between unalloyed columbium and Al_2O_3 after hot isostatic pressure bonding for 1 hour at 1650°C at 10,000 psi. Figure 5 shows the microstructure of the graded concept. Grading is produced by mixing various Al_2O_3 -metal powder ratios and spraying or painting on layer of various metal-to-ceramic ratios on the Al_2O_3 surface before hot-gas-isostatic bonding. When bonded, the structure is brought to full density by the isostatic pressure. The metal-ceramic grade is such that interface stresses caused by mismatch differences in the thermal expansion of materials often developed during thermal cycling are minimized. In the case of Al_2O_3 and Cb-1Zr, the thermal expansion rates are essentially identical and therefore it is not necessary to grade. The only precaution required is to make sure that the surfaces are suitably prepared to develop mechanical interlocking at the interface. When bonded, Cb-1Zr and Al_2O_3 are not only mechanically interlocked, but there is strong evidence that bonding is also chemical.

Ceramic-to-metal graded structure, tested to develop information concerning the thermal stability and compatibility of this system, have always proven to be structurally sound after many hours of thermal cycling. Figure 6 shows a group of photomicrographs taken of the interface structure

after various lengths of time at 1600°C. From all observations, no evidence has ever been found showing the loss of integrity. The interface bond areas are relatively strong. Tensile tests have shown strength ranging from 12,000 to 20,000 psi. (5)

Hot isostatic pressure bonded ceramic-to-metal systems either graded or ungraded are highly reproducible and quite resistant to both thermal shock and thermal cycling. The use of Cb-1Zr clad Al₂O₃ insulator slab will raise the temperature capabilities above that of unclad Al₂O₃ or any other oxide system. It will also enable the designer to build a more compact channel with a subsequent increase in the overall efficiency of the MHD system.

Along each side of the MHD (Figure 1) channel are two electrical shunt bars. In this design it is proposed that the shunts be operated at the lithium fluid temperature as any attempt to cool them will reduce the overall efficiency of the device. Heat losses by radiation can be minimized by thermal shielding each shunt bar. Figure 7 shows a series of curves depicting the electrical resistance of Ag, Cu, Al, Li, Mo and Cb. Because the normal operating temperature is above the point where Ag, Cu, or Al have any substantial strength, it is suggested that either of two courses be taken. The simplest and least difficult approach is to use molybdenum as the electrode material as its electrical conductivity is relatively good. Molybdenum bars could easily be clad with 20 mils thick Cb-1Zr alloy. Cladding would be bonded to the molybdenum by hot-isostatic techniques. A second possibility is to use a liquid lithium housed in a Cb-1Zr as a shunt. Such a shunt could be prepared by using a hollow rectangular polygon of Cb-1Zr and filling it with lithium. Some bellows

arrangement would be necessary to compensate for the difference in thermal expansion. Lithium filled shunt bars have one paramount advantage of being light weight, thus, decreasing mechanical stress on the structure during earth bound operation or by G-loading during launch. Because of the advantage offered by an uncooled shunting electrode, it is suggested that strong consideration be given to the use of a lithium or molybdenum shunt.

The assembled channel after the attachment of front and exit headers would be insulated from the stator coils using a zirconium textile product. This product is manufactured by Union Carbide Corporation as a zirconia cloth or felt. The zirconium oxide has been stabilized in the tetragonal form by the addition of Y_2O_3 . The tetragonal form of zirconia ceramic offers the highest density and the lowest thermal conductivity and linear coefficient of thermal expansion of all the zirconia phase modifications. The zirconia textiles maintain its fibrous form to temperatures above 3000°F. Figure 8, prepared by Union Carbide,⁽⁷⁾ shows the thermal conductivity of this material in various atmospheres. From this data by a quick calculation with the assumption of a temperature differential of 500°F show that the heat transfer through ~0.050 inch of this material will be ~0.5 KW of thermal energy. This material offers exceptional thermal resistance and will eliminate any need for dynamic cooling either by NaK or cesium vapor.

It is believed that these design modifications made possible by the development of the ceramic-to-metal bonding technology will substantially increase the efficiency of the MHD system. Revised calculations find that the can losses (induction heating losses generated in duct wall) of the proposed composite duct design as applied to this MHD generator design are

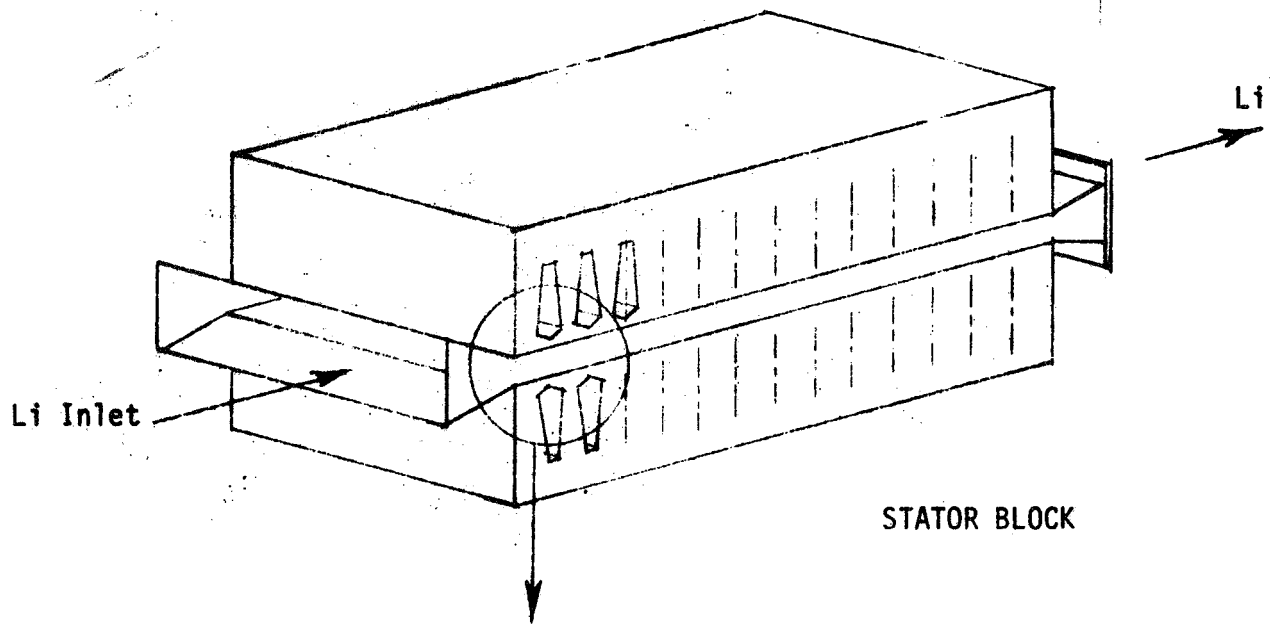
less than 10 KW, which is a completely acceptable level of loss. This results from reduced field strength, reduced field wave velocity and reduced metallic duct wall volume.

Summary

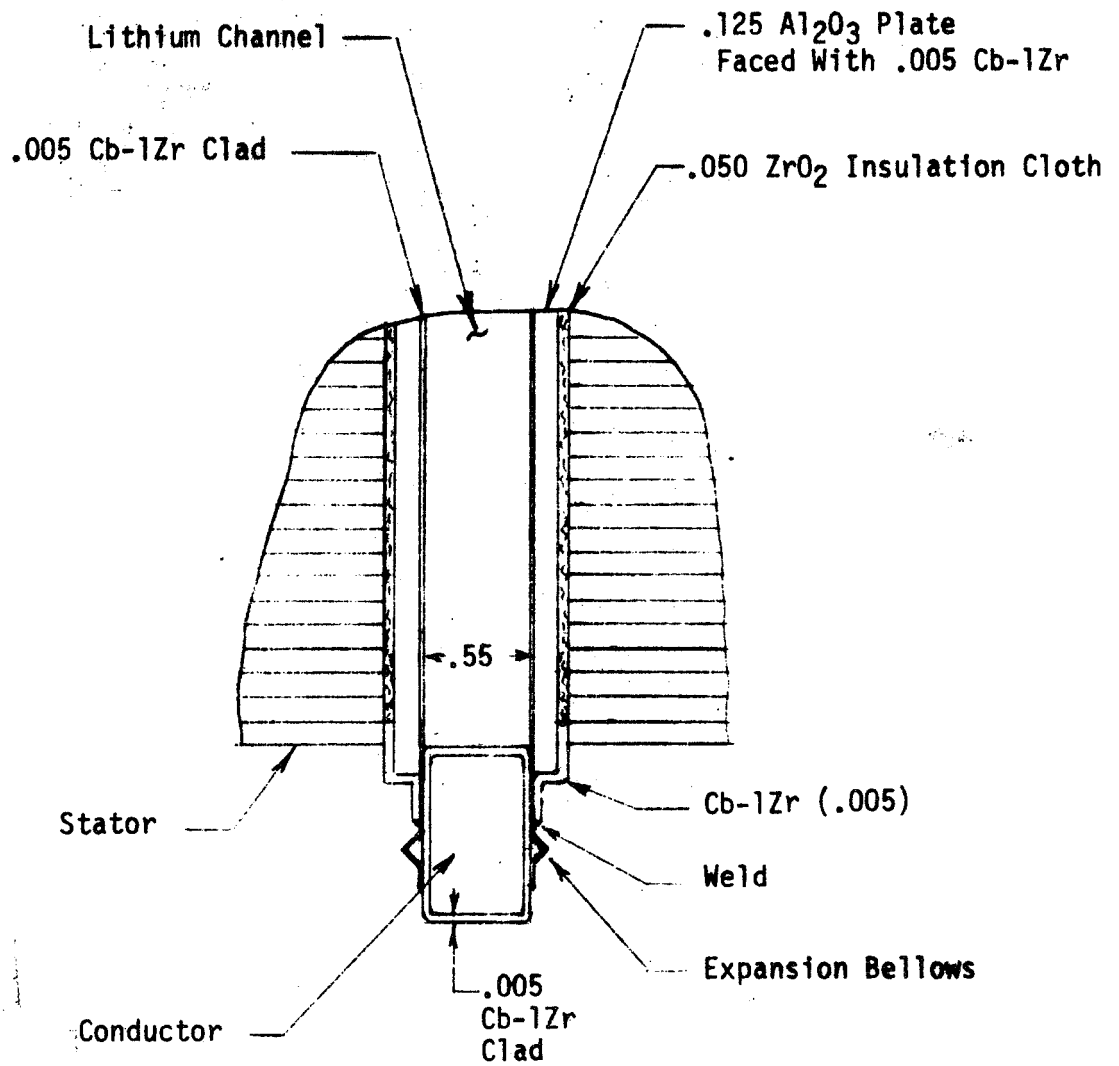
The design presented takes advantage of newly developed techniques for bonding Cb-1Zr sheath to Al_2O_3 structures and offers a direct solution to solving any problem associated with lithium corrosion. Fabricating the shunt electrodes by cladding with Cb-1Zr over molybdenum removes any need of cooling. The removal of cooling requirements for the electrodes as well as removing the need for cooling in the area between the channel and the stator makes it quite attractive for increasing the total efficiency of the system. The design as described is based on current technology and all suggested methods of fabrication have previously been established.

References - Corrosion Resistance of Cb-1Zr to Lithium

1. Hoffman, E. E. and Harrison, R. W., "The Compatibility of Refractory Metals with Liquid Metals", Refractory Metal Alloys, Metallurgy and Technology, Editors, I. Machlin, et al, Plenum Press, New York, 1968, p. 265.
2. Hays, L.G., "Corrosion of Niobium - 1% Zirconium Alloy and Yttrium by Lithium at High Flow Velocities", Jet Propulsion Laboratory Technical Report 32-1233, December 1, 1967.
3. Cowles, J. O. and Pasternak, A.D., "Lithium Properties Related to Use as a Nuclear Reactor Coolant", Lawrence Radiation Laboratory Technical Report UCRL-50647, April 18, 1969.
4. Cook, W.H., "Corrosion Resistance of Various Ceramics and Cermets to Liquid Metals, Oak Ridge National Laboratory, Report ORNL-2391, 1960.
5. Kaufman, W., Tischler, R., and Breitwiesser, R., "High Temperatures, Electrical Insulation Cermet Seal Having High Strength and Thermal Conductivity", Thermionic Conversion Specialists' Conference, Palo Alto, California, October 30, 1967.
6. 200 kWe MHD System design calculations (D. G. Elliott) of March 11, 1970
7. Developmental Product Information Bulletin No. CER-101, Union Carbide Corporation, April 1968.



STATOR BLOCK



MHD GENERATOR Li CHANNEL

Figure 1. Proposed MHD Channel Design.

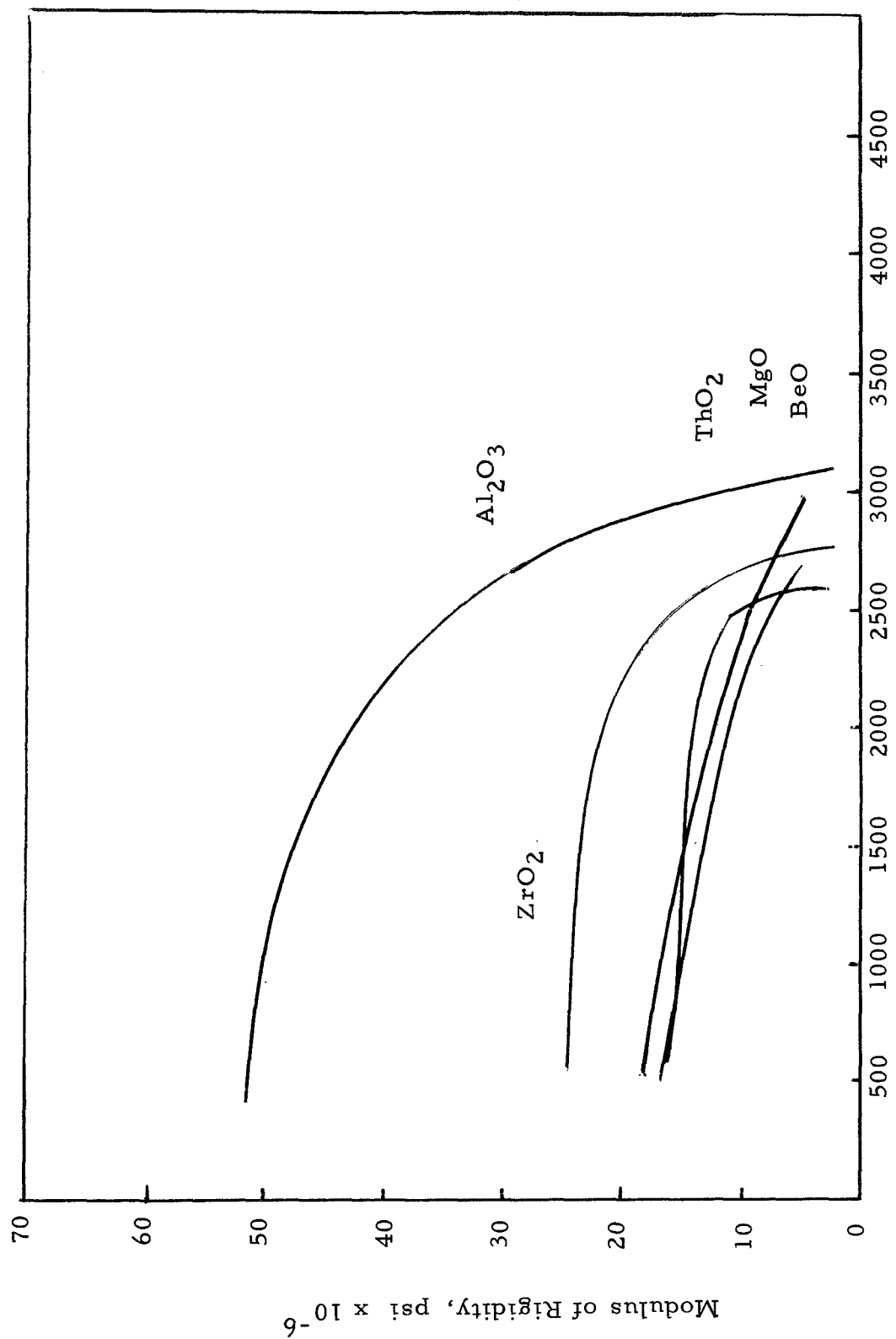


Figure 2 - Modulus of Rigidity - - Al₂O₃, ZrO₂, BeO, MgO and ThO₂

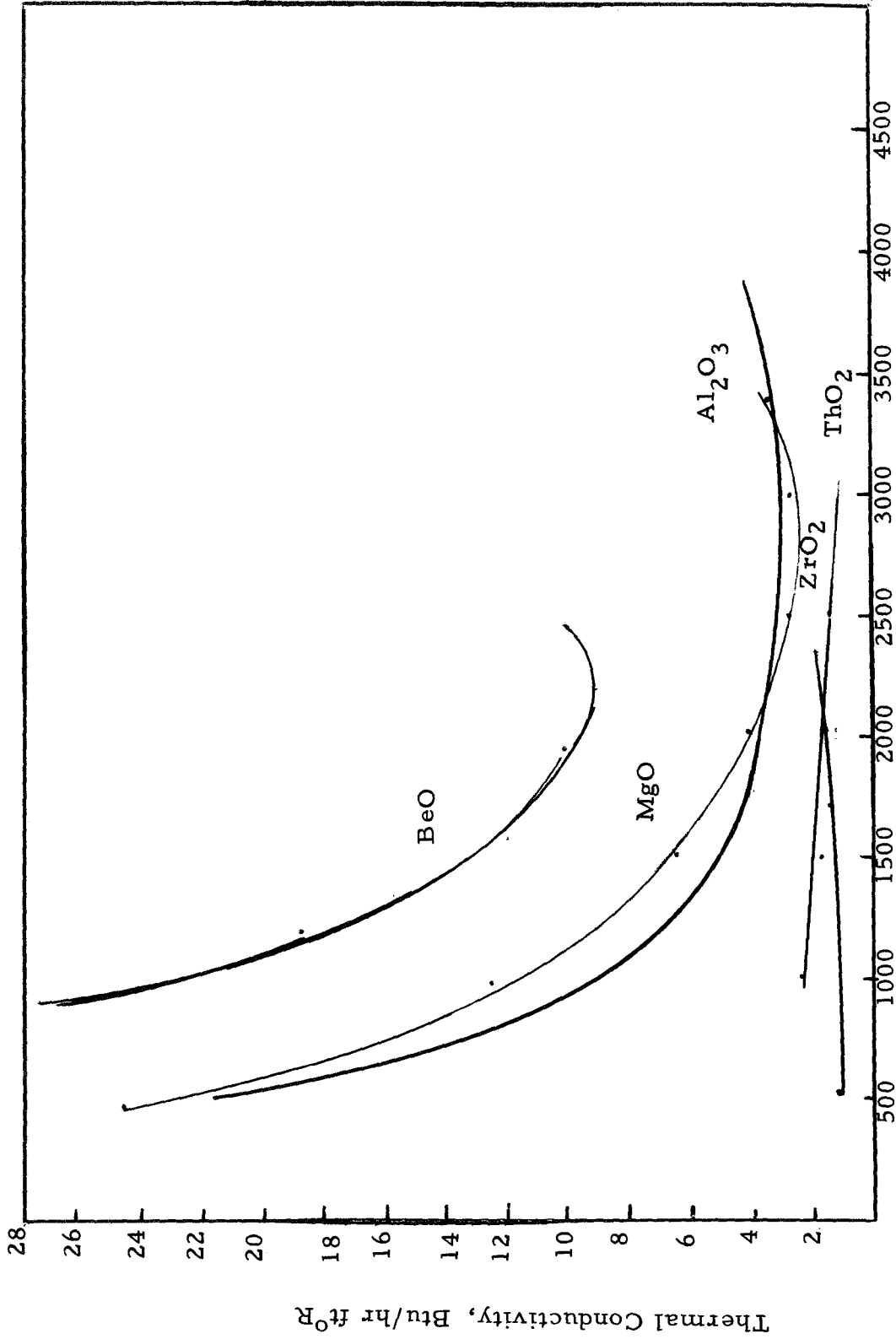


Figure 3 - Thermal Conductivity - - Al₂O₃, ZrO₂, MgO, BeO and ThO₂



Neg. No. 3510 500X As-polished

Figure 4 - Photomicrograph showing the interface formed between Nb and Lucalox after pressure bonding with 700 kg/cm^2 at 1600°C .

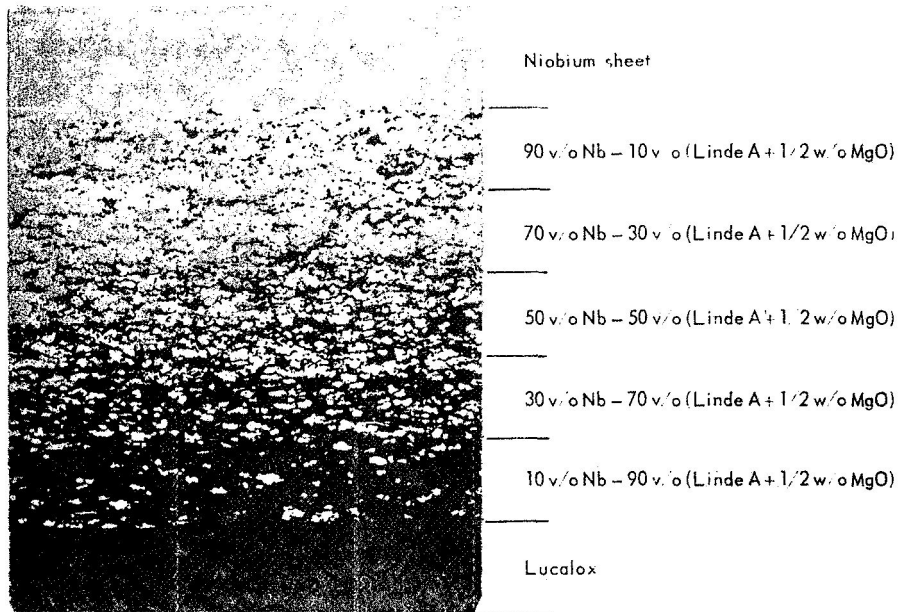
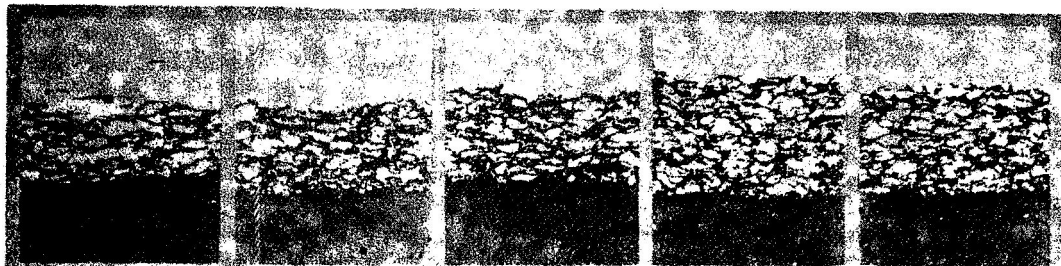


Figure 5 - Niobium to Lucalox graded interface after bonding. Vacuum-tight after 100 thermal cycles between 650° and 1450°C at heating and cooling rates of 300°C per minute. (100X)

METAL TO CERAMIC SEAL
Life Test at 1600°C



After autoclave
at 1650 C
and 10,000 psi

After 115 hours

After 500 hours

After 1234 hours

After 1738 hours

Figure 6 - Illustration of seal thermal stability

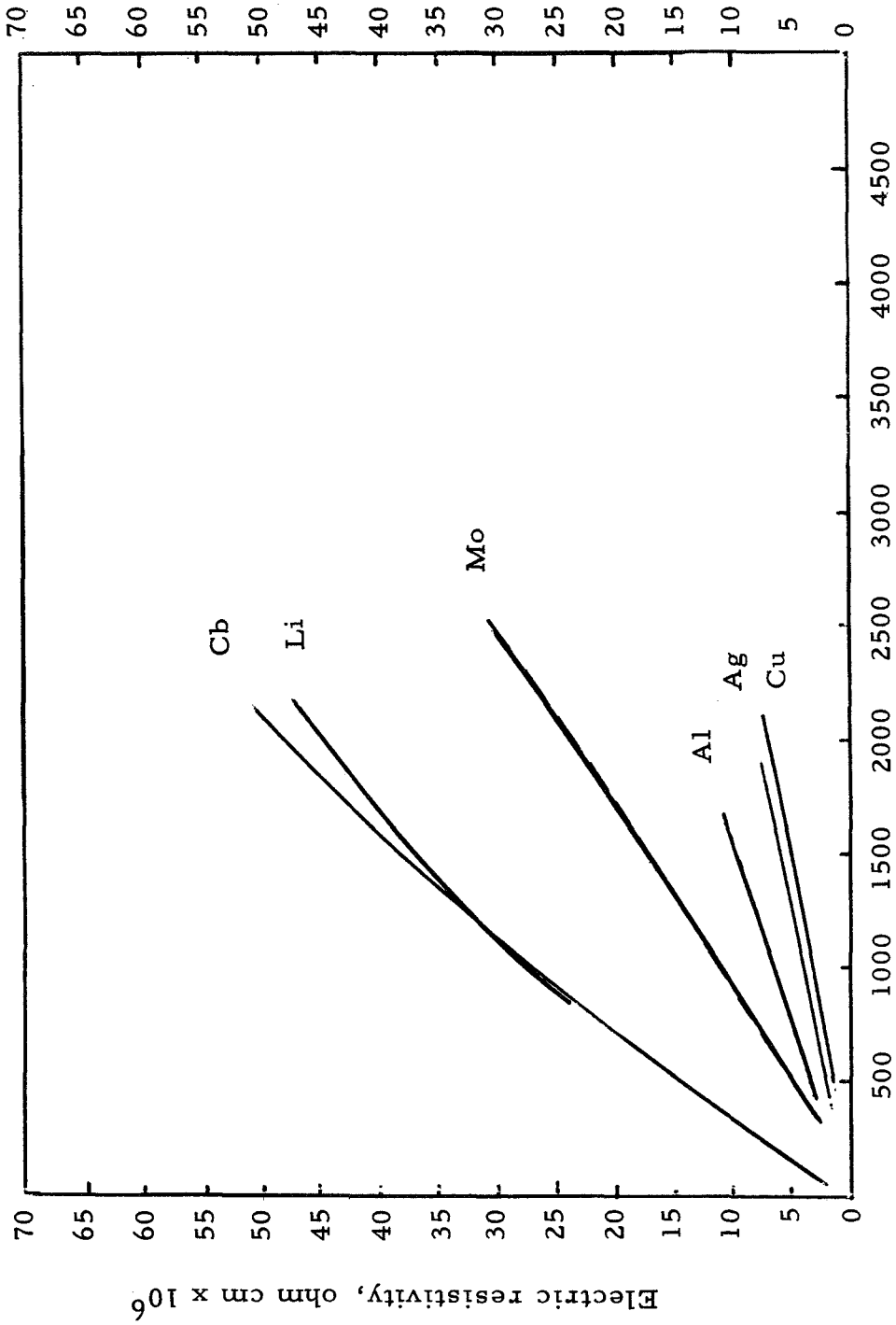


Figure 7 - Electrical Resistivity of Cb, Li, Mo, Al, Ag and Cu

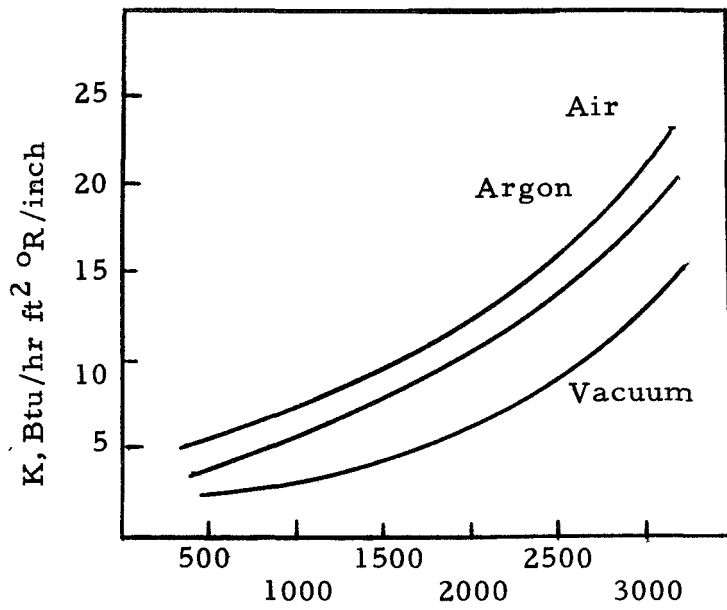


Figure 8 - Thermal Conductivity of Zirconia Felt in Various Atmospheres

GENERAL  ELECTRIC
SPACE DIVISION
SPACE SYSTEMS ORGANIZATION